AN EXPERIMENTAL AND FINITE ELEMENT ANALYSIS OF TEMPERATURE AND STRESS FIELDS IN GIRTH WELDED 304L STAINLESS STEEL PIPES

Ming Li
B.S., Shanghai Jiao Tong University, Shanghai, China, 1984
M.S., Shanghai Jiao Tong University, Shanghai, China, 1987

A dissertation submitted to the faculty of the
Oregon Graduate Institute of Science & Technology
in partial fulfillment of the
requirements for the degree
Doctor of Philosophy
in
Materials Science and Engineering
April, 1995

The dissertation "An Experimental and Finite Element Analysis of Temperature and Stress Fields in Girth Welded 304L Stainless Steel Pipes" by Ming Li has been examined and approved by the following Examination Committee:

David G. Atteridge, Thesis Advisor
Professor

William E. Wood
Professor and Chairman

Jack H. Devletian
Professor

Lemmy L. Meekisho
Assistant Professor

Dr. Scott L. West
Westinghouse Savannah River Company

This thesis is dedicated to my parents and my wife.

ACKNOWLEDGEMENTS

First of all, I would like to express my deep appreciation to Dr. David Atteridge for his encouragement, enthusiasm and support during the course of this work.

Special thanks are also due to Mr. William Anderson, Dr. Scott West and Dr. Lemmy Meekisho for their guidance at various stages of the research. Thanks are also extended to the other members of my dissertation committee, Dr. William Wood and Dr. Jack Devletian, for their time and effort in reviewing the manuscript.

I would also like to express my gratitude to all of the students, staff, and faculty in the Materials Science and Engineering Department with special thanks to Jessie Atteridge, Ken Burns, Doug Davis, Dr. Vivek Dikshit, Dr. Lu Fang, Youping Gao, Kristen Terry, Bob Turpin, and Andy Villeneuve for their help at various stages of this research.

Last, and certainly not least, I would like to thank my wife, Dr. Gengying Gao, my son, Bobby, and my mother for their patience, encouragement and support during the difficult times of writing this thesis.

Funding for this research was provided by Westinghouse Savannah River Company of the U. S. Department of Energy under subcontract no. AA46386. Part of this research (neutron diffraction stress measurement) was carried out at Oak Ridge National Laboratory (ORNL). I am very grateful to Drs. Xunli Wang, Steve Spooner, and Camden Hubbard of ORNL for their help during my experiment there. The welding experiment of this research was conducted at Arc Machines, Inc. at Pacoima, California. I am also grateful to people there for their help.

TABLE OF CONTENTS

LIST OF TABLES

LIST OF FIGURES

ABSTRACT

AN EXPERIMENTAL AND FINITE ELEMENT ANALYSIS OF TEMPERATURE AND STRESS FIELDS IN GIRTH WELDED 304L STAINLESS STEEL PIPES

Ming Li

Supervising Professor: David G. Atteridge

This research sought to understand the residual stress development during 304L stainless steel pipe girth welding process with an emphasis on thermomechanical history measurements, residual stress measurements, and computational modeling of welding and stress mitigation precesses.

Thermomechanical histories were measured for three 406-mm-diameter, schedule 40 pipe girths welds. Two welds were standard V groove prepared and completed in six and nine passes with multiple start-stop positions, while the third one had a narrow groove configuration and was finished with four passes and one start-stop position. Thermomechanical history measurements were taken on pipe inner surfaces to monitor weld shrinkage, surface temperatures, surface temperatures, surface strains, and radial deformations. The results show that: 1). the temperatures profiles in V groove weldments are axisymmetric, while in the narrow gap groove weldment they are axisymmetric except in locations near welding start-stop position; 2). the strain/deformation value is decided by the last one or two welding passes; 3). the strain/deformation profile in the weldment is not axisymmetric suggesting that the residual stress is not axisymmetrically distributed; 4). the four-pass narrow gap weldment has the lowest level of radial deformation among the three pipe weldments indicating that

the narrow gap weldment would have the lowest overall residual stress level among the three pipe weldment.

Residual stress measurements were performed on outer surfaces of the four- and six-pass weldments by the air-abrasive hole-drilling method and on the inner surface of four-pass weldment by the neutron diffraction method. The results show that the residual stress distribution is not axisymmetric. This comparison between the residual stress measurements demonstrates that the four-pass weldment has the lowest residual stress level among the three pipe weldments.

A 3D finite element model was established to simulate the narrow gap pipe girth welding process. The calculated temperature histories and their distributions are in good agreement with the experimental data. The calculated residual stress distribution is axisymmetric except in locations near the welding start-stop position. This is not in agreement with the experimental observation. The overall comparison between the calculated and experimental stress results demonstrated reasonable agreement between them.

An axisymmetric 2D finite element model was conducted for four-pass welding and welding plus cooling stress improvement (CSI). The results indicate that the weld induced stresses on the pipe inner surface are tensile in weld region and remain so for a certain distance from the weld centerline. CSI treatment after welding can convert the tensile stresses to compressive values.

CHAPTER 1
INTRODUCTION

Many austenitic stainless steel (SS) pipes, such as Types 304 and 316, are used in various plants including nuclear reactors because they have excellent corrosion resistance, strength at high temperatures, and fracture toughness at low temperatures. Nevertheless, incidents of intergranular stress corrosion cracking (IGSCC) in austenitic stainless steel piping systems in boiling water rectors (BWRs) have been reported for more than a decade. To date over one thousand incidents have occurred worldwide. While pipe cracking does not constitute a hazard or safety issue to the public, it has significantly reduced plant availability and reliability. The economic impact has been considerable; the replacement power cost for a 1000 mega watt (MW) electric plant is estimated at $240,000 per day excluding costs for repair (1,2). These cracking incidents have also increased radiation exposure to workers in inspection and repair operations.

A model for the mechanism of IGSCC in welded Type 304 and 316 SS pipes was developed (1-4). The basis for this model was the coexistence of three key factors on the inner surface of the pipe weld heat-affected zone (HAZ): 1) tensile residual and/or applied stress, 2) sensitized material, and 3) an "aggressive" aqueous environment. The IGSCC susceptibility of the welded Type 304 and 316 SS pipe depends on the severity or intensity of the three contributing factors. A minimum of one of these three factors must be controlled in order to prevent IGSCC. A schematic representative of these three factors is illustrated in Figure 1 (1,2).

In reality, it is usually very difficult to control the environment to such a degree that IGSCC is impossible. Thus, there is the need to study material sensitization and tensile residual stress development in weldments.

Sensitization is a process by which austenitic stainless steels lose their inherent

excellent corrosion resistant properties. It is characterized by localized corrosion in the vicinity of grain boundaries. As proposed by Strauss *et al* (5) and Bain *et al* (6), it is now well established that sensitization of austenitic stainless steels is caused by Cr depletion at grain boundaries due to Cr-rich carbide precipitation in grain boundaries. Grain boundary regions depleted in Cr to less than 13 at.% are susceptible to corrosive attack. Three commonly employed methods for preventing sensitization are: 1) avoidance of the critical temperature range for Cr-rich carbide formation (773 to 1223 K), 2) reduction of carbon levels, and 3) addition of a carbide stabilizing element (Ti, Cb). During the past decade, experimental and theoretical research of sensitization of austenitic stainless steels has been conducted extensively at Oregon Graduate Institute of Science & Technology (OGI) and Pacific Northwest Laboratory (PNL) (7-13), and the nature of this phenomenon is now well understood. This subject will not be discussed further in this thesis.

A localized intense moving heat source produces a non-uniform, transient temperature field in arc welding. The non-uniform heating and cooling of metal during and after the welding operation causes non-uniform thermal expansion and contraction, generating plastic deformation in the neighborhood of the weld. This results in residual strains/stresses and permanent distortions of the weldment upon cooling. In the conventional multipass girth welding of austenitic stainless steel pipes, thermal expansion and shrinkage are produced during the welding process, and they can be divided into axial, circumferential and through-wall expansion and shrinkage, as shown in Figure 2 (14). This expansion and shrinkage produces corresponding deformation and result in the final residual stress state, as expressed in Table 1 (14). A peak axial weld residual stress measured on the inner surface of Type 304 stainless steel pipes is displayed in Figure 3 (1,3,4), and the through-wall distribution of weld residual stress in a 66 cm diameter, Type 304 stainless steel pipe is given in Figure 4 (15). These figures and table indicate that the residual stresses on the inner surface near the fusion zone of a conventional multipass girth weld of an austenitic SS pipe exhibit high tensile

values and is the region of main concern for IGSCC. Thus one method for reduction and/or prevention of IGSCC in austenitic SS pipe weldments is to control and/or mitigate weld tensile residual stresses, requiring studies such as presented herein.

The objective of this research was to develop an understanding of residual stress development during austenitic SS pipe multipass girth welding process, with an emphasis on the following:

(1) Thermomechanical history measurements.

(2) Residual stress measurements.

(3) Computational modeling of welding process.

(4) Computational modeling of residual stress mitigation process.

Table 1. Mechanisms of Production of Welding Residual Stresses in Pipe Weldment

Component of Stress	Location	σ_A	σ_C	σ_R
σ_z	O. S.	0	-	-
	I. S.	0	+	+
σ_θ	O. S.	0	+	+
	I. S.	0	+	+

σ_z : Axial Stress
σ_θ : Circumferential Stress
σ_A : Stress due to Axial Expansion and Shrinkage
σ_C : Stress due to Circumferential Expansion and Shrinkage
σ_R : Estimated Residual Stress
O.S. : Outer Surface in Weld Zone
I.S. : Inner Surface in Weld Zone

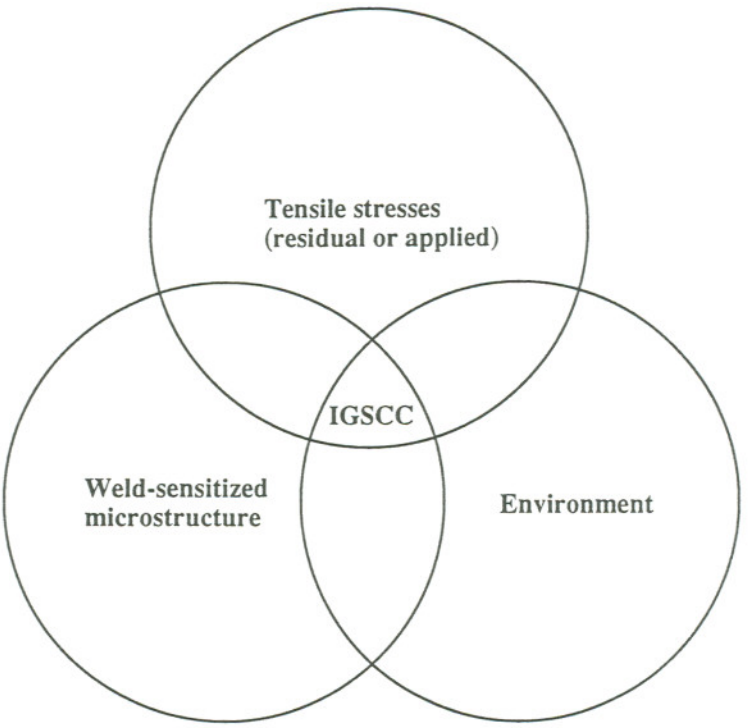

Figure 1. Major Factors Contributing to IGSCC in Welded 304 and 316 SS Pipes (1,2)

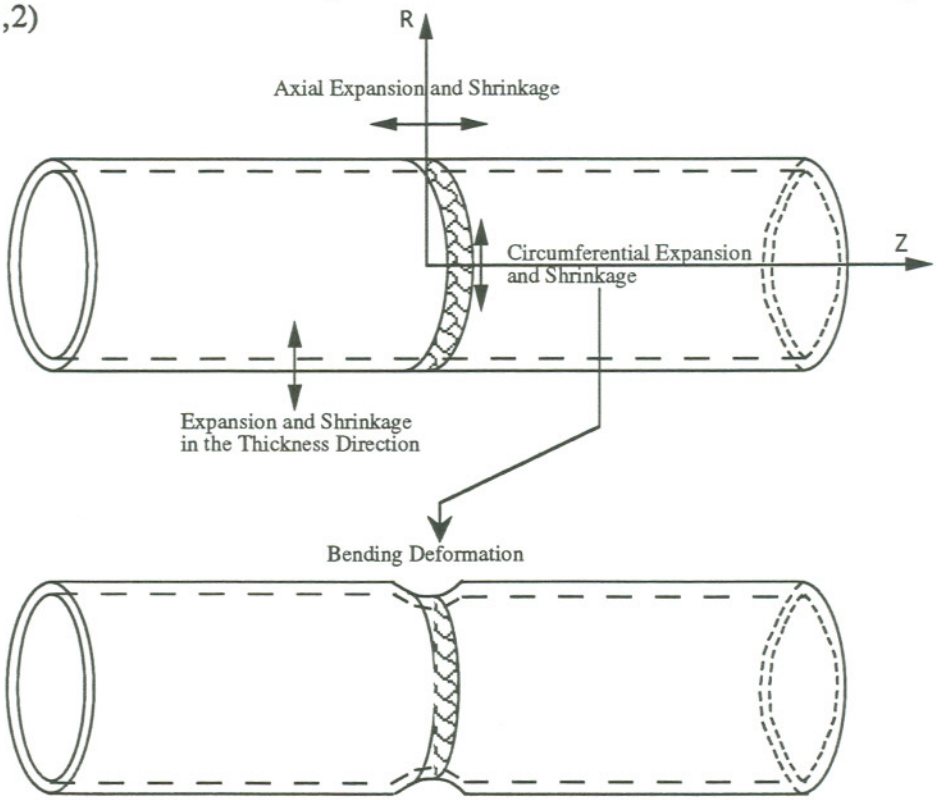

Figure 2. Expansion and Shrinkage at the Joint of a Pipe Circumferential Butt Welding (14)

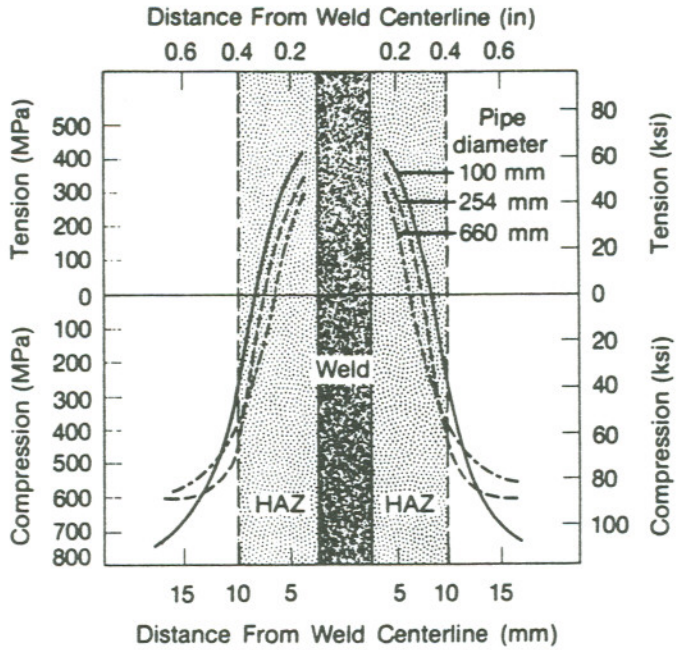

Figure 3. Peak Axial Inner Surface Tensile Residual Stresses in Welded 304 SS Pipes (1,3,4)

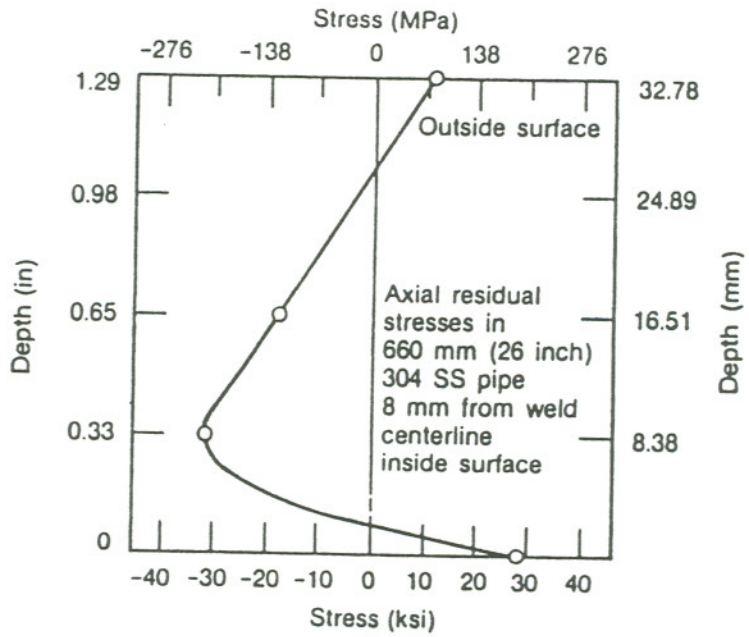

Figure 4. Through-Wall Axial Residual Stresses for a Girth Welded 304 SS Pipe (15)

CHAPTER 2
BACKGROUND

RESIDUAL STRESSES

Residual Stresses are those stresses that would exist in a structure in the absence of external loads (mechanical, thermal or chemical) and restraints. They are also called internal stresses, initial stresses, locked-in stresses, and inherent stresses (16-18).

Residual stresses in a structure occur as a result of many manufacturing processes. They may be produced

- in many materials, in many product forms such as plates, bars, and sections, during rolling, casting, heat treatment, and forging;
- during forming and shaping of parts by such processes as shearing, bending, machining, and grinding;
- during fabrication, such as welding.

Localized (or unevenly distributed) inelastic strains in a structure due to external loads and restraints will generate residual stresses in this structure after all external loads and restraints are removed. An important feature of residual stresses in a unconstrained structure is that they are self-equilibrating.

Residual Stresses in Weldments

Because a weldment is heated locally by the welding heating source, the temperature distribution in the weldment is not uniform, and there is a temperature difference between the weld area and areas adjacent to the weld which, in effect, creates a restraint on the higher temperature metal to prevent it from expanding and contracting

freely. As metal is heated to a higher temperature its strength is greatly reduced (see Figure 5). Thus inelastic strains are introduced in the weld metal and regions near the weld. After welding is completed and the weldment has cooled down, external loads and external restraints have been released, the stresses that remain are due to these inelastic strains. They are called the residual stresses in the unconstrained weldment.

Figure 6 shows the residual stress distribution in a butt weld of flat plate. The weld metal, originally subjected to the highest temperatures, tends upon cooling to contract more than other areas. This contraction is hindered by the other areas of the joint, thus resulting in the formation of high longitudinal tensile stresses in the weld metal. Similar tensile stresses arise in the transverse direction too, but of a smaller magnitude. As the distance from the weld increases, the tensile stresses decrease and then change to compressive as required by the equilibrium condition of residual stresses.

In examining a girth weld around a cylinder (pipe) and by analogy to the previous example for a flat plate, one might expect high hoop tensile stresses near the weld (direction parallel to the weld), and somewhat lower axial stresses along the length of the pipe. However, in a cylinder (pipe), the stress distribution may be modified by radial displacements (deflections or deformations). This mode of deformation is not available to the flat plate unless it is very thin and can buckle in regions of residual compressive stress. A deflected shape as shown in Figure 7 will reduce hoop tensile or compressive stresses, but will induce bending stresses in the axial direction. Thus the state of stress in a girth welded cylinder may be quite different from that in a flat plate (19,20).

A multipass weldment experiences complicated thermal heating and cooling cycles. Thus, welding procedure, parameters, joint design, and pass sequence may influence the finial residual stress state. For a multipass girth pipe weldment, the final few passes may decide the degree of final residual stress. It is quite possible, through changing welding parameters, joint design, and welding sequence, that the residual stresses in a pipe girth multipass weldment may be altered (21).

Residual stresses in a welded structure are unavoidable, but they should not

always be considered an adversity. They may have no effect or may have a beneficial effect on the service life of structure.

THERMOMECHANICAL HISTORY MEASUREMENT

Residual stresses in the weldment are closely associated with the temperature and strain development in the weldment during the welding process. Thus, measuring temperature and strain, or thermomechanical history measurement on welds, is the first step towards a general understanding of the nature of residual stress development during the welding process.

So far, very few studies on this subject have been reported. Atteridge and Anderson (7,22,23) investigated the thermomechanical history of a 60 cm diameter Type 304 stainless steel schedule 80 pipe girth weld. Thermal and strain histories during each weld pass, together with welding parameters, were recorded. Measurements were taken on the inside counterbore surface, including the heat affected zone (HAZ). These thermomechanical history measurements included weld shrinkage parallel to the pipe axis, counterbore surface temperature, counterbore surface strains parallel and perpendicular to the weld fusion line, and counterbore radial deflections.

The experimental data indicate that complex strain and thermal cycles take place in the HAZ. Counterbore strain history is controlled by expansion of the heated metal around the weld pool as well as shrinkage of the metal in the weld pool. The HAZ is subjected to both tension and compression strain components during each weld pass. These strain cycles induce work hardening in the HAZ and result in elevation of the HAZ flow stress above that of the base metal. This work also shows that cyclic strain is proportional to axial contraction. This indicates that the reduction of axial shrinkage (contraction) may reduce the final residual stress level on the inner surface of a pipe weldment. The phenomenon that the plastic strain is largely dependent on later welding passes was also observed in this work.

Disney (21), in work at the EPRI-NDE center, conducted research to monitor and document the weld thickness per layer and weld shrinkage per layer for different joint designs, welding parameters, and welding sequences. His work indicates that, by the optimization of welding parameters, joint designs, and welding sequences, the residual stress state on the inner surface of a pipe weldment may be minimized.

Jonsson and Josefson (24-26) studied both single and multi-pass girth-welding of mild steel pipes. In the multi-pass case, single U and narrow gap groove designs were used. The transient strain was measured at different positions during welding. The residual stress was measured after welding. Deviations from rotationally symmetric strain and stress fields in the pipe weldment were observed. The measured residual stresses and radial deflections on the outer surface were found to be somewhat larger for the narrow gap groove as compared to the single U groove.

Ueda *et al* (14) measured the temperature distribution in the wall thickness direction of a 10 cm diameter 304 SS pipe weldment. They concluded that the temperature difference between the inner and the outer surface of a pipe weldment during welding would decide the final residual stress state on the inner surface.

In all above studies, relatively small R/t (pipe radius to wall thickness) ratio, *i.e,* thicker pipes were used. In the present work, a relatively large R/t ratio (or thinner) pipe was employed. This type of thinner pipe would be expected to demonstrate different thermomechanical history behavior during welding. Thus one generic objective of this research was to record thermal cycles and deformation development during welding of 40-cm-diameter, schedule 40 304L SS pipes. A more specific goal was to document thermal and strain/deformation histories using different weld groove geometry designs and welding parameters. These results would then provide a solid experimental database for further optimization of welding procedures to minimize weld residual stresses.

Thermomechanical history measurement of welding process is essential but proves to be prohibitively expensive and time-consuming, and it often fails to provide a complete

picture of temperature and strain/deformation distribution in the weldment. Mathematic modeling proves to be a more effective way, but it must have a solid experimental basis.

COMPUTATIONAL MODEL

Over the past two decades, a number of investigators have attempted to predict temperatures and stresses during welding using both analytical and numerical models. The type of model used and the sophistication of the analysis has often hinged on the accuracy required and the type of computational resource available to solve the problem.

The computational model used to predict temperatures and stresses in a weldment generally consists of two parts: heat transfer and flow analysis, and thermal stress analysis. These two parts may or may not be coupled. Usually, prediction of welding residual stress using the finite element method is simplified by uncoupling the thermal and mechanical aspects of the problem so that the heat transfer analysis can be solved independently of the stress analysis. The assumptions for uncoupling are the dimensional changes during welding are negligible and that the mechanical work done during welding is insignificant compared to the thermal energy changes. Hibbitt (27) has shown that both assumptions are reasonable for the modeling of welding of steel. In the uncoupled approach, the link between the heat transfer analysis and the stress analysis is the temperature history which is used as the thermal load in the stress simulation.

Heat Transfer and Flow Analysis Model

The conservation of energy is the fundamental principle that underlies the analysis of heat flow. It is usually expressed in the form of a partial differential equation which can be found in any text on heat transfer (28,29). A finite difference approximation to the derivatives leads to the finite difference method (30). The error depends on the difference between the finite difference approximation and the derivatives. However,

finite element analysis, FEA, is based on an integral formulation which minimizes the error in a least square sense, *i.e.*, the error is made orthogonal to the test function space. The complete statement of a well posed heat flow problem requires the domain in space (geometry), the boundary conditions, initial conditions and the thermal properties be specified and consistent (31,32).

It is not difficult to model the geometry, initial conditions, the total heat input or to specify the thermal properties. The difficult tasks are to measure the thermal properties and to estimate the distribution of energy in a weld pool. Ideally, the heating effect of the arc should be modeled by solving the Boltzman equations coupled to the fluid mechanics of the weld pool. This is a problem of extreme difficulty from mathematical, numerical, computational, and experimental viewpoints. The flow patterns inside the molten pool are the result of the contending forces of gravity, buoyancy, surface tension, electromagnetic force, droplet momentum and surface drag from gas flow. These are in turn affected by the arc voltage, current, shielding and chemistry. Although the coupling between the arc and the weld pool is strong and this coupling is the proper method for determining the energy distribution, solutions to this coupled problem have not yet been demonstrated (33-38).

If the uncoupled energy equation is to be solved, there are two fundamental options. Either the thermal flux and power density distribution can be specified, *i.e,* natural boundary conditions, or the temperature can be specified, *i.e.*, essential boundary conditions. An infinite number of functions can be chosen for either option. In general, the greatest success has been obtained by constraining the heat input to the region of the weld pool. This means that the heat transfer is not used to predict the shape and size of the weld pool but only to predict the temperature field outside of the experimentally determined or estimated weld pool. Having restricted the heat input to the weld pool, the next question is how to distribute the heat input in the weld pool. For simplicity, early simulations used closed-form analytical representations of the heat source, e.g., line or point models (39,40). Theses models neglected the spatial distribution of the arc

energy and typically ignored the temperature dependence of material properties. As a result, the computed temperature histories were usually valid only at a location far from the weld fusion boundary. For the simulation of the spatial distribution of the arc energy, the simplest function is a constant distribution. The next simplest is a Gaussian distribution function (41,42). The simplest shape is a circle in 2D or a sphere in 3D. The latest shapes of energy distribution in the arc are ellipses or double ellipses in 2D or ellipsoids or double ellipsoids in 3D . Almost all research to date has chosen to specify the flux or power density distribution.

Although the power density models were able to analyze non-spherical weld pools, such as electron beam and MIG welds with nail heads (42,43), attempts to analyze welds with complex pools such as a double pool achieved limited success. In addition, recent advances in experimental techniques enable the temperature distribution of the weld pool to be measured accurately. These factors have motivated the study of prescribed temperature heat source models. The prescribed temperature model is only valid after the weld pool has reached steady state. This is typically two to five weld pool diameters from the arc starting point. In this region, use of the prescribed temperature model has the potential to analyze more complex weld pool shapes. In addition, the distributed flux and power density computed from the prescribed temperature model can be applied to analyze the starting and ending transients.

From all the above mentioned arc energy models, Goldak's double ellipsoidal model (41,42) for the welding heat input distribution appears to be the most convenient and accurate model to date. This distribution model assumes a Gaussian heat flux distribution on the top of weld pool simulated by one half ellipsoid and a Gaussian power density distribution in the weld imitated by one half of another ellipsoid (see Figure 8). It requires an estimate of the net heat into the weld and the distribution of this net heat into each of the ellipsoids to properly simulate the heat flow in the longitudinal direction. The net heat input to the weld is generally calculated from the energy supplied (the product of welding current and voltage) and the welding arc efficiency. This model also

allows the heat distribution to be changed by the simple change of various geometric parameters rather than changes to the finite element mesh, which is practically useful in attempting to simulate a weld pool.

The heat supplied to the weld pool is primarily transferred to the parent metal by conduction and convection within the weld pool. A simple approach commonly used by many researchers is to compensate for the weld pool convective heat transfer with an artificially high conductivity for the metal in the weld pool (44,45). Typically, conductivities an order of magnitude higher than its value at the solidus temperature have been used. The difficulty associated with this technique is that various values of conductivity for the molten metal must be tried until a reasonable weld pool shape and temperature distribution within the weld pool are obtained.

On the exposed surface of the weldment, heat is lost by free convection and radiation. Heat loss due to thermal radiation is dominant in the vicinity of the weld pool where the temperature difference between the weldment and the environment is large. Radiative heat loss can be calculated with the Stefan Boltzman equation which requires a value of the surface emissivity. Since this is often unknown or approximate, radiative weld pool heat losses are often compensated for by decreasing the welding efficiency.

Heat losses by surface convection are dominant away from the weld pool and appear to have a significant effect on the cooling rate of the weld. The heat loss by free convection can be modeled by Newton's cooling law which requires a knowledge of the surface heat transfer coefficient. These coefficients will vary with the orientation of the surface and may not be readily available for some orientations and surface finishes.

Absorption and liberation of latent heats of fusion have a significant effect on the predicted weld temperature distribution. The latent heat effect is often modeled by modifying the specific heat or enthalpy as a function of temperature.

The finite element heat transfer analysis requires accurate values of the thermal conductivity, specific heat, material density and latent heat of fusion up to the melting point. Low temperature data is readily available, but high temperature data must be

estimated or extrapolated from the low temperature data as little high temperature data exists in the literature. Above the melting point, the complex convective heat transfer mechanisms in the weld pool are very difficult to model even with accurate thermal properties. Instead the thermal conductivity above melting is usually increased six- to ten-fold to simulate the convective mechanism so that an accurate prediction of the weld temperature distribution can be reached.

At the present time, full 3D thermal analysis for welds is possible but expensive and time consuming. The issue is how to reduce the computational cost/time and still achieve useful accuracy to acceptable levels (46). This is a challenge to the modeling community.

Thermal Stress Analysis

The thermal stress analysis of the welding problem is considerably more complex than the heat transfer analysis. The basic equations are the conservation of linear momentum, angular momentum, the constitutive relation between stress and strain, and the compatibility or continuity relation between strain and displacement (47,48). The difficulties arise almost entirely in decomposing the deformation into a translation, rotation and stretch on the one hand and then decomposing the deformation into contributions due to elasticity, plasticity, thermal expansion, transformation plasticity and creep on the other hand. The thermo-elasto-plastic constitutive model which describes the materials behavior in the thermal elastic-plastic regime is critical to the accuracy of the results. Unfortunately, the material properties required to characterize the constitutive relationship are seldom available, particularly at the higher temperatures. In addition, the restraint of the material and support of the weldment play a key role in the formation of the residual stresses.

The von Mises yield criterion is usually used to define the onset of yielding. Once yielding has occurred, an associated flow rule is employed to calculate the

incremental plastic strains. Generally, a rate independent plasticity model with a kinematic hardening theory is adopted to characterize the material behavior during welding. The kinematic hardening theory has been adopted as the simplest theory that can model the reverse plasticity and Bauschinger effect which is expected to occur during welding. It requires the material behavior in the plastic range to be linearized into a constant work-hardening slope. Time dependent creep effects are generally not considered because of the short time the material spends at high temperature during welding (49).

A more accurate hardening model such as the combined kinematic-isotropic hardening model could be used (50,51). However, unless more accurate stress-strain curves are available, a more complex hardening model will not improve the accuracy of the results.

The material properties required for the stress analysis are the Elastic (Young's) Modulus, Poisson's ratio, Virgin Yield Stress (Yield Strength), Tangent (Plastic) Modulus, and the Average Coefficient of Thermal Expansion. Since the molten material re-solidifies as a damage-free material, any deformation occurring above the melting point will not affect the final residual stress. Based on this argument the temperature histories of the molten material are assumed to be limited by the melting temperature, thus, only material properties up to melting point are required in the stress analysis.

The Virgin Yield Stress and the Tangent Modulus characterize the material behavior in the elastic-plastic regime. In a kinematic hardening model a zero Tangent Modulus must be specified at temperatures above melting so that the molten material can re-solidify as damage-free material. The Virgin Yield Stress at melting should be very small but not zero as this may create division by zero problems in the computation. It was found that a value of about 0.5% of the room temperature value for temperatures above melting would give reasonable results. The temperature dependent Tangent Modulus can be approximated based on the assumption that the Tangent Modulus/Young's Modulus ratio remains constant up to the melting temperature. In

order to save computing cost, some researcher set a cutoff temperature in the analysis. They assume that the thermal strains, Young's modulus and yield strength do not change above a cutoff temperature. It is valid if viscous effects play an important role above a cutoff temperature. For the steels, the cutoff temperatures used have ranged from 873 to 1473 K (52).

At the higher temperatures where the material behaves in a plastic manner, the Elastic Modulus and the Poisson's Ratio have little influence on the calculated stresses. A Poisson's Ratio approaching 0.5 at temperatures above the melting point is not really necessary because the material is assumed to behave in a fully plastic manner (zero tangent modulus) so that the incompressible condition is satisfied. In addition, specifying a Poisson's Ratio approaching 0.5 is computationally unattractive since during the first iteration in each increment of the solution the material is assumed to behave elastically, and this can result in a large initial material stiffness matrix, thus causing the solution to diverge or at best converge slowly.

The extent of thermal straining during welding is determined by the product of the Average Coefficient of Thermal Expansion and the maximum temperature change at any point in the material. Therefore, it is important that accurate values of Coefficient of Thermal Expansion be used.

To date, state-of-the-art computational modeling can give reasonable values of residual stress away from the weld fusion line (53). The area around the weld fusion line experiences high temperature cycles during welding and there is a lack of accurate material, thermal-mechanical properties, and correct work-hardening models in the high temperature range to allow correct analysis at the present time. This is the main obstruction that the mathematic modeling researcher now faces. However, with the development of more efficient numerical methods and more powerful computers, the potential for accurately predicting residual stresses in the vicinity of the weld pool will be increased in the near future (48,52).

Computational Model for Pipe Girth Welding Process

Because of the limitation of the computational tool, the early research usually used analytic methods for thermal and stress analysis of pipe girth welding process. Vaidyanathan *et al* (19,54) and Ueda *et al* (14) applied analytic techniques to predict residual stresses and provided limited accuracy results. This is because they idealized the pipe girth welding situation.

In reality, welding thermal-mechanical analysis is a nonlinear problem, and numerical methods must be used to improve understanding of the welding process. Fortunately, with the rapid development of computing tools, it is now possible to carry out complicated thermo-elasto-plastic analysis of pipe girth welding by using finite element analysis.

Rybicki *et al* (55-60) developed a model to calculate residual stresses in a two-pass girth welded pipe based on the moving point heat source and the finite element method. The analytically calculated values were within 9% (for the first pass) and 17% (for the second pass) of the temperature data obtained by thermocouples. Quasi-steady state was assumed for the thermal analysis. Only thermal history after the weld metal had cooled down to 1423 K was used for stress calculations. The model was axisymmetric and a zero value was assigned to the stiffness matrix corresponding to filler metal elements before they were added. Melting of the pipe material was neglected and the shape of each weld pass cross-section (two-dimensional analysis) was obtained from photographs of the experiment. The agreement between the numerical and experimental values was good for the residual axial stress but poor for residual hoop stress.

Heat transfer and residual stress analysis becomes expensive for multipass welding if each individual pass has to be analyzed. Rybicki and Stonesifer (56) economized the stress analysis cost by grouping several passes together in a layer. The same thermal model as described above for the two-pass pipe welding was used to obtain the temperature distribution for each pass. The thermal histories for each pass in a given

layer were then examined as a function of each stress model element and it was determined which pass caused each element to experience the highest temperature change. Theses maximum temperatures were subsequently submitted to the stress analysis model as though they were obtained from the temperature distribution of a "super" weld pass that melted the entire multipass layer at one time. This method results in a combined temperature distribution which is actually an envelop of all the distributions for the passes of the layer being modeled. A seven-pass weld was analyzed in four layers and a thirty-pass weld in nine layers. Geometric symmetry about the weld centerline (WCL) was assumed so that only one-half of the pipe section was modeled. Calculated stresses were found to be in good qualitative agreement with the experimental data. Grouping of layers was also attempted in this analysis. The thirty-pass welded pipe was modeled by grouping the nine layers into three "super" layers. The results, however, did not agree with the experimental data.

Brust and Stonesifer (61) investigated the effect of weld parameters on residual stresses in BWR piping systems. They used the same computational model which was developed by Rybicki and discussed above. Their results indicate that, for conventional pipe welding, 1) lowering the applied heat input causes less tensile axial residual stress in the weld heat-affected zone (HAZ) along the pipe inner surface while hoop residual stresses in this region are not affected significantly; and 2) varying the weld heat input affects the stress state in smaller pipes more than larger pipes.

So far, the above mentioned computational models are based on a common assumption, namely, that residual stresses and deflections of girth welded pipes are axisymmetric. This assumption is made primarily because the expense associated with conducting the fully three-dimensional analysis is often prohibitive. As discussed before, in realty, this assumption may not be true. A better result would be reached if a 3D analysis were carried out.

Karlsson and Josefson (62,63) studied temperatures, stresses and deformations in a single-pass girth welded carbon steel pipe with a full three-dimensional finite element

model. The model covers the whole circumference and the complete welding sequence; *i.e.*, no assumption of axisymmetry is made. They used the ADINA code. The weld metal was modeled with the birth and death facility in ADINA, *i.e.*, an element in the weld metal was not activated until the heat source passed it. They used Kojic's effective stress function for a constitutive model. Notable calculated results are the residual compressive stress variations, especially in the beginning and end regions of the weld. Calculated stresses outside the fusion zone are in good agreement with experimental results; fusion zone weld stresses are not. They indicated that numerical calculations of this kind are very time consuming. It is hypothesized that research can be focused on axisymmetric models, after having examined and established the deviations from axisymmetry in this type of weldments, and bearing in mind the actual/expected deviations.

Lindgren and Karlsson (64) computed transient and residual stress for a complete girth-welded steel pipe. They used the Hughes-Liu shell element. The result is in good agreement with experimental data in the far field region. The residual stress field is close to axisymmetric except for the start position of the welding.

The above 3D modeling work only involved single pass girth welding. To date, there is no report on 3D modeling of multi-pass girth welding. The latest works (25,65) on modeling of multi-pass girth welding were 2D models using elements birth and death feature to simulate the filler metal addition during each welding pass, which was much closer to realty than Rybicki's grouping technique. Multi-pass welding is much more complicated than single pass welding. As stated before, there are many factors, like pass sequence, and welding start-stop position, that will influence the final stress state in a weldment. Thus, it is necessary to model multi-pass girth welding in 3D mode. One objective of this work is to establish a full 3D model for multi-pass girth welding.

RESIDUAL STRESS MEASUREMENT

Many techniques have been used to measure residual stresses in weldments. These methods can be classified into: 1) destructive (or semi-destructive) measuring methods, and, 2) non-destructive measuring methods.

Destructive (Semi-Destructive) Measuring Methods

Destructive (or semi-destructive) methods are stress-relaxation techniques (66-72) which use mechanical means to measure the macroscopic (long range) stresses. Sectioning, hole drilling, and indentation with measurement of dimensional changes, are examples; strain gages (73), or photoelastic coatings, or brittle lacquer coatings are usually used to sense the resulting deformation and Hooke's law is invoked to calculate the stresses from the measured strains.

In the hole drilling method (74-76), a specially designed strain gage rosette is used to measure the relaxation strain around a hole with a specific diameter and depth. One then calculates a stress field sufficient to cause the measured relaxation strain and then assumes, from the superposition principle, that the actual residual stress field in the element of material removed was equal in amplitude but opposite in sign to the calculated strain field. Since an analytical solution is only available for a uniform stress distribution, experimentally or numerically driven attempts have been made to relate the released strains and stresses for more general stress distributions. Since hole drilling technique involves removing a small amount of material, it is a semi-destructive and surface measuring method.

Destructive methods involve the removal of material, or cutting, to determine the residual stress in the region that was cut or removed. Thus, they are usually used to measure through thickness stress distributions.

Probably the most common and representative destructive technique is the

"sectioning method" in which strain gage rosettes are located at a number of axial and circumferential locations on the inner and outer surface of the pipe. A strip which contains one or more rosettes is then cut from the pipe. Successive layers must then be removed from the strips to determine the variation of residual stresses through the thickness (66). This method is applicable to non-axisymmetric as well as axisymmetric residual stress distributions. However, a great deal of machining, or other material removal methods, are required, and error may arise if the stress gradient in the axial direction is large. There exist other destructive techniques which are derivations of the sectioning method.

Popelar, Barber and Groom (77) proposed a method which was limited to an axisymmetric residual stress distribution. As in the sectioning method, strain gages are located on both inner and outer surfaces. However, instead of splitting the welded pipe into strips, only one complete cut is made perpendicular to the axis of the pipe. Since the resultant force of the axial residual stresses at such a section is zero, the unknown stresses are assumed to be expandable in terms of Legendre polynomials. Using the superposition principle, a stiffness matrix is formed by the finite element method. The measured strains are then used to determine the coefficients in the series expansion. One limitation of this method is that only one set of strain measurements is available for determination of the coefficients.

Cheng and Finnie (78-85) developed the compliance method which is based on fracture mechanics solutions for a circumferential crack to measure the through thickness stress distribution in pipe weldments. The major advantage of this method over other techniques is its simple experimental implementation with minimum material removal since only a single cut of increasing depth is required for a test. However, it is limited to axisymmetric residual stress distributions in thin-walled pipe.

Ueda, Fukuda and Kim (86-88) presented a new approach for the measurement of residual stresses in which inherent strains (the source of residual stresses) were dealt with as parameters, and formulated a basic theory using the finite element method.

Based on this new approach, a basic theory for the measurement of axisymmetric three-dimensional residual stresses was developed and a practical procedure of measurement was established.

In all above mentioned destructive or semi-destructive methods, only the hole drilling method has been proved to be reliable and field applicable.

Non-Destructive Measuring Methods

Nondestructive measuring methods mainly apply to surface stress measurement. Major nondestructive techniques are: x-ray diffraction, neutron diffraction, ultrasonic, and magnetic methods (74,89).

X-ray Diffraction

The most widely used nondestructive method for assessing residual stress states is x-ray diffraction (90-93). This method is based on Bragg's law and the fact that the inter-planar spacing of atomic planes in a crystalline solid is changed by applied stress up to 0.1%. If a monochromatic (wavelength λ) x-ray (beam P in Figure 9) is incident at a surface of a crystal under an angle of incident θ_o, the atomic planes with separation D_o act like a diffraction grating. The reflected beam has an intensity-maximum when,

$$n\lambda = 2D_o \sin\theta_o \qquad (1)$$

where n = 1,2,3, ... is an integer, so that $n\lambda$ is multiples of the x-ray wavelength. With applied stress, the inter-planar spacing is altered,

$$D = D_o + \Delta D, \quad \theta = \theta_o - \Delta\theta. \qquad (2)$$

The strain ΔD in the lattice is thus given by

$$\frac{\Delta D}{D_o} = -\cot\theta_o \cdot \Delta\theta \qquad (3)$$

The shift in the angle $\Delta\theta$, where the intensity-maximum is observed for a given strain ΔD, increases as the angle of incidence θ_o increases. In practice $70° < \theta_o < 85°$ is preferred.

Stress analysis by X-ray diffraction calls for a combination of the Bragg interference condition with Hooke's law,

$$\epsilon_1 = \frac{\sigma_1 - \mu(\sigma_2 + \sigma_3)}{E} \qquad (4)$$

$$\epsilon_2 = \frac{\sigma_2 - \mu(\sigma_3 + \sigma_1)}{E} \qquad (5)$$

$$\epsilon_3 = \frac{\sigma_3 - \mu(\sigma_1 + \sigma_2)}{E} \qquad (6)$$

ϵ_i - strain, σ_i - stress in the 1,2,3 directions of a rectangular coordinate system, E - Young's modulus, μ - Poisson's constant. Assuming a bi-axial-stress/strain state in the surface of a specimen ($\sigma_3 = 0$) and introducing the two angle-coordinates ϕ,ψ, the basic equation for x-ray stress measurement is given as:

$$\epsilon_{\phi,\psi} = \frac{\sigma_\phi(\mu+1)\sin^2\psi - \mu(\sigma_1 + \sigma_2)}{E} \qquad (7)$$

It is assumed, that $\epsilon_{\phi,\psi}$ is coincident with the measured lattice strain in this direction $(\Delta D/D_o)_{\phi,\psi}$, *i.e.*,

$$\epsilon_{\phi,\psi} = \left(\frac{\Delta D}{D_o}\right)_{\phi,\psi} \qquad (8)$$

Because the diffraction of the x-radiation takes place from a thin surface layer, about 5

to 100 μm, the pre-assumption of a plane stress/strain state is correct.

Advantages

- The technique is widely used, therefore instruments are available
- The technique is non-contacting with measurements possible at temperature and in aggressive environments
- For welded constructions the technique is sufficiently accurate
- Components with curved surfaces can be tested
- The technique can be applied for on-line surveillance

Restrictions

Only a 5 - 100 μm layer at the surface is analyzed, *i.e.*, stress distribution into the material can be analyzed only by successively removing the surface layers electrochemically.

Neutron Diffraction

Neutron diffraction (94-100) has many similarities to x-ray diffraction, replacing the x-ray beam by a neutron beam, thus it closely parallels and complements the x-ray diffraction method. The exact principle and equations discussed in above x-ray diffraction method also apply to the neutron diffraction method. The main advantage of neutron diffraction over x-ray diffraction is the large penetration depth (several millimeters) of thermal neutrons, whereas the x-ray method examines near-surface stress fields to a maximum depth of 100 μm. A comparison of linear absorption coefficients and depths below the surface from which 50% of the diffracted beam originates for neutrons and x-rays is shown in Table 2. This main advantage leads to two fundamental types of problems that are particularly appropriate for neutron diffraction and complementary to the use of the x-ray diffraction method: (1) the measurement of triaxial macro-stress gradients in components (such as weldments), and (2) the measurement of micro-stresses in composites and multi-phase alloys. In addition, the study of micro-

strain/stress distribution and applied stress problems, such as the determination of diffraction elastic constants and differential yield, is also well suited to the neutron diffraction method.

Figure 10 illustrates in outline the principles of a constant wavelength neutron strain scanner. Thermal neutrons from an intense source, such as a nuclear reactor, are monochromated by reflection from a single crystal and collimated to emerge as a parallel beam. The beam is then masked and positioned, using precisely made absorbing slits, to a specified cross-section passing through a reference point defined at a fixed height above the common axis of rotation of the detector and specimen. The Bragg diffracted beam is similarly defined by an absorbing slit aligned in front of the detector. The collimation together with the input and output slits thus define a "gauge volume", centered at the reference point, from which all the detected neutrons are scattered. The intensity profile of the Bragg peak is essentially Gaussian. The precise angular position of the peak center, and other peak parameters such as width and intensity, are determined by computer fitting a Gaussian function to the detected neutron intensity profile.

The shape and size of the gauge volume may be selected by varying the dimensions of the masking slits. For general applications a 2x2x2 mm^3 volume is often used but in regions of high stress gradient, such as at a crack tip or weld HAZ region, smaller dimensions are employed. If symmetry indicates that there is no significant strain change in one or more directions then the gauge volume is elongated whenever possible to a matchstick-like shape along that direction to reduce counting time and to improve the statistical quality of the data. Optimum spatial resolution of the gauge volume occurs with the detector at an angle of 90° (*i.e.* $2\theta_o=90°$) but angular dispersion, which is related to the strain sensitivity of the instrument, increases as $\tan\theta_o$. In practice, wherever possible, a strong characteristic reflection near or above 90° is selected for the measurements.

In a typical macro-strain scan the spatial strain variation is determined by translating the components to be investigated through the gauge volume, using three

automated orthogonal translators, and measuring the peak position from each chosen location. The directional dependence of the strains may be determined by rotating the component about the reference point and observing the shift as a function of orientation. Strains are calculated from the peak shift data and are then combined, using an elastic modulus appropriate to the reflection and material, to derive the residual stresses by applying equations 4, 5, and 6.

The main constraints to the uses of the neutron techniques are non-portability and absorption. Objects to be investigated must be taken to the neutron source, which is usually a high flux nuclear reactor (steady source) or a particle accelerator-based, time-pulsed neutron source. Neutrons, being uncharged, are one of the most penetrating particles but neutron beams are attenuated exponentially when passing through materials. For example, 10% of the neutrons will pass through 20 mm and 1% will penetrate 40 mm of most engineering steels. The time required for a measurement is that needed to count a sufficient number of neutrons to give statistically adequate data for analysis to a specified accuracy which, to a first approximation, is related to the square of the counting time. Costs are related to the neutron beam time required for counting and the 'setting-up' time for each run. Other difficulties or problems associated with the application of the neutron diffraction stress measurement technique are: (1) determining stress-free reference d-spacing, (2) texture, (3) grain size, (5) conversion of strain to stress, and (6) the limited volume element. Nevertheless, the neutron technique has been used for non-destructive internal and through-surface strain and stress measurements more and more often. It is anticipated that the neutron technique will become the standard against which other less direct but portable methods are calibrated. If internal and through-surface data are required, the neutron technique is often the only option. When comparisons with other techniques are possible, measurements on a cost per point basis are often cheaper than traditional strain gage methods.

Ultrasonic Methods

The newer ultrasonic methods of measuring residual stress (74,89,101) are based on the influence of stress on the propagation velocity of elastic waves. The velocity in stressed components can be expressed in terms of the second and third order elastic constants of the material under test. Although the change in velocity is only a few parts in 1000, it can be measured to this accuracy and thus used to evaluate stress states in components.

The relationships between elastic wave velocity and stress have been established a long time ago. By evaluating the sound velocity absolutely, *i.e.*, by measuring the time of flight and the path length, the strain and the stress (using Hooke's law), can be determined.

Advantages

- The birefringence methods are independent of sound path length, only times of flight need to be measured absolutely.
- The method has a high precision.

Limitations

- The ultrasonic methods average the stress distribution along the sound path and laterally over the beam diameter.
- Further investigation is required into the influence of an inhomogeneous microstructure on the elastic constants.
- Most of the experimental set-ups require further development before they can be applied *in situ.*

Magnetic Methods (74,89)

The relationships between magnetic properties and residual stresses in ferromagnetic materials was first investigated in the 1930's. Some sensitive parameters

have subsequently been observed, *i.e.*, the reversible magnetic energy, the initial susceptibility, the permeability and the remanence. All of these can be derived from the hysteresis curves. The initial susceptibility, as well as the remanence, is proportional to $1/\sigma$. Micro-stresses produced by dislocations and precipitations reduce the remanence but they are also correlated with a microstructure change.

Generally the behavior shown in Figure 11 is observed, for the hysteresis curve of iron-based materials, when a macro-stress is present. With a tensile stress the coercivity becomes smaller, and for a compressive stress it becomes larger, and the change is observed in the slope of the curve.

From micro-magnetic theory, it is known that the macroscopic hysteresis is produced by microscopic Bloch-wall movements and their interaction with microstructure and stress-fields. The physical origin of the stress dependence is known as the magneto-elastic effect. Deformation of a material produces changes in the relative energies of various magnetic domain configurations, which influence the macroscopic magnetic response measured in the hysteresis curve.

In the last decade, techniques have been investigated which appear more suited to NDT-stress measurement. One of these is Barkhausen-noise-analysis. There exist two possibilities of signal pick-up for this method. The first uses magneto-inductive sensors. The second possibility of signal pick-up is the application of an acoustic-emission sensor.

The other two techniques which have been developed are incremental permeability and dynamic magneto-striction measuring methods.

Advantages

- All magnetic methods have high sensitivity with regard to stress.
- Where the geometry of the specimen allows the application of the transducers, the measurement is performed in a few seconds, so that dynamic loading can be monitored.

Limitations

- The methods only analyses the surface layer. The thickness of this layer depends on: the analyzing frequency (Barkhausen-noise, magneto-inductive reception), < 1 mm; the magnetizing frequency (Barkhausen-noise, acoustic reception), < 4 mm; the eddy-current frequency (incremental permeability, dynamic magneto-striction), < 100 μm.
- The lateral resolution depends on the transducer size: < 2 mm diameter (Barkhausen-noise, magneto-inductive reception); > 0.2 mm^2 (incremental permeability); < 10 mm diameter (Barkhausen-noise, acoustic reception); < 400 mm^2 (dynamic magneto-striction). The methods require yoke magnetization in a hysteresis loop, pool shoe distance < 40 mm, and the size of this transducer can hinder the applicability of the technique at a weld, especially if the weld bead is not grounded. The weld should be scanned both in the lengthwise and transverse directions.
- The methods are also sensitive to microstructure changes (inhomogeneous microstructure, texture), *i.e.*, stress and microstructure influences must be separated and normally the information of more than one measuring value is needed for interpretation.
- The stress-free microstructure state must be well known, well defined test samples are required for calibration.
- At present no theory exists to describe the influence of stress in more than a qualitative manner, *i.e.*, empirical calibration is required since interpretation models only exist for mono-axial stresses.
- The methods are restricted to the measurement of ferromagnetic materials.

At present x-ray diffraction is the preferred NDT method for (residual) stress analysis in welds. The method has been developed extensively, although the technique

itself is time-consuming and restricted to simple shaped components. More is known about the interpretation of the results for this method, (*i.e.*, the influence of parameters other than stress) than for any other technique. In fact the other methods tended to rely on x-ray diffraction for calibration in the past. The newly developed neutron diffraction method appears to be an effective, nondestructive measurement technique for multipass weldment residual stress measurement, although not inexpensive. This new diffraction method is going to replace the x-ray technique and combine with the latest numerical technique to set the new standard for residual stress study in the near future.

STRESS MITIGATION TREATMENT

A stress mitigation treatment is the application of a special thermal or mechanical process during, or after, conventional pipe girth welding. Each treatment alters conventional weld induced tensile residual stresses at the inner surface and partially through wall, into compressive residual stresses.

Several techniques involving thermal processes for controlling or altering residual stresses at the inside surface of girth-welded pipes have been investigated within the pressure vessel and piping industry (1-4,102). These include induction heating stress improvement (IHSI) (58-60,103-106), last pass heat sink welding (LPHSW), heat sink welding (HSW) (14) and weld overlay (WO) (107). These techniques are based on the principle that the residual stresses are influenced by the thermal history of the pipe. In each process, a heat sink, such as running water, is applied on the inside of the pipe while the exterior is heated. It is the means of exterior heating which distinguishes one process from the others.

In the case of LPHSW, the first passes are conventionally welded and the heat sink is used only in the last pass welding. During the last pass welding, a very high heat input is used to established a large temperature gradient across the pipe wall. Studies of this procedure have demonstrated feasibility based on computational and experimental

results. LPHSW differs from HSW in that HSW employs a heat sink inside the pipe after the first few weld passes and maintains the normal level of welding heat input.

The weld overlay (WO) process consists of reinforcing a completed girth weld with axial stringers of weld beads at the outside diameter. In this process, a 308L filler material with a starting ferrite number (FN) of 11-17 is selected in order to produce an as-deposited FN of 8. The reason for a minimum delta ferrite level of FN8 is to arrest IGSCC in the WO. Low heat inputs are used for the initial deposit to minimize dilution while high heat inputs are used for subsequent weld layer deposits. Also, a heat sink of running water (or reactor coolant) is present while several layers of weld stringers are placed on the pipe. This process was initially designed to provide structural reinforcements of the piping system. However, as a result of the pipe shrinkage, favorable compressive residual stresses were induced on the inner surface in most pipes. This method was examined experimentally by Burst and Kanninen (108) and analytically by Brust and Rybicki (107) for 10 cm diameter, Schedule 80 Type 304 stainless steel pipe. There was agreement between the computed values and the data for residual stresses on the inside surface of the pipe. Both studies showed compressive residual stresses for this case. Weld overlay can be applied either immediately following the original girth weld or at some later time after the girth weld has been completed.

The IHSI process involves induction heating of the outer surface of a completed girth weld, while simultaneously cooling the inside surface with flowing water. Thermal expansion caused by the induction coil heating plastically yields the outside surface (OS) in compression while the cool inside surface (IS) is plastically yielded in tension. After cool-down, contraction of the pipe outside surface causes the stress state to reverse, leaving the IS in compression and the OS in tension.

When the temperature differential between the pipe inside and outside surface during IHSI is a linear gradient, the thermal stress induced can be approximately written as:

$$\sigma = \frac{E\alpha\Delta T}{2(1-\mu)} \qquad (9)$$

where

σ: Thermal stress at each surface, both axial and circumferential (Mpa)

α: Linear thermal expansion coefficient (m/m-K)

ΔT: Temperature difference between inner and outer surface (K)

E: Young's modulus (Mpa)

μ: Poisson's ratio

As shown in Figure 12, if this thermal stress calculated by the above equation is below the yield stress, then it is relieved when the temperature difference is removed, and no residual stress is produced. However, if the thermal stress is greater than the yield stress, then removal of the temperature difference changes the pipe inner wall surface stress-strain condition. Compressive residual stresses are thus produced.

Japanese investigators (103),who originated the IHSI concept, have performed extensive research on it. They defined optimum heating and cooling conditions for IHSI. The key parameters were determined to be, 1) the heating coil width, 2) through-wall temperature profile, and 3) temperature difference across the wall thickness (ΔT). It was determined that a coil width of $3\sqrt{Rt}$ is sufficient, where R is pipe radius and t is thickness. Based upon the thermal-stress relationship, the minimum ΔT has been calculated as 488.6 K. Although ΔT is of primary importance, the shape of the through-wall temperature distribution also influences maximum compressive residual stress. In order to reach this maximum compressive stress, it was found that the quantity $\alpha\tau/t^2$ should exceed 0.7, where α = thermal diffusivity, t = thickness and τ = heating duration. Other parameters such as induction frequency and power, and cooling water flow rate were found to be of secondary importance, once the key parameters were established.

Since the IHSI method is based on placing an induction heating coil completely

around the pipe weldment, IHSI induced residual stress distribution is more axisymmetric than the residual stress distribution resulting from welding. Hence, IHSI is appropriately represented by an axisymmetric model.

As described by the above thermal stress equation, the key to applying the heating stress mitigation treatments is to maintain high temperature gradients through the thickness in the weldment. From the symmetry point, the IHSI is the best among the above mentioned heating stress mitigation methods.

There is only one mechanical stress mitigation method reported to date (109,110). This method is the mechanical stress improvement process (MSIP). Instead of using thermal force, this method applies a mechanical force to altering the stress state. This is accomplished by a special tool (see Figure 13) consisting of a mechanical clamp connected with circumferential studs which are tightened by a hydraulic tensioner. As the tensioners are hydraulically pressurized, the halves of the clamp load the pipe circumference elastically and then plastically. The amount of deformation is precisely controlled. The operation is very simple, it is accomplished in 15 to 20 minutes and can be repeated if necessary. In applying the MSIP, the pipes may be filled with reactor coolant or emptied. Deformation of the pipe extends throughout the weldment, and the reduction in the pipe diameter imparts residual compressive stresses at the inner surface in both axial and hoop directions. The residual compressive hoop stresses extend through the entire pipe wall.

From the theoretical stand point, there is no difference between the thermal and mechanical mitigation methods. They both attempt to change the plastic deformation and restraint in the conventional welding joint, but by different means.

All of the above mentioned thermal and mechanical stress mitigation treatments were developed between late 1970s and early 1980s. Recently, Japanese researchers (111) have proposed two interesting methods which are based on the principle mentioned above and have good practical application potential. The first one is local heat treatment; the second one is the ice plug method.

The basic procedure of the local heat treatment is as follows (Figure 14): 1) apply heating in a certain width on both sides of the circumferential weld line of a pipe from the outer surface; 2) the temperature distribution should change suddenly as shown in Figure 15; 3) cool down the pipe.

By this treatment, the welded portion deforms inward and large tensile plastic strain is produced on the inner surface of the pipe. After the pipe is cooled down, the inward deformation decreases and tends to revert to the original shape. At this stage, the tensile over-strained portion on the inner surface is subjected to unloading. This reduces the tensile residual stress and even changes it to compressive stress.

The basic idea of the ice plug method is to apply internal pressure to the circumferential joint of a pipe. This process produces outward deformation which results in compressive stress on the inner surface of the joint.

By this method, the internal pressure to the pipe is applied by taking the following steps (Figure 16): 1) fill the pipe with water; 2) cool down the pipe from the outside by the LN_2 jacket to form ice plugs so as to enclose water near the weld joint; 3) cool down the water enclosed by the ice plugs so that the water becomes ice with a volume expansion. This produces outward deformation of the pipe and the residual stress changes as shown in Figure 17.

A newly proposed post-weld stress mitigation treatment is presented in this study. This new method is cooling stress improvement (CSI) (112) which keeps a very low temperature around the inner surface of the weldment while it maintains a slightly elevated temperature around the outer surface of the weldment. The idea behind this method is the same as the above mentioned heating induced stress mitigation treatments (especially IHSI), *i.e.*, using large through-thickness temperature gradients in the weldment to alter the stress state. In CSI, thermal contraction caused by the cooling plastically yields the inner surface in tension, while the outer surface plastically yields in compression. Once the cooling cycle is terminated and pipe weldment reaches room temperature equilibrium, the expanded pipe inside diameter results in stress state

reversal, leaving the outside diameter in tension and the inside diameter in compression. Because of the symmetric nature of this method and elimination of the relatively high temperatures needed to achieve stress reversal by IHSI, CSI would be expected to have great potential for industrial application.

Table 2. Linear Absorption Coeffients (μ) and Depth From Which 50% of the Diffracted Beam Originates ($G_{50\%}$) for 1.3 Å Neutrons and Cu K_α X-Rays at a Diffraction Angle $2\theta = 90°$

	Neutrons		X-Rays	
Elements	μ (cm^{-1})	$G_{50\%\ (mm)}$	μ (cm^{-1})	$G_{50\%}$ (μm)
Al	0.10	24.5	131	19
Ti	0.45	5.4	938	2.6
Fe	1.12	2.2	2424	1.0
Ni	1.86	1.3	407	6.0
W	1.05	2.3	3311	0.74

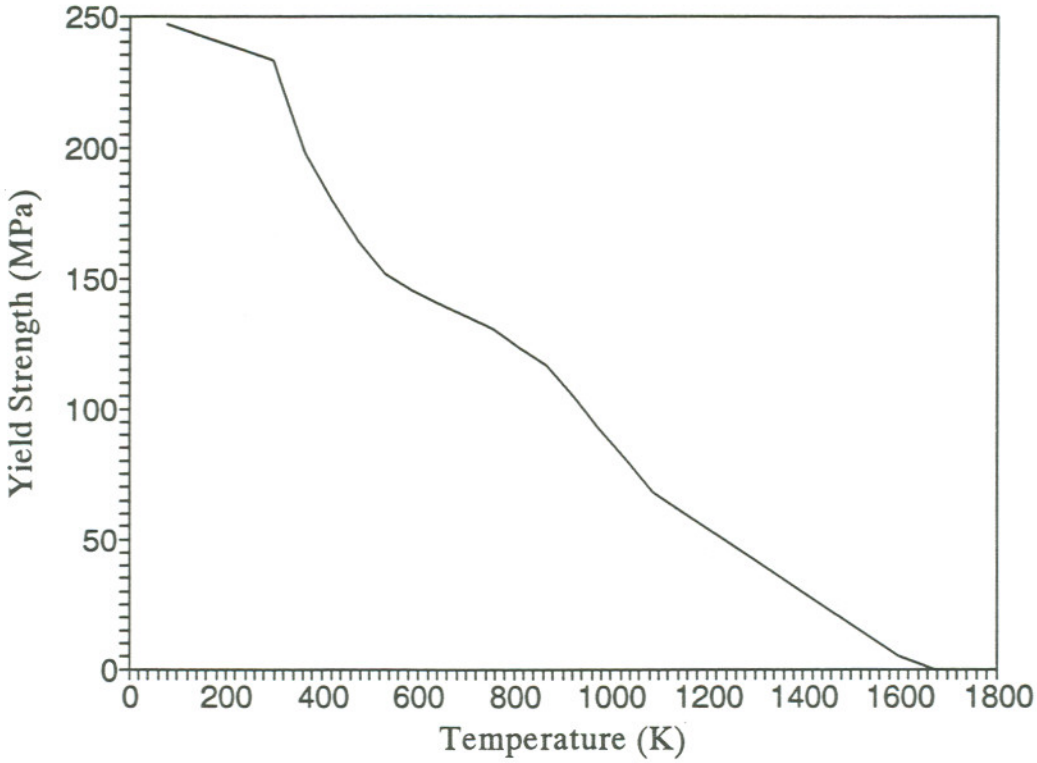

Figure 5. 304L Stainless Steel Temperature Dependent Yield Strength (115)

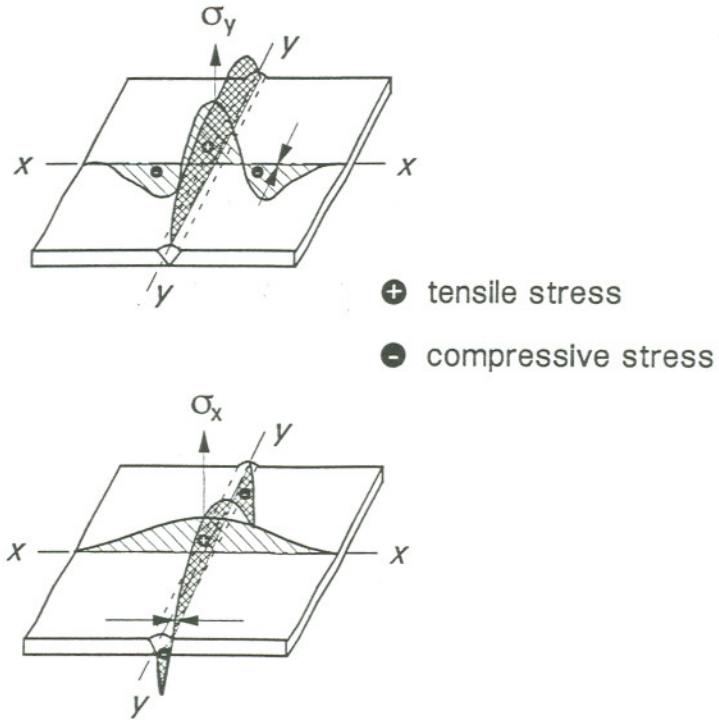

Figure 6. Residual Stress Distribution in a Butt-Welded Flat Plate (89)

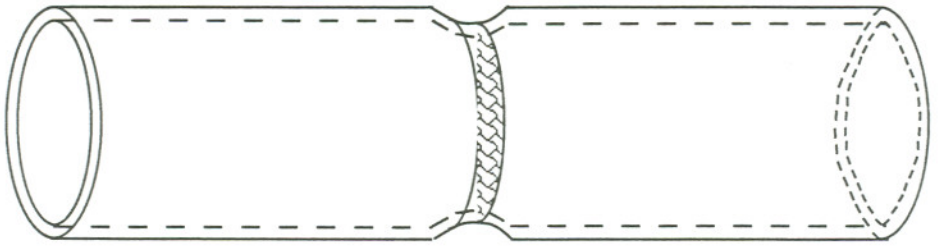

Figure 7. Radial Deflection in a Pipe Girth Weld (20)

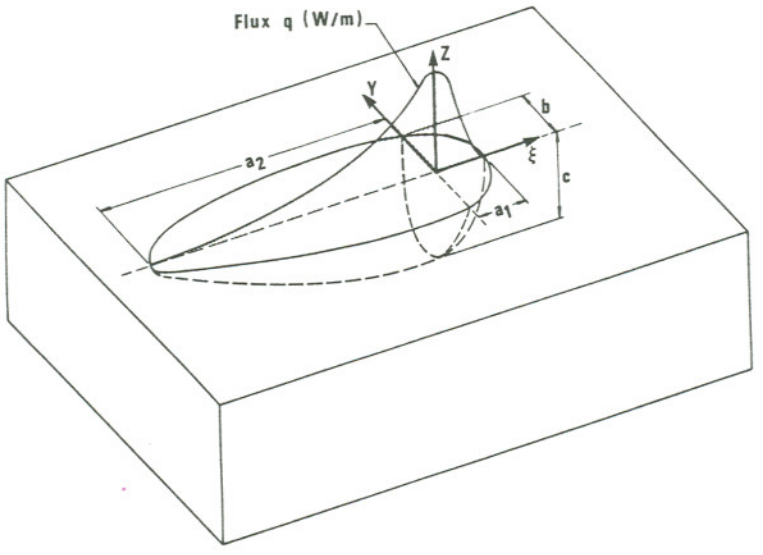

Figure 8. Arc Heat Source Model With a Distribution of Flux over the Surface and the Power Density throughout the Volume of the Double Ellipsoid (52)

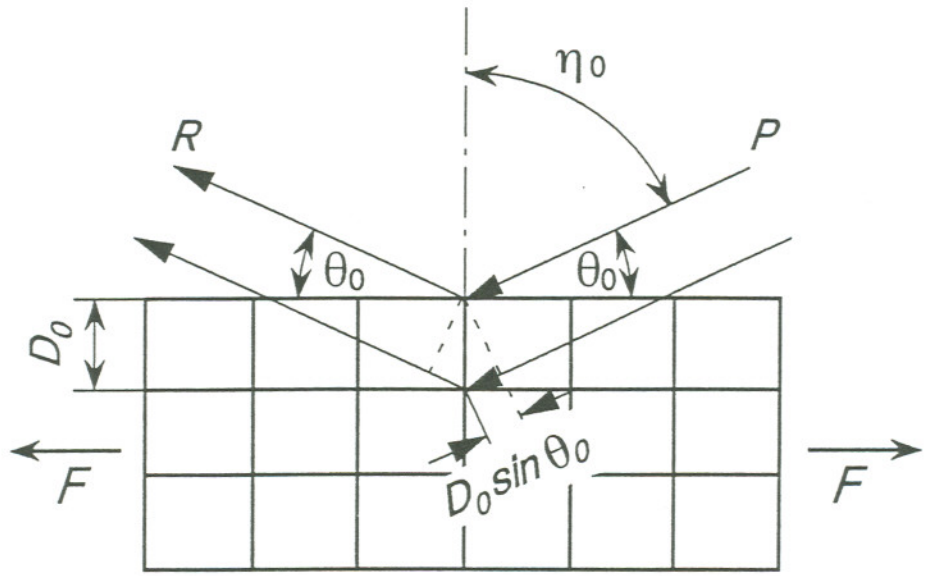

Figure 9. Bragg Reflection Lattice as a Diffraction Grating (89)

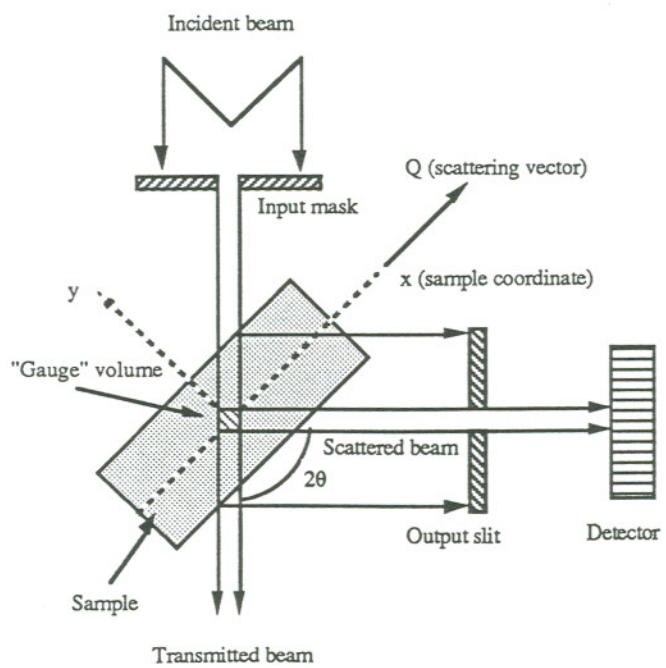

Figure 10. Schematic of Neutron Diffraction Stress Measurement System (97)

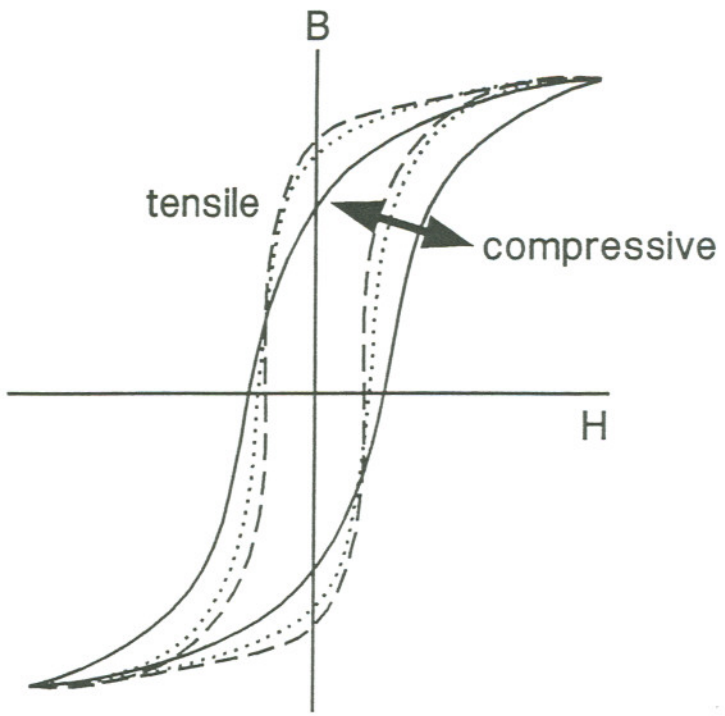

Figure 11. Hysteresis Changes with Tensile and Compressive Stress, Magnetization Parallel to the Mono-axial Stress State (89)

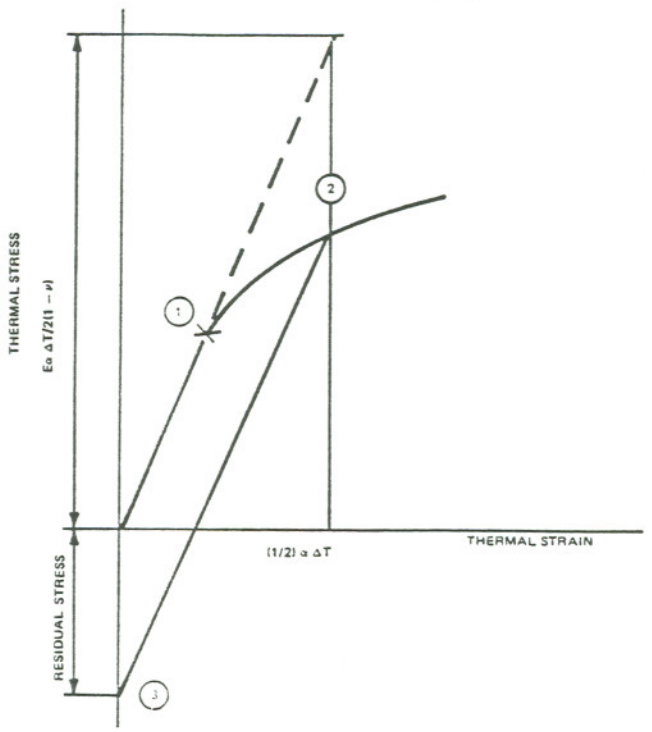

Figure 12. Schematic of Thermal Stress and Thermal Strain Relationship (105)

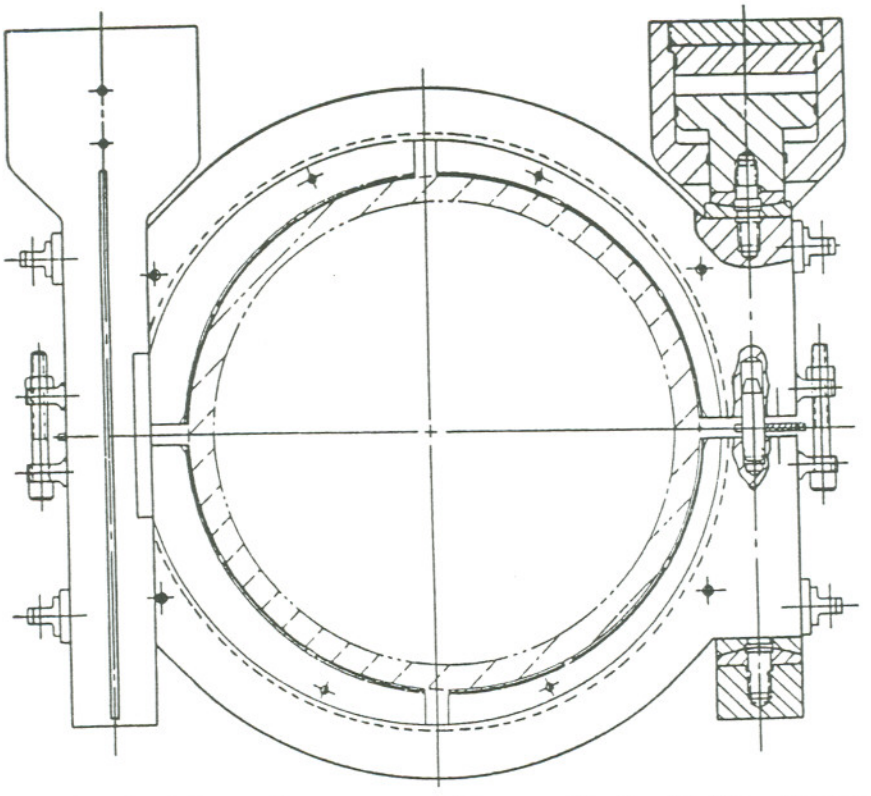

Figure 13. Mechanical Stress Improvement Process Tool with Box Presses for 600 mm Pipe (109,110)

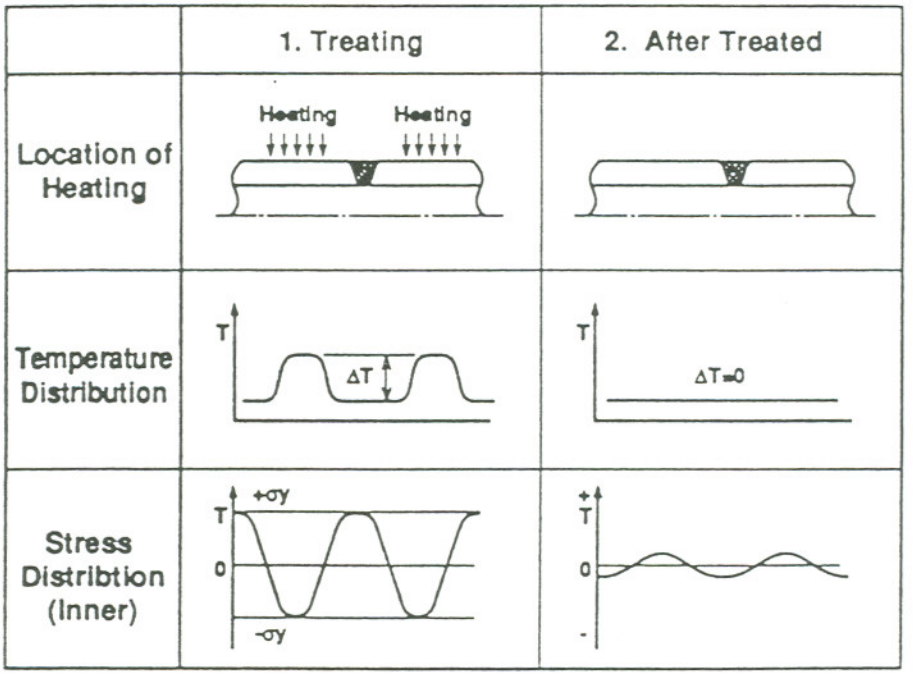

Figure 14. Concept of the Local Heat Treatment Stress Relief Method (111)

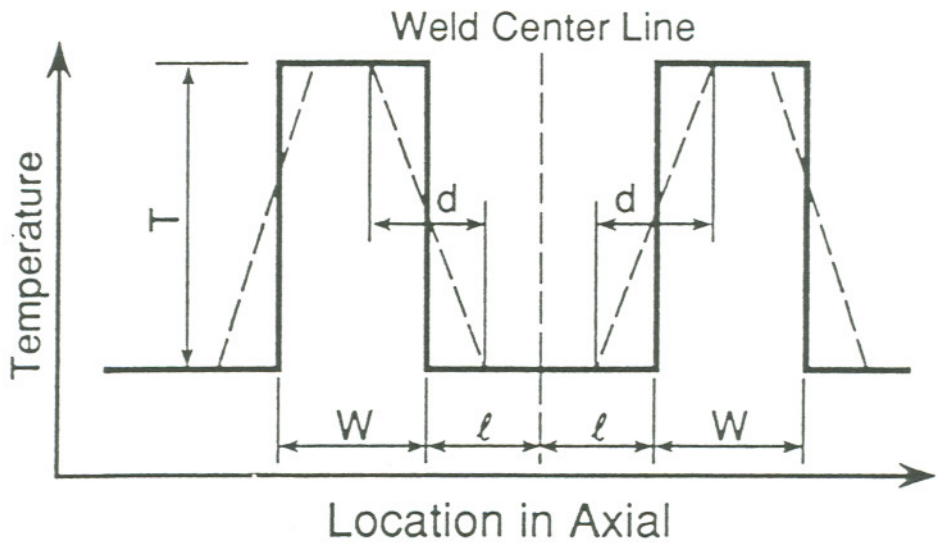

Figure 15. Temperature Distribution Model in Local Heat Treatment Method (111)

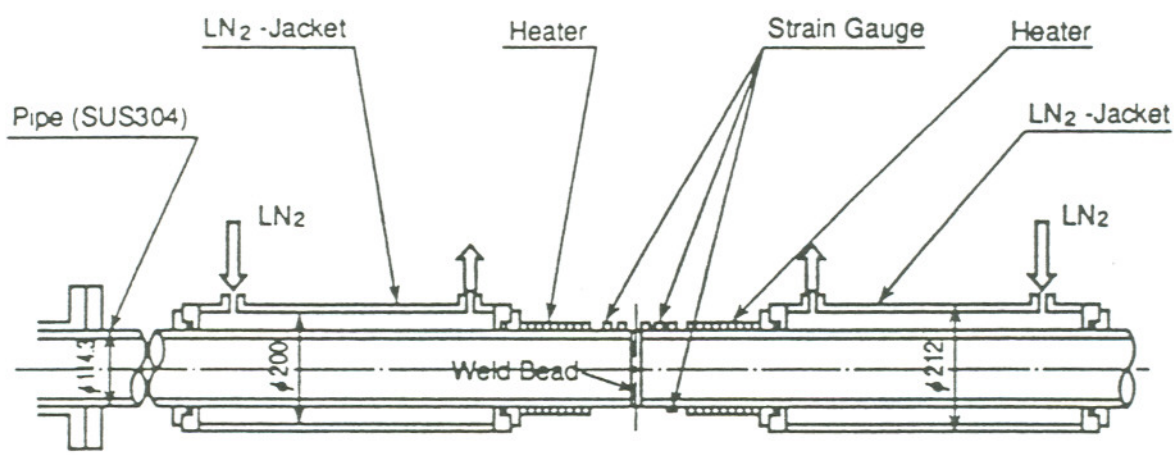

Figure 16. Experimental Apparatus of the Ice Plug Method (111)

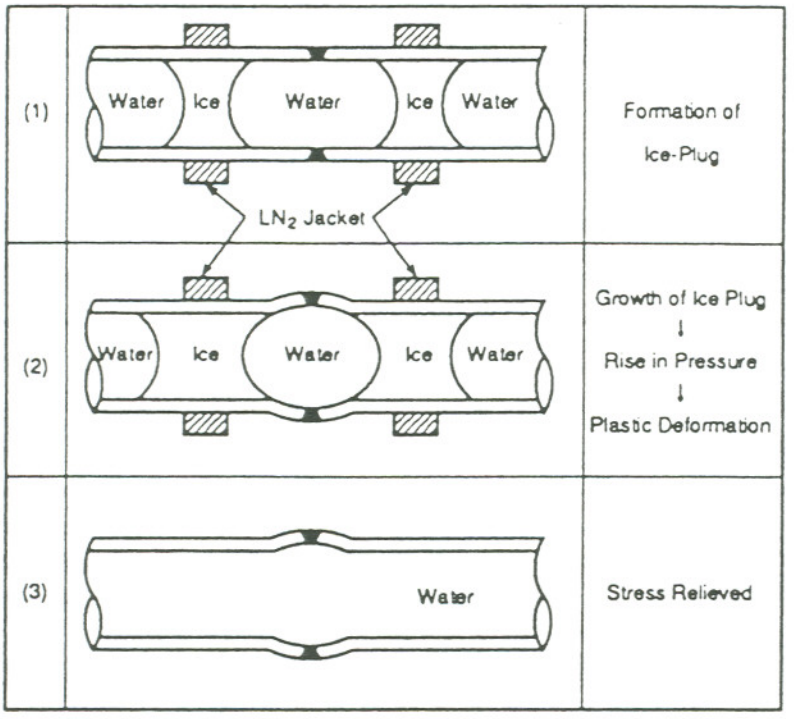

Figure 17. Concept of Stress Relief Using Ice Plug (111)

CHAPTER 3
EXPERIMENTAL PROCEDURES

THERMOMECHANICAL HISTORY MEASUREMENTS

Introduction

One specific goal of this experimental work is to increase the understanding of residual stresses and deformations developed during pipe girth welding of Type 300 series stainless steel pipe used in the construction of the existing Savannah River Site (SRS) nuclear defense production reactors. Construction is defined as existing piping systems, replacement piping sections and/or piping repair weldments. Thus the weldments being chosen for analysis under this study have a direct relationship to SRS reactor piping systems.

Five experimental girth weldments were completed in this research. One weldment was fabricated by manual tungsten inert-gas (TIG) welding at SRS while the second weldment was finished at OGI using a mechanized TIG welding workstation; the other three weldments were made at Arc Machines Inc. (AMI), in Pacoima, California, using a computer-controlled, automatic TIG pipe welding system. All weldments came from the same 6 m length of Type 304L stainless steel, 40 cm diameter, schedule 40 pipe, furnished by SRS, and typical of SRS reactor piping. All weldments were welded with 308L filler material to give the weld sufficient delta ferrite to prevent solidification cracking. The base metal of this 304L stainless pipe has a ferrite number (FN) of 4 and the chemical compositions of the base metal are shown in Table 3.

The SRS Weldment

Two 120 cm sections were cut from original 600 cm length of the pipe. A standard V groove, shown in Figure 18, was prepared by plasma-arc cutting followed by grinding to clean up the surface and then the sections were welded together. The welding was carried out by manual TIG welding for all passes using standard welding parameters with the pipe being held horizontal and rotated under the arc (1G position) to facilitate all uphill welding. A consumable insert ring was used during root pass welding. The weld was completed in seven passes with 3.175 mm diameter ER308L filler material and 2% thoriated tungsten electrode. No instrumentation was carried out during pipe welding.

A 40 cm section which contained the SRS weldment out of the mid-section of the 240 cm pipe was cut at OGI for further study. Care was taken not to introduce permanent plastic deformation during the cutting operation. Wooden fixtures were made to insure that pipe cutting stresses, mainly induced by clamping forces, would not be large enough to introduce permanent deformation of the pipe to alter the final residual stress state in the pipe. Strain gages were mounted on the pipe outer surface before cutting. No strains were found during the cutting process. Figure 19 presents a view of the SRS weld being cut out of the 2.4 m pipe; note the wooden pipe fixtures. All other pipe sectioning operations were performed using these wooden fixtures.

The OGI Weldment

The OGI weldment was fabricated to allow assessment of the thermomechanical history measuring instrumentation and data collection package proposed for use on the three weldments produced at AMI. It was welded in the middle of a 40 cm length of pipe cut from the remaining 360 cm portion of the original 600 cm SRS pipe. Note that this was the same length of pipe cut for further analysis of the SRS weldment; this was

done so that further analysis techniques proposed for used on the SRS and AMI weldments could be first assessed using the OGI weldment.

The OGI weld preparation was the same geometry as the SRS V groove, except that the pipe was not parted, but remained connected by the weldment land, see Figure 20. A weld counterbore region was machined on both the outer and inside surface of the pipe. Circumferential instrumentation placement marks were machined on the weld counterbore areas during the weld preparation operation; axial instrumentation marks were scribed on the counterbore surface at OGI. Figure 21 shows a head-on view of the 40 cm pipe section cut out of the 360 cm pipe section; note the instrumentation placement marks on the counterbore surface and that the weld groove was not parted. Figure 22 presents an angled view of interior of the pipe to be welded. It illustrates the surface marks placed on the pipe at the same time as the weld groove was machined. Axial marks were subsequently placed every 45 degrees and their intersections with pre-machined circumferential marks were used to determine where the various deformation indicating devices and thermocouples were placed.

Weldment Instrumentation

The OGI weldment instrumentation included thermocouples as well as deformation measuring devices. Axial, radial deformation and hoop strain measurements were taken during welding. The radial deformation devices and hoop strain gages were placed at selected intersections of the circumferential and axial marks. Thermocouples were placed the same distance from the weld center line as the deformation devices and strain gages, but 6.35 mm away from the gage positions, in the circumferential direction. Placement of the thermocouples and gages in exactly the same place would have allowed absolute temperature and deformation history equivalency, but this was physically impossible.

The axial deformation device was attached near the edges of the counterbore symmetrically across the weld centerline. The radial devices consisted of deformation

sensing ceramic tips held against the counterbore surface by modified CTOD clip gages. Each clip gage was attached to an individual clip gage holder that was, in turn, attached to an instrumentation mandrel. The instrumentation mandrel was about 50 cm long and was made from 30 cm diameter, schedule 80 carbon steel pipe. It was centered in the stainless steel pipe to be welded prior to welding by a series of bolts. The bolts were threaded through the instrumentation pipe wall and pressed against the inside surface of the SS pipe. The reason for this mandrel was to give the instrumentation a rigid reference.

The radial attachment apparatus consisted of a welded "L" bracket with the long leg welded to the mandrel and the CTOD gage bolted to the short leg; a schematic of the experimental setup is illustrated in Figure 23. The radial CTOD clip gage holders were attached to the inside of the instrumentation mandrel which meant that the ceramic tip needed to pass through the mandrel and press against the SS pipe inner surface. Each sensing tip had its own hole and individual attachment apparatus. The mandrel holes needed for tip access were drilled into the mandrel using a radial arm drill press which has been modified into a welding, measurement, and machining workstation, as shown in Figure 24. Note that the radial arm drill press was modified to accommodate a controlled rotation fixture.

Deformation devices were installed in the pipe after the mandrel was centered in the SS pipe. The axial measuring unit included a threaded rod with cone tip at one end, three pieces of metal with a hole to fit the rod, nuts, and a CTOD clip gage. The metal pieces were welded on the inside surface of SS pipe with the rod through two of the metal pieces fixed by nuts and leaving a gap between the third metal piece and rod tip. The CTOD gage was inserted into the gap. This can be seen in Figure 25. The radial measuring devices were placed between the SS pipe inside surface and CTOD gages that were bolted to the L brackets, which were attached the inside surface of the mandrel. It took great effort to install all the planned deformation measurement devices, but several of them were still not functioning during welding. This was due to the limited

size of the access holes drilled in the mandrel.

High temperature strain gages (M&M WK-09-062AP-350), with a working temperature up to 300°C, were glued on the inside surface of the pipe by using high temperature adhesive (M&M-Bond 610) and following the guideline of the manufacturer (M&M Instruction Bulletin B-130).

Chromel-Alumel K type thermocouples, with temperature range from -133°C to 1400°C and 0.1° resolution, were attached onto the surface by spot welding as carefully/accurately as possible. The lead wires from the thermocouples were protected by high temperature insulation.

Pipe welding was performed in the radial drill press, which was modified to accommodate a TIG welding head. The pipe was rotated under the welding torch (1G position) using the same setup used for mandrel hole drilling, shown in Figure 26.
A TIG welding machine was used and the weld was finished in twelve passes with each pass using the same start-stop position. The root (first) pass was autogenously welded, and the subsequent passes were welded with 308L cold filler wire. This 308L filler metal gave the weld a FN of 8. The chemical compositions of the weld are given in Table 3. Table 4 shows the welding parameters, while Figure 27 presents the pass sequence in the weldment.

Analysis of data collected during welding of the OGI weld indicated that the instrumentation system was monitoring and recording thermomechanical histories correctly, but that the radial deformation gage installation techniques used needed to be modified prior to fabrication of the AMI welds.

The Data Acquisition System

A data acquisition system capable of monitoring thermal and mechanical deformation data during pipe girth welding has been developed at OGI. The data is collected by a computer via a Keithley Asyst Viewdac 2.0 software system. Viewdac

is an integrated software system for data acquisition, process control, and data processing. The system capabilities allow the user to create customized data collection applications which can be automated and controlled interactively via push buttons, switches and user inputs. It runs under DOS using a mouse/menu-driven windowing interface and is a multi-tasking system. This system is designed exclusively for the 386/386SX/486 family of 32-bit IBM compatible personnel computers (Pc's).

The temperature signals from thermocouples were taken into OMEGA OM3 signal conditioners and converted into 0 to 10 V linearized voltage outputs. Here 0 V represents a thermocouple reading of -100°C and 10 V represents 1350°C. These analog voltage outputs were converted into digital signals via A/D boards and recorded in real time by a 486 PC via Viewdac software system.

The deformation/strain signals from CTOD/strain gages were converted into 0 to ± 10 V linearized voltage outputs by M&M 2100 strain gage conditioner and amplifier system. Here, 0 V represents zero deformation or strain, ± 10 V represents ± 5 mm deformation or ± 2000 $\mu\epsilon$ strain. Again, these voltage outputs were the inputs of A/D boards and recorded in a 486 PC via Viewdac software system in real time.

The 486 PC has two A/D boards. One board consists of 16 channels. Thus, initially this 486 PC can handle 32 data inputs at the same time. In order to collect as many data points as possible, a stand alone 16 channel multiplexer board was added to the PC by replacing one of the original 32 data input channels with this multiplexer board. Hence, a total of 47 channels can be handled by the 486 PC at once. The 47 channels can sample any combination of thermocouples, CTOD gages, or strain gages through voltage conditioners.

The maximum theoretical sampling rate for one channel using one A/D convertor is 50 Khz. However, the actual sample rate is much lower due to both the Viewdac software system and the multiplexer board. Choosing the proper sample rate is very important to the whole experiment. It is true that a higher sampling rate generates more detailed information about thermomechanical history development during welding.

However, it is physically impossible to chose a higher sampling rate as it requires more storage space, and is practically impossible as it takes excessive time to process the data. After careful consideration and comparison, a sample rate of 2 Hz was chosen in this study.

The data acquisition system was functional during welding at OGI, except the PC was shut down by high frequency ignition of the TIG arc. This was not a problem for the AMI machine as it uses a different igniting system. Figure 28 shows the whole set up of the data acquisition system.

The AMI Weldments

Welding Experiments

Three experimental girth pipe weldments were completed at AMI. These pipes have an outer diameter of 40 cm, a wall thickness of 1.27 cm, and a total length of 160 cm. The pipe material was AISI Type 304L stainless steel.

Each pipe for the three experiments was parted into two sections of 80 cm in length and machined on both the outer and inner surface for about 10 cm from either side of the weld centerline to ensure a constant thickness throughout the weldments. Two different groove designs were used in this work as shown in Figure 29. The first weld groove geometry was a standard V design (37.5 degree bevel at each side). The second groove geometry was a narrow gap preparation (1 degree bevel at each side). Axial markings, as well as circumferential lines, were placed every 45 degrees at specific distances from the weld centerline on both inner and outer surface during machining. Their intersections were used to determine where the various deformation indicating devices, hoop strain gages and thermocouples were placed, as well as for pipe alignment. The pipes were manually tack-welded with four tack-welds, equally spaced around the circumference before welding. All pipes were placed in an upright position and welded

in the vertical (2G) position with the pipe welder travelling along the pipe circumference.

The three pipes involved in this experiment were gas tungsten arc welded with cold filler wire (308L) using an Arc Machines' computer controlled automatic pipe welding system. This welding system consisted of a 300 amp Model 215 power supply with a Model 15 weld head and "D" torch. This torch has a EWTh2 tungsten electrode with 2% thoria added. The electrode has a diameter of 6.4 mm with its tip's diameter of 0.768 mm. The shielding gas was argon with a flow rate of 0.85 m^3/hour. The computer controlled welding equipment allowed pre-programming of the various welding variables including; 1) current (pulsed); 2) voltage; 3) welding speed; 4) torch oscillation; 5) gas flow; and, 6) wire feed rate.

All three welds were fabricated using as close to expected standard field weld parameters as possible. However, no consumable insert rings were involved in these weldments. A land was used instead of a consumable insert ring to facilitate the positioning of sensors with respect to the weld centerline. The main difference between the two standard V groove welds was that the filler wire (308L) for one was 0.9 mm in diameter while the other was 1.1 mm in diameter. Also, side to side torch oscillation was employed in the 1.1 mm diameter weldment after the root pass while pulsed arc stringer bead welding was used in 0.9 mm diameter weldment after the root pass. Minimum heat input was used in the 0.9 mm diameter weldment while maximum heat input was employed in 1.1 mm diameter weldment. This change in welding variables resulted in the smaller wire weldment being finished in nine passes while the larger wire weldment was completed in six passes. The V groove weld passes were conducted as typical interrupted passes, *i.e.*, each weld pass was initiated at a given point and continued until after the starting point was reached; it was then terminated in a manner that minimized the discontinuity due to starting and stopping. The resultant weld bead was then prepared for the next pass welding by wire brushing, and then the next pass was started. Each new pass was started 45 degrees beyond the initiation point of the previous pass to eliminate the potential for multiple weld start-stop discontinuities that

might result in a rejectable defect. Generally, the weld parameters were set before welding and were not changed during each welding pass. The narrow gap weld was finished in four continuous passes with 1.1 mm filler wire (308L) and a pulsed stringer bead welding technique after the root pass; the weld was completed without interruption. Figure 30, 31, and 32 show the welding pass sequence in the weldments. The weld parameters used for the various weldments are presented in Tables 5, 6, and 7.

Instrumentation Setup

The weld instrumentation included 28 thermocouples as well as 15 deformation devices and 4 strain gages. Figures 33 and 34 show the layout of instrumentation on the inner surface of the pipe weldment.

Axial and radial deformation measurements were taken during welding. Thirteen radial deformation devices and four hoop strain gages were placed at strategically selected intersections of the circumferential and axial markings. Two axial deformation devices were attached near the edges of the counterbore symmetrically across the weld centerline. Figure 35 shows the schematic of the axial deformation device placement. The hoop strain gages (M&M WK-09-062AP-350) were glued to the inside counterbore surface in the circumferential direction by following the installation requirement of the manufacturer. The radial deformation devices were attached perpendicular to the counterbore surface. The radial devices consisted of deformation sensing ceramic tips held against the counterbore surface by modified MTS CTOD clip gages. The clip gages were attached to gage holding "bridges" that were, in turn, attached to a "floating" instrumentation mandrel. Figure 36 illustrates this gage design and installation technique. The instrumentation mandrel was slightly longer than the total length of the two sections of pipes to be welded and was fabricated from 30 cm diameter schedule 80 carbon steel pipe. It was centered in the pipe sections to be welded prior to welding by a series of bolt "spacers". The bolts were threaded through the instrumentation pipe wall and

pressed against the inside surface of the stainless steel pipe.

Chromel-Alumel K type thermocouples were spot-welded to the pipe inside surface at the same distance from the weld centerline as the radial deformation devices, but 6.35 mm in the circumferential direction away from the gage positions. As stated before, placement of the thermocouples and devices/gages in exactly the same place would have allowed absolute temperature and deformation history equivalency, but this was physically impossible.

The weld axial shrinkage at the outer surface of the pipe weldments was also measured after each pass and after the weld was finished.

Data Acquisition System Setup

The data acquisition system capable of monitoring thermal and mechanical strain data during pipe girth welding was the same as used in the OGI weldment study. The system consisted of two A/D boards with a multiplexer extension which were capable of handling 47 channels of thermal and deformation/strain inputs at a sampling rate of 2 HZ per channel, a 486 PC, and voltage conditioner/amplifiers. This system was controlled by the commercial software Viewdac 2.0. The data was stored on the computer hard disk in real time, and subsequently downloaded to a storage disk after weld completion. The data for four narrow gap girth weld passes was taken continuously while the data for the standard V groove weldments, which took either six or nine passes, was broken down into an individual file per pass, as the welding operations were temporarily terminated at the end of each V groove pass.

RESIDUAL STRESS MEASUREMENTS

Residual Stress Measurements by Hole-Drilling Method

Introduction

The hole-drilling method was proposed nearly six decades ago and is based upon the measurement of the change in surface strain caused by stress relief due to machining a shallow hole in a test piece. The principle being that when stressed material is removed, the surrounding material must readjust its stress state in order to attain equilibrium. This rebalancing is manifest as a strain change in the system which is most noticeable near the place of metal removal. Thus, the strain change is measured in the immediate vicinity around a hole. Rotating cutters, such as drill bits or milling cutters, and gas jets of abrasive materials have been used to form the holes. Bonded electric resistance strain gages, rosettes, are used almost exclusively to measure the strain change.

In summary, this hole-drilling method involves attaching strain gages (or rosettes) to the surface of test part, drilling a hole through the center of the gages (rosettes) and into the test part, and measuring the relieved strains. The measured strains are then related to relieved principal stresses through a series of equations. This method has been standardized in ASTM Standard Test Method E837-92.

In order to calculate the principal stresses through relived strains, three individual strain gages should be accurately spaced and oriented on a small circle. This is neither easy to do nor advisable, since small errors in gage location or orientation can produce large errors in calculated residual stresses. The rosette configurations shown in Figure 37 have been designed and developed by the Micro-Measurements Division of Measurements Group, Inc. specifically for residual stress measurement. The rosette designs incorporate centering marks for aligning the boring tool precisely at the center

of the gage circle, since this is critical to the accuracy of the method.

There are three designs, RE, RK, and UM available. Only the RE design is offered in different sizes (031RE, 062RE, and 125RE), where the three-digit prefix represents the gage length in mils (0.001 in or 0.0254 mm). The RK and UM configurations are supplied in 1.6 mm gage length, and both types are fully encapsulated. Easily accessible copper solder terminals are provided in the RK design. All residual stress rosettes are constructed with self-temperature-compensated constantan foil, mounted on a flexible polyamide carrier. Gage resistance is 120 ohms $\pm 0.4\%$. In this study, M&M TEA-09-062RK-120 residual stress strain gage rosette was used. This three-element strain gage rosette has two gages in mutually perpendicular directions, with a third along one of the bisectors.

Surface preparation for installing the rosettes is basically standard, as described in Measurements Group Instruction Bulletin B-129. Caution should be observed, however, in abrading the surface of the test object, since abrasion can alter the initial state of residual stress. In general, it is important that all surface-preparation and gage-installation procedures be of the highest quality, to permit accurate measurement of the small strains typically registered with the hole-drilling method.

An optic alignment milling guide is positioned directly over the strain gage rosette either by cementing it to the test part or by using a special fixture to keep it in place. The milling guide is then adjusted to allow the precise machining of a hole in the center of the rosette.

The production of the hole is critical to the usefulness and accuracy of the measurement method. The optimum hole is the one machined in a "stress-free" manner (*i.e.*, with minimal induced machining stresses). In addition, the hole should be circular (in plain view) and straight sided (*i.e.*, cylindrical) to completely satisfy the conditions in the hole drilling data analysis equations.

Several drilling techniques have been investigated and reported to be suitable for the hole drilling method: 1) abrasive jet machining, a method for hole drilling in which

a high-velocity stream of air containing fine abrasive particles is directed against the test part through a small-diameter nozzle, 2) drilling at very high speed (up to 400 000 rpm) with an air turbine, and 3) end mills, carbide drills, and modified end mills. Studies show that abrasive jet machining (AJM) is the better technique for hole-drilling in stainless steels. In this study, AJM was chosen to produce the hole.

Hole-Drilling Test System

In this study, the hole was machined by an air/alumina power mixture which was directed onto the surface by an eccentrically mounted rotating nozzle. The testing system required for making air-abrasive center hole measurements comprises:

1. The air-abrasive drilling head (shown in Figure 38) fitted with a 0.46 mm diameter sapphire nozzle.
2. The optical alignment and hole measuring unit (shown in Figure 39).
3. A nozzle aligning jig and optics alignment block.
4. A S.S. White Abrasive (R) machine, model 6500.
5. A control box containing power supplies for the drilling head and optical unit, the air filter and time controllers for the Air-abrasive machine.
6. A clean dry air supply of minimum 5.2 bar (80 ibf/in^2) pressure.
7. A vacuum extraction unit.
8. Stain gage rosettes (M&M TEA-09-062RK-120s).
9. Strain measurement instrument (M&M 2100 Strain Gage Conditioner and Amplifier System with Digital Readout)

The whole measuring system is shown in Figure 40.

Measurement Procedures

Two AMI weldments were cut into 40 cm sections with welds in the middle. These two sections together with the OGI weldment were used in the hole-drilling residual stress study. The residual stresses were measured on the pipe outer surface at various axial and circumferential positions (see Figure 41). The residual stresses should be measured on the pipe inner surface as this is main interest of this research. However, it is impossible to put the drilling head system into the pipe inside diameter, and the residual stresses measured at outer surface can be the experimental database to verify the modeling effort.

The pipe weldment was mounted on to the radial arm drill press workstation with carbon steel mandrel inside it. This pipe section was then rotated to a certain position to attach the strain rosette on the surface. The strain rosettes were carefully installed according to the manufacturer's instructions. The strain rosette was aligned so that gage one of the rosette was assigned in the axial direction. The strain rosettes were connected to the 2100 strain conditioner system by using the three-lead wires. The resistance insulation between gages and gage to ground was checked and the instrument was balanced.

A specially machined stainless steel rod was used to connect the hole-drilling system guide bush with the radial arm drill press drill holder. The guide bush was adjusted so that the tip of the nozzle would be 1.5 mm above the rosette surface. The guide bush with the optical unit in it was also adjusted and aligned so that it would be perpendicular to the rosette surface and the center marks on the strain rosette coincided exactly with the fixed cross-wire in the optical unit. After the guide bush was properly aligned, the optical unit was removed and it was replaced with the drilling head. The flow rate in the S.S. White machine was set at 7, and 50 micron aluminum oxide was used. Then, the air supply to the machine was turned on and the air regulator was adjusted to 5.2 bar. The drilling time on the timer in the control box was the last

parameter to be set. In stainless steel a drilling time of 6 to 8 minutes is required for 1.6 mm diameter holes. Before starting the drilling operation, the vacuum extraction unit was connected to the drilling head and switched on, followed by turning on the drilling head motor. Finally, the drilling operation was engaged by pushing the start button on the control box.

After the complete drilling operation was finished, the drilling head was removed and replaced with the optical alignment unit. This optical unit was employed to measure the depth and diameter of the hole which were used in the calculation of the residual stresses. The depth of the hole can be measured by checking the micrometer readings in the optical unit when the surface and the bottom of the hole were in focus respectively. The difference between the two readings indicated the hole depth. For the type of rosette used here, the best hole depth should be 1.9 mm. If the hole was not sufficiently deep, a further period of drilling was necessary, after which the checking procedure should be repeated. The diameter of the hole was measured by using the micrometer head, aligning the moving graticule with each side of the hole in turn, and noting the micrometer readings. The difference between the two values indicated the hole diameter.

Residual Stress Calculation

By using the strain gage readouts of the 2100 system after the hole drilling, together with values for the hole geometry (diameter and depth of the hole) and Young's Modulus for 304L stainless steel, the residual stresses were calculated as follows:

$$\begin{matrix}\sigma_1 \\ \sigma_2^1\end{matrix} = -\left(\frac{E}{2}\right)\left(\frac{1}{K_1}\right)\left[\frac{\epsilon_1+\epsilon_3}{1-\mu K_2/K_1} \pm \frac{1}{1+\mu K_2/K_1}\sqrt{(\epsilon_3-\epsilon_1)^2+[(\epsilon_1+\epsilon_3)-2\epsilon_2]^2}\right] \quad (10)$$

$$\alpha = \frac{1}{2}\arctan\frac{(\epsilon_1+\epsilon_3)-2\epsilon_2}{\epsilon_3-\epsilon_1} \qquad (11)$$

where,

σ_1, σ_2 = Principal stresses.

E = Young's Modulus.

$1/K_1$ = Constant dependent upon hole diameter obtained from Table appropriate to type of rosette being used.

$\mu K_2/K_1$ = Value given by manufacturer appropriate to the type of rosette being used. If the holes are drilled to a nominally constant depth and diameter the value is a constant of 0.3, independent of Poisson's Ratio.

ϵ_1, ϵ_2, ϵ_3 = Relaxed strains.

α = Directions of the most positive principal stress measured from gage 1.
If α is positive measure in direction of rosette.
If α is negative measure in counter direction of rosette.
(See Figure 42).

Equation 11 has two solutions in the $-90° \leq \alpha \leq 90°$. These two solutions correspond with the directions of the two principal stresses. To determine the direction of the most positive principal stress, the signs of $[(\epsilon_1+\epsilon_3) - 2\epsilon_2]$ and $(\epsilon_3-\epsilon_1)$ are ascertained, and appropriate value of α selected from Table 8.

Residual Stress Measurements by Neutron Diffraction Method

Introduction

As restricted by time and neutron beam availability, only the four-pass narrow gap pipe weldment was analyzed by neutron diffraction method. The measurements were

conducted on the pipe inner surface and at the 180° azimuthal position from the welding start position. The measuring positions were located at 0, 5, 20, 40 and 60 mm from the weld centerline in the axial direction, respectively. The inner surface residual stress measurement can be performed by penetrating the neutron beam through the pipe thickness. This is one obvious advantage of the neutron diffraction method over the hole-drilling method which can only measure the residual stress at the outer surface of the pipe. The main purpose of this neutron diffraction residual stresses measurement of the narrow gap pipe weldment was to provide the experimental database to verify the numerical modeling results and to justify the selection of the 3D finite element model over the 2D finite element model.

Experimental Setup

Neutron diffraction measurements were made using the HB2 triple axis spectrometer at the high flux isotope rector (HFIR at Oak Ridge National Laboratory), adapted to measure strain distributions. Neutrons of wavelength 0.165 nm were provided by diffraction from the (103) planes of a beryllium crystal at a take-off angle $2\theta_m$ of 90°. The wavelength was selected to give a scattering angle $2\theta_o$ of 96.4° for the (311) reflection of face centered cubic austenitic 304L stainless steel. The detector position was fixed throughout the experiments. The (311) reflection was chosen for measurement of strain, because the diffraction elastic constants are close to the bulk values, and the assessment of residual stresses is simplified. Also, the (311) reflection has a high multiplicity, so texture in the fusion zone would result in minimal perturbations on the intensities of the diffraction peaks.

A coupon was cut from the pipe, far from the weld fusion zone, and was machined into a 5x5x80 mm^3 square bar. This square bar was slow heated to 1100°C, annealed for one hour, and then slow cooled down to room temperature to provide a zero stress reference specimen. The whole annealing process was carried out under a vacuum

condition.

The neutrons were counted in a position sensitive detector (PSD), 100 mm in length, manufactured by Oredela (Oak Ridge, TN), and located 800 mm from the center of the spectrometer sample table. The PSD had nine horizontal resistive wire anodes, spanning a height of 50 mm. The angular range subtended by the detector was approximately 7°. The spatial resolution was between 2 and 3 mm, which was equivalent to an angular resolution between 0.14 and 0.21°. The PSD permitted effective measurement of a complete diffraction peak at a single angular setting of the detector. The detector response was collected in a 512 channel multichannel analyzer. The channel-angle conversion was determined by scanning the detector in angular steps through a beam of width 0.5 mm. The function relating channel number n to angular shift Δ had the form of a cubic polynomial

$$\Delta = -4.426 + 0.018n - 9.196x10^{-6}n^2 + 1.313x10^{-1}n^3 \qquad (12)$$

The data had the form of a peak superimposed on a sloping background that originated from incoherent scattering in the material and ambient fast neutrons. The data were analyzed by fitting the raw data, neutron counts versus scattering angle, with a Gaussian peak (of variable position, width, and intensity) plus a sloping background. Typically, the peak had a maximum of 200 to 300 counts above background per channel and a width of at least 30 channels, so the statistical precision of fitted peak parameters was good. The peak position was determined to a precision of $\pm 0.006°$ at 96.4°, the width to a precision of $\pm 0.01°$ ($\pm 2\%$) and the intensity to within $\pm 2\%$. Measurements repeated at the same locations in the pipe weldment gave the same peak parameters within the respective uncertainties.

The pipe weldment, which has a length of about 40 cm and the weld in the middle of the pipe section, was mounted on a computer controlled XYZ translator table manufactured by Klinger Inc. (Garden City, NY). This pipe section was also count-balanced by a lead dead-weight through a hoist to provide a stability to the whole testing

system. This is shown in Figure 43. Sample positions were set to a precision of ± 0.01 mm and were read by encoders on the step motor shafts. Labview data acquisition software, run on a Macintosh Quadra 950 computer, controlled the translators and the sample half angling drive, as well as the multichannel analyzer data acquisition, data storage, and translation to ASCII for off-line analysis of the peak parameters.

Neutron absorbing masks manufactured from cadmium, with slits of width 2 mm and selectable height, were rigidly mounted on optical benches to define the incident and scattered beams at the same position. The gauge volume (the intersection of the incident and scattered beams) was centered on the rotational axis of the spectrometer sample table. This was achieved by first locating a 1 mm plastic pin on the rotational center of the table using a travel-scope and then translating the incident slit across the neutron beam to find the maximum scattering from the pin. This process was repeated using the scattered beam slit, with the scattering angle set at 96.4°. The spatial coordinates of the pipe inner surface were determined by measuring the diffracted intensity as each surface was translated through the gauge volume.

Strain measurements were made along a line in the axial direction on the pipe inner surface and at the 180° azimuthal position from welding start position. The geometry for measurement of the three principle strain components, namely, axial strain ϵ_a, hoop strain ϵ_h, and radial strain ϵ_r, is shown in Figure 44. The beam defining slits were 2 mm in height for the measurements of all three strain components. As discussed before, the neutron beam is attenuated exponentially when passing through the materials. Thus, from Figure 44, it is obvious that the hoop strain ϵ_h was the most difficult one to measure among the three strain components. Each hoop strain measurement took about 300 minutes to reach a statistically sound peak. The is the axial strain ϵ_a was the most easily acquired and took about 30 minutes to measure and each radial strain ϵ_r took about 220 minutes to finish.

Table 3. Chemical Compositions of 304L Stainless Steel Pipe Base Metal and Weld

	Mn	Si	P	S	Cr	Ni	Mo	Cu	C	Fe
Base M.	1.64%	0.69%	0.021%	0.009%	18.31%	8.98%	0.43%	0.34%	0.015%	Bal.
Weld	1.51%	0.43%	0.022%	0.012%	19.41%	11.46%	0.12%	0.12%	0.026%	Bal.

Table 4. OGI Weldment Welding Parameters

Pass Number	Welding Current (A)	Welding Voltage (V)
1	140 - 145	9.3 -9.4
2	190	10.7
3	230	11.5
4	188	11.4
5	188	10.9
6	185	10.9
7	180 - 200	11 - 11.4
8	190	11
9	225	11
10	215 - 220	11
11	210	11
12	225	11

Table 5. Nine-Pass Standard V Groove Weldment Welding Parameters

Pass#	Current (A)		Travel Speed (cm/min)	Voltage (v)	Pulse (s)		Wire Feed Speed (cm/min)	
	Peak	Back-ground			Peak	Back-ground	Primary	Back-ground
1	90	50	9.4	8.0	0.35	0.4	0	0
2	130	85	11.43	8.8	0.25	0.3	177.8	139.7
3	155	95	10.16	8.8	0.3	0.3	177.8	139.7
4	180	120	10.16	9.2	0.3	0.3	228.6	177.8
5	200	130	10.16	9.2	0.3	0.3	228.6	177.8
6	200	120	10.16	9.2	0.3	0.3	228.6	177.8
7	195	135	10.16	9.2	0.3	0.3	228.6	177.8
8	140	85	10.16	8.8	0.3	0.3	114.3	88.9
9	140	85	10.16	8.8	0.3	0.3	114.3	88.9

Table 6. Four-Pass Narrow Gap Groove Weldment Welding Parameters

Pass#	Current (A)		Travel Speed (cm/min)	Voltage (v)	Pulse (s)		Wire Feed Speed (cm/min)	
	Peak	Back-ground			Peak	Back-ground	Primary	Back-ground
1	135	80	9.4	8.0	0.35	0.4	0	0
2	230	135	10.16	8.5	0.25	0.4	127.0	88.9
3	185	120	10.16	8.8	0.3	0.3	114.3	76.2
4	190	120	10.16	9.2	0.3	0.3	114.3	76.2

Table 7. Six-Pass Standard V Groove Weldment Welding Parameters

Pass#	Current (A)		Travel Speed (cm/min)	Voltage (v)		Pulse (s)		Wire Feed Speed (cm/min)	
	Peak	Back-ground		Peak	Back-ground	Peak	Back-ground	Primary	Back-ground
1	104	55	9.4	7.7	0	0.35	0.4	0	0
2	105	105	7.62	8.6	7.8	N/A	N/A	139.7	114.3
3	188	120	7.62	8.8	8.2	N/A	N/A	139.7	101.6
4	188	120	9.4	8.8	8.0	N/A	N/A	152.4	76.2
5	200	140	7.62	9.7	8.6	N/A	N/A	152.4	101.6
6	180	140	7.62	9.1	8.6	N/A	N/A	114.3	68.58

	OSC Ampli (cm)	Out DWL (s)	Exc Time (s)	In DWL (s)
1	N/A	N/A	N/A	N/A
2	0.38	0.6	0.4	0.25
3	0.51	0.75	0.36	0.5
4	0.46	0.85	0.3	0.25
5	0.74	0.7	0.7	0.45
6	0.33	0.83	0.4	0.45

Table 8. Directions of Principle Stresses in Hole Drilling Strain Gage Rosette

$(\epsilon_1+\epsilon_3) - 2\epsilon_2$	$\epsilon_3-\epsilon_1$	Range of α
Less than 0	Less than 0	$-90° < \alpha < -45°$
Less than 0	Greater than 0	$-45° < \alpha < 0°$
Greater than 0	Greater than 0	$0° < \alpha < 45°$
Greater than 0	Less than 0	$45° < \alpha < 90°$

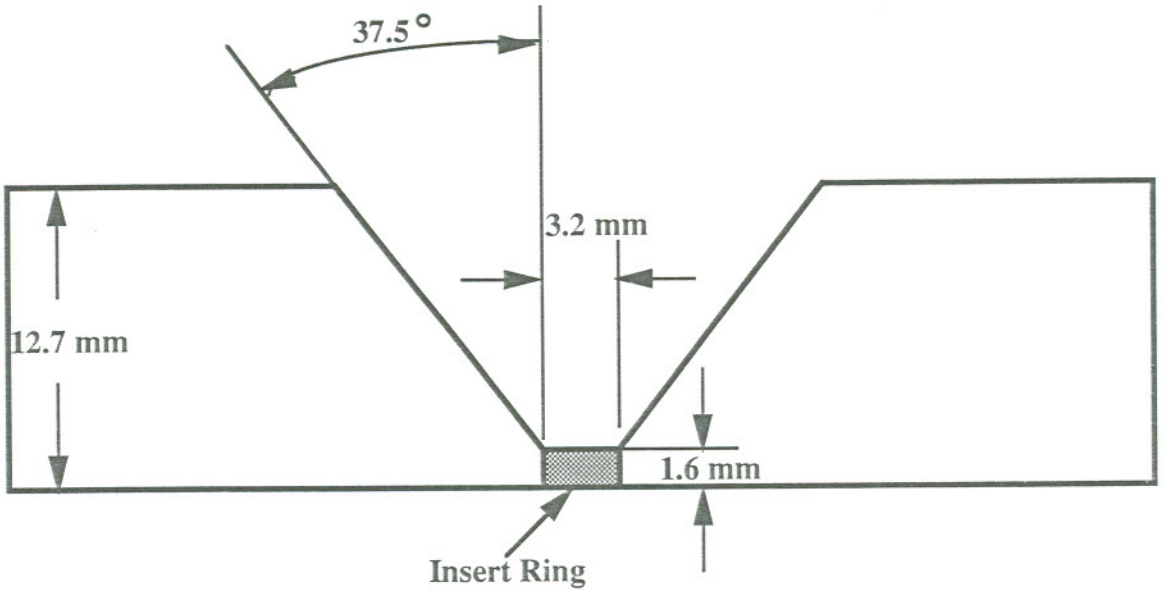

Figure 18. Weld Groove Geometry of the SRS Weldment

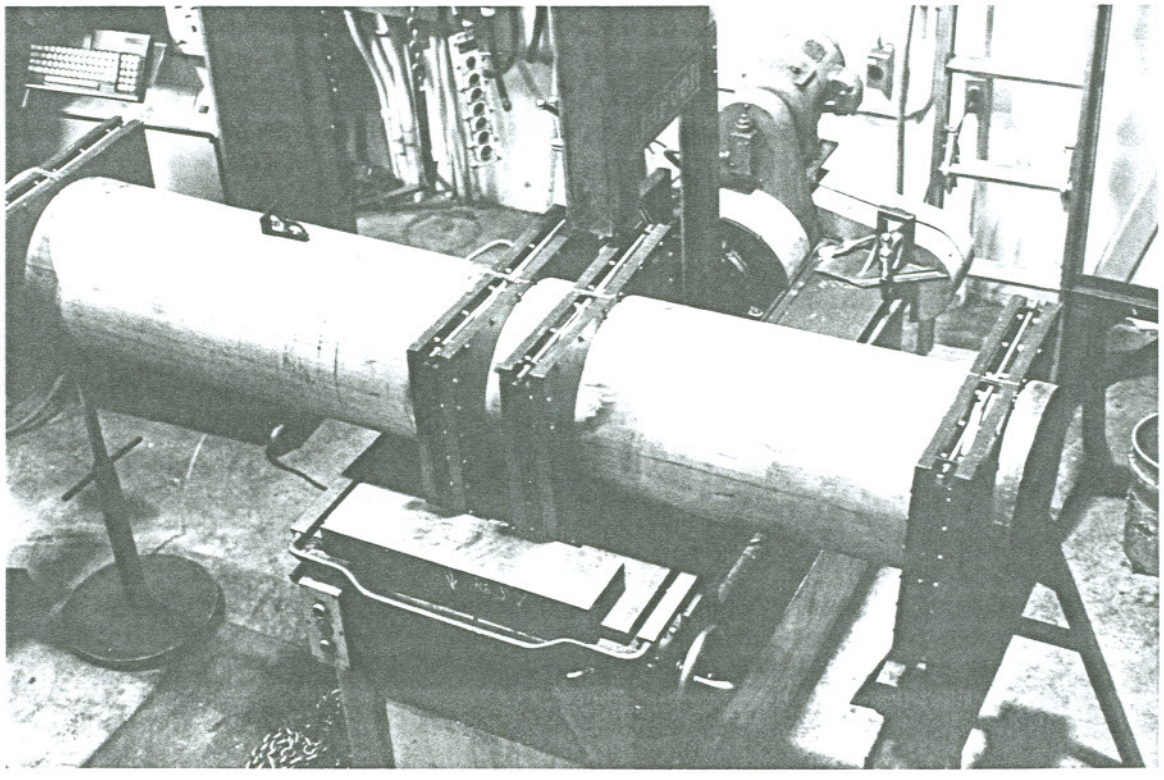

Figure 19. 240 mm Pipe Being Cut

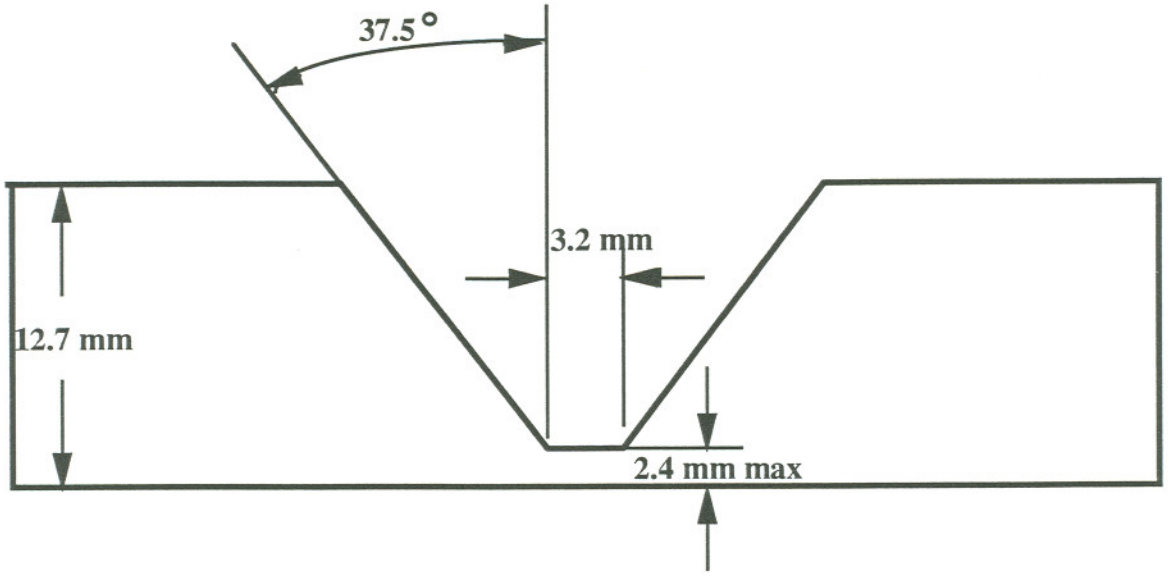

Figure 20. Weld Groove Geometry of the OGI Weldment

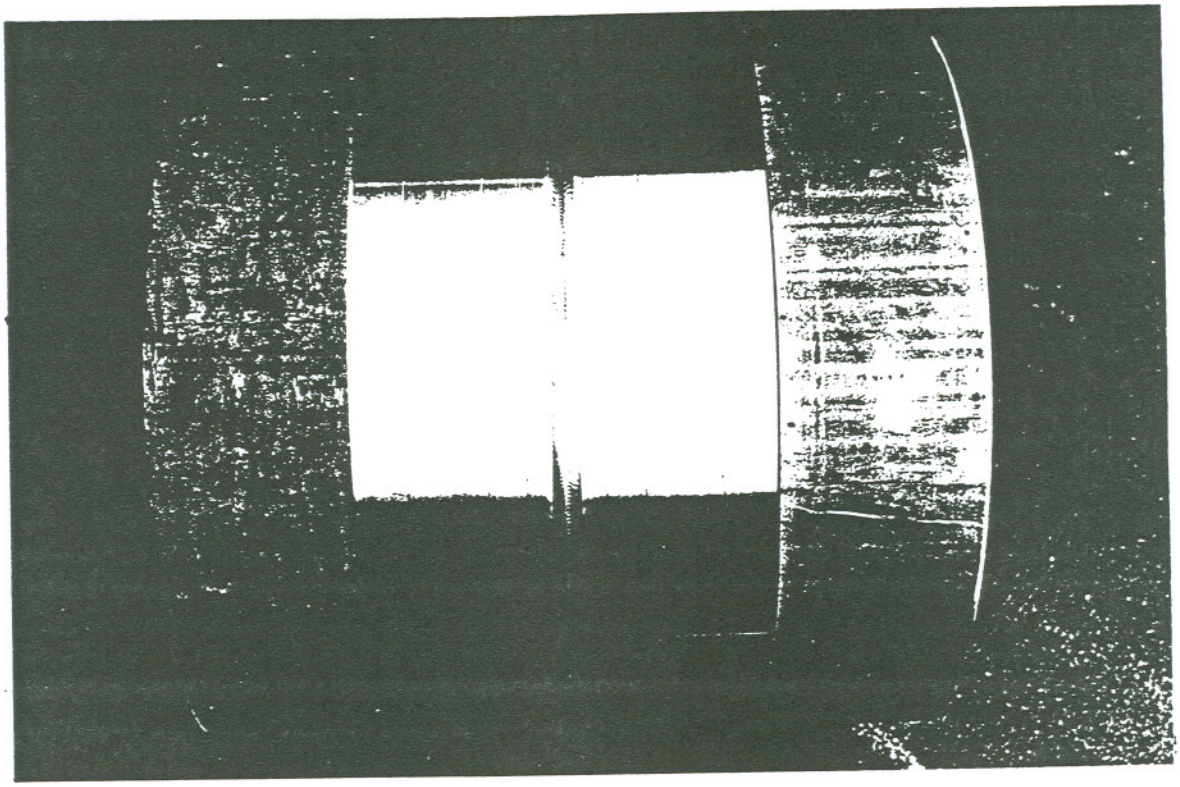

Figure 21. Head-on View of the Grooved 40 cm Pipe Section

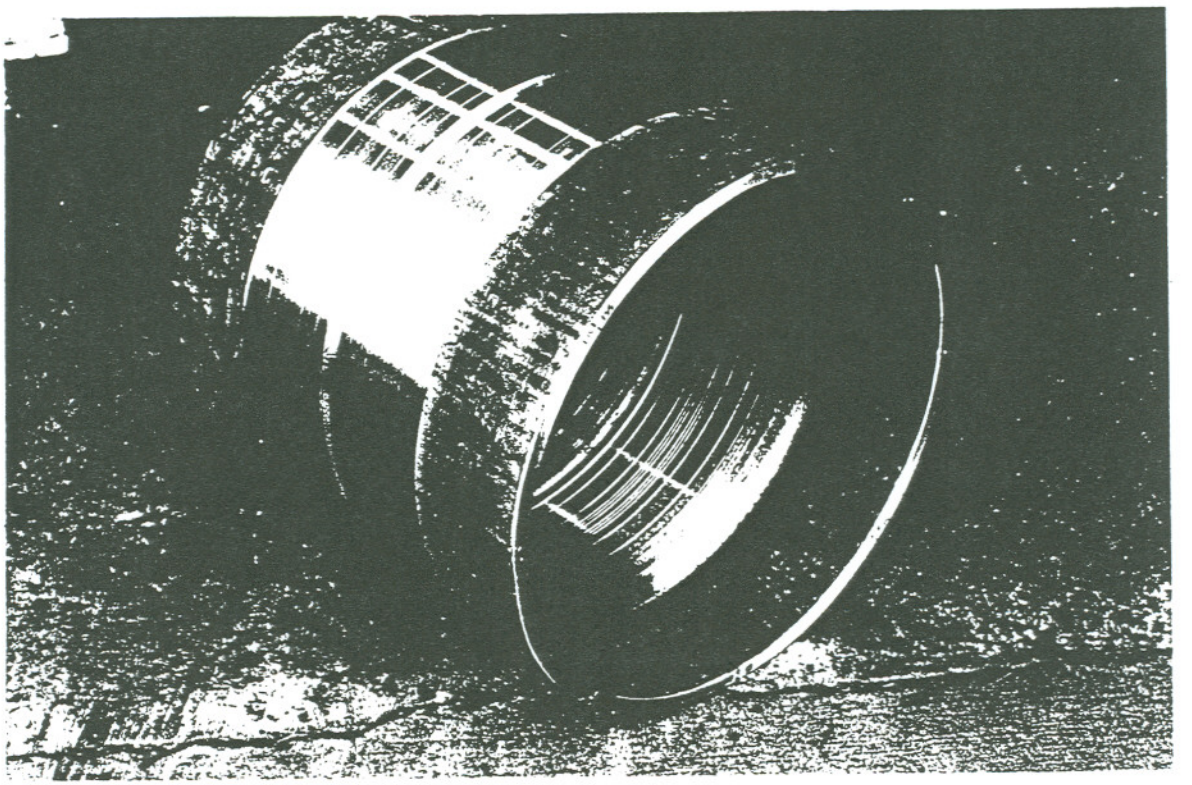

Figure 22. Angled View of the Grooved 40 cm Pipe Section

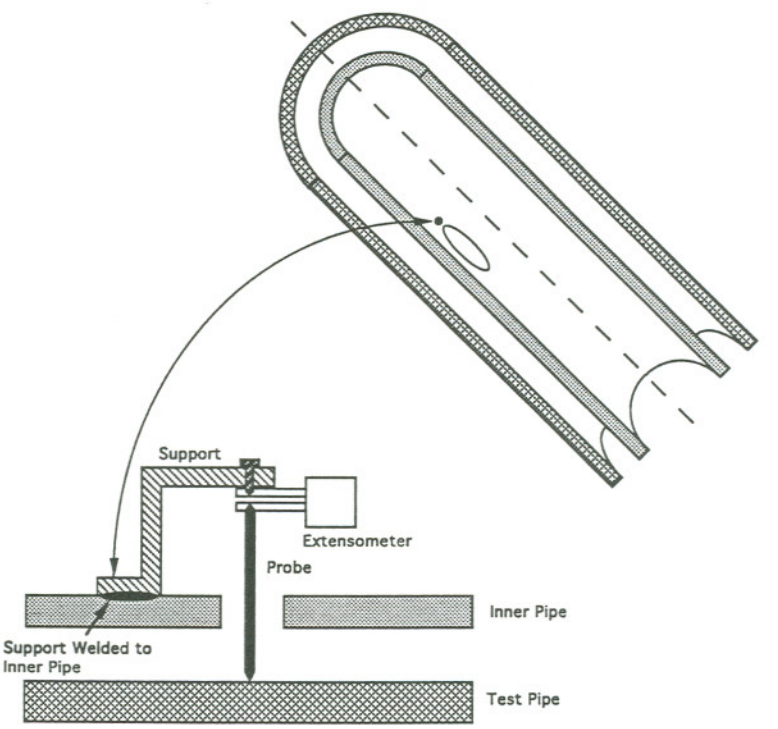

Figure 23. Schematic Illustration of Radial Deformation Device Setup Used in the OGI Weld

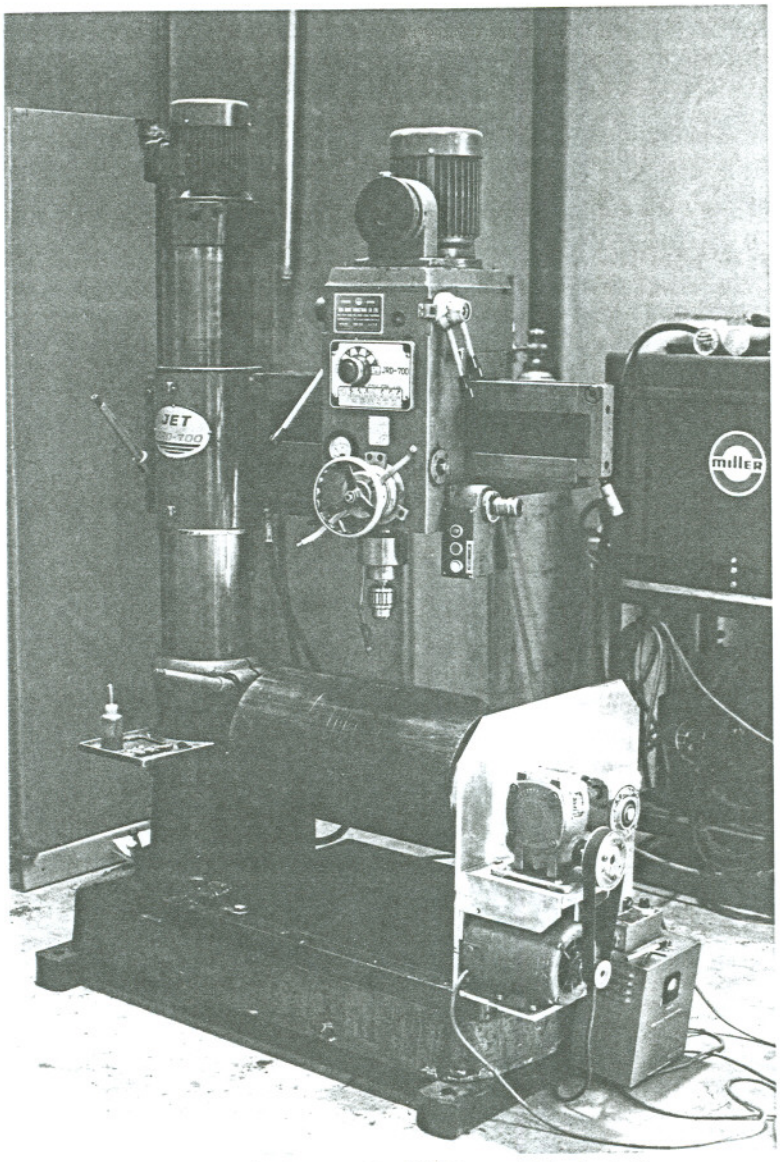

Figure 24. Radial Arm Drill Press Workstation

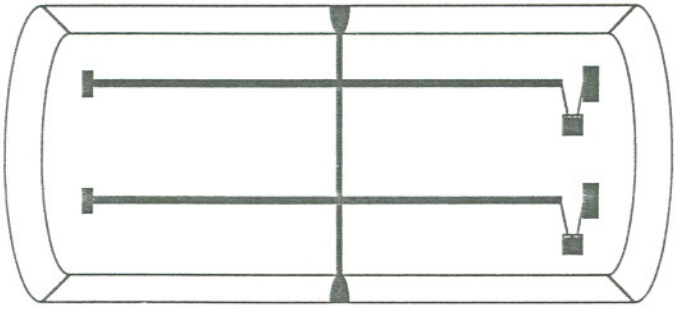

Figure 25. Schematic of Axial Deformation Measuring Unit

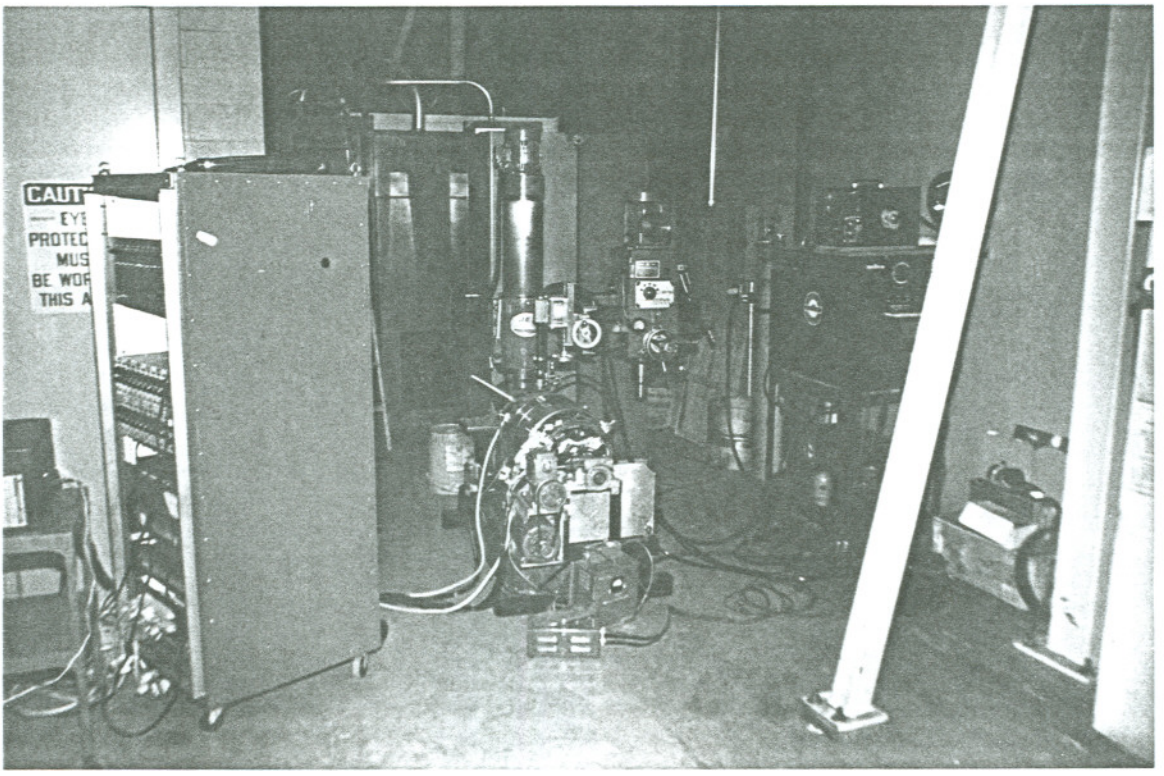

Figure 26. Setup for Pipe Weld Made at OGI

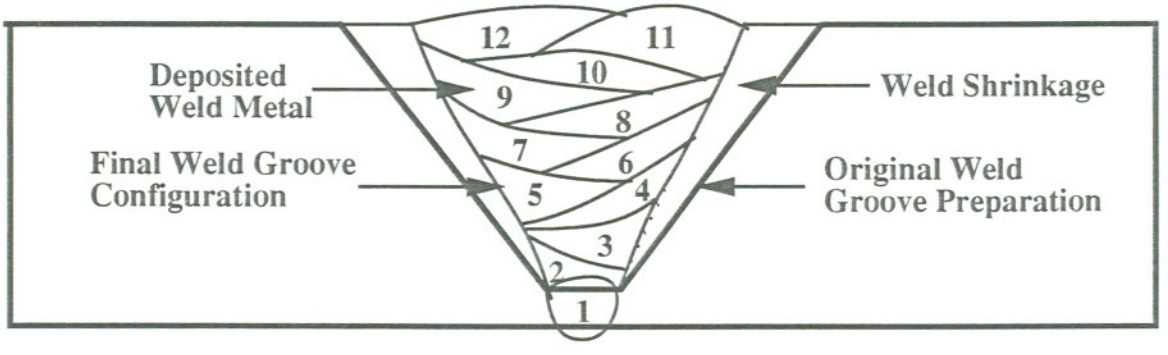

Figure 27. The OGI WeldmentPass Sequence

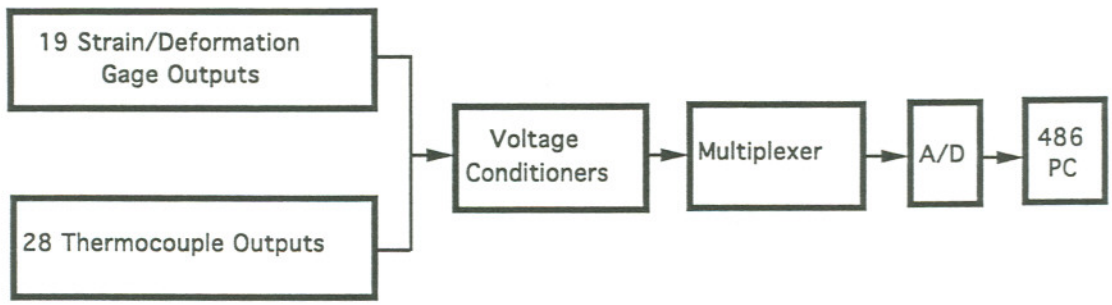

Figure 28. Setup of the Data Acquisition System

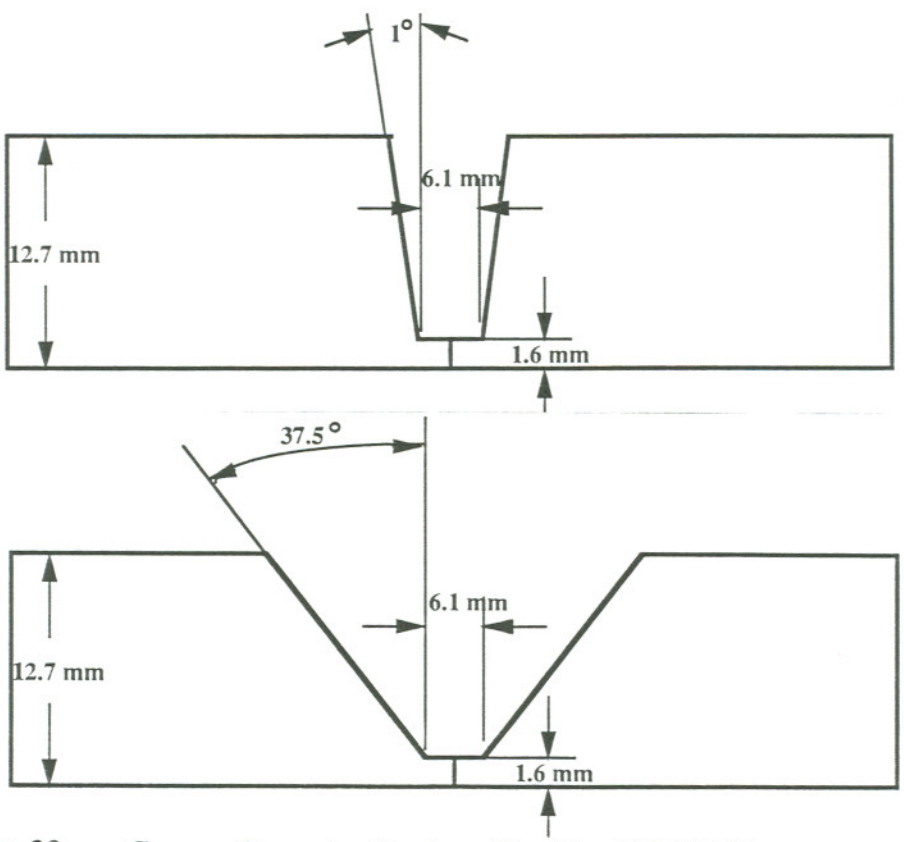

Figure 29. Groove Geometry Designs Used in AMI Weldments

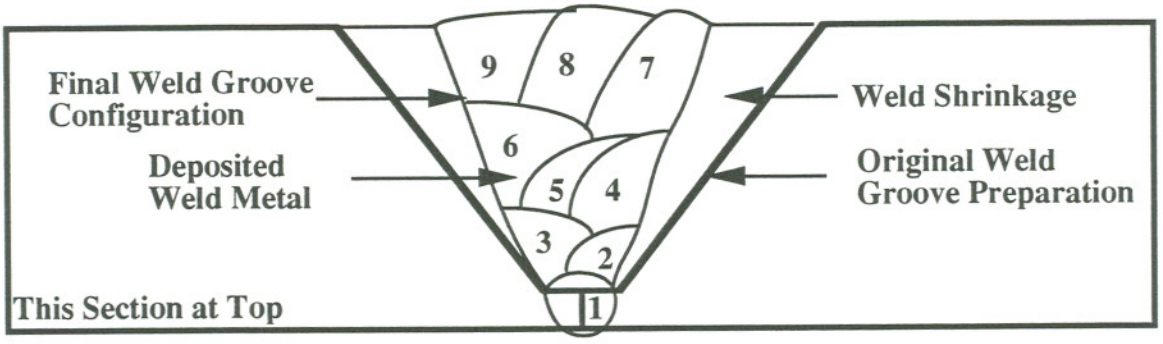

Figure 30. Nine-Pass Weldment Pass Sequence

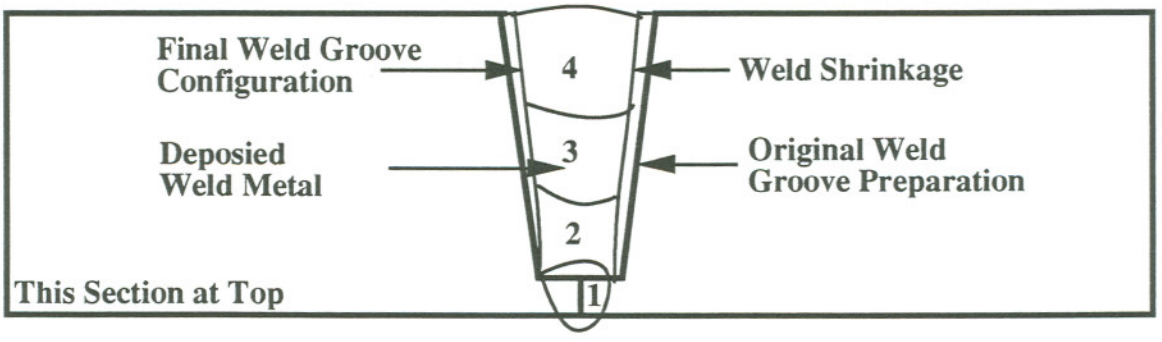

Figure 31. Four-Pass Weldment Pass Sequence

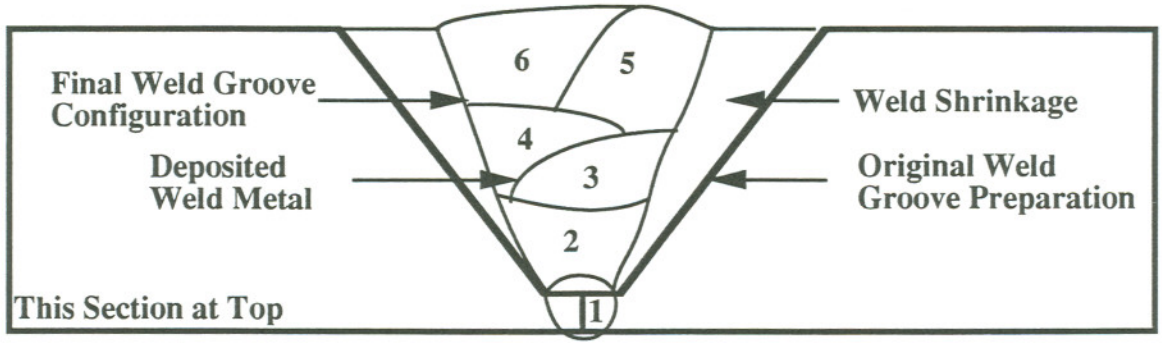

Figure 32. Six-Pass Weldment Pass Sequence

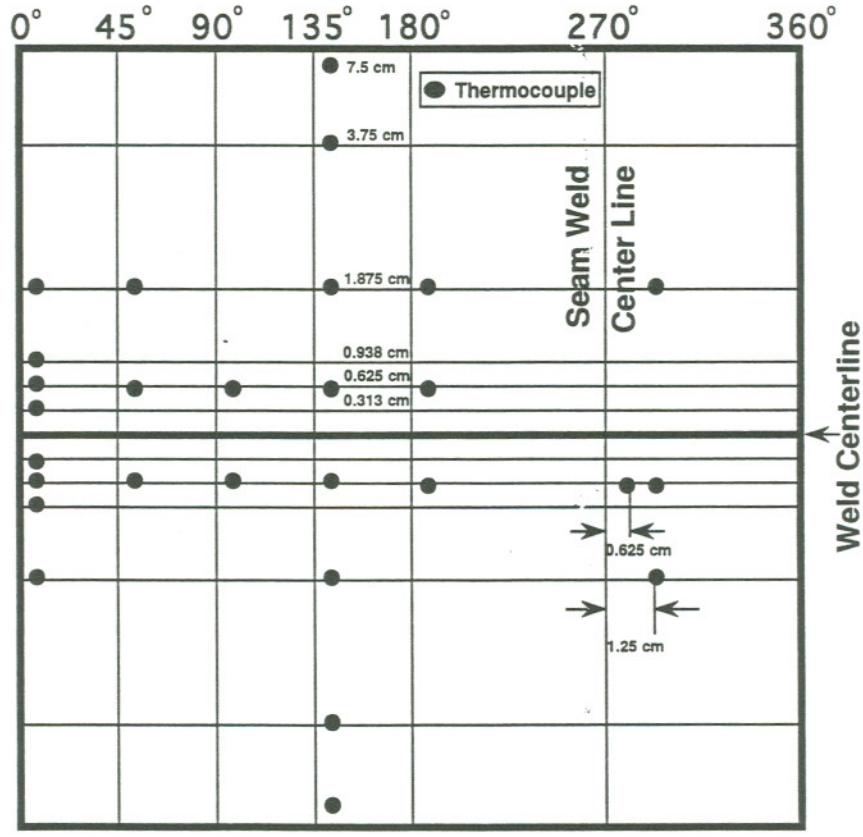

Figure 33. Layout of Thermocouples on the Inner Surface of the AMI Pipe Weldment

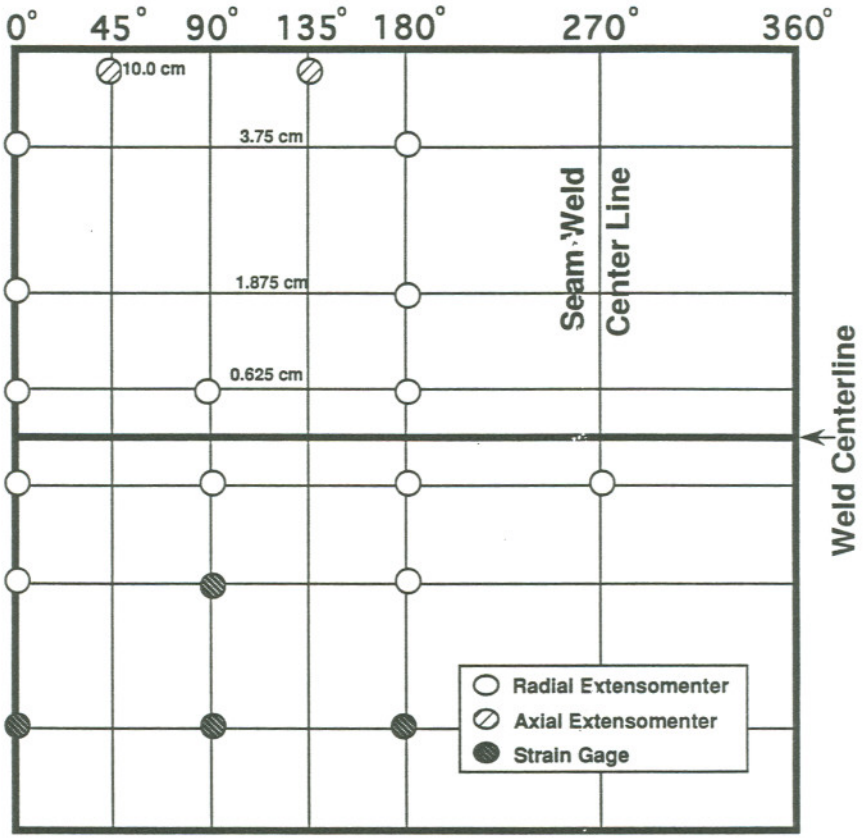

Figure 34. Layout of Deformation Devices and Strain Gages on the Pipe Inner Surface

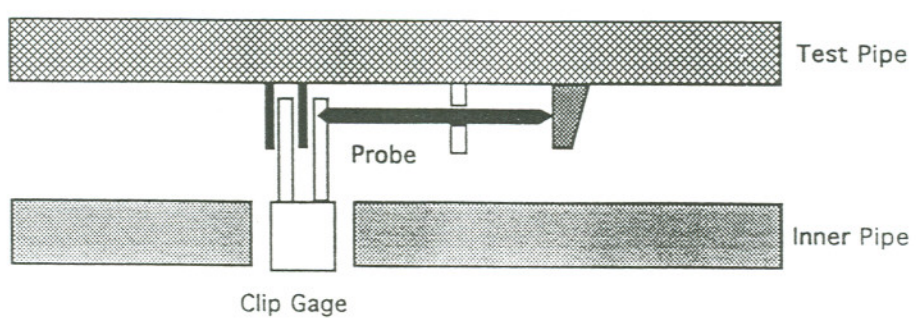

Figure 35. Schematic of the Axial Device Unit

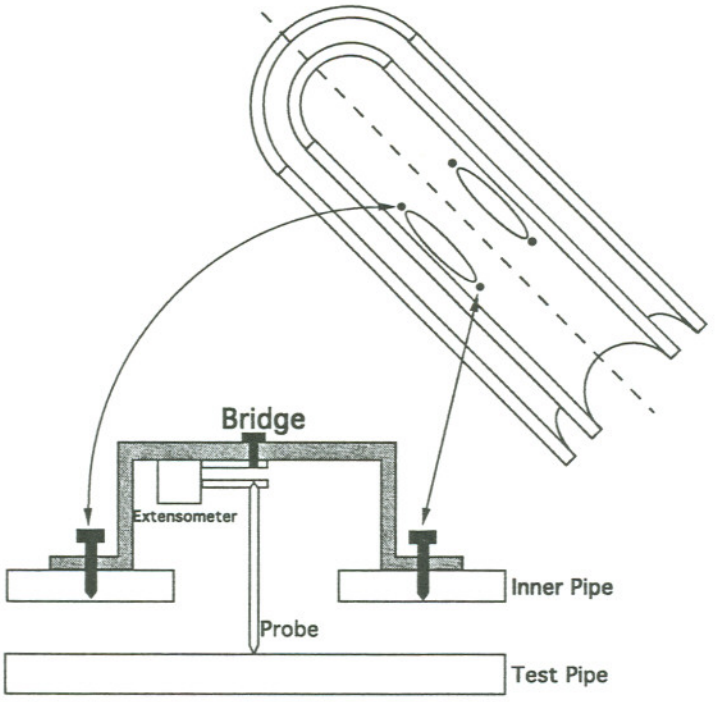

Figure 36. Schematic of Radial Deformation Device Installation Technique

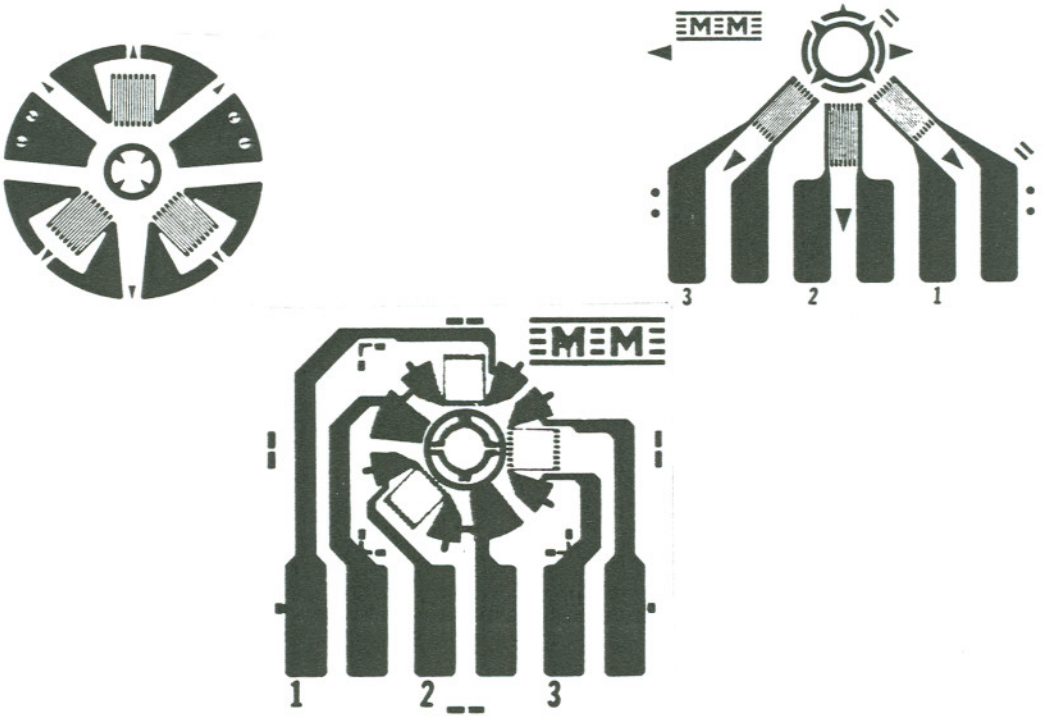

Figure 37. Hole-drilling Stain Gage Rosette Configurations (75)

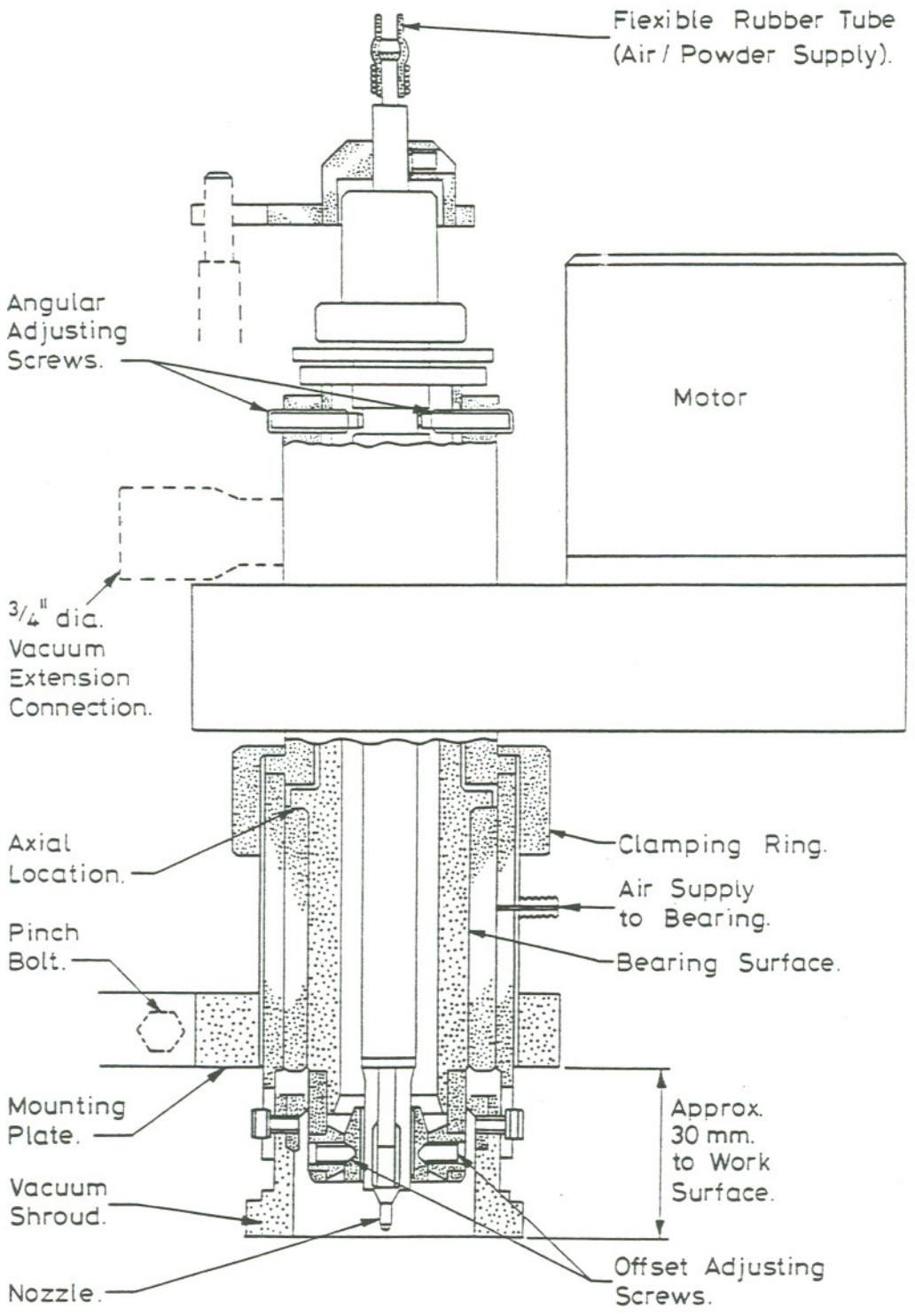

Figure 38. The Air-Abrasive Drilling Head

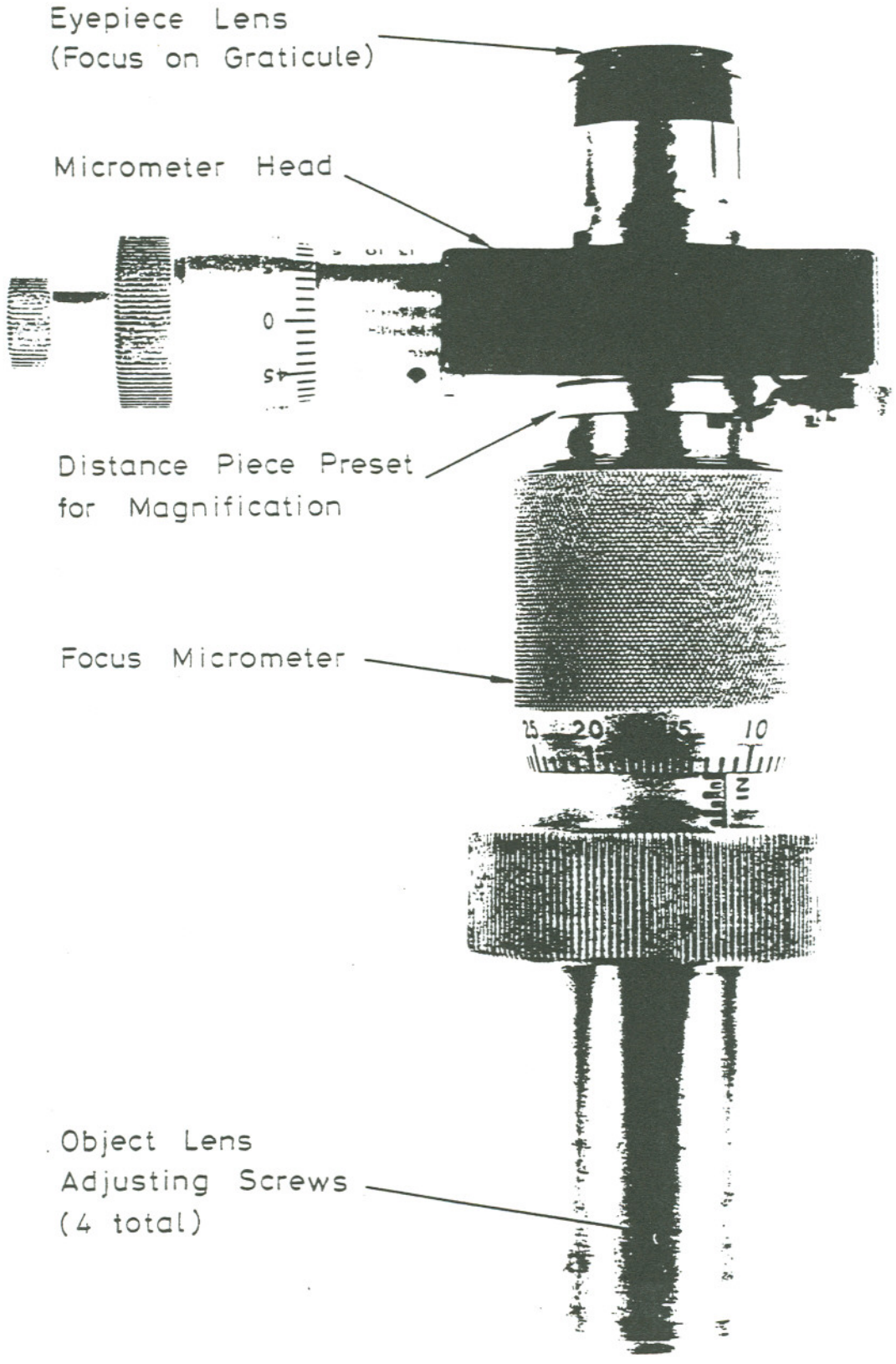

Figure 39. Optical Alignment Unit

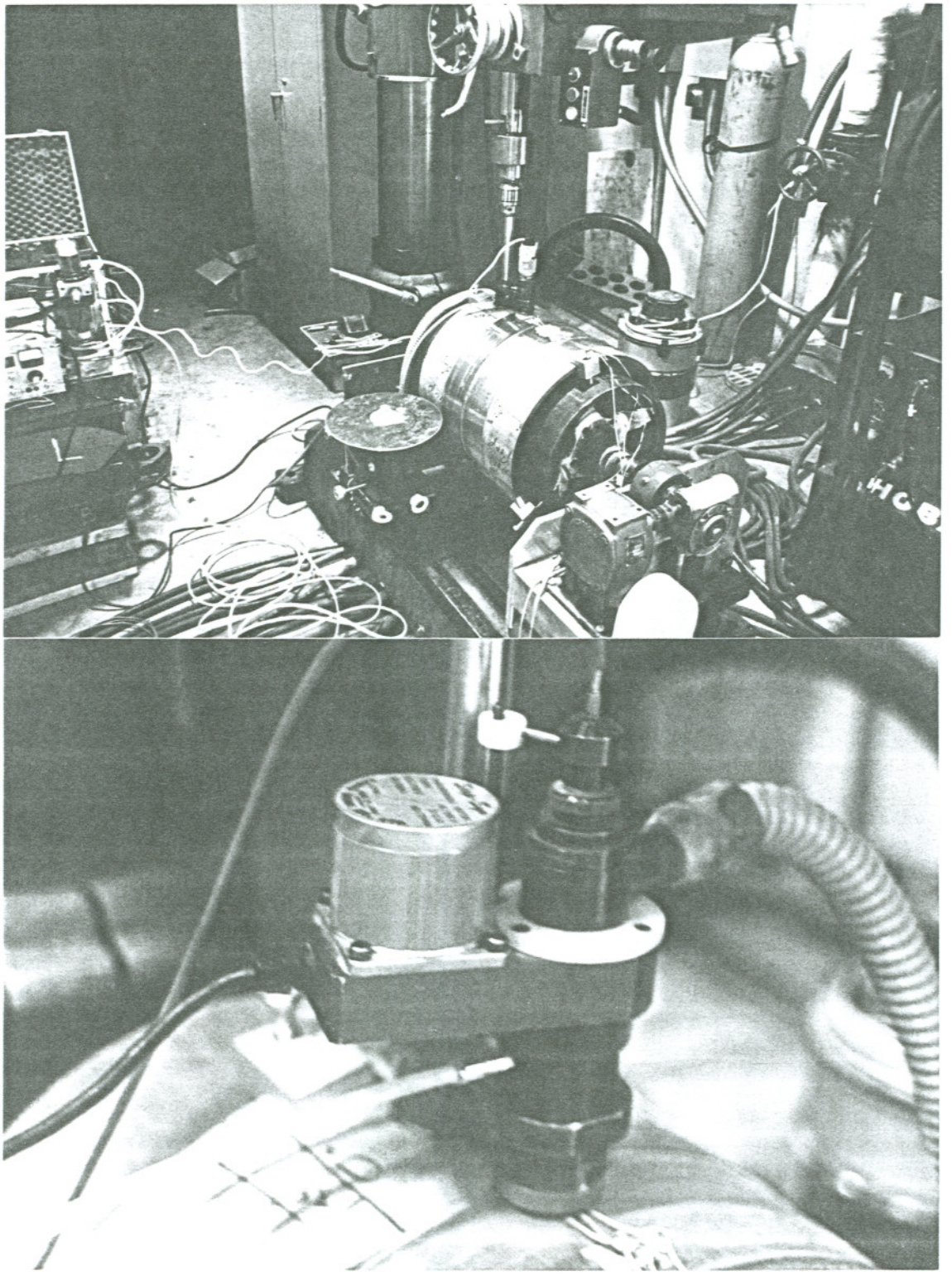

Figure 40. Hole-Drilling Stress Measuring System

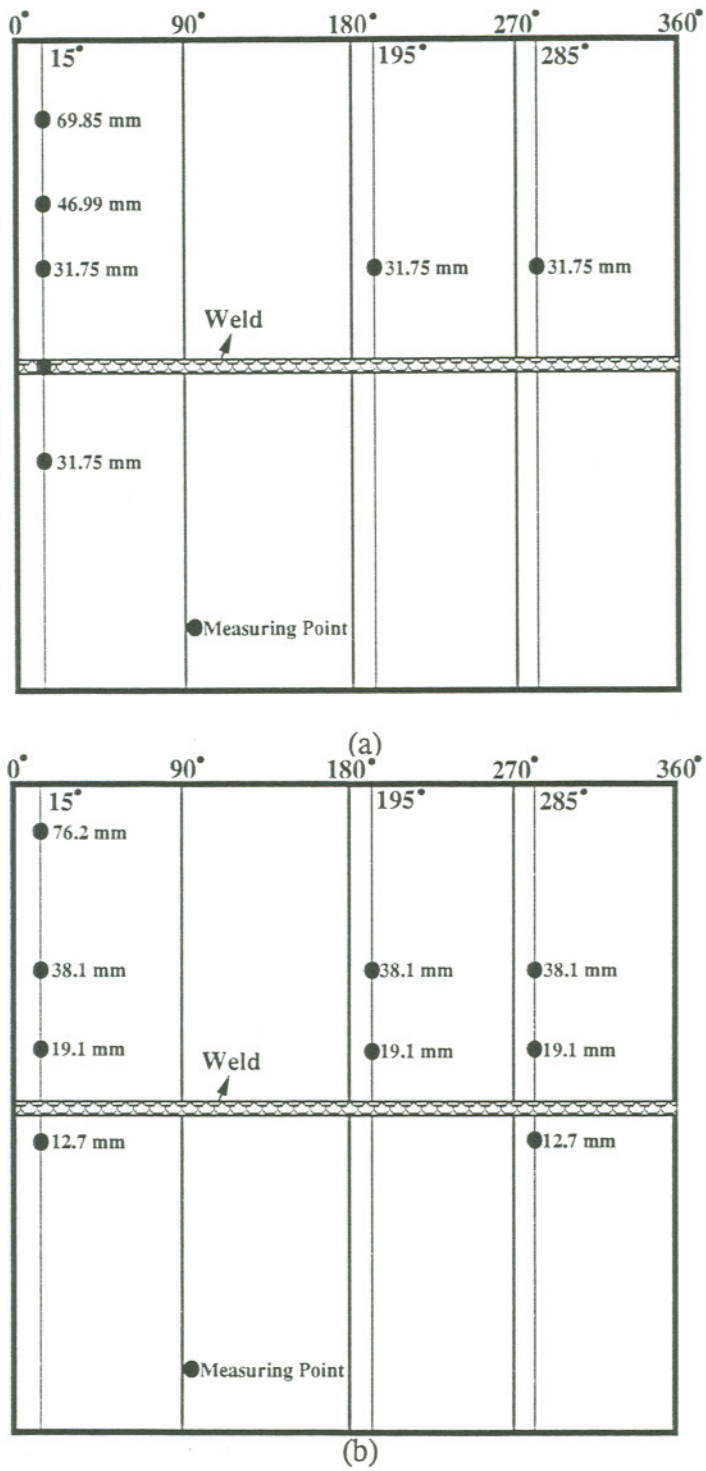

Figure 41. Layout of the Residual Stress Measuring Positions on Pipe Outer Surface for Three Pipe Weldments (a) OGI Weldment (b) Four-Pass Weldment (c) Six-Pass Weldment

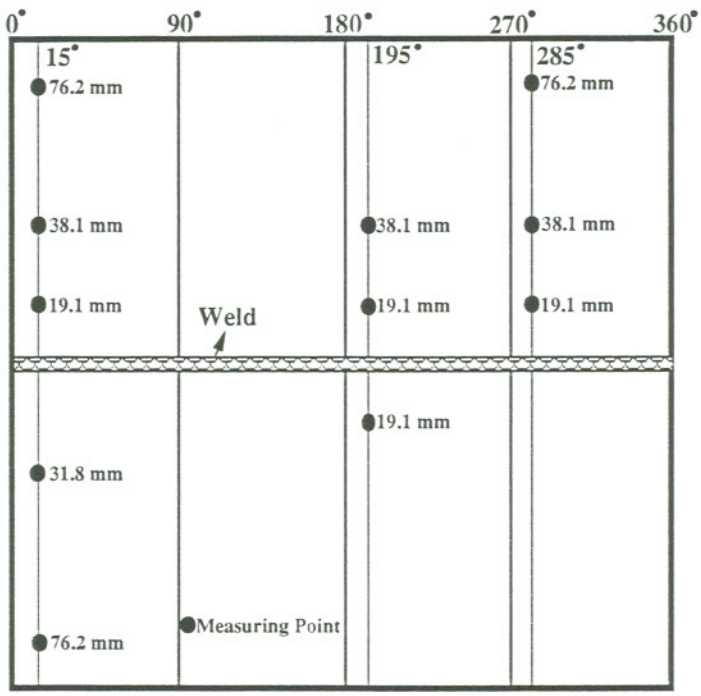

(c)

Figure 41. Layout of the Residual Stress Measuring Positions on Pipe Outer Surface for Three Pipe Weldments (a) OGI Weldment (b) Four-Pass Weldment (c) Six-Pass Weldment

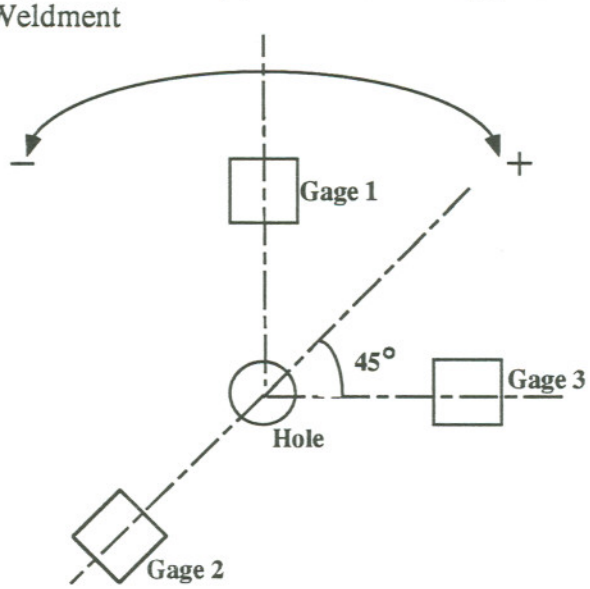

Figure 42. Direction of the Most Positive Principal Stress in Strain Gage Rosette

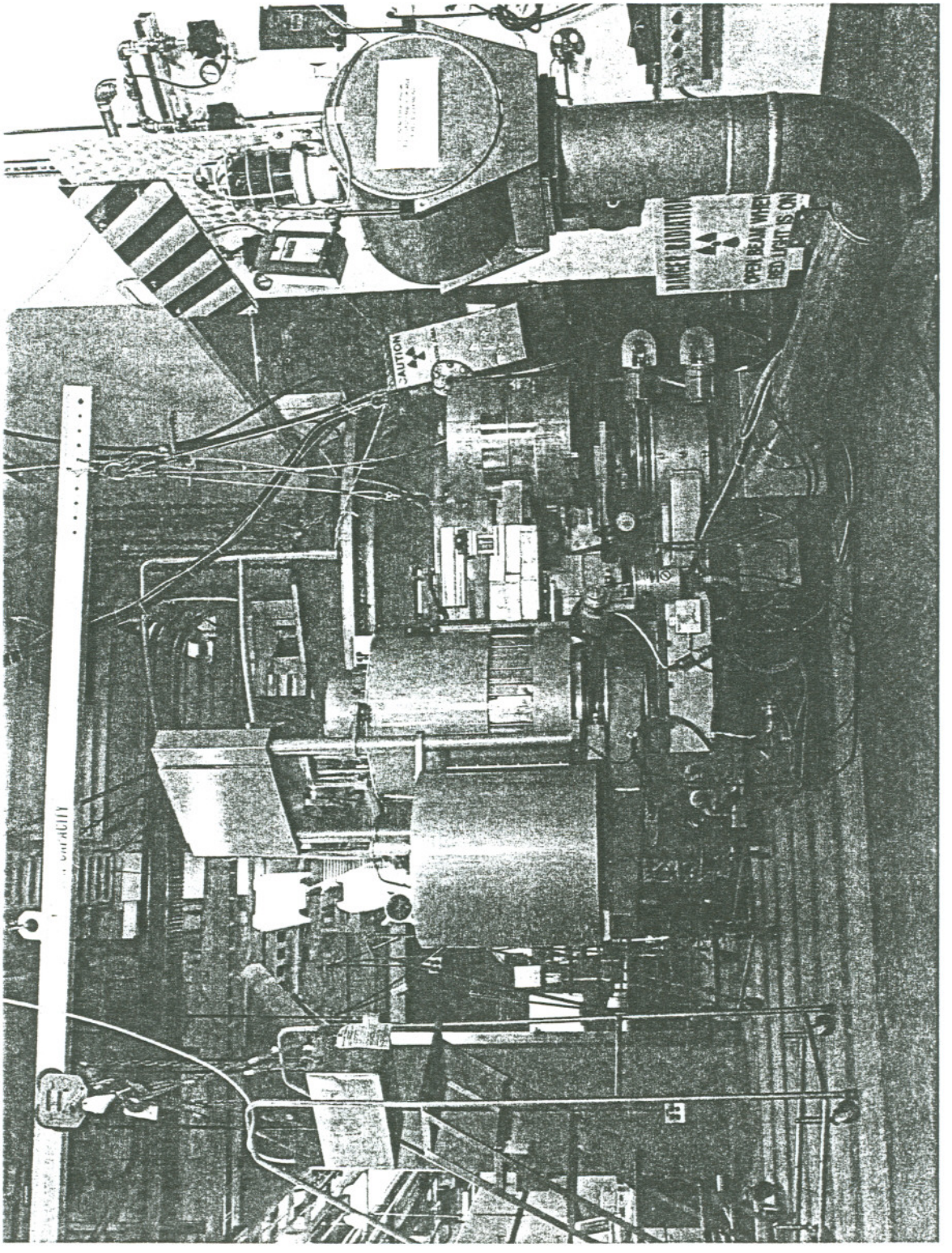

Figure 43. Neutron Diffraction Residual Stress Measuring System Setup

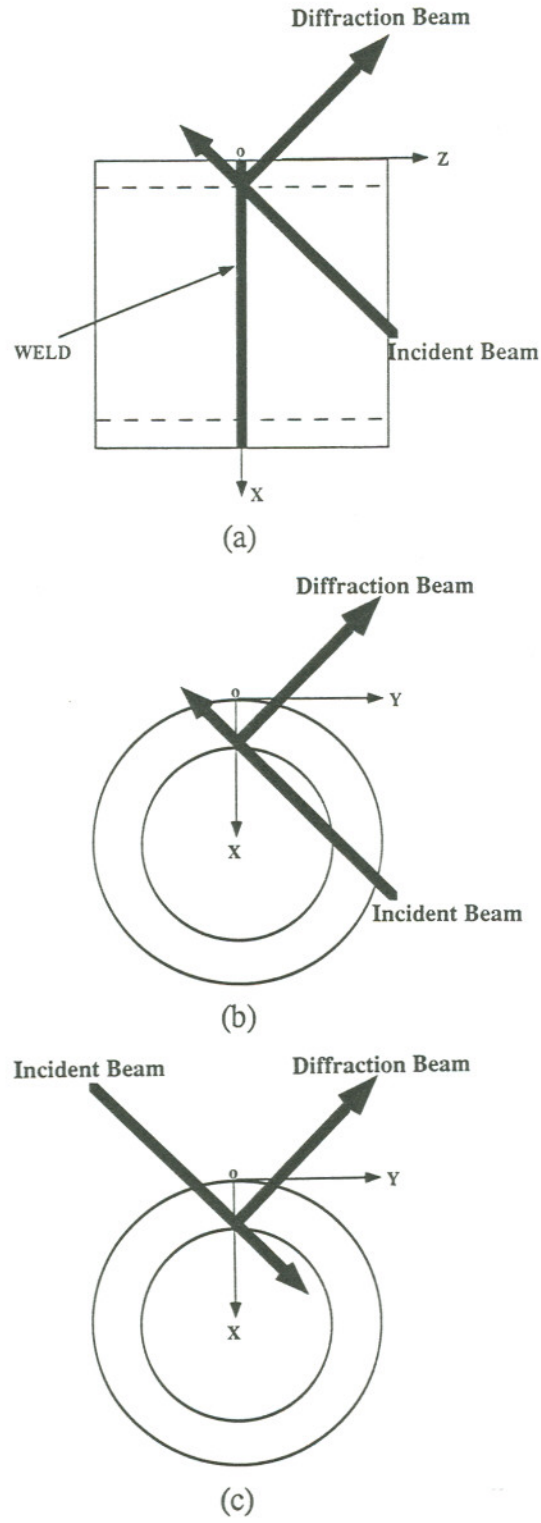

Figure 44. Orientations of Pipe with Respect to Neutron Beams to Measure (a) Axial, (b) Hoop, and (c) Radial Strain Components

CHAPTER 4
NUMERICAL PROCEDURES

INTRODUCTION

The goal of this numerical study was to model the whole multipass weldment in detail to establish a baseline for further simplified numerical analysis of other weldments. Certainly, it would be very helpful to model every weldment involved in this work in detail, but it is impossible in terms of computing resources and time. Thus far, no other study on 3D model of pipe multipass girth welding process has been reported.

In this study, the narrow gap weldment was modeled by the finite element analysis (FEA) technique. The reasons to choose the narrow gap weldment instead of other weldments were: 1) narrow gap weldment had the fewest number of welding passes involved, requiring the least computing time to model; 2) the narrow gap weldment was continuously welded, this allows one to continuously model the welding process and avoids the start-stop interruptions; 3) the narrow gap weldment had geometric symmetry with respect to the weld centerline, thus only half the pipe weldment was required to be modeled, saving half of the computing cost and time. In modeling of the narrow gap weldment, a 3D transient thermal analysis was conducted first, followed by a 3D thermal stress analysis. Figure 45 shows the flow chart of 3D thermal/stress analysis.

In addition to the 3D model of the narrow gap weldment, a simplified 2D model was developed to simulate the narrow gap weldment and CSI process. The pipe welding process is certainly not an axisymmetric case. But the main purpose of this work was to study the effectiveness of the CSI method and if CSI is appropriately represented by an axisymmetric model. Thus this 2D axisymmetric approach was justified. The flow chart of this model is presented in Figure 46.

FINITE ELEMENT CODE AND ASSUMPTIONS

The narrow gap pipe girth welding and CSI process were modeled by using the computer code ANSYS 5.0 (113). The ANSYS program is a general purpose finite element code which can be used in all disciplines of engineering - structural, mechanical, electrical, electromagnetic, electronic, thermal, fluid, and biomedical. Revision 5.0 version of the ANSYS program is a complete rewrite of the software, which allowed implementation of the current state-of-the-art technology. One of the major developments in the Revision 5.0 is the enhancement of the nonlinear capabilities. It has elements with the death and birth feature which is very critical in terms of modeling an arc welding process. It also has the ability to model the phase change (or melting) of metal by application of enthalpy (including heat of fusion) as a function of temperature.

The numerical approaches are simplified by making certain assumptions. This work assumes that the heat generated by the deformed solid is negligible. Thus thermal and stress analysis were conducted sequentially in the model. This work also meshes the weld pool using simplified weld groove shape and pass structure. As stated before, the physics of the heat transfer at the arc/weld pool interface is highly complex (114), and requires a computationally intensive and highly specialized computer analysis. For the TIG weld, the complete simulation of heat transfer and fluid flow mechanics in the weld pool should account for conduction, convection and electro-magnetic body forces in the liquid weld pool; radiative, convective, and evaporative losses at the weld pool surface, as well as surface tension effects; and heat conduction into the solid surrounding the weld pool. In this study, use of a heat conduction code to model the complete weld pool physics provides only a crude approximation of the actual heat transfer solution. In addition, the assumed heat flux profiles for the arc are not a true representation of the gas tungsten arc physics. As a result, "tuning" of the heat conduction thermal model is employed in the analysis. In the present study, "tuning" of the thermal solution was done by using experimental data to baseline the numerical calculations. This tuning was

accomplished by bringing the calculated temperature histories in agreement with those measured by the thermocouples at a comparable position. The "free" parameters in the thermal solution, which included the spatial distribution of the heat source, the vaporization efficiency under the arc, and the liquid thermal conductivity, were adjusted to fit the numerical results to the experimental data. Once the thermal solution was tuned, a thermal-mechanical analysis was performed without further adjustments or tuning. In realty, a structural analysis should be conducted at every time solution from the heat transfer analysis. However, one could examine the temperature solution at various locations in the structure and using engineering judgment, then decide at what time solutions produce the worst temperature gradients. Structural analysis would then be conducted at these selected times as these large gradients produce the worst stress states. Thus, it was felt that the reduced number of sequential structure solutions would produce reasonably accurate results, while saving substantial computer time.

3D MODEL FOR NARROW GAP WELDMENT

Thermal Analysis

Governing Equation and Boundary Conditions

The fundamental equation for conservation of thermal energy (the first law of thermodynamics) in a solid is:

$$\nabla \cdot k \nabla T + Q_s = \rho c_p \frac{\partial T}{\partial \tau} \qquad (13)$$

where ∇ is the 3D vector operator, $\partial/\partial\tau$ is the material derivative operator, T is temperature, τ is the time, k is thermal conductivity, Q_s is the internal heat generation rate per unit volume, ρ is density, and c_p is specific heat.

Boundary conditions are given by the well-known Fourier law of heat conduction

which can be derived from the statement of the second law of thermodynamics:

$$Q = -k \cdot \nabla T \qquad (14)$$

Heat flux Q consists of one or more of the following modes of heat transfer depending upon the boundary:

(1) $h(T-T_a)$, the convective heat loss, h, T, and T_a are the convective heat loss coefficient, surface temperature, and ambient temperature, respectively;

(2) $\epsilon\sigma(T^4-T^4_a)$, the radiative heat loss, ϵ and σ are the emissivity and the Stefan-Boltzmann constant, respectively;

(3) $-q''_s$, if the surface is receiving a specified heat flux, q''_s.

Finite Element Mesh Generation

Because of symmetric nature of the narrow gap weldment, only half of the pipe weldment with one end at the weld center plane was modeled. In this study, this half pipe weldment length is about 20 cm as shown in Figure 47, where z=0 line (plane) is the weld center line (plane). Eight node brick elements (solid45 3-D structure element and solid70 3-D thermal element in ANSYS 5.0, shown in Figure 48) were used to discrete the pipe. A nonuniform mesh with 3360 elements and 4800 nodes was generated over the entire 20 cm length pipe section. There are 7 nonuniform elements placed in the pipe axial length (20 cm and z direction) and 120 uniform elements in the pipe circumference (40 cm diameter and θ direction) and 4 nonuniform elements in the pipe thickness (1.27 cm and r direction). The density of elements varies as a function of distance from the weld center line (plane) with the greatest concentration near the weld center line (plane). A total of 960 elements were placed in the weld area (about 6.35 mm from weld centerline). The smallest element has a width and height of about 1 mm each. In the mesh, many nodes were carefully positioned to match the thermal and deformation/strain measuring points. The mesh of this pipe section is presented in

Figure 49.

Mesh design is one critical factor in modeling of the welding process. What is a good mesh? How fine a mesh is needed to achieve a specified accuracy? What is the error associated with a given mesh and how is it distributed? These are all valid questions without proper answers yet. In the present study, the mesh was made as fine as possible. Accuracy was primarily evaluated by comparison with the experimental data. Halving the mesh size could increase the computing cost by a factor of about 100 (53). This is simply impossible and unaffordable under present computing conditions. Although more powerful computers will be helpful, they clearly will never provide the power needed to analyze a finer mesh.

Heat Source Model and Material Thermal Properties

Table 9 summarizes the 304L stainless steel thermal properties used in the model. The thermal properties in the melting temperature were based on Argonne data (115) for liquid 304L SS. The surface emissivity factor, ϵ, and the heat transfer coefficient, h, were estimated from thermal data and held constant in the analysis (45), since they had little impact on the accuracy of the overall thermal solution. However, the liquid thermal conductivity was enhanced linearly with temperature for the reasons to be discussed later.

The gas tungsten arc heat source distributed in the weld was modeled as a combination of transient heat flux and power density boundary conditions applied to the top surface of the weld pool and to the weld pool itself, respectively. The center of the heat source is in the weld center line (plane). The distribution of the heat flux was assumed to be Gaussian as described below:

$$Q(r,t) = f\eta_a [3Q_\infty(t)/\pi r_{2\sigma}^2] e^{-3[r/r_{2\sigma}]^2} \qquad (15)$$

where $r_{2\sigma}$ represents the radius within which 95% of the energy is transferred. The radius represent a free parameter in the heat source model. After several tries, this

radius value was set at 3 mm.

The total power, $Q_\infty(t)$, in the Gaussian distribution was varied as a function of time according to the experimentally measured power input, *i.e.*, $Q_\infty(t) = E \bullet I$ (Watts), where E is welding voltage (V), I is average welding current (A). A constant efficiency factor (η_a) of 90% was applied to the Gaussian distribution in order to account for radiative and other losses from the arc to the ambient environment, *i.e.*, it was assumed that some portion of the energy ($1-\eta_a$) leaving the electrode never reached the weld pool surface. This efficiency factor represented another free parameter in the heat source model.

A constant factor (f) was introduced in the model to account for the surface heat flux portion in the total energy. The other portion (1-f) of energy in the total energy was the power density or internal heat generation Gaussian distributed inside the weld pool and can be represented in the following form:

$$Q_s(r,t) = (1-f)\,\eta_a\,[6\sqrt{3}Q_\infty(t)/\pi\sqrt{\pi}r_{2\sigma}^3]\,e^{-3[r/r_{2\sigma}]^2} \qquad (16)$$

here, f was again a free parameter. A value of 50% was selected for in this model.

Heat transfer effects due to fluid flow in the weld pool were approximated by enhancing the temperature-dependent thermal conductivity, k(T), in the melting temperature region, as done by many other researchers. In the current model, enhanced thermal conduction was prescribed by linearly increasing k (W/m-K) by a factor of six over the temperature range of 1673 to 3100 K. This is shown in Figure 50 and can be expressed as:

$$k = 8.116 + 1.618\times10^{-2}T\ (T \le 1673K),\quad k = f(T)\times35.2\ (T > 1673K) \qquad (17)$$

where f(T) increases linearly with temperature from 1 to 6 up to T = 3100 K. The effective thermal conductivity in the melting temperature range represented an additional free parameter in the present GTA model.

A phase change was modeled by defining the enthalpy (ENTH in ANSYS) of the material as a function of temperatures (see Figure 51). The specific heat c_p (J/kg-K) of 304L SS can be expressed as:

$$c_p = 465.4 + 0.1336T \ (T<1673K), \ c_p = 788 \ (T>1723K) \qquad (18)$$

where T is temperature in absolute value K. Enthalpy, which has units of heat/volume, is defined as the integral of density times specific heat (see Figure 52) with respect to temperature:

$$H = \int \rho c_p(T)\, dT \qquad (19)$$

The latent heat of fusion due to melting and resolidification was taken into account in the calculation of the enthalpy H over the melting range of the 304L alloy (*i.e.*, solidus to liquidus temperatures as 1673 K to 1723 K, respectively). The value of the latent heat of fusion, L_f, was 2.65×10^5 J/kg in this model. The latent heat of evaporation due to vaporization was considered in calculation of the enthalpy H at vaporous temperature (3100 K for 304L SS in this model). The value of the latent heat of evaporation, L_v, was 7.35×10^6 J/kg in this model. The density (ρ) of 304L SS is 8000 kg/m^3 at room temperature. At higher temperatures metal usually expands resulting in lower density. However, the uncoupled heat conduction analysis assumes that the material occupies the same volume throughout the analysis. Therefore, a constant density value of 8000 kg/m^3 has been used in the current study.

Heat losses from the pipe surface were modeled as three distinct heat flux boundary conditions. The three boundary conditions accounted for: 1) natural convection, 2) thermal surface radiation, and 3) heat loss due to evaporation at the weld pool surface. In each case, the local heat loss was expressed as a function of the local surface temperature.

Natural convection was modeled using the Newton's law of cooling applied uniformly over the top, bottom and far end side surfaces of the pipe as:

$$Q_c = h(T - T_a) \qquad (20)$$

where Q_c, h, T, and T_a are the local convective heat loss rate per unit area, convective heat loss coefficient, surface temperature, and ambient temperature, respectively. The convective heat loss coefficient, h, was assumed to be a constant of 1.0 W/m^2-K.

Thermal radiation was modeled as gray body radiation emanating from the top, bottom, and far end side surfaces as:

$$Q_r = \epsilon\sigma (T^4 - T_a^4) \qquad (21)$$

where Q_r, ϵ, and σ are the local radiative heat loss rate per unit area, the emissivity, and the Stefan-Boltzmann constant (5.6696x10^{-8} W/m^2-K^4), respectively. In this study, the emissivity was assumed to be a constant of 0.7.

The dominant heat loss mechanism in this problem is the evaporative heat loss from the weld pool surface (44,114,116,117). Unfortunately, the physical details of this heat loss mechanism are extremely complex. However, a simple kinetic argument can be used in which it is assumed that local thermal equilibrium exists at the weld pool surface between the molten weld metal and its vapor. The driving potential for evaporation (and hence heat loss) then becomes the pressure difference, p_v - p_a, where $p_v(T)$ is the equilibrium vapor pressure corresponding to the local liquid surface temperature and p_a is the ambient pressure. An approximation of the heat loss due to evaporation based on the Langmuir rate equation (117) was proposed by Block-Bolten and Eagar (118) and expressed as:

$$Q_e = 4.5\times10^7 p_v(T)\,[M/T]^{1/2}\cdot L_v \qquad (22)$$

where Q_e is the heat loss rate per unit area, $p_v(T)$ is the partial pressure of 304L stainless steel, M is the molecular weight, T is absolute temperature, and L_v is the heat of evaporation of 304L stainless steel.

Unfortunately, the above equation leads to a gross overestimate of the evaporative loss, since it neglects the presence of the cover gas and plasma directly above the weld pool. The cover gas and plasma can greatly reduce the evaporative loss by shielding the weld pool surface from the lower pressure ambient conditions existing outside the arc (114). To account for the presence of the cover gas and plasma in the present study, an efficiency factor, η_e, of 20% was applied to the above equation to bring the surface temperatures into agreement with the experimental measurements. Hence, η_e represents an additional free parameter in the model.

Thus, in the weld pool, the net energy (Q') transferred from the arc should be:

$$Q' = (1-\eta_e)\ (Q+Q_s) \qquad (23)$$

or the net efficiency factor (η') should be:

$$\eta' = (1-\eta_e)\cdot\eta_a \qquad (24)$$

Solution Procedure

The transient heat transfer of the narrow gap pipe girth welding process was modeled by using ANSYS 5.0. This was done by inputting a file (see Appendix A) which consisted of ANSYS commands in sequence. Solid70 3-d thermal solid element in ANSYS was chosen in thermal analysis. Temperature dependent material thermal properties were defined, followed by meshing of the pipe section. This finished the preparation phase of the ANSYS program.

In the solution phase of ANSYS program, transient analysis option was chosen first, followed by choosing a full Newton-Raphson solution procedure. The thermal analysis initial condition was set as room temperature (here 298 K) at the start of welding. This was:

$$T(r,\theta,z,t)=T_{RT} \quad (at\ t=0) \tag{25}$$

The boundary condition was fixed as convection at the pipe inside surface (*i.e.*, r = 19.05 cm surface). The boundary condition was convection at the pipe outside surface except the weld area. The weld center line or plane (z = 0 plane) was modeled as an adiabatic boundary condition. The other end pipe side surface (z = 20 cm plane) was considered as a convective boundary condition. The boundary conditions in weld area were a mixture of convective and heat flux conditions and changed as the weld advanced. The radiative heat loss in the weld was considered in the calculation of net heat energy being transferred from the arc into the weld pool and not considered as a boundary condition in this study.

As stated before, this narrow gap weldment was welded in four passes. The first pass was the root pass with no filler material added during welding. The other three passes were welded with filler material addition. The pipe weldment was modeled using four layers of elements in the thickness direction (r direction). Thus, in the model, the top three layers of elements in the weld area had to be deactivated before starting the second welding pass. In the ANSYS program, this was done right after the initial and boundary conditions were set. In this analysis, the continuous moving of the weld and arc (heat source) were modeled by using discontinuous time step Δt, *i.e.*, the weld and arc would stay in one area (here one element in circumference) within one time step and would advance to next adjacent area (element) for next time step. There were 120 elements in the circumference. Therefore, there would be 120 time steps for one pass welding. The time step Δt could be represented as:

$$\Delta t=\frac{c}{120\cdot v} \tag{26}$$

here v is the arc travel speed (cm/s), c is the circumference of the pipe. Clearly, the time step would be the same within one pass and varied as the arc travel speed changed from pass to pass. One time step was automatically adjusted to several (from one to one

hundred in this study) sub-time step to make sure the numerical process was stable. For the last three welding passes, the addition of filler material was modeled by activating previously deactivated elements one set (there are two parallel elements in one set) by one set as the weld and arc progressed from one time step to the next time step.

There are 497 time steps involved in this thermal analysis. This generated a huge thermal result file to be stored as a load file for further stress analysis.

Stress Analysis

Governing Equation and Boundary Conditions

As in the usually thermo-elasto-plastic analysis, the stress, strain and temperature are related as follows.

The strain is:

$$\epsilon_{ij} = \epsilon^{e}_{ij} + \epsilon^{p}_{ij} + \epsilon^{T}_{ij} \qquad (27)$$

where the superscripts e, p, and T refer to elastic, plastic, and thermal strain, respectively. Creep strain is neglected here, as in most welding problems, on the basis that time spent at high temperature is short for a weld. Plastic strain due to the change in volume during allotropic phase transformation is neglected in this study.

The stress state is

$$\frac{\partial \sigma_{ij}}{\partial \tau} = D_{ijkl}(T)\,\frac{\partial \epsilon^{e}_{ij}}{\partial \tau} + \frac{\partial D_{ijkl}}{\partial T}\epsilon^{e}_{kl} \qquad (28)$$

where $D_{ijkj}(T)$ is the temperature dependent elastic stiffness matrix and repeated indices are summed. Plastic flow occurs when

$$\kappa(\overline{\sigma}, \overline{\epsilon^{p}}, T) = 0 \qquad (29)$$

and

$$\frac{\partial \kappa}{\partial \sigma_{ij}} \cdot \frac{\partial \sigma ij}{\partial \tau} > 0 , \qquad (30)$$

where κ is the flow surface. Here,

$$\bar{\sigma} = (3\sigma'_{ij}\sigma'_{ij}/2)^{1/2} \equiv Mises\ equivalent\ stress, \qquad (31)$$

$$\bar{\epsilon}^p = \int_0^\tau (\frac{2}{3} \cdot \frac{\partial \epsilon_{ij}}{\partial \tau} \cdot \frac{\partial \epsilon_{ij}}{\partial \tau})^{1/2} d\tau \equiv equivalent\ plastic\ strain, \qquad (32)$$

and

$$\kappa(\bar{\sigma}, \bar{\epsilon}^p, T) = \bar{\sigma} - y(\bar{\epsilon}^p, T) \qquad (33)$$

where σ'_{ij} is the deviation stress component and y is the flow stress for a uniaxial tensile test under plastic strain and temperature. Thus, strain hardening results from plastic work, $\int \sigma'_{ij}(\partial\epsilon/\partial\tau)dt$.

The requirement of equilibrium are satisfied by application of the principle of virtual work:

$$\int_s t_i v_i^* dS + \int f_i v_i^* dV = \int \frac{1}{2} \sigma_{ij} (\frac{\partial v_i^*}{\partial x_j} + \frac{\partial v_j^*}{\partial x_i}) dV \qquad (34)$$

where t_i are the boundary tractions, f_i are the components of the body force, S is the surface of the body, V is the volume of the body, and v^* is a virtual velocity field that satisfies the imposed displacement boundary conditions. The formulation considers large strains and finite displacements. It suffices to point out that the above 3D governing equations of thermo-elasto-plasticity form a set of 15 quasi-linear partial differential equations with 15 unknowns

$$\sigma_{ij}, \epsilon_{ij}, u_i, \ where\ i,j = 1,2,3, \ \sigma_{ij} = \sigma_{ji}, \ \epsilon_{ij} = \epsilon_{ji}, \qquad (35)$$

where u_i is the displacement component in the x_i direction. In pipe welding analysis,

these equations are usually solved for given boundary conditions with external thermal loads.

The boundary conditions for the pipe welding stress analysis are (in cylindric coordinate system):

1. traction free inner and outer surfaces (radii) of the pipe

$$\sigma \cdot n = 0 \quad at \; r = r_i, r_o \; (0 \le \theta \le 2\pi), \tag{36}$$

where n is the outward normal and σ is the stress tensor,

2. no displacement in all three directions at one pipe end

$$u_r, u_\theta, u_z = 0 \quad at \; z = 20 \; cm \; (r_i \le r \le r_o), \tag{37}$$

3. no displacement in the axial direction (z direction) at one pipe end

$$u_z = 0 \quad at \; z = 0 \; (r_i \le r \le r_o). \tag{38}$$

Rate-Independent Plasticity

As stated before, in welding, a local area in the weldment experiences an extreme thermal cycle which results in plastic yielding in this local area. Thus, plasticity is closely associated with the welding process. Usually, rate-independent plasticity is considered as the local area is exposed for only a short time under the welding heat source and the weldment will pick up strength during cooling.

Rate-independent plasticity is characterized by the irreversible straining that occurs in a material once a certain level of stress is reached. The plastic strains are assumed to develop instantaneously, *i.e.*, independent of time. The ANSYS program provides seven options to characterize different types of material behaviors.

Plasticity theory provides a mathematical relationship that characterizes the elasto-plastic response of materials. There are three ingredients in the rate-independent

plasticity theory in the ANSYS program: the yield criterion, flow rule and the hardening rule. The yield criterion determines the stress level at which yielding is initiated. The flow rule determines the direction of plastic straining. The hardening rule describes the changing of the yield surface with progressive yielding, so that the conditions (*i.e.*, stress states) for subsequent yielding can be established. Two hardening rules are available: work (or isotropic) hardening and kinematic hardening. In work hardening, the yield surface remains centered about its initial centerline and expands in size as plastic strain develops. For materials with isotropic plastic behavior this is termed isotropic hardening and is shown in Figure 53. Kinematic hardening assumes that the yield surface remains constant in size and the surface translates in stress space with progressive yielding, as shown in Figure 54.

In this study, classical bi-linear kinematic hardening with von Mises yield criterion, associative (Prandtl-Reuss equations) flow rule, kinematic hardening rule, and bi-linear material response were chosen in the model. Figure 55 shows stress-strain behavior of the bi-linear kinematic plasticity option in ANSYS. Table 10 presents temperature dependent bi-linear material plasticity properties of 304L stainless steel.

Material Mechanical Properties

The 304L SS mechanical properties used in the model are summarized in Table 11. Like the thermal properties, the mechanical properties are assumed to be dependent on temperatures. The thermal expansion coefficient, α, and Poisson's Ratio, μ, can be expressed as follows:

$$\alpha = 16.12\times10^{-6} + 2.85\times10^{-9}T \qquad (39)$$

$$\mu = 0.262 + 5.98\times10^{-5}T \qquad (40)$$

where T is temperature in absolute value (K).

Solution Procedure

The stress analysis of narrow gap pipe welding was conducted immediately after the thermal analysis. The structural finite element model was obtained directly from the thermal model by using the conversion in ANSYS, ETCHG. The same mesh was retained in stress analysis so that the node temperature history in thermal analysis could be directly inputted into stress analysis as a thermal load. The material property ALPX, the coefficient of thermal expansion, allowed the temperatures to load the structure. The solid70 element in thermal analysis was changed to corresponding solid45 3-d stress element. The temperature dependent mechanical properties were defined. This concluded the PREP7 phase of ANSYS program.

In the solution phase of ANSYS program, the stress analysis was set to be static stress analysis first. The reason to use static instead of transient stress analysis is to reduce the computing cost but still achieve reasonable results. It is impossible under current computing conditions to conduct stress analysis at every time solution from the thermal analysis. The boundary conditions were given next, followed by numerical procedure options, such as, autoloading to track the load and monitor convergence, large strain option, and Newton-Rawson solution procedure. The loads were chosen from the thermal analysis to represent thermal history as close as possible. There were a total of 188 load steps in stress analysis. It was felt that the reduced number of sequential structural solutions would produce reasonably accurate results, while saving substantial computer time. The program for stress analysis was given in Appendix B.

2D MODEL FOR NARROW GAP WELDMENT AND CSI PROCESS

Finite Element Model and Assumption

The narrow pipe girth welding and CSI process were modeled by using the

computer code ANSYS 5.0. The numerical approach was simplified by making certain assumptions. The major assumption is that the pipe welding process can be modeled assuming a condition of axisymmetry. The pipe welding process is certainly not an axisymmetric case. But the main purpose of this work is to study the effectiveness of the CSI method and CSI is appropriately represented by an axisymmetric model. Thus this 2D axisymmetric approach is justified. Figure 56 shows the finite element mesh of the half pipe cross section from the weld centerline. The length of this section is 25.4 cm. Four node plane elements with axisymmetric option were used in the model. The mesh density varies continuously from the weld centerline to the end of the pipe cross section with a fine mesh around the weld centerline. This work also assumes that the heat generated by the deformed solid is negligible. Thus thermal and stress analysis were conducted sequentially in the model. The numerical analysis for pipe girth welding and the CSI process had four steps: 1) thermal model for welding, 2) stress model for welding, 3) thermal model for CSI, and 4) stress model for CSI.

Thermal Analyses

Transient thermal analyses were performed for pipe girth welding and the CSI process. Temperature dependent thermal material properties as described in previous 3D model (see Table 9) were used in the model. An increase of conductivity value for temperatures above the melting point was adopted to compensate for the convection and stirring effect in the molten pool. The latent heat at melting was implemented into the thermal model by defining the enthalpy of the material as a function of temperature. A constant value of surface heat convection coefficient was assumed. The initial temperature of the pipe to be welded was set to be 298 K. The adiabatic boundary conditions was set at the pipe weld centerline side. The natural convective boundary condition was set at the pipe other surfaces. Plane55 2D thermal solid element in ANSYS was chosen in thermal analyses.

In the welding model, the net arc efficiency was assumed to be 73 percent (45), the weld pool heat input was generated by a Gaussian distributed element heat flux and internal heat generation as described in previous 3D model. The element birth capability in ANSYS was used to model the deposition of filler metal into the groove for the last three welding passes. The radiation effect was not considered in the welding model. In the CSI model, the cooling on the inner surface of the pipe was modeled by prescribing a node temperature of 77 K (liquid nitrogen temperature) for a length of 3.8 cm from the weld center line, while keeping a node temperature of 323 K for a length of 5 cm from weld center line on the outer surface. The cooling cycle lasted about 6 minutes. Then the node temperatures were deleted and the pipe was naturally convected to reach the room temperature equilibrium. The ANSYS programs for thermal analysis of pipe welding and the CSI process are enclosed in Appendix C.

Stress Analyses

Structural static analyses were preformed for pipe girth welding and the CSI process. Temperature dependent material mechanical properties (see Table 11) were used in the analyses. A temperature dependent bi-linear elasto-plastic stress-strain curve (from Table 10) was used. The kinematic strain hardening option was considered to include the Bauschinger effect in the model. The associative flow rule (Prandtl-Reuss equations) in conjunction with the von Mises yield criterion was assumed in the model. The symmetric boundary condition in axial direction was set at pipe weld center line side, while the free boundary condition was set at the pipe other end. ANSYS command ETCHG was used to automatically transfer the plane55 thermal element into plane42 2D structural solid element while retained the exact node position. Again, the structural analyses were not conducted at every time solution from the heat transfer analysis. The carefully selected data points from the temperature histories of pipe girth welding and the CSI process were introduced into the stress model as the thermal loads. The ANSYS

program for stress analyses is presented in Appendix D.

Table 9. 304L Stainless Steel Temperature Dependent Thermal Properties

Temperature T (K)	Thermal Conductivity k (W/m-K)	Specific Heat c_p (J/kg-K)	Enthalpy H (J/m^3)
0	8.116	465.4	0.0
100	9.734	478.76	$3.78x10^8$
200	11.352	492.12	$7.66x10^8$
300	12.97	505.48	$1.17x10^9$
400	14.588	518.84	$1.57x10^9$
500	16.206	532.2	$2.0x10^9$
600	17.824	545.56	$2.43x10^9$
700	19.442	558.92	$2.87x10^9$
800	21.06	572.28	$3.32x10^9$
900	22.678	585.64	$3.78x10^9$
1000	24.296	599.0	$4.26x10^9$
1100	25.914	612.36	$4.74x10^9$
1200	27.532	625.72	$5.24x10^9$
1300	29.15	639.08	$5.74x10^9$
1400	30.768	652.44	$6.26x10^9$
1500	32.386	665.8	$6.79x10^9$
1600	34.004	679.16	$7.33x10^9$
1673	35.185	688.913	$7.72x10^9$
1673.1	35.186	688.914	$9.84x10^9$
1723	41.358	788.0	$1.01x10^{10}$
3100	211.111	788.0	$1.88x10^{10}$

Table 10. 304L Stainless Steel Plasticity Properties

Temperature T (K)	Yield Stress σ_y (Mpa)	Plastic Modulus E_p (Mpa)
77	246.8	450.00
297	233.1	420.00
311	226.2	418.00
366	197.9	410.00
422	179.3	402.00
477	163.4	394.00
533	151.7	387.00
589	144.8	380.00
644	140.0	372.00
700	135.1	364.00
755	130.3	356.00
811	123.4	348.00
922	116.5	300.00
977	92.0	250.00
1033	80.0	190.00
1089	68.0	50.0
1600	5.0	10.0
1673	0.1	1.0

Table 11. 304L Stainless Steel Temperature Dependent Mechanical Properties

Temperature T (K)	Thermal Expansion α ($x10^{-6}$)	Poisson's Ratio μ	Young's Modulus E (Mpa)
0	16.12	0.262	$202x10^3$
100	16.405	0.268	$200x10^3$
200	16.69	0.274	$199x10^3$
300	16.975	0.28	$197x10^3$
400	17.26	0.286	$191x10^3$
500	17.545	0.292	$184x10^3$
600	17.83	0.298	$177x10^3$
700	18.115	0.304	$169x10^3$
800	18.40	0.31	$159x10^3$
900	18.685	0.316	$146x10^3$
1000	18.97	0.322	$133x10^3$
1100	19.255	0.328	$120x10^3$
1200	19.54	0.334	$110x10^3$
1300	19.825	0.34	$85x10^3$
1400	20.11	0.346	$60x10^3$
1500	20.395	0.352	$10x10^3$
1600	20.68	0.358	$1x10^3$
1673	20.888	0.5	$0.1x10^3$

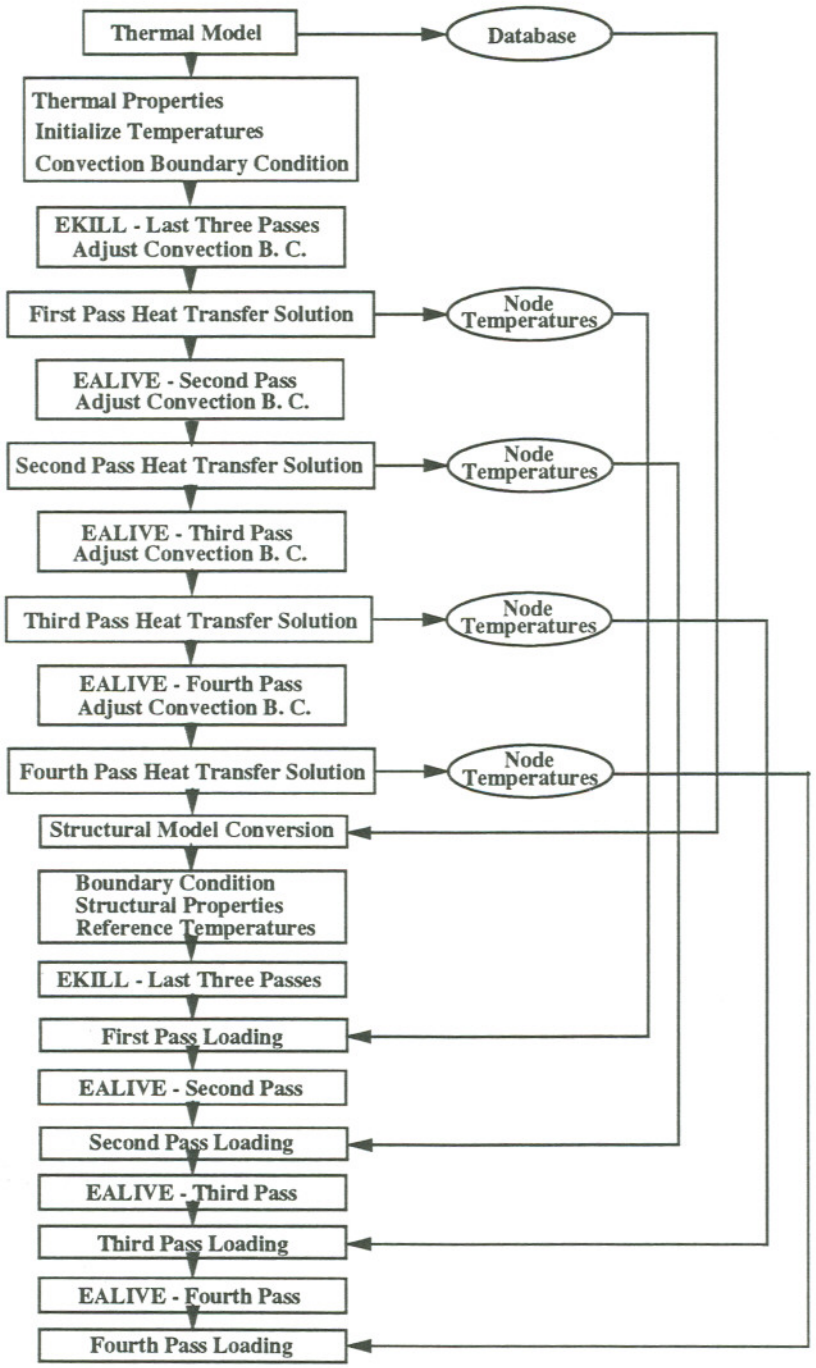

Figure 45. Flow Chart of 3D Thermal and Stress Analysis

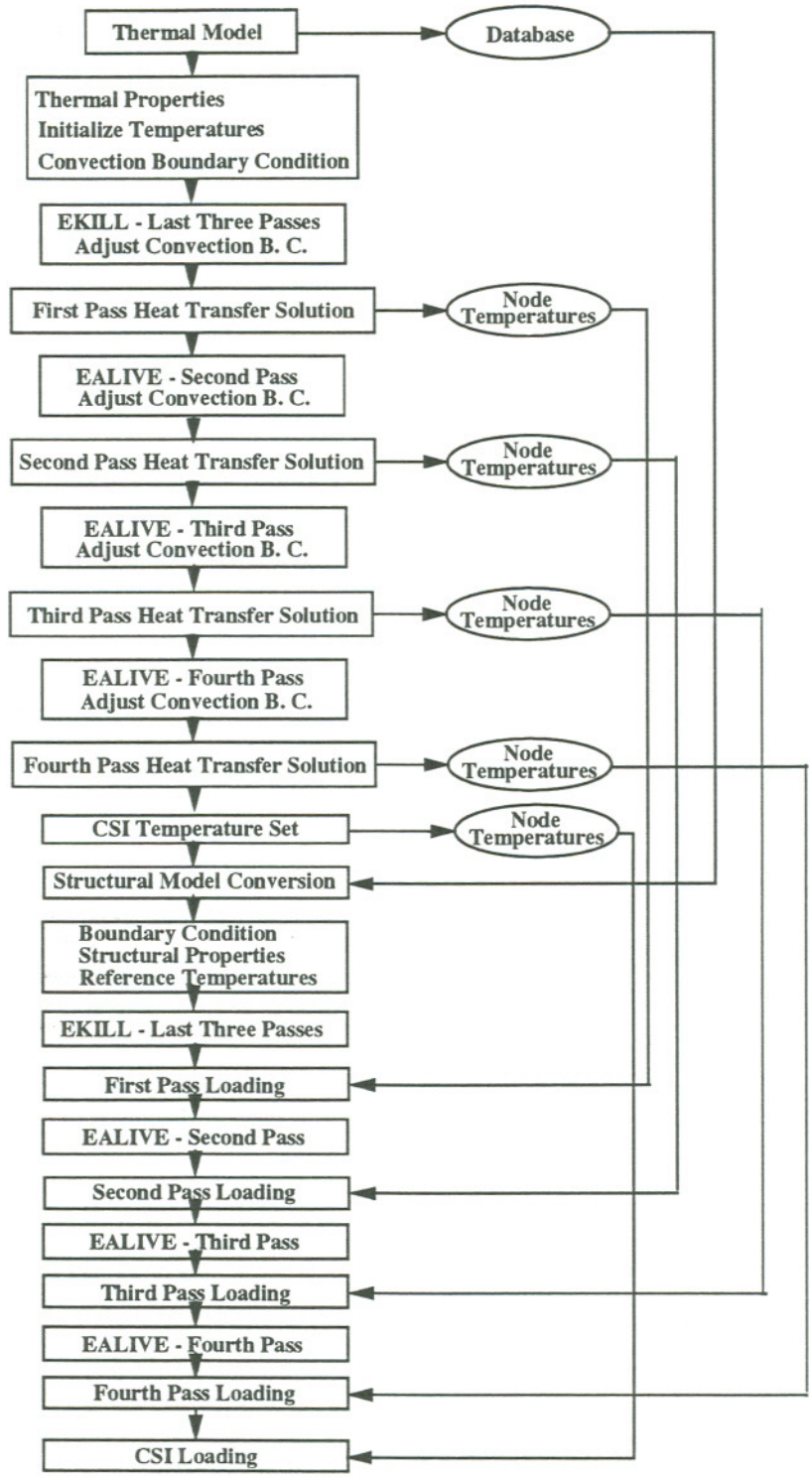

Figure 46. Flow Chart of 2D Axisymmetric Thermal and Stress Analysis

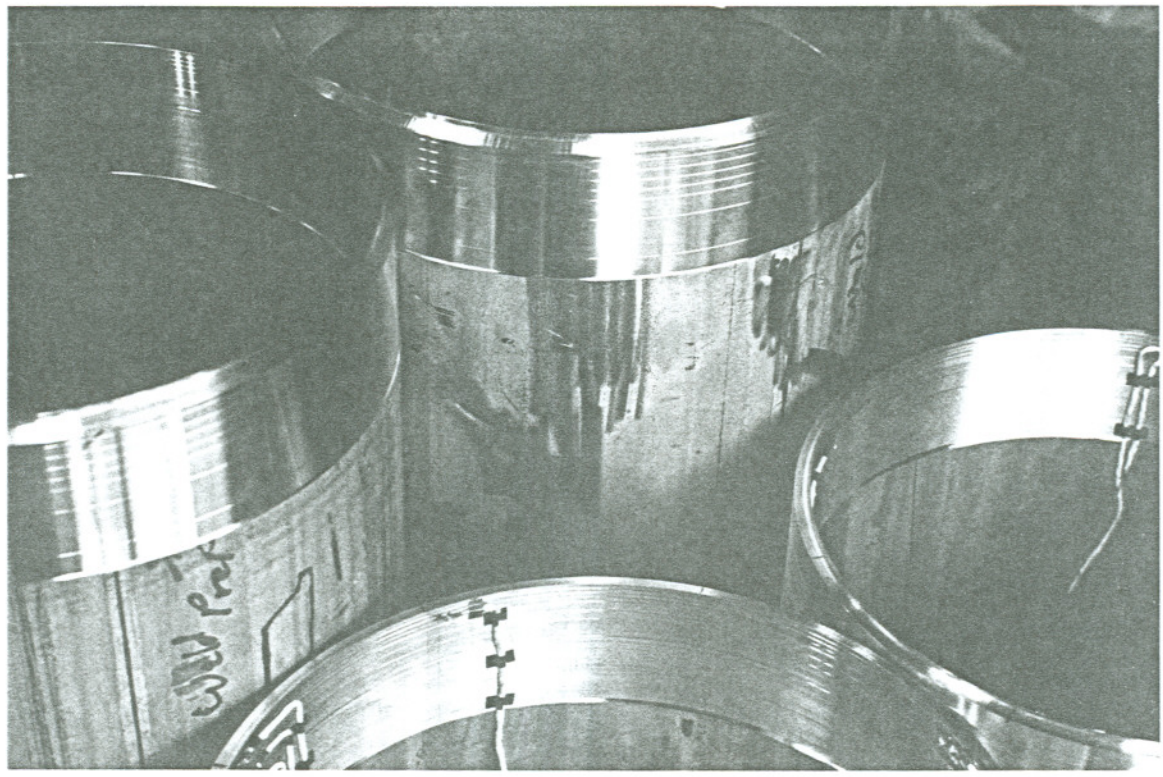

Figure 47. The Half Pipe Section to Be Modeled

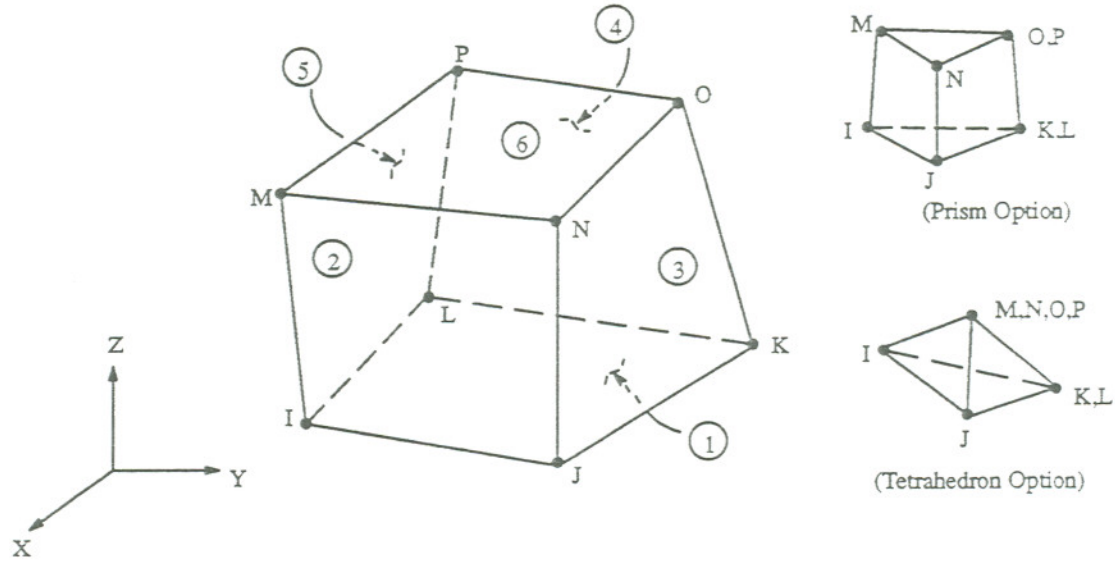

Figure 48. Eight Node Brick Thermal and Structure Element in ANSYS 5.0 (113)

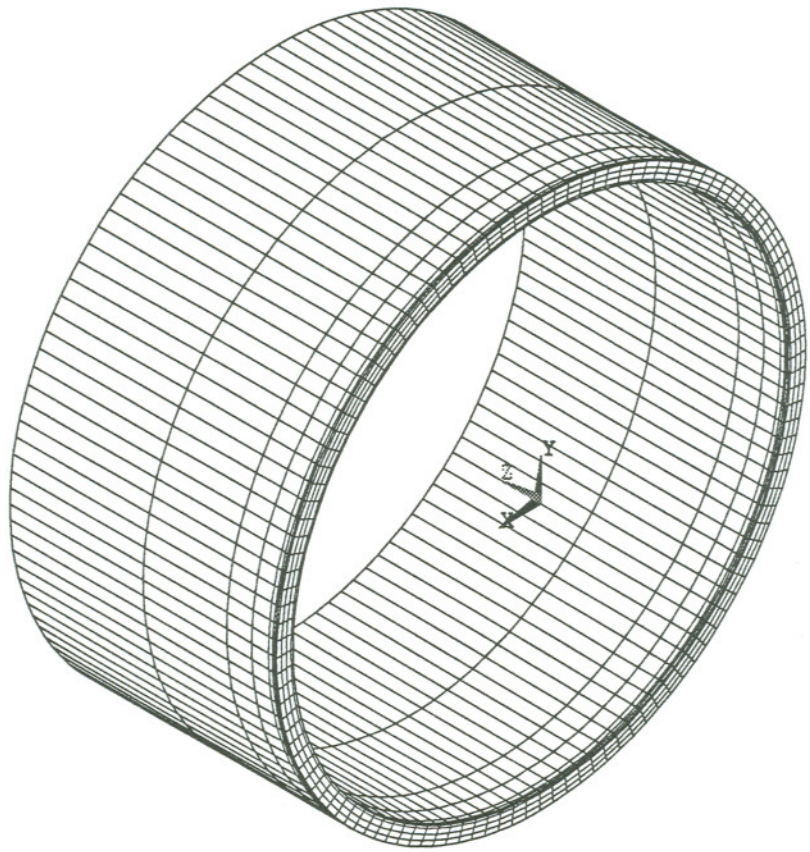

Figure 49. 3D Finite Element Mesh for Narrow Gap Pipe Weldment (Half Section)

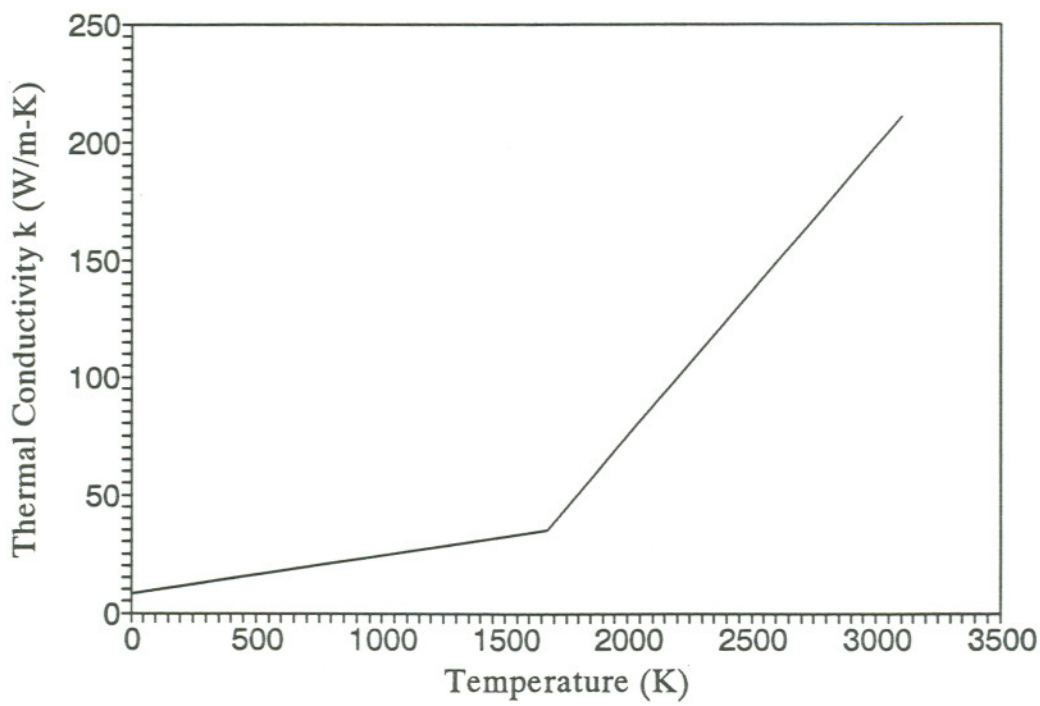

Figure 50. 304L SS Temperature-Dependent Thermal Conductivity k(T) (45)

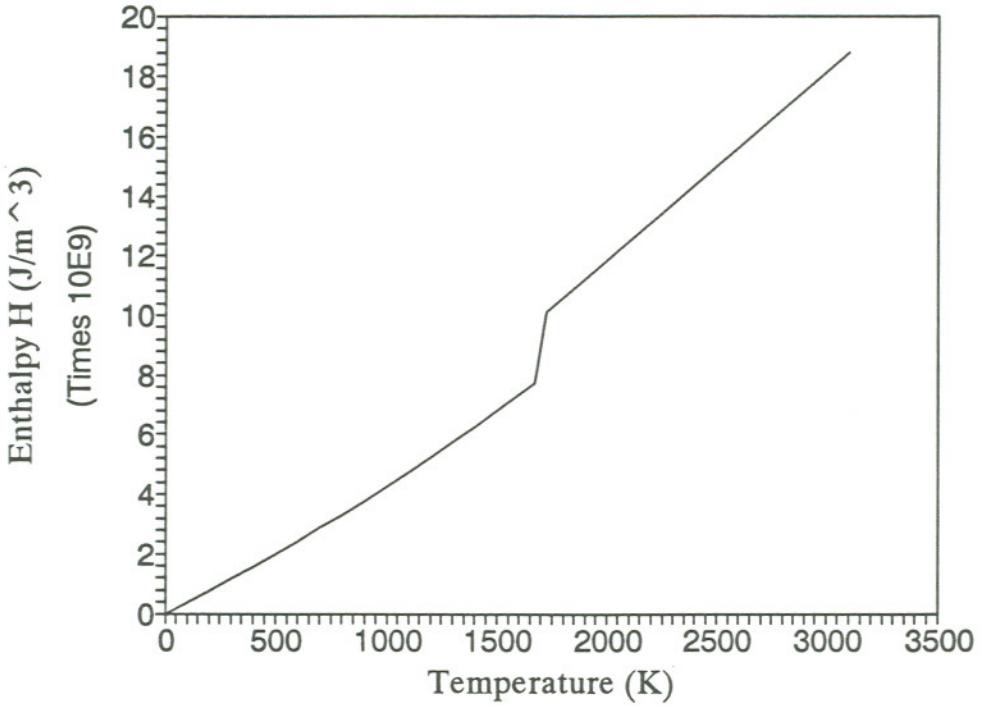

Figure 51. 304L SS Temperature-Dependent Enthalpy H(T) (45)

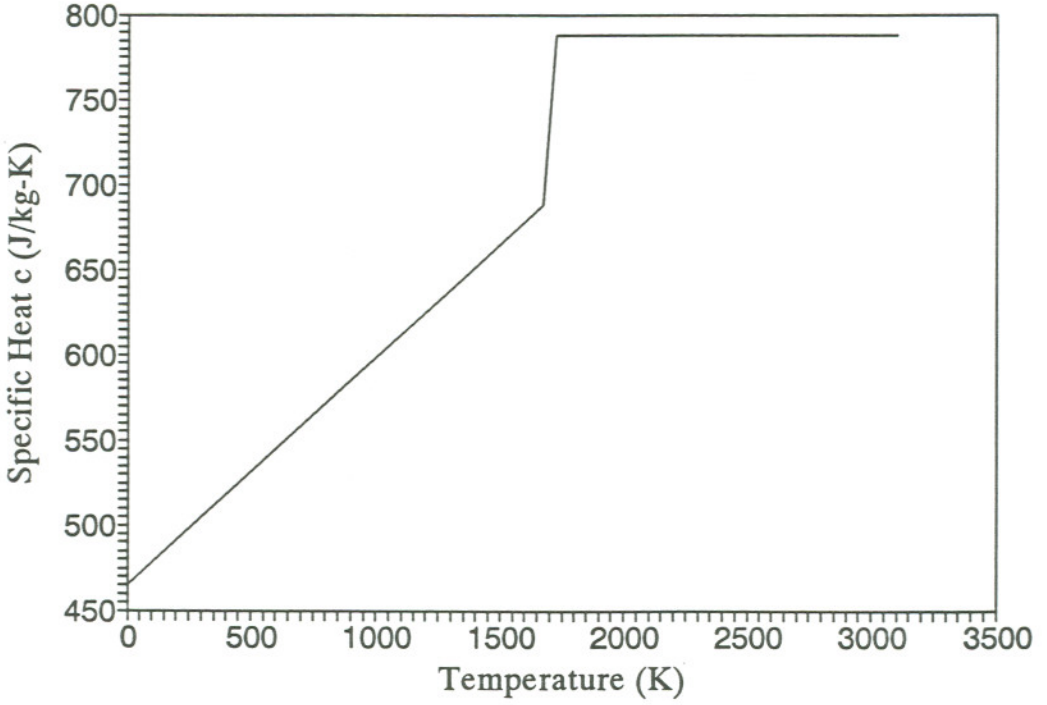

Figure 52. 304L SS Temperature-Dependent Specific Heat $c_p(T)$ (45)

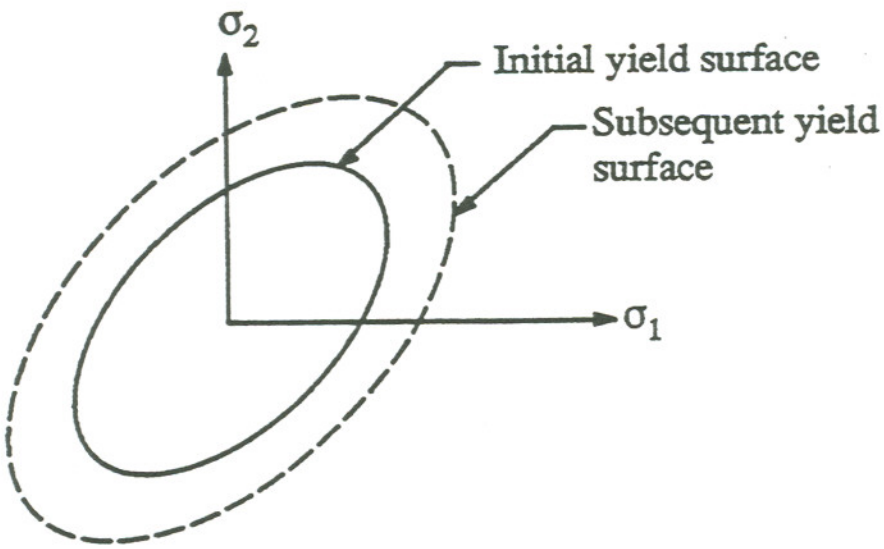

Figure 53. Isotropic Work Hardening Rule (113)

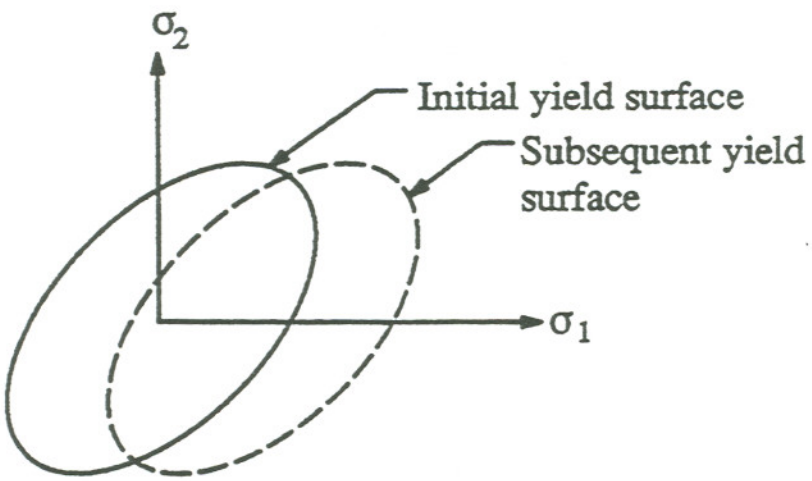

Figure 54. Kinematic Hardening Rule (113)

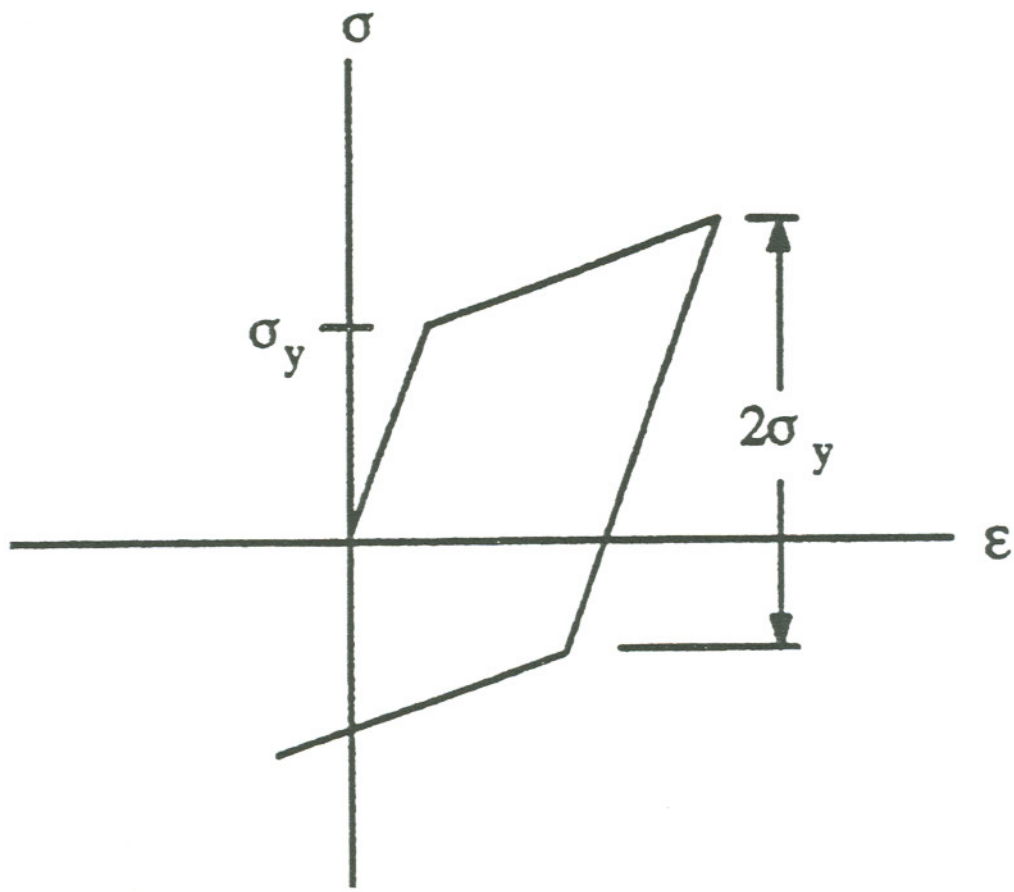

Figure 55. Stress-Strain Behavior of Bi-linear Kinematic Plasticity Option in ANSYS (113)

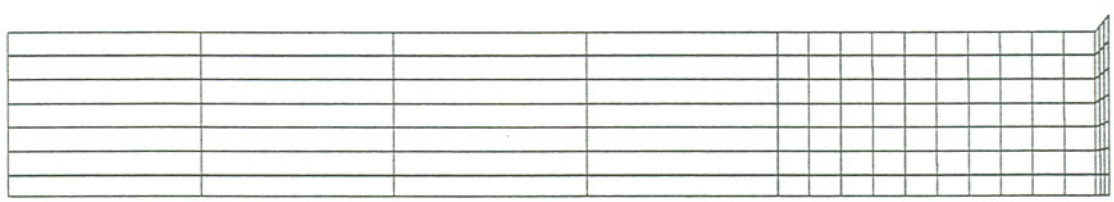

Figure 56. Finite Element Mesh of 2D Axisymmetric Model

CHAPTER 5
EXPERIMENTAL RESULTS

THERMOMECHANICAL HISTORY MEASUREMENTS

This research yielded a large number of experimental data including thermal cycles, transient hoop strains, and radial/axial deformations developed during welding. It is impossible to list all of the experimental data here. Typical thermal cycles (or the peak temperature for each thermal cycle), transient hoop strains (or hoop strain for each pass), and radial and axial deformations recorded during welding for each AMI pipe weldment will be reviewed and analyzed in the following sections.

Four-Pass Narrow Gap Weldment

This weldment was completed in four continuous passes with one start-stop position. The welding started at 0° and proceeded from low azimuthal position to high azimuthal position as shown in Figure 33. The first pass was welded with no filler metal addition, while the three passes subsequent were welded with filler metal addition. The temperature, strain and deformation histories were recorded in real time and continuously during the welding.

Thermal Results

Figure 57, 58, 59, 60, 61, and 62 show the thermal histories at different distances from weld centerline (WCL) and 0°, 45°, 90°, 135°, 180°, and 270° azimuthal position from welding start, respectively. Most of the thermal histories have four temperature

cycles (or temperature peaks) which represent the corresponding four welding passes. The exceptions are the thermal histories at 0 and 45° azimuthal positions where a fifth temperature cycle is evident. This is due to the fact that weld was terminated somewhere between 0 and 45°. These thermal histories indicate excellent agreement of thermal history curve characteristics. The most noticeable feature in the thermal cycle is the peak temperature. Thus, in order to simplify the analysis, the temperature cycles of thermal history will be represented by the peak temperature of the cycle in the rest of the analysis.

Figure 63 shows peak temperatures at 0° azimuthal position from welding start and different distance from WCL. In this plot, positive or negative distance value represents the distance above or below the WCL as the pipe was positioned vertically during welding. From this plot, the first observation is that the comparable peak temperatures on the top side of the pipe appear to be greater than those for the bottom. One explanation of this phenomenon is that the welder torch was tilted towards top side of the weld groove for all four pass welding. This would result in the lack of fusion in the bottom part of the pipe. Examination of the welded pipe reveals no such lack of fusion and the weld beads were symmetrically laid across the weld centerline. The another explanation is that a "chimney" effect is present, due to welding with the pipe in vertical position and the heat was built up at the top of the pipe. This explanation seems reasonable. The second observation is that the first pass (root pass) has the lowest comparable peak temperatures and largest thermal gradient around WCL. This is because the pipe was welded starting from room temperature, and, as the welding proceeded, the heat was built up in the pipe, thus reducing the thermal gradient. Also, the root pass involved no filler material addition and has the lowest heat input, thus the peak temperatures for the root pass are lower than those for the other three passes. The thermal gradient between 3.175 and 6.35 mm from WCL for the root pass is about 100 K/mm. Thus, placement of the thermocouple is really critical to this research.

Figure 64 presents peak temperatures at 135° azimuthal position from welding

start as a function of distance from WCL. This plot confirms the previous observation that the "chimney" effect is present and the root has the highest thermal gradient around WCL and the lowest comparable peak temperatures. In this plot, the peak temperatures around WCL were the lowest for the first pass and the highest for the second pass, then decreased as pass number increased. This trend is expected for all sets of temperatures measured at the inner surface. But in the previous plot, the highest peak temperatures occur at the third pass, and the fourth pass has higher peak temperatures than those at the second pass. The other noticeable difference between theses two plots is that there exists large temperature difference at same distance from WCL but different azimuthal position, especially at the third pass where the 0° set has very high peak temperature. These differences are due to the fact that a given pass is not completed until the 0° mark is reached and/or passed. Thus the 0° thermal histories tend to agree better with the previous pass thermal histories rather than the pass they are included with. The other fact is that 0° thermal histories is due to a need of pass-by-pass weld heat input adjustment as described in Table 6. This effect is exaggerated for this weld as it was a one-of-a-kind, non-standard groove geometry which resulted in the welding parameters being continuously adjusted in going from one pass to the next, and sometimes during a given pass.

Comparisons of peak temperatures for all passes at 6.35 mm above and below WCL as a function of azimuthal position are shown in Figure 65 and 66. Figure 67 and 68 give the peak temperatures for all passes at 19.05 mm above and below WCL as a function of azimuthal position. The main observation noted from these four plots is the peak temperature difference among the data at 0° and at other azimuthal positions. This conforms previous observation and has been explained before. The peak temperatures at the same distance from WCL and at the azimuthal positions away from 0^0 are generally azimuthal position insensitive. The exception is the first two pass peak temperature at 6.35 mm up from WCL and 90° from welding start, where the value is much lower than that of other azimuthal positions. The only explanation of this

phenomenon is that the welding torch is tilted towards lower side of the pipe around 90° for the first two weld passes as the peak temperatures at the lower side around 90° and same distance have higher than nominal values for the first two weld passes. The thermocouple seems to be placed properly as the peak temperatures for the last two pass are nominal.

One generic conclusion from the thermal results of this pipe weldment is that the thermal history is generally axi-symmetric at the azimuthal position away from welding start and stop area.

Deformation and Strain Results

Axial displacement measured at 135° from welding start is illustrated in Figure 69. The deformation history is complex and not obviously symmetrical between passes. This is felt to be due to the complex piping system stiffness change caused by the combination of the heat buildup and filler metal addition during continuous welding. It does appear, however, that the steep change in deformation initiates prior to the comparable thermal spike at 135°, illustrated in Figure 60, reaches its maximum increase at/near maximum temperature, and rapidly decreases in magnitude as arc/heat zone travels away from the measuring position. As stated before, the stiffness of 304L SS decreases as the temperature increases. The pipe welding starts from room temperature when the pipe has the highest stiffness. As the welding proceeds, the pipe is warmed up and the stiffness of whole pipe is gradually reduced. Locally, the area under arc has the lowest stiffness surrounded by the area with higher stiffness. This local unbalance of stiffness plus the addition of filler material will affect the balance of stiffness in whole pipe. Pipe is a self-restrained system and it will response and adjust to the new balance dynamically as the welding proceeds. This is the reason that the deformation change is very sensitive and always prior to the temperature change. Every spike in this plot clearly represents one weld pass for this weldment. The low deformation values between

passes indicate a completion between component expansion due to the welding process and axial shrinkage due to weld metal shrinkage on cooling. Component heating appears to cause pipe expansion until after pass three where a definite trend towards axial shrinkage is evident.

Figure 70 shows the radial deformation histories at 0° from welding start as a function of distance from WCL. The corresponding thermal histories are given in Figure 57. The data set appears to be reasonable, with trends for each pass being replicated for all distance from WCL. Again, the steep increase in radial deformation initiates prior to the corresponding thermal spike, reaches its maximum increase at/near maximum temperature, and rapidly decreases in magnitude as the arc/heat zone travels away from the measuring point. One observation of this plot is that the magnitude of a given pass-induced radial deformation change appears to be relatively independent of distance from WCL, particularly for the last two passes. Careful examination of deformation history along with corresponding thermal history reveals that the excessive high heat input at the start of the third pass welding is responsible for the phenomenon that the radial deformation change being independent of distance from WCL. High third-pass peak temperature results in larger thermal radial expansion (or higher spike in the plot). This large thermal expansion will not only reverse the shrinkage caused by the first two pass welding but also let the piping system take longer time to shrink and result in larger shrinkage if the shrinking process is not interrupted. In this pipe welding, there exists the fourth pass. If the third pass peak temperature is larger enough so that the shrinking process takes long enough time to be interrupted by the fourth pass thermal expansion, this fourth pass thermal expansion will effectively relieve the shrinkage caused by the third pass and leads to less total shrinkage after the weld is finished. This appears to be the case of 6.35 mm from WCL. The opposite case is present for finial shrinkage at 19.05 mm from WCL where the third pass peak temperature is not high enough to result in the interruption of the fourth but is still lager enough to cause larger final shrinkage. This is why the shrinkage at 19.05 mm from WCL is larger than that of 6.35 mm.

Figure 71 gives the radial deformation at 90° from welding start and 6.35 mm above or below WCL. The initial observation is the magnitude of a given pass-induced radial deformation change appears to be larger for the bottom side of the pipe than that for the top side. This can be explained from the thermal histories of both sides. The peak temperatures at top side are less than that at bottom side for the first two welding passes caused by possible tilting of welder torch towards bottom side of the weld. The lower temperature peaks at top side cause lower thermal expansion on heating and less shrinkage upon cooling than that at bottom side. A comparison of deformation history between 0 and 90° shows that the area around 90° is deformed much easier than at 0°. The radial shrinkage or contraction occurs right after the first pass. This is because the stiffness at 90° is lower than that at 0° due to the heat buildup at this 90° gap.

Figure 72 presents the radial deformation at 180° from welding start and 6.35 mm above or below WCL. Careful examination shows that the magnitude of a given pass-induced radial deformation change is relatively larger for the top side of the pipe than for the bottom side. This is also evident at 0°. The reason behind this kind of phenomenon is the chimney effect which gives the top side higher peak temperature than that at bottom side and comparable position. Again, a comparison of deformation history between 0 and 180° shows that the area around 180° is deformed much easier than at 0°. The radial shrinkage or contraction occurs right after the first pass. This is because the stiffness at 180° is lower than that at 0° due to the heat buildup at this 180° gap.

The hoop strain histories at 38.1 mm above WCL, 90 and 180° from welding start are illustrated in Figure 73 and 74, respectively. The corresponding thermal histories are not available in this analysis. Nevertheless, both hoop strain histories show four spikes which represent four pass welding. One spike can be broken down into expansion and shrinking parts, with expansion corresponding to the arc heating at the measuring point and shrinking corresponding to the cooling resulting from the arc moving away from the measuring point. The shrinking part is the dominant part which leads to the final compressive strain after weld is completed. Both hoop strain histories are similar

with each other and reach comparable final compressive strains.

To simplify the analysis, the radial deformation and hoop strain histories will be represented, in the following sections, by the deformation and strain value at the time data acquisition is terminated. The measured final radial deformation at different azimuthal position as a function of distance from WCL for this pipe weldment is exhibited in Figure 75. From this plot, the effect of thermal history on deformation is clearly noted. In general, the higher the peak temperature is (but is still lower than a certain value for welding pass other than the last pass), the larger the final shrinkage would end up with. This is evident by comparing the deformation and peak temperature results between 6.35 mm above and below WCL at 0° and 90° from the welding start. At 0° from welding start, the peak temperatures at 6.35 mm above WCL are larger those at 6.35 mm below WCL due to the "chimney" effect, this results in larger radial deformation value for 6.35 mm above WCL than that for 6.35 mm below WCL. At 90° from welding start, the peak temperatures at lower side have larger value than that at upper side due the possible tilting of the welder torch, this results in higher deformation value at lower part of the pipe. This is also supported by comparing the radial deformation and peak temperature results between 19.05 mm above and below WCL at 0° and 90° from the welding start. The radial deformation values at 19.05 mm above and below WCL are almost the same due to similar peak temperatures experienced at 19.05 mm above and below WCL. The exception is that if the peak temperature exceeds certain value and the weld has succeeding pass, the final shrinkage would end up with lower than expected value. This is supported by comparing the radial deformation results between 6.35 and 19.05 mm above or below WCL with the corresponding peak temperatures. A comparison of radial deformation at 6.35 mm above WCL as a function of azimuthal position (see Figure 76) reveals that the radial deformation changes as a random function of azimuthal position, *i.e.*, the radial deformation is not axisymmetrically distributed around the pipe during pipe welding.

The above analysis of the data set generated during narrow gap welding indicates

reasonable and self consistent thermal histories and complex, but apparently self consistent deformation histories.

Nine-Pass Weldment

This weldment was completed in nine discontinuous passes with multiple start-stop positions. Every pass started at a new position and stopped at, or a little beyond, this position after one full circle of welding. The first pass welding started at 0° (or 360°) and proceeded from high azimuthal position to low azimuthal position as shown in Figure 33. The next pass started at 45° away from the current pass' start point in welding direction, which was 315° for the second pass welding. The rest of weld passes followed this sequence and finished the weld. The first pass was welded with no filler metal addition, while the rest of weld passes (eight passes) were welded with filler metal addition. The temperature, strain and deformation histories were recorded in real time and continuously within every welding pass, but not between passes.

Thermal Results

Figure 77 shows peak temperatures at 0° from the first pass welding start point and different distance from WCL as a function of weld pass number. These peak temperatures can also be represented as a function of distance from WCL, which is exhibited in Figure 78. Here, the positive or negative value of the distance from WCL in the plot represents the position at distance above or below WCL. From these plots, the "chimney" effect can be clearly noted from the first pass peak temperature results, which give higher peak temperature values for the side above WCL than those for the side below WCL at the comparable position. Another observation from these plots is the weld bead placement or the position of the addition of filler metal for each welding pass starting from the second pass. The beads for the second and third pass, which formed

one layer of weld metal, were placed below and above WCL, respectively. The beads for the fourth, fifth, and sixth pass, which formed another layer of weld metal, were positioned at the bottom, middle (a little tilted towards top), and top part of the groove, respectively. The beads for the last three pass, which formed a layer to fill the groove, were placed in the same sequence as the previous three beads. These bead placements are in good agreement with one shown in Figure 30.

Figure 79 presents the peak temperature at 135° from the first pass welding start point and different distance from WCL as a function of weld pass number. This data set is also plotted in Figure 80 as a function of distance from WCL. These two figures confirm the above observations except that the fifth pass was placed in the middle with a little angular tilt towards bottom part of the groove.

Figure 81 and 82 show peak temperatures for different passes at 6.35 mm above and below WCL as a function of azimuthal position from the welding start, respectively. Figure 83 and 84 give peak temperatures for different passes at 19.1 mm above and below WCL as a function of azimuthal position from the welding start, respectively. The general trend observed from these four plots is that the peak temperature (or the thermal history it represents) is axisymmetric for this weldment. This is evident in plots of 19.1 mm from WCL, but not so convinced in plots of 6.35 mm from WCL. The peak temperature difference between 90° and other azimuthal positions at 6.35 mm above WCL is very clear in the plot. Also, the peak temperature at 6.35 mm below WCL for the first four passes is not completely consistent for all azimuthal positions. One possible explanation of this kind of behavior is the misplacement of thermocouples. The thermal gradient at the area close to WCL is very large during welding, especially for the first several weld passes. For instance, the thermal gradient at 6.35 mm and 0° from welding start is about 160 K/mm. Such great thermal gradient requires careful and accurate placement of thermocouples to reflect the nature of the thermal profile during welding. It is very hard using current thermocouple placement conditions to fulfill this requirement. This thermal gradient will be reduced as the welding proceeds and the pipe

is warmed up. Thus, the peak temperatures are less sensitive to the misplacement of thermocouples for the later weld passes. The other possible explanation is that the first weld pass started from room temperature and 0°, thus the peak temperature at 0° for the first pass is less than other azimuthal position due to the fact that the pipe is a large heat sink at weld initiation.

In general, the thermal histories from this weldment are consistent for all azimuthal positions at comparable distance from WCL. In other words, the thermal histories are axi-symmetric for this pipe weldment. This is probably due to the multiple start-stops during welding.

Strain and Deformation Results

The axial deformations at 45 and 135° from the first welding start as a function of weld pass number are illustrated in Figure 85. The axial deformation at 45° shows nice trend which gives almost linear decrease of axial deformation for the first seven weld passes and almost no change for the last two weld passes. The axial deformation at 135° is total different from the previous one and exhibits no general trend except for the first three weld passes. The first three passes show the linear decrease of axial deformation, but the last six passes give parabolic curve type change of axial deformation, the only reasonable explanation of this irregularity is that the measuring device was not functional for the last six passes.

The radial deformations at 0° from the first pass welding start and different distance from WCL as a function of weld pass number are shown in Figure 86. One general trend from this plot is that the absolute value of final radial deformation (or contraction) decreases as the distance from WCL increases. The final radial deformation is almost zero at 38.1 mm from WCL and reaches the largest negative value in the plot at 6.35 mm above WCL. This is because the area close to WCL experiences much more severe stiffness change induced by the large temperature change and the addition of filler

metal than the area far from WCL. An another observation from this plot is that the final radial deformation is almost the same between the two positions at 19.05 mm above and below WCL, but is not equal at the two positions at 6.35 mm above and below WCL, where the final radial deformation is larger in absolute value at the position above WCL than that at the position below WCL. Careful examination of this figure reveals that the radial deformation curves for 6.35 mm above and below WCL follow almost the same line for the first seven weld passes but differ for the last two passes, while those for 19.05 mm above and below WCL maintain certain gap for the first eight passes but close the gap at last pass. It seems that the last one or two weld passes play an important role in deciding the final radial deformation value. This can be explained by looking into the corresponding thermal histories in Figure 77. The peak temperatures for last two passes are higher for 6.35 mm above WCL than that for 6.35 mm below WCL. The higher peak temperature will induce higher thermal expansion and shrinkage. The shrinking process will not be interrupted as every weld pass is stopped after its completion (this is very obvious for last pass of the weld). For the area far from WCL, like 19.05 mm from WCL, the magnitude of the peak temperature is much lower than that at area close to WCL, like 6.35 mm from WCL, thus the stiffness change is less active (dramatic) and the difference of the peak temperature at above and below WCL would not make any large impact on final radial deformation.

The radial deformations at 180° from the first pass welding start and different distance from WCL as a function of weld pass number are presented in Figure 87. The trends in this plot repeat those observed in the previous plot. The peak temperature at 6.35 mm above WCL at last pass is 907 K, while the peak temperature for 6.35 mm below WCL at last pass is 757 K. This explains why the final radial deformation at 6.35 mm above WCL is larger than that at 6.35 mm below WCL.

Figure 88 and 89 show the radial deformation for different azimuthal position, at 6.35 mm above and below WCL as a function of weld pass number, respectively. They clearly demonstrate that the radial deformation is not axisymmetric, or is azimuthal

position sensitive at the area close to WCL. This is probably due to the stiffness change at different azimuthal position. For the area far from WCL, like 19.5 mm from WCL, the final radial deformation (see Figure 90) is not so azimuthal position sensitive. This is because the magnitude of peak temperature is relative low in this area and resultant stiffness change is not so dramatic. The hoop strain at 180° from the first pass welding start and 38.1 mm below WCL as a function of weld pass number is illustrated in Figure 91.

In general, it is noted that the thermal history at last one or two weld passes and at area close to WCL plays a significant role in the formation of final radial deformation. This is not quite as evident in the area far from WCL. It is also noted that the symmetric to WCL and axisymmetric distribution of the final radial deformation is found at the area far from WCL but not in the area close to WCL.

Six-Pass Weldment

This weldment was completed in six discontinuous passes with multiple start-stop positions. Every pass started at a new position and stopped at, or slightly past this position after one full circle welding. The first pass welding started at 0° and proceeded from low azimuthal position to high azimuthal position as shown in Figure 33. The next pass started at 45° away from the current pass' start point in welding direction, which was 45° in Figure 33 for the second pass welding. The rest of weld passes followed this sequence and finished the weld. The first pass was welded with no filler metal addition, while the rest of the following five passes were welded with filler metal addition and welder torch oscillation. The oscillation of the welder torch was carried out by moving the torch along a zigzag path with dwelling at two ends of the oscillation cycle. The dwelling times, distance between two ends, and time traveling between two ends can be found in Table 7. The temperature, strain and deformation histories were recorded in real time and continuously within every welding pass except the third pass.

Thermal Results

The peak temperatures at 0° from the first welding start point and different pass as a function of distance from WCL is shown in Figure 92. Here, the positive value of distance from WCL means the distance above WCL, while the negative value means the distance below WCL. Several trends are found in this plot. The first one is the "chimney" effect. This is clearly noticed from the first pass data, which gives higher peak temperature values at the side above WCL. The second trend is the weld bead placement noted from this plot. The first pass welding involved no filler metal and only root melting. Thus, this pass was placed in the middle and bottom of the weld groove. Starting from the second pass, torch oscillation and filler metal addition were employed during welding. The second pass was welded on top of the first one. The bead was laid in the middle of the groove slightly tilted towards the upper part of the pipe. This bead was able to fill the groove and form a layer in the groove due to the oscillation of the welder torch. The third pass data is missing here, due to unexpected computer system malfunction, but the bead should be placed on top of the second bead and tilted towards upper part of the pipe. The fourth pass was welded on top of the second bead and tilted towards the lower part of the pipe. The third and fourth beads formed another layer and filled the groove. The fifth bead was laid tilted towards the upper part of the pipe, while the sixth bead was placed in the middle tilted towards the lower part of the pipe. These two beads formed the last layer and completed the weld. This layer had the widest gap to be filled. This was accomplished by applying a large oscillation amplitude and thermal heat input in the fifth pass welding (see Table 7). These bead placements are in good agreement with one in Figure 32. The last observation from this plot is that this weldment employs high thermal heat input and this results in high peak temperature, large thermal gradient, and broad microstructure sensitization range. The thermal gradient at 6.35 mm from WCL is about 150 K/mm.

The peak temperatures at 135° from the first pass welding start and different

passes as a function of distance from WCL is presented in Figure 93. The general trends found in this plot are in agreement with those shown in previous plot.

Figure 94 and 95 give the peak temperature for different passes, as a function of azimuthal position, at 6.35 mm above and below WCL, respectively. Figure 96 and 97 present the peak temperature for different passes, as a function of azimuthal position, at 19.05 mm above and below WCL, respectively. From these four plots, it is noted that the peak temperature is axisymmetric or azimuthal position insensitive in general. One exception is low peak temperatures at 135° from welding start during the fourth pass welding. This is probably due to the low heat input at this local area during welding. The other exception is low peak temperature at 90° and 6.35 mm above WCL during the second welding pass. The reason for this phenomenon is unknown. The axi-symmetry of peak temperature is mainly due to the multiple start-stop position during welding.

Strain and Deformation Results

The axial deformations at 45 and 135° from the first pass welding start point as a function of weld pass number are shown in Figure 98. From this plot, it is noted that the negative axial deformation (or axial contraction) at 135° almost linearly increases as the weld pass number increases, while the axial deformation at 45° follows the 135° line almost exactly for the first five passes and differs at the last pass. The reason why there is a net increase of negative axial deformation at 45° for the last pass welding is unknown. However, the general trends are: 1). the axial deformation is linear function of weld pass number; 2). the axial deformation is axisymmetric. The axisymmetric distribution of axial deformation in this pipe weldment is due to the measuring position far from WCL (about 80 mm from WCL). At this distance, the temperature and stiffness changes are not large enough to make any difference.

The radial deformations at 0° from the welding start and different distance from WCL as a function of weld pass number are illustrated in Figure 99. The general trends

observed from this plot are: 1). the final radial deformation (absolute value) is larger for the area close to WCL (like 6.35 mm from WCL) than that for the area far from WCL (like 19.05 mm from WCL); 2). the final radial deformation (absolute value) is larger for the side above WCL than that for the side below WCL; 3). the last one or two passes have large impact on the final radial deformation results. It is obvious that the deformation at near side is larger than that at far side as the far side has less temperature/stiffness change during weld than that at near side (see Figure 92) and the expansion/shrink due to temperature change is not interrupted in this multiple start-stop welding. These trends can also be explained by looking into the stiffness change during welding. As stated before, the stiffness change during welding is due to the temperature change and the addition of the filler metal. In this pipe welding, the addition of filler metal associated with the oscillation of the welder torch plays an important role in the stiffness change. It is noted from Table 7 that the fifth pass has the largest thermal heat input and oscillation amplitude and the fifth pass was welded tilted towards top side of the pipe. This explains why the deformation value is determined by the last one or two pass and why the upper side has larger value than the low side at comparable position.

Radial deformations at 180° from welding start and different distance from WCL as a function of weld pass number are given in Figure 100. The general trends observed in this plot confirm the trends found in the previous plot.

Radial deformations from different azimuthal positions, at 6.35 mm above and below WCL, as a function of weld pass number, are exhibited in Figure 101 and 102, respectively. Figure 103 and 104 show the radial deformations from different azimuthal positions, at 19.05 mm above and below WCL, as a function of weld pass number, respectively. The general trend observed from these four plots is that the radial deformation in this pipe weldment is not distributed axisymmetrically. This is mainly due to the stiffness change along the pipe induced by the temperature change and filler metal addition during welding. The torch oscillation and high heat input employed in this pipe welding make the distribution of radial deformation much more inconsistent. The

final radial deformations at 38.1 mm below WCL and different azimuthal position (see Figure 105) confirm the above finding but with much close gap, this is mainly due to large distance from WCL resulting in the influence of temperature and stiffness changes being small.

The hoop strains at 38.1 mm above WCL and different azimuthal position as a function of weld pass number is shown in Figure 106. Again, the distribution of the hoop strain is asymmetric. This is due to the same reason which is explained above.

In summary, the oscillation of torch during welding made the deformation/strain histories of this pipe weldment much more complicated than those of the previous two weldments. But the general trends noted from this pipe weldment are still in good agreement with those observed in the other two pipe weldments.

RESIDUAL STRESS MEASUREMENTS

Residual Stress Measurements by Hole-Drilling Method

In this research, residual stress measurements were made on OGI weldment, four-pass weldment, and six-pass weldment. The residual stresses were measured at pipe outer surface as a function of azimuthal position and distance from WCL (see Figure 41). The residual stress should be measured at pipe inner surface which is the most critical area. But it is impossible to access the pipe inner surface using the current measuring technique which is abrasive jet hole drilling technique. Since the purposes of the residual stress measurement are: (1) to establish an experiment database for the verification of numerical modeling result, which will be presented in the later part of this thesis, and (2) to roughly compare the residual stress level among the pipe weldments or to roughly know the residual stress level in the pipe weldments, it is reasonable to measure the residual stress on the pipe outer surface. Only surface residual stresses are measured here, this means that only two principle residual stresses, axial residual stress and hoop

residual stress, are derived from the measurement. The residual stress measuring results from three pipe weldments are presented in the following section.

OGI Welded Pipe Residual Stress Measurement

The residual stresses measured at OGI pipe outer surface and different azimuthal position as a function of distance from WCL are presented in Figure 107. From this plot, it is noted that the distribution of residual axial and hoop stresses is not axisymmetric but is kind of symmetry to WCL. In the weld, the residual hoop stress is positive, while the axial stress is negative. The residual hoop stress changes from positive to negative and approach zero as distance from WCL increases, while the residual axial stress changes from negative to positive as distance from WCL increases. In general, the measurement results look reasonable, though the high axial residual stress at a distance far from WCL is hard to understand. One possible explanation is that this high axial residual stress is induced by machining during groove preparation and pipe outer surface cleaning.

Four-Pass Weldment Residual Stress Measurement

The residual stresses measured at four-pass pipe outer surface and different azimuthal position as a function of distance from WCL is shown in Figure 108. The general trends observed from this plot are: 1). the distribution of residual hoop and axial stresses is not axisymmetric; 2). the residual axial stress changes from negative to positive as distance from WCL increases, while the residual hoop stress changes positive to negative as distance from WCL increases. Again, the high axial residual stress far from WCL could be induced by machining during weld groove preparation and pipe surface cleaning.

Six-Pass Weldment Residual Stress Measurement

The residual stresses measured at six-pass weldment outer surface and different azimuthal position as a function of distance from WCL is illustrated in Figure 109. The general observations from this plot are: 1). the distribution of residual hoop and axial stresses, in general, is not axisymmetric but getting close to axisymmetric at area far from WCL; 2). the residual hoop and axial stresses are asymmetric to WCL in general but getting close to symmetric at area far from WCL; 3). the residual axial stress changes from negative to positive as distance from WCL increases, while the residual hoop stress changes positive to negative as distance from WCL increases.

Residual Stress Measurements by Neutron Diffraction Method

The residual stresses along an axial line on the inner surface of the four-pass narrow gap pipe weldment were measured by neutron diffraction facility at Oak Ridge National Laboratory's Residual Stress User Center. This is the first pipe weldment to be measured by the neutron diffraction method. More pipe weldments are expected to be measured by the neutron method in the near future. The reason to chose the four-pass pipe weldment is to provide more experimental data, especially on the pipe inner surface, to verify the numerical modeling effort and to justify the numerical model selection.

Figure 110 and 111 show the axial and hoop residual stress distribution as a function of distance from WCL, respectively. Both residual axial and hoop stress change from positive to negative as distance from WCL increases, this is expected. In the area close to WCL, residual stress has a much higher value than residual axial stress value, this is unexpected. More measuring points are needed in this area to further investigate this phenomenon. In general, the measurement results look reasonable, they do confirm that there exists a tensile zone on the inner surface of the pipe weldment which will cause the IGSCC with the presence of microstructure sensitization and water chemistry.

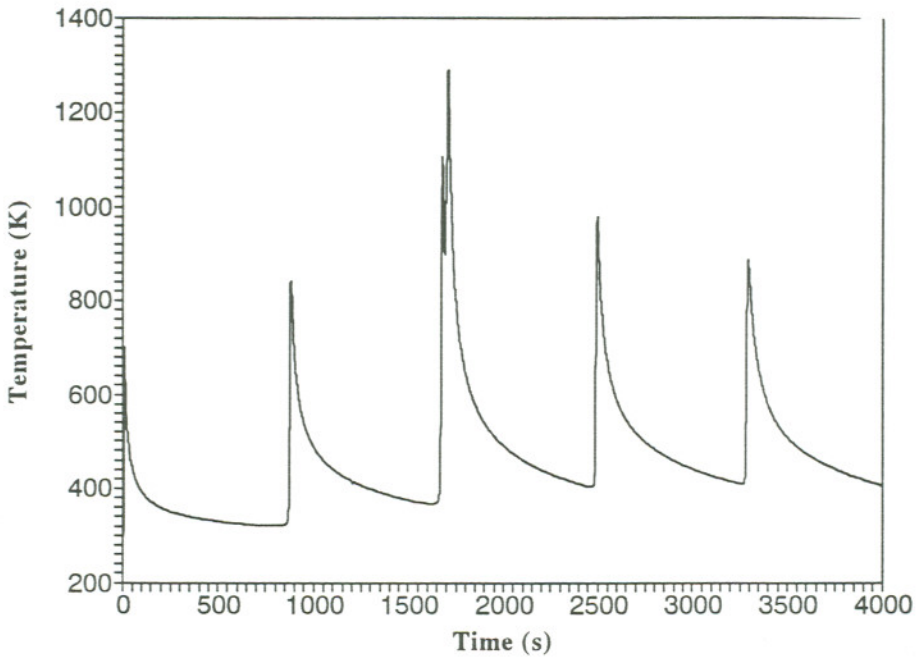

(a) 6.35 mm above WCL

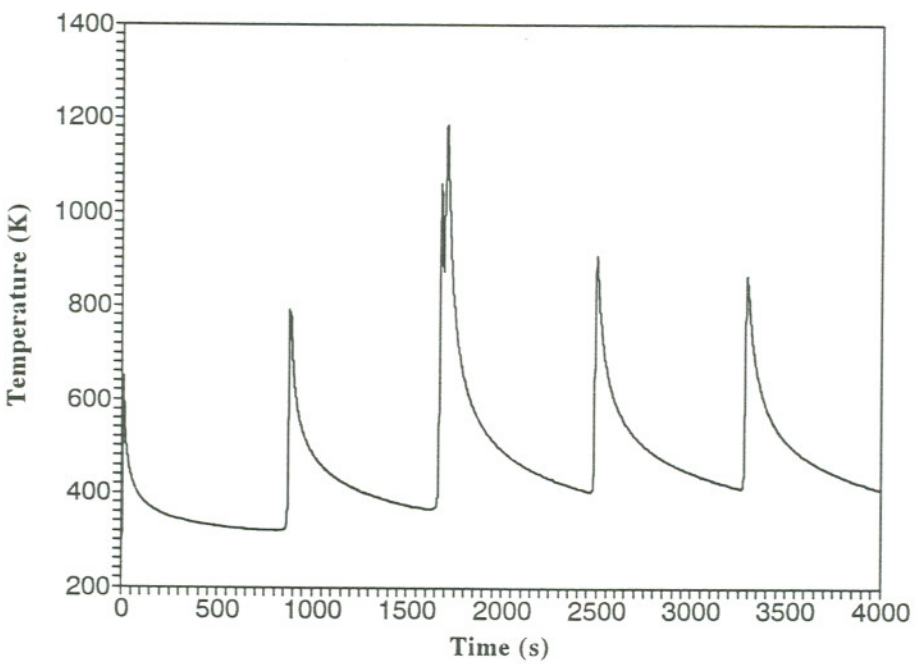

(b) 6.35 mm below WCL

Figure 57. Thermal Histories at 0° from the Welding Start and Different Distances from WCL

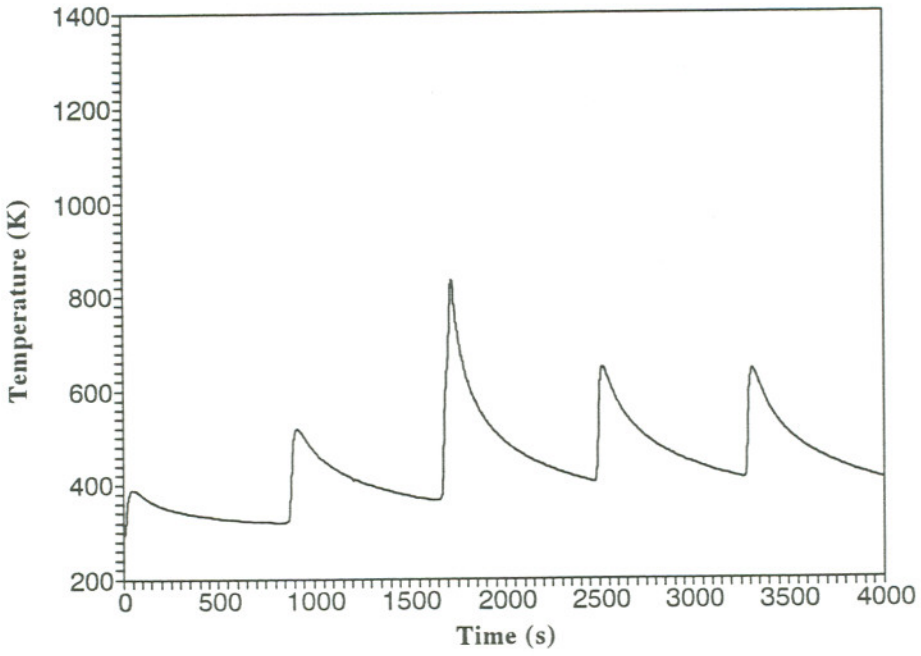

(c) 19.05 mm above WCL

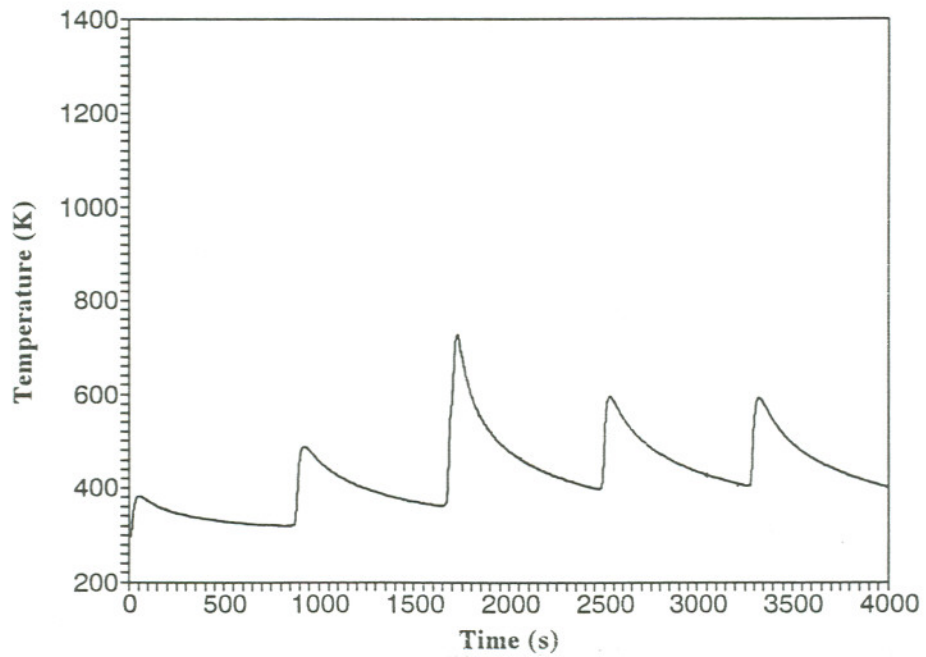

(d) 19.05 mm below WCL

Figure 57. Thermal Histories at 0° from the Welding Start and Different Distances from WCL

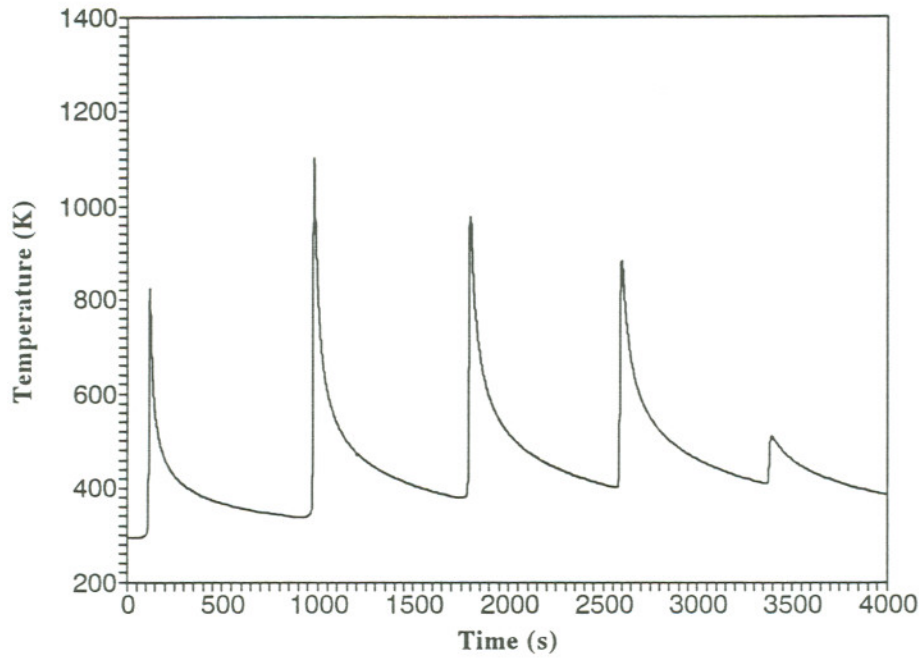

(a) 6.35 mm above WCL

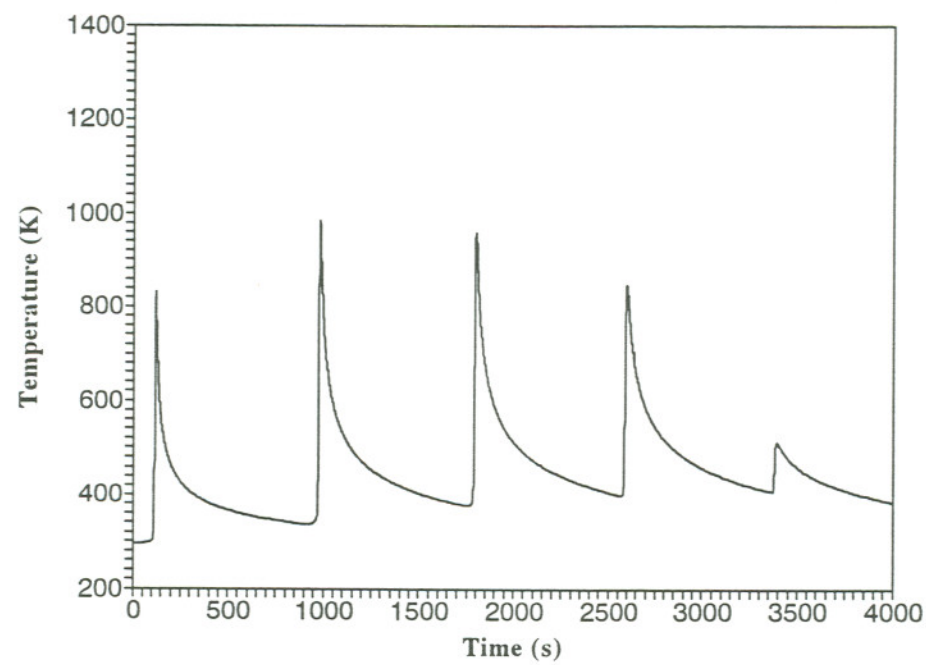

(b) 6.35 mm below WCL

Figure 58. Thermal Histories at 45° from the Welding Start and Different Distances from WCL

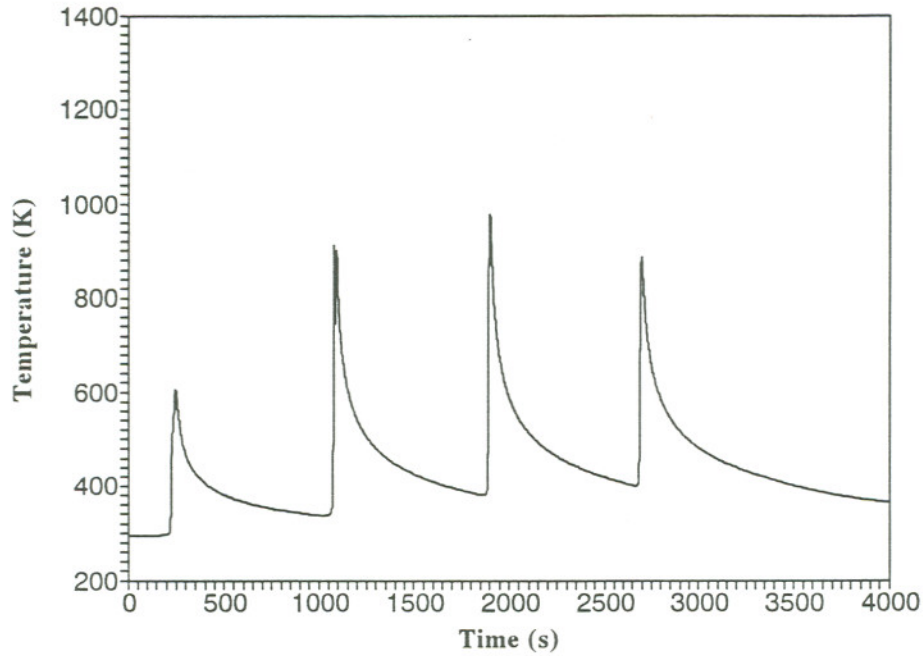

(a) 6.35 mm above WCL

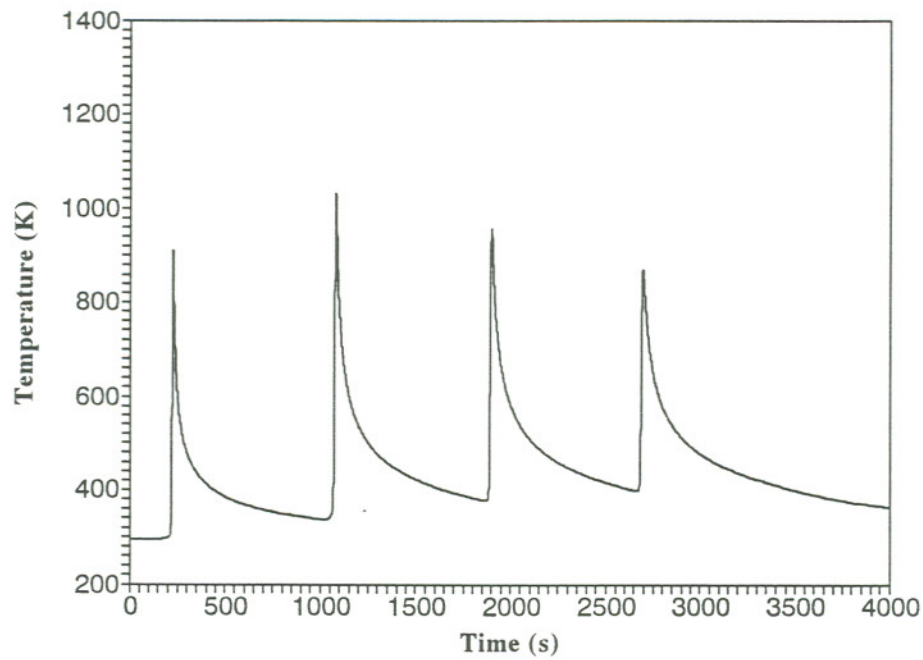

(b) 6.35 mm below WCL

Figure 59. Thermal Histories at 90° from the Welding Start and Different Distances from WCL

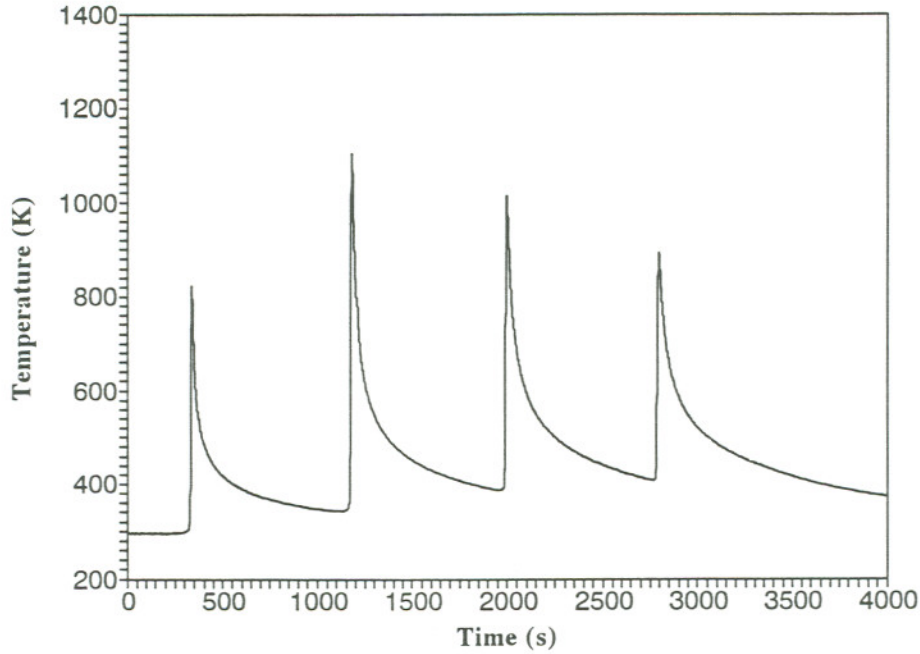

(a) 6.35 mm above WCL

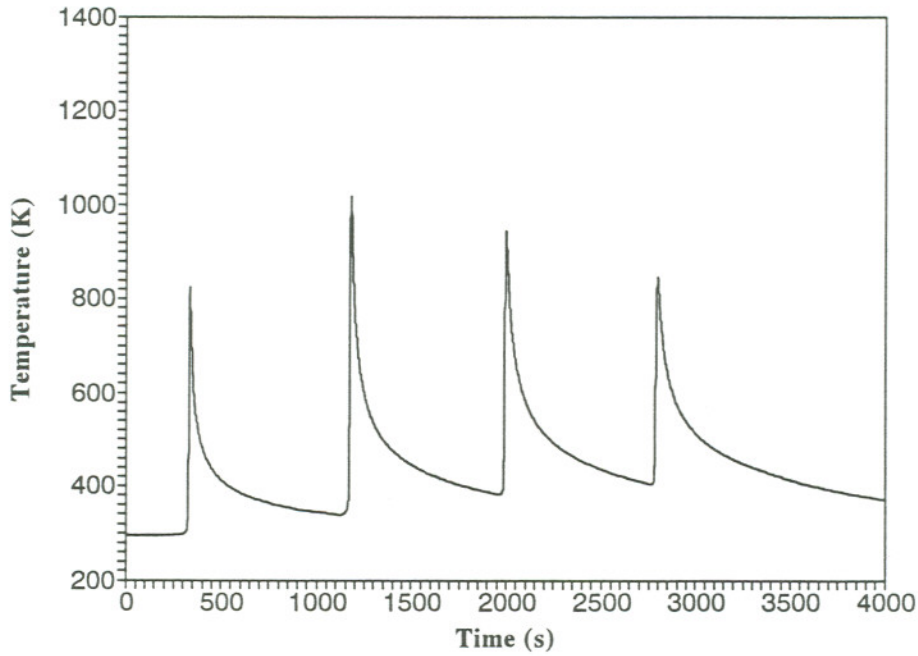

(b) 6.35 mm below WCL

Figure 60. Thermal Histories at 135° from the Welding Start and Different Distances from WCL

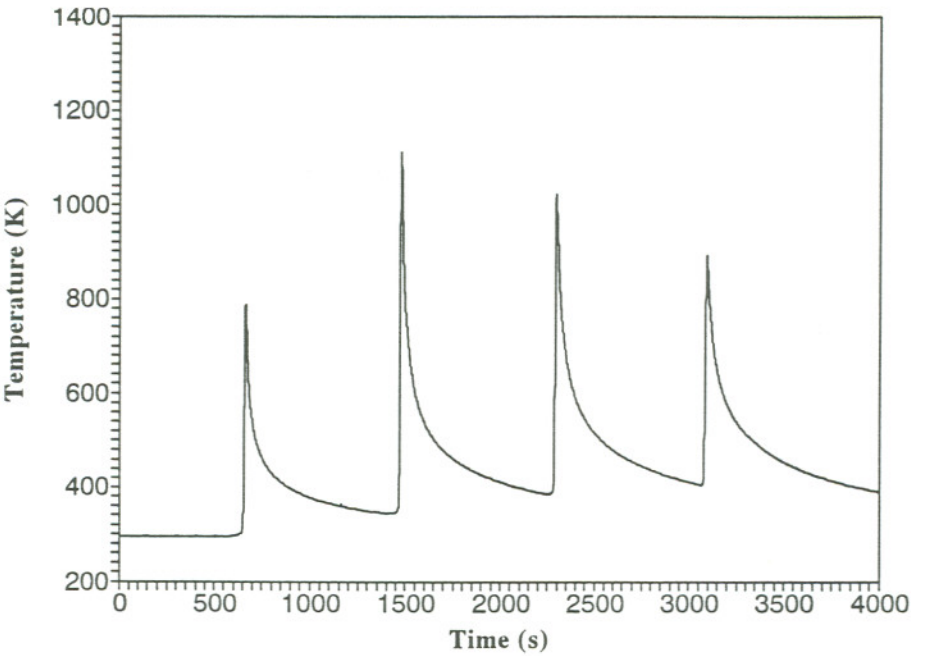

(a) 6.35 mm above WCL

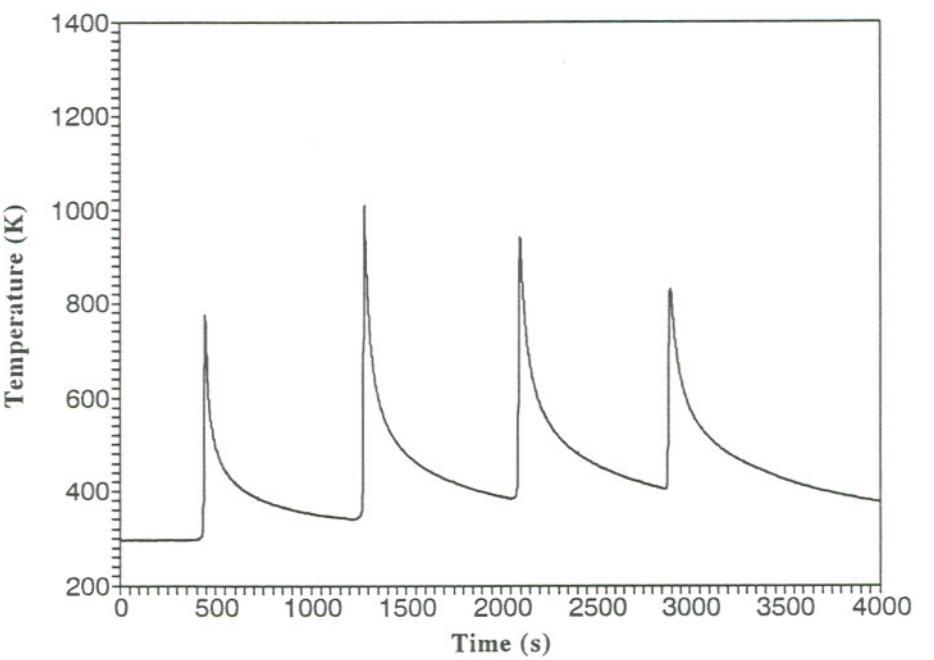

(b) 6.35 mm below WCL

Figure 61. Thermal Histories at 180° from the Welding Start and Different Distances from WCL

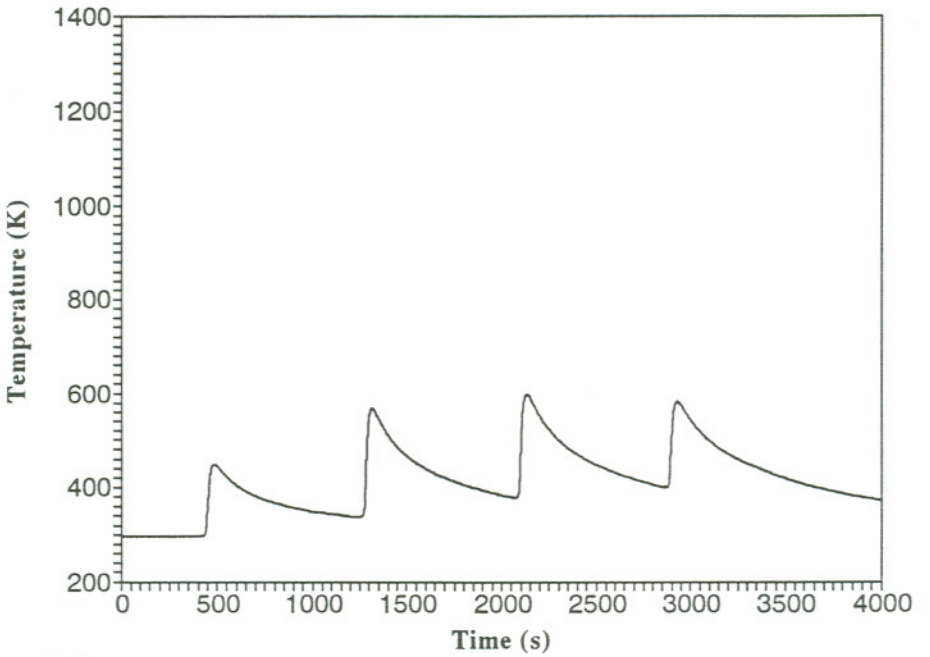

(c) 19.05 mm below WCL

Figure 61. Thermal Histories at 180° from the Welding Start and Different Distances from WCL

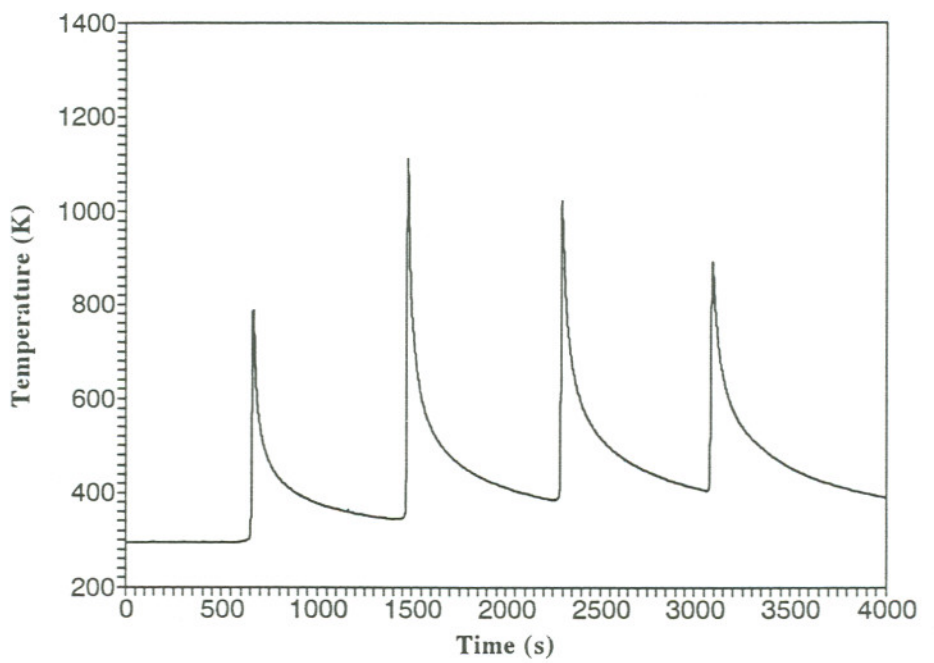

Figure 62. Thermal Histories at 270° from the Welding Start and 6.35 mm above WCL

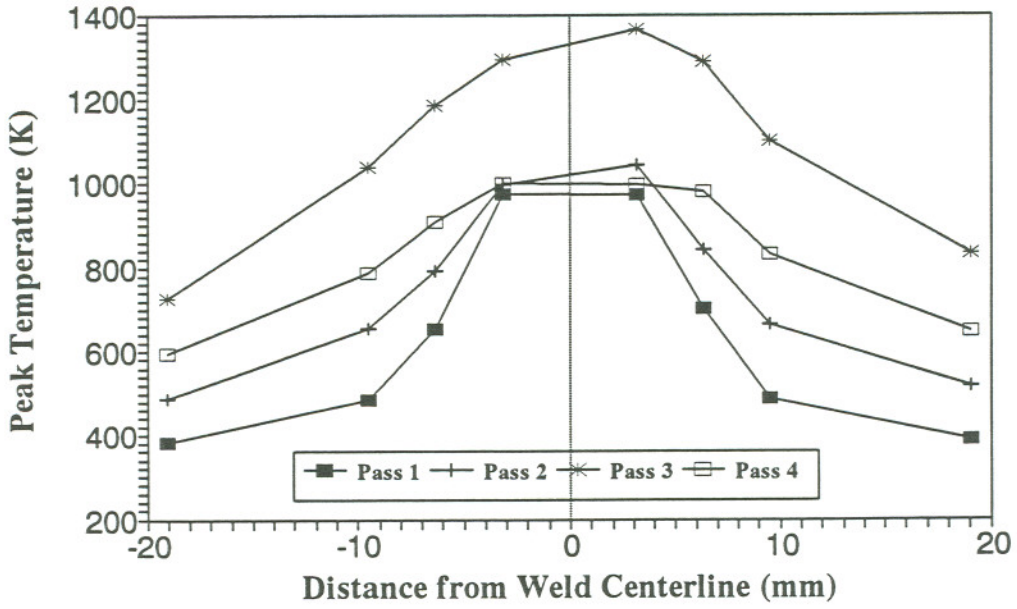

Figure 63. Peak Temperatures at 0° from the Welding Start as a Function of Distance from WCL

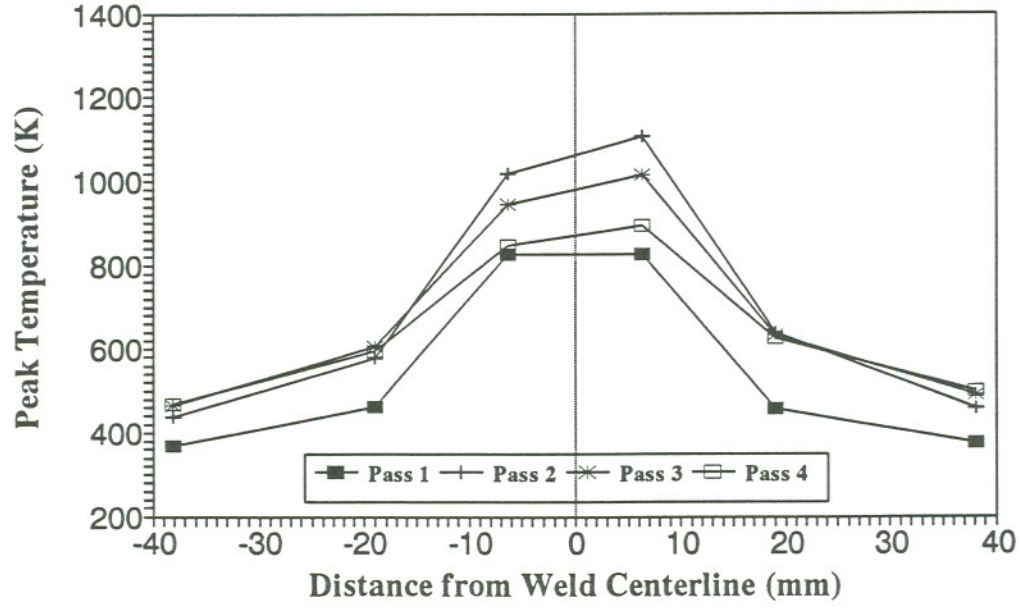

Figure 64. Peak Temperatures at 135° from the Welding Start as a Function of Distance from WCL

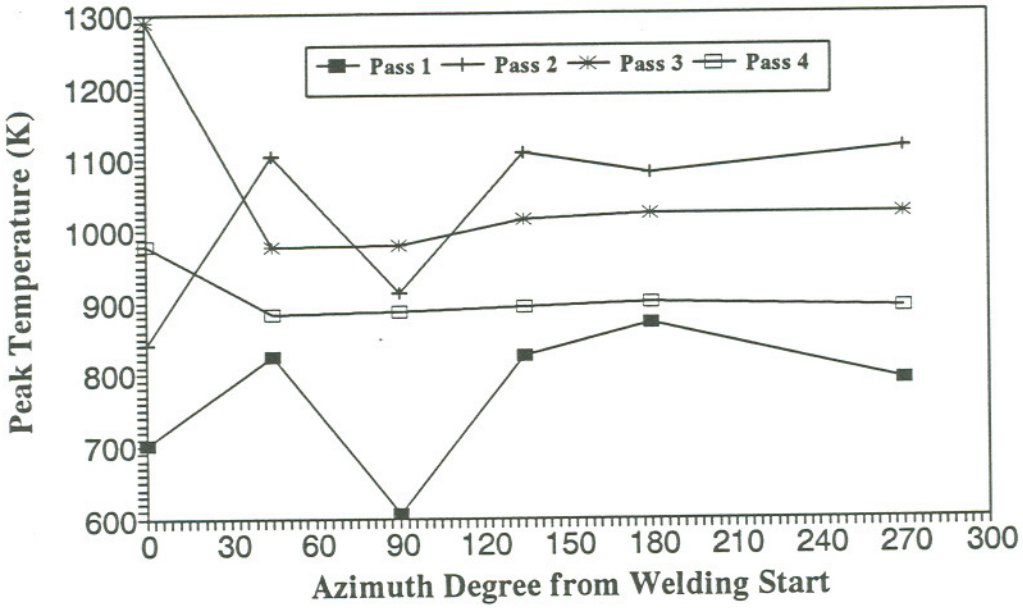

Figure 65. Peak Temperatures at 6.35 mm above WCL as a Function of Azimuthal Positions

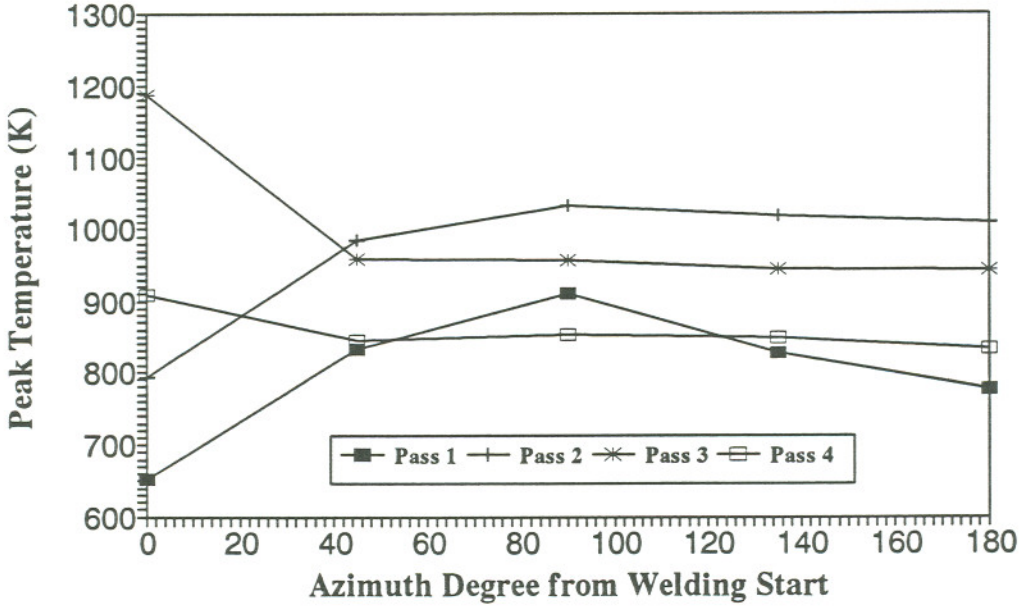

Figure 66. Peak Temperatures at 6.35 mm below WCL as a Function of Azimuthal Positions

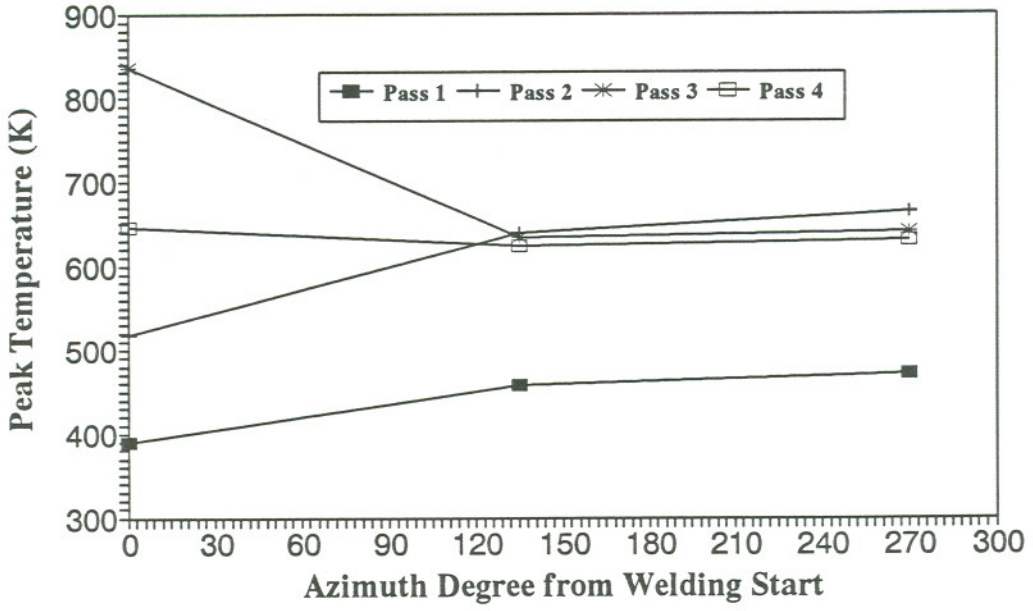

Figure 67. Peak Temperatures at 19.05 mm above WCL as a Function of Azimuthal Positions

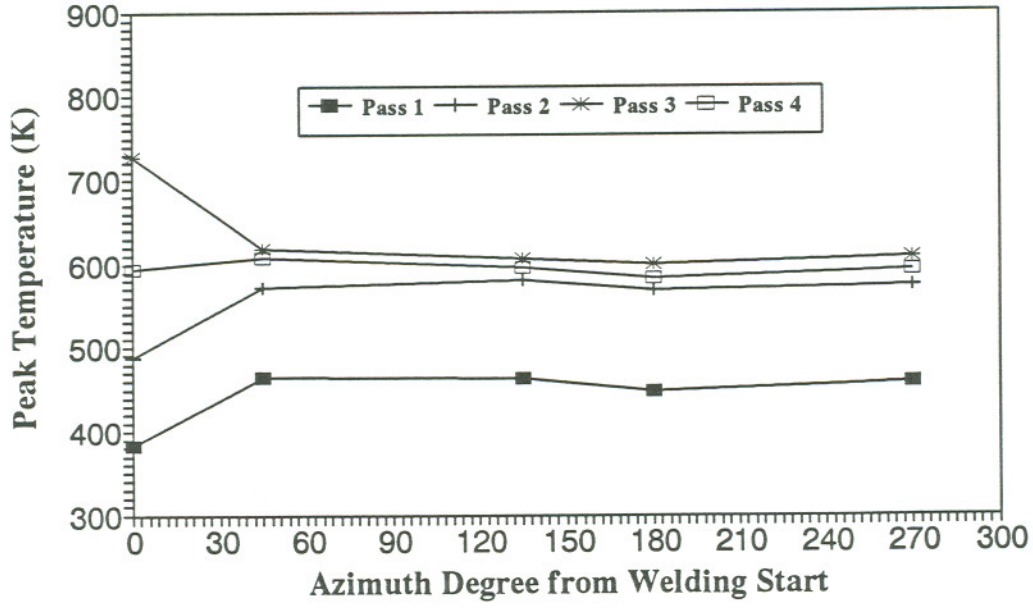

Figure 68. Peak Temperatures at 19.05 mm below WCL as a Function of Azimuthal Positions

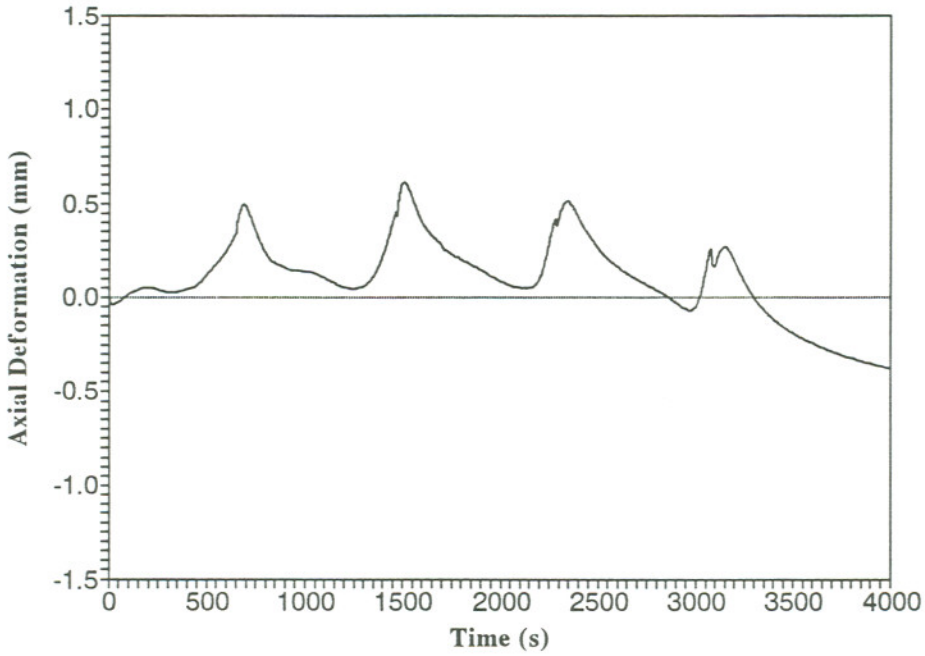

Figure 69. Axial deformation History at 135° from Welding Start

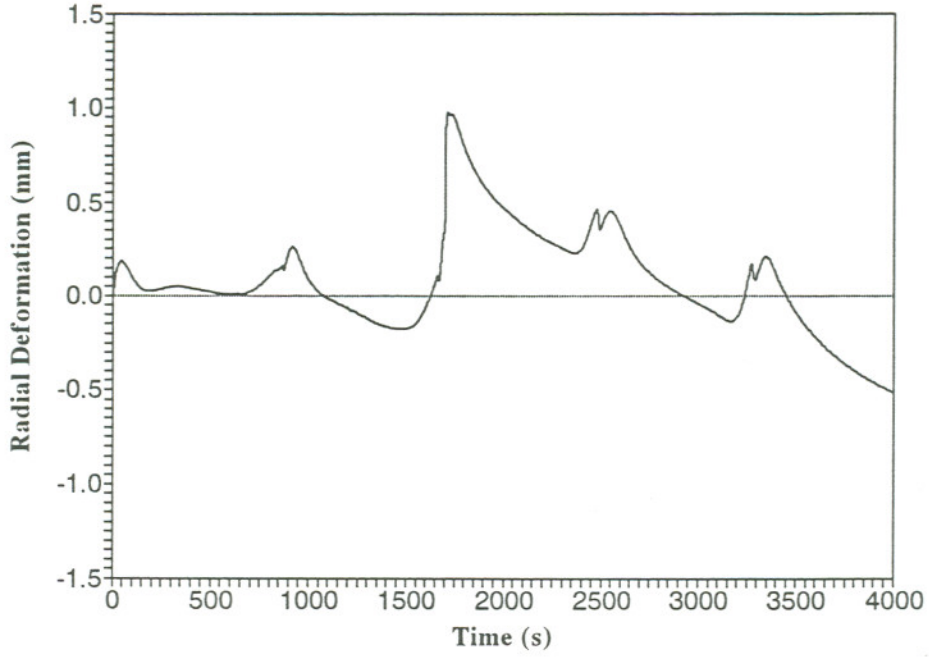

(a) 6.35 mm above WCL

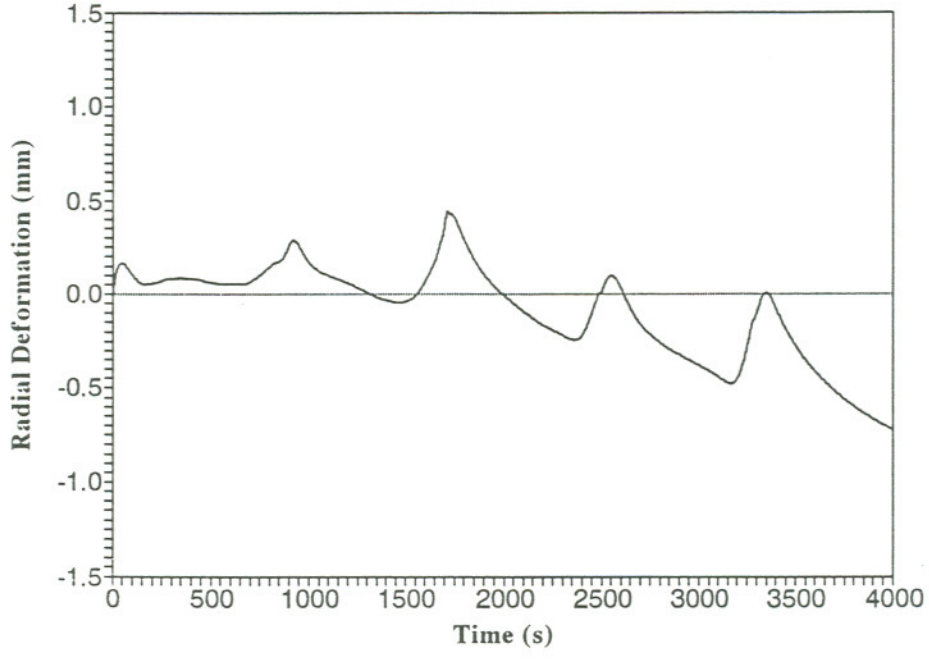

(b) 19.05 mm above WCL

Figure 70. Radial Deformation Histories at 0° from Welding Start and Different Distances from WCL

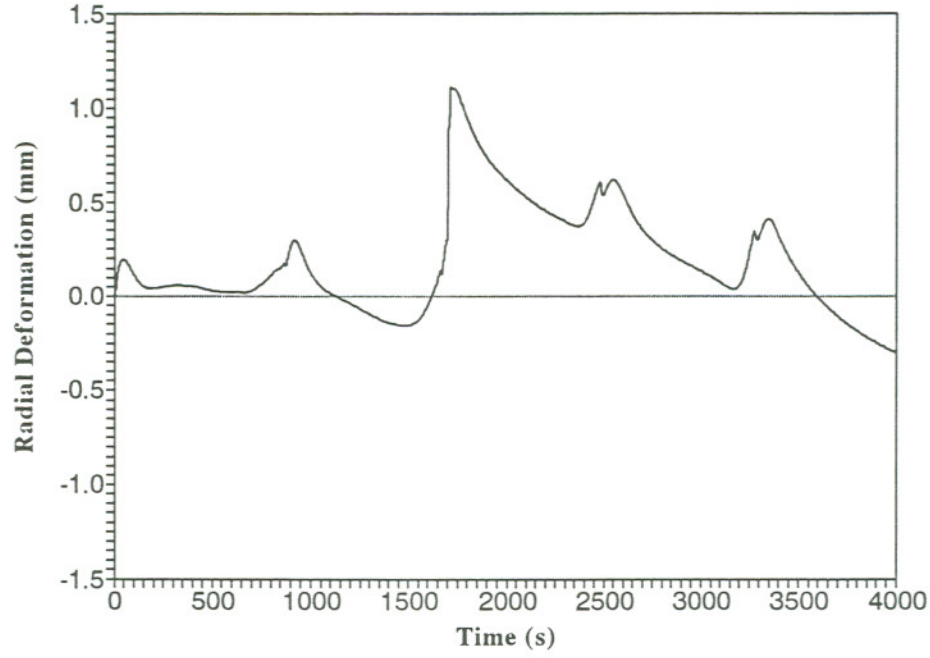

(c) 6.35 mm below WCL

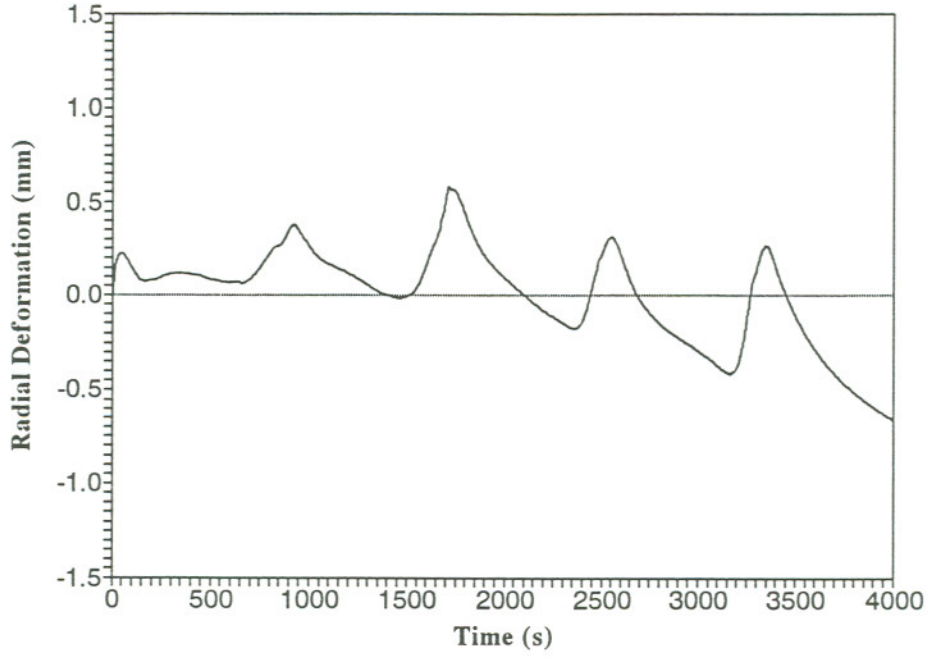

(d) 19.05 mm below WCL

Figure 70. Radial Deformation Histories at 0° from Welding Start and Different Distances from WCL

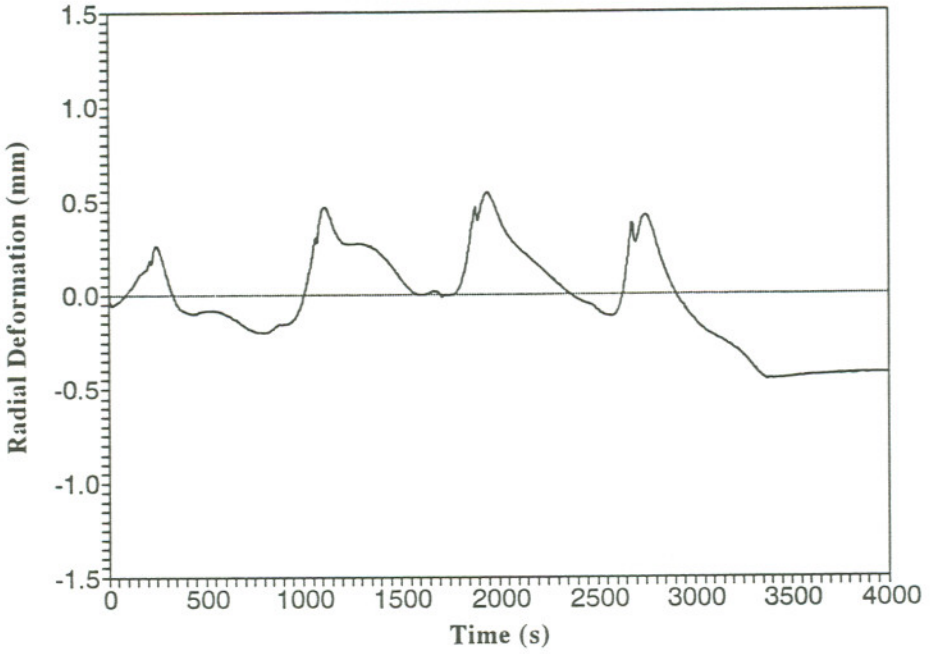

(a) 6.35 mm above WCL

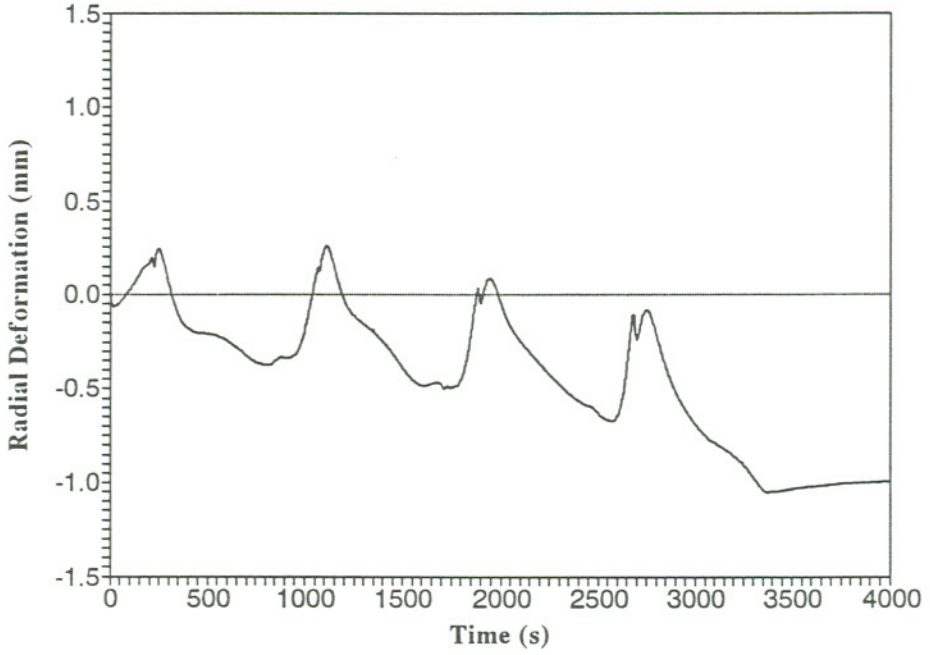

(b) 6.35 mm below WCL

Figure 71. Radial Deformation Histories at 90° from Welding Start and Different Distances from WCL

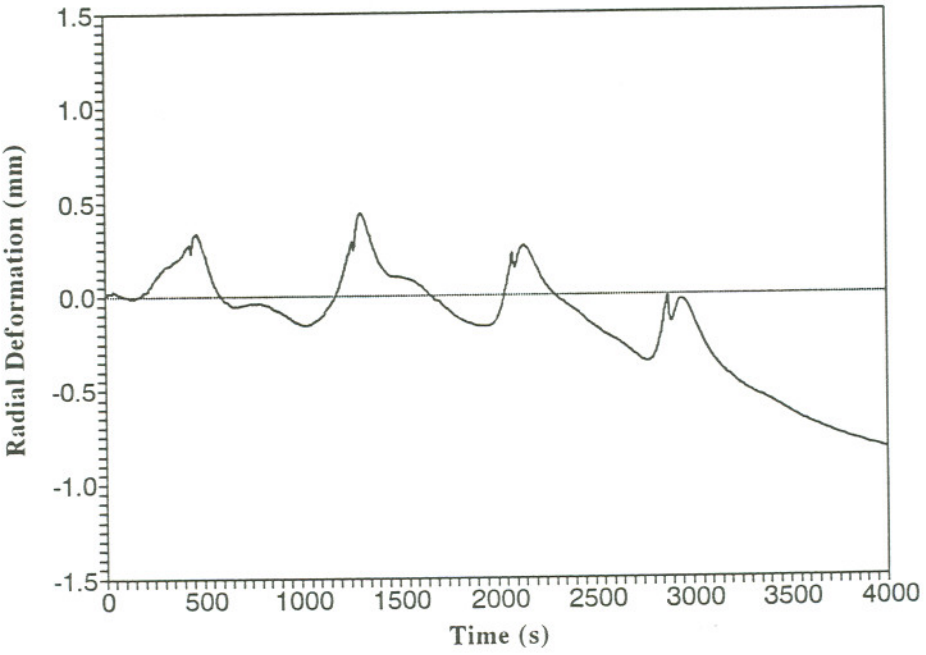

(a) 6.35 mm above WCL

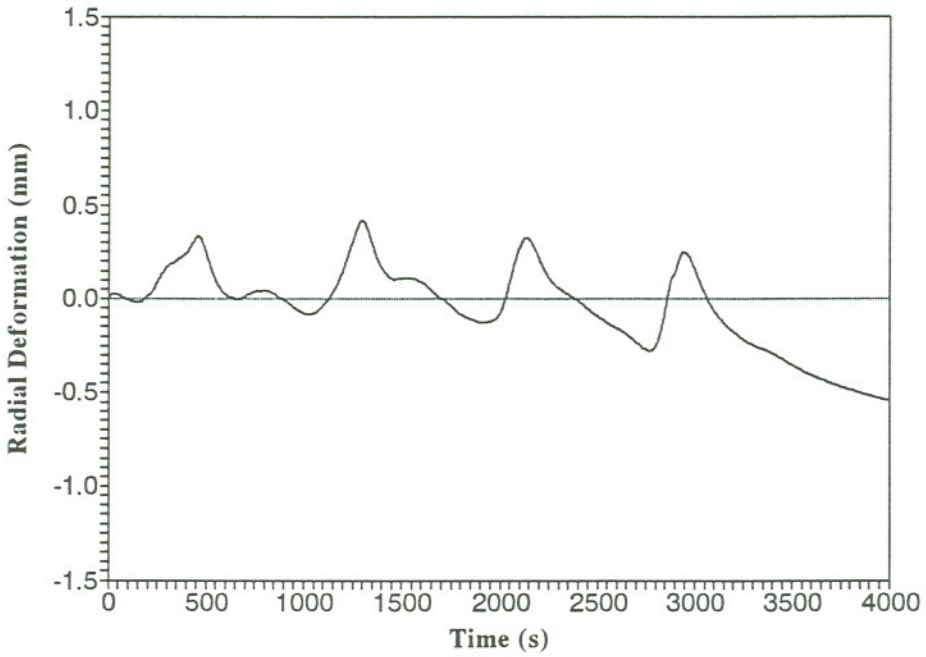

(b) 19.05 mm below WCL

Figure 72. Radial Deformation Histories at 180° from Welding Start and Different Distances from WCL

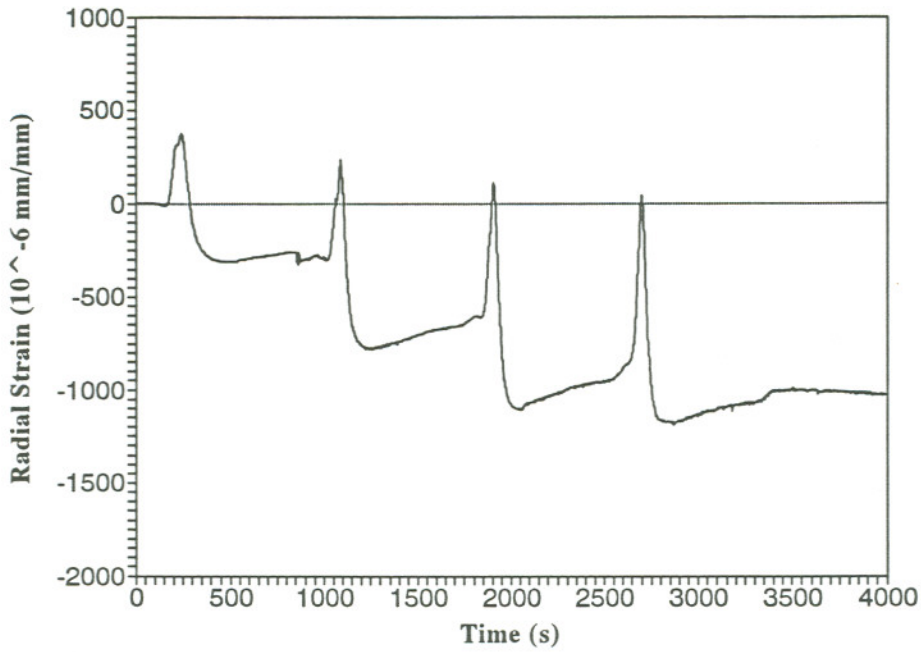

Figure 73. Hoop Strain History at 90° from Welding Start and 38.1 mm above WCL

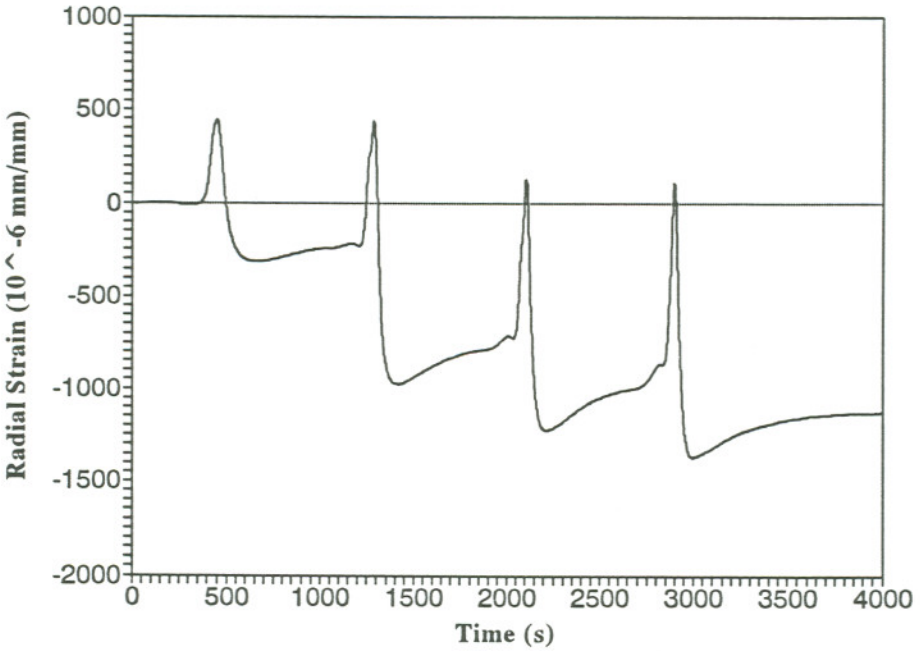

Figure 74. Hoop Strain History at 180° from Welding Start and 38.1 mm above WCL

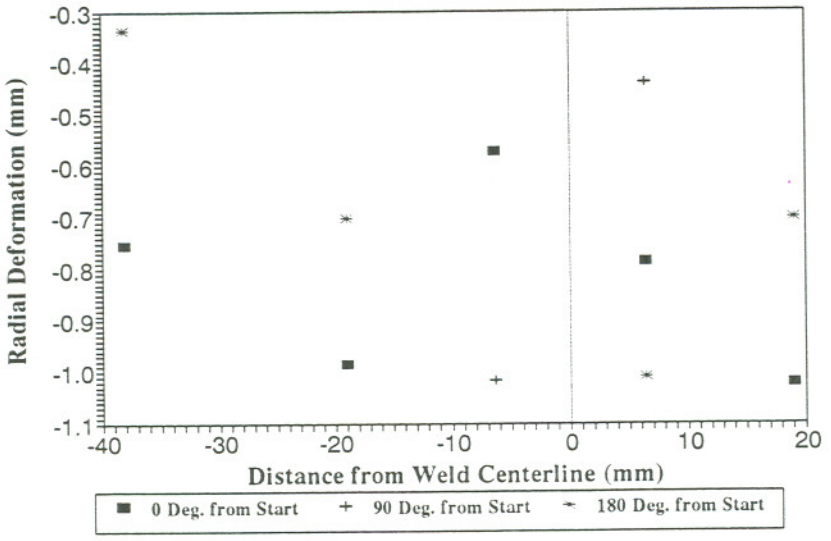

Figure 75. Final Radial Deformations as a Function of Distance from WCL

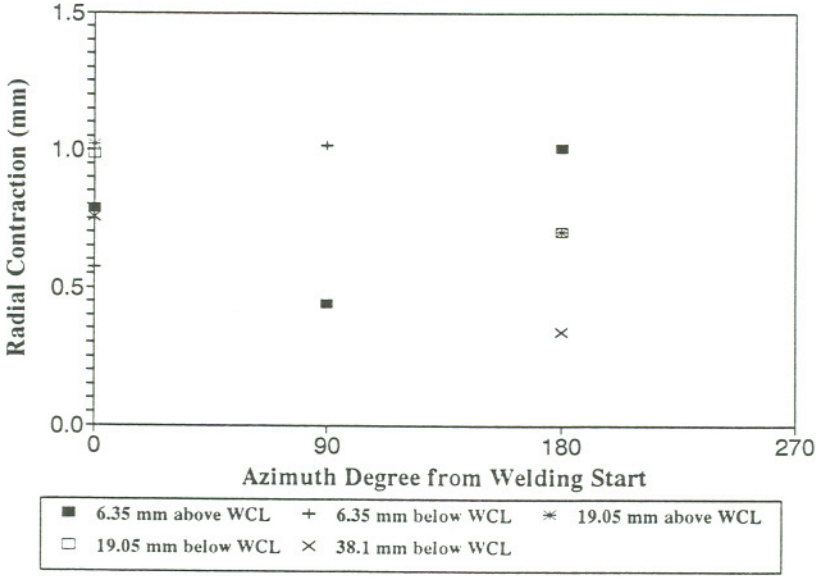

Figure 76. Final Radial Deformations as a Function of Azimuthal Position from Welding Start

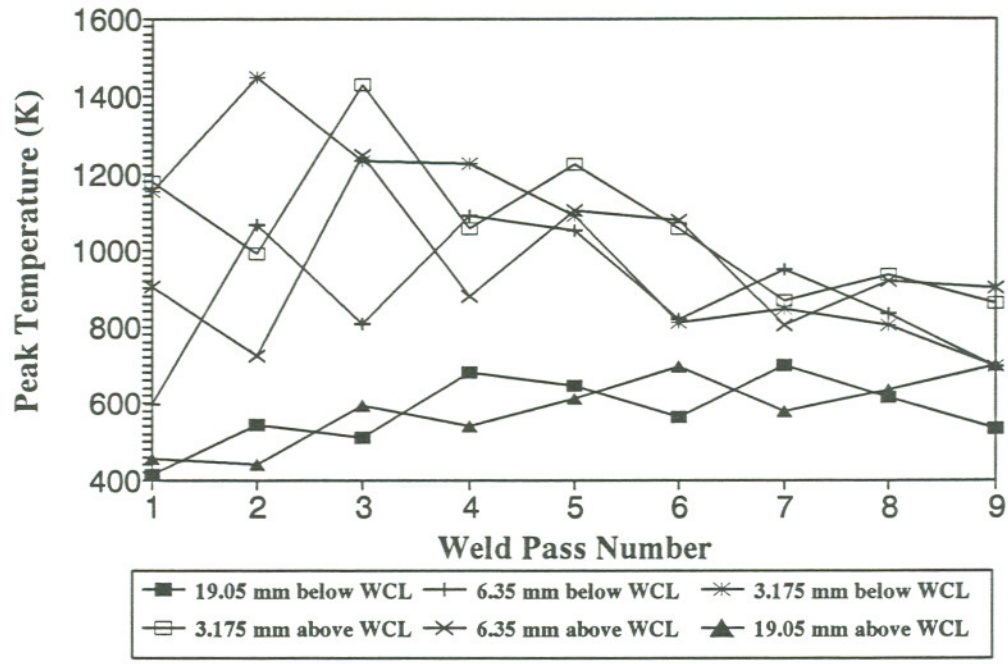

Figure 77. Peak Temperatures at 0° from Welding Start as a Function of Weld Pass Number

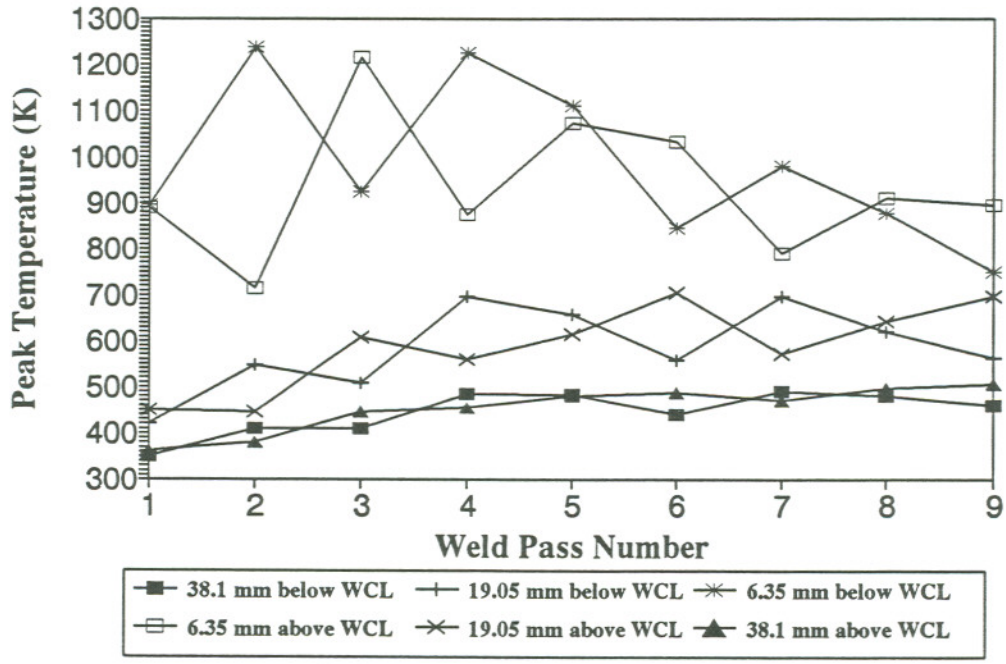

Figure 78. Peak Temperatures at 135° from Welding Start as a Function of Weld Pass Number

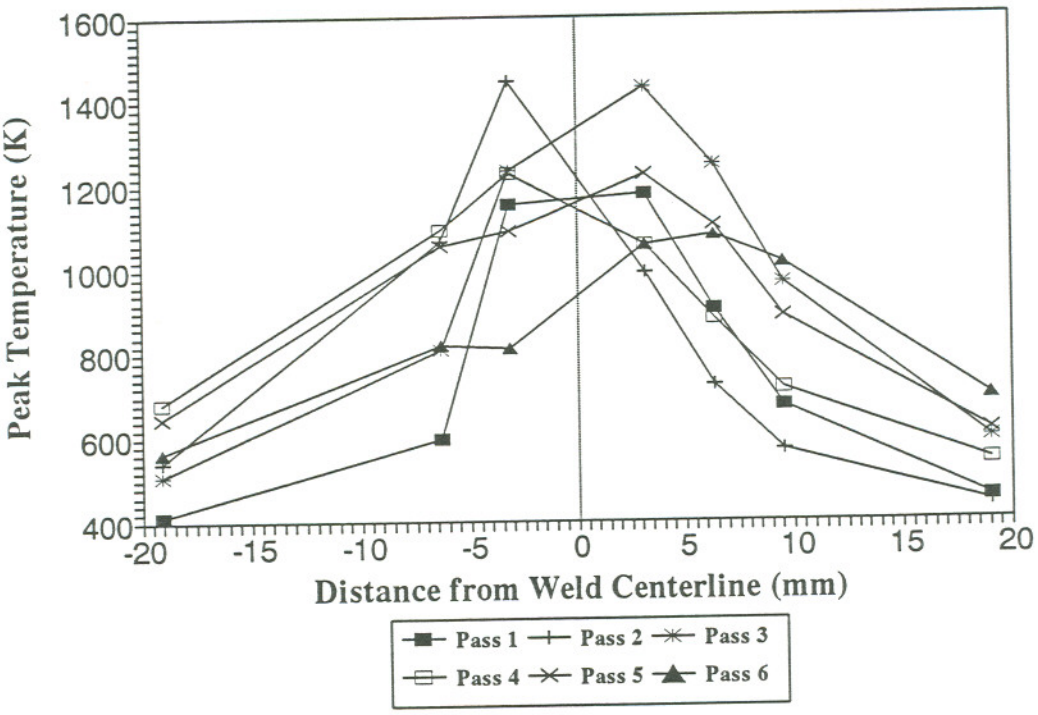

Figure 79. Peak Temperatures at 0° from Welding Start as a Function of Distance from WCL

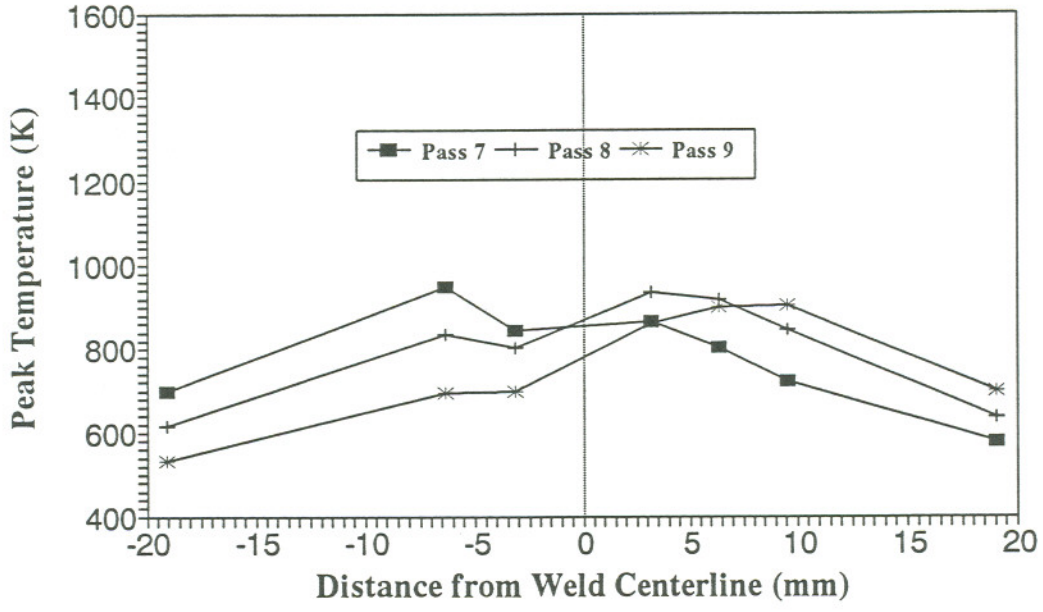

Figure 79. Peak Temperatures at 0° from Welding Start as a Function of Weld Pass Number

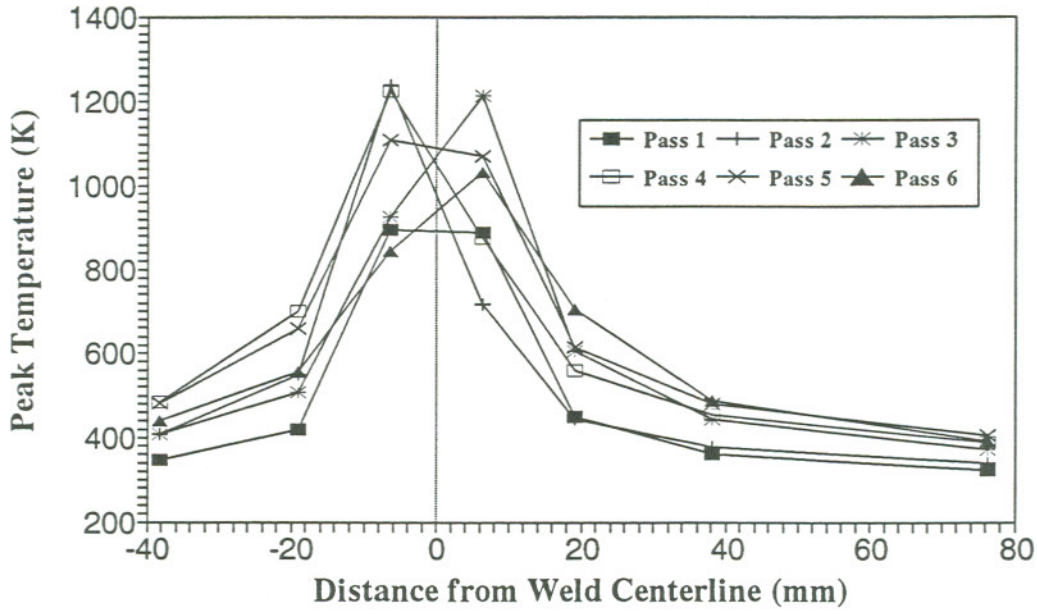

Figure 80. Peak Temperatures at 135° from Welding Start as a Function of Distance from WCL

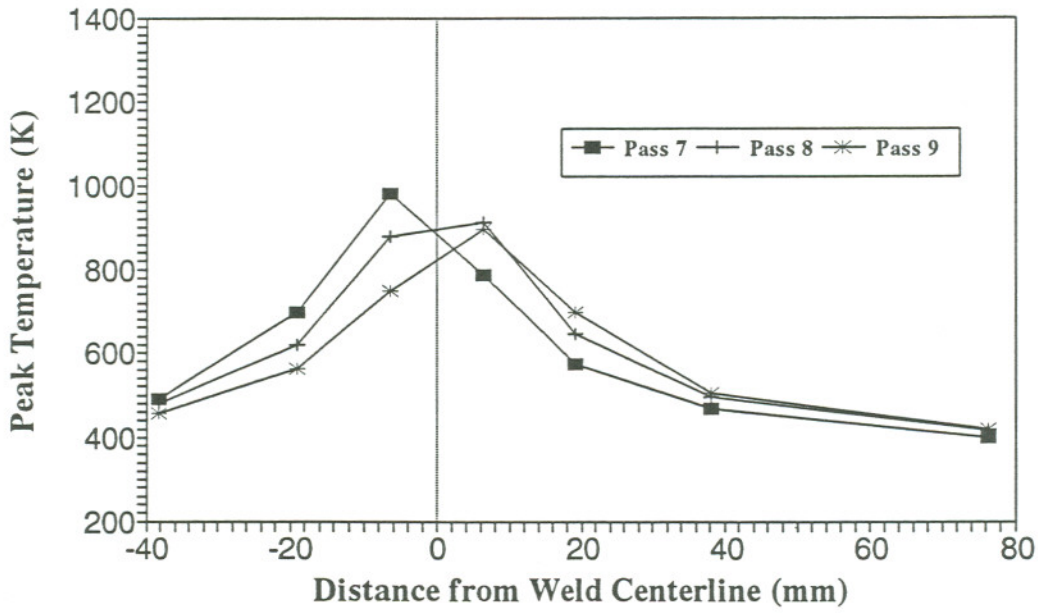

Figure 80. Peak Temperatures at 135° from Welding Start as a Function of Distance from WCL

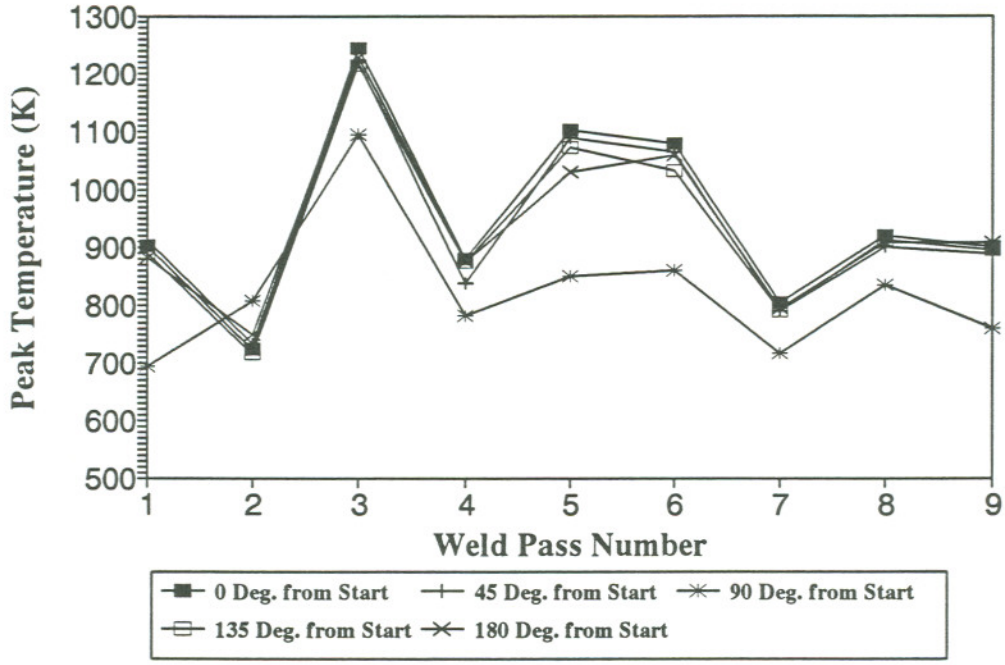

Figure 81. Peak Temperatures at 6.35 mm above WCL as a Function of Azimuthal Position

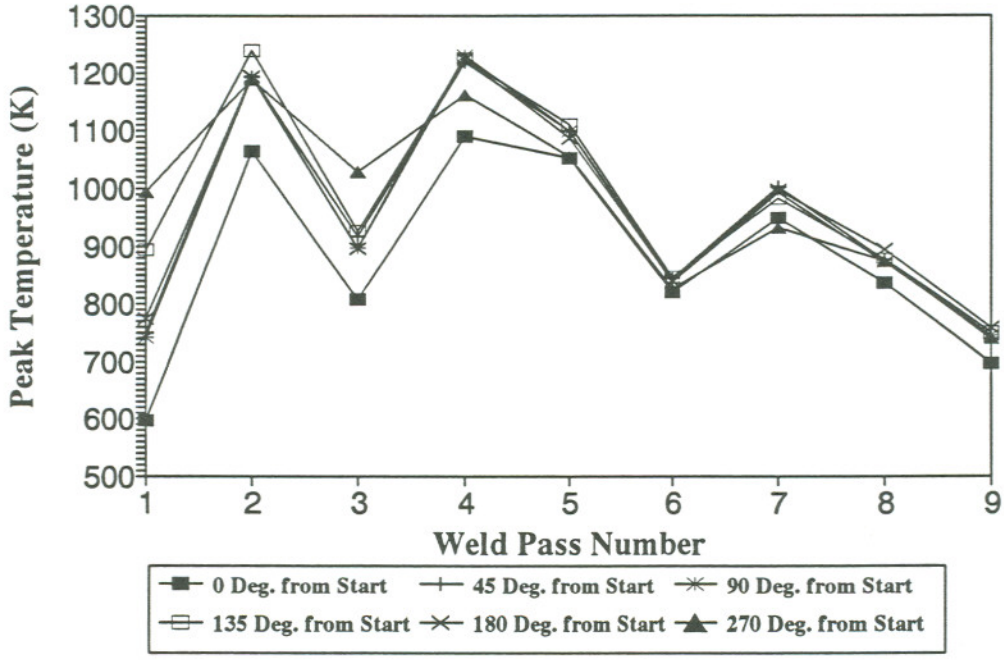

Figure 82. Peak Temperatures at 6.35 mm below WCL as a Function of Azimuthal Position

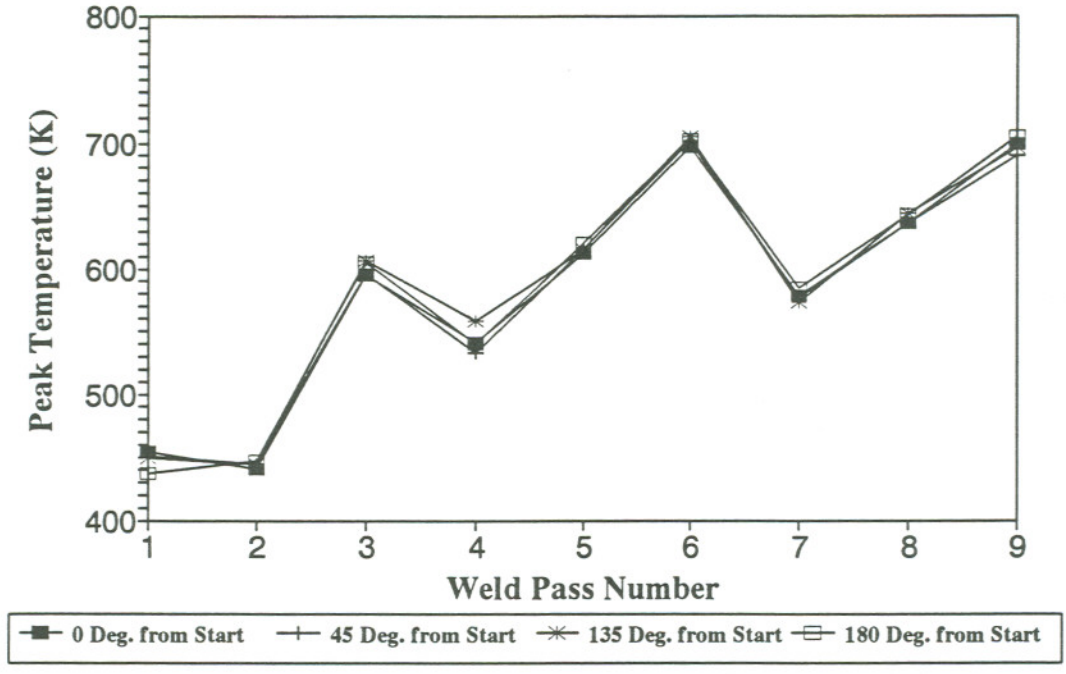

Figure 83. Peak Temperatures at 19.05 mm above WCL as a Function of Azimuthal Position

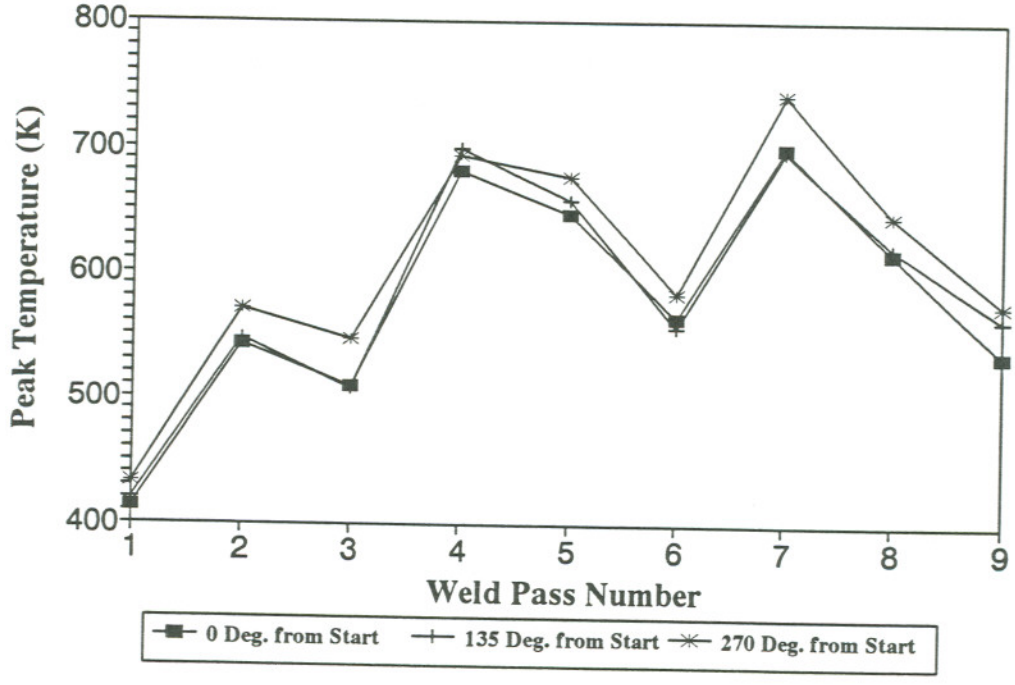

Figure 84. Peak Temperatures at 19.05 mm below WCL as a Function of Azimuthal Position

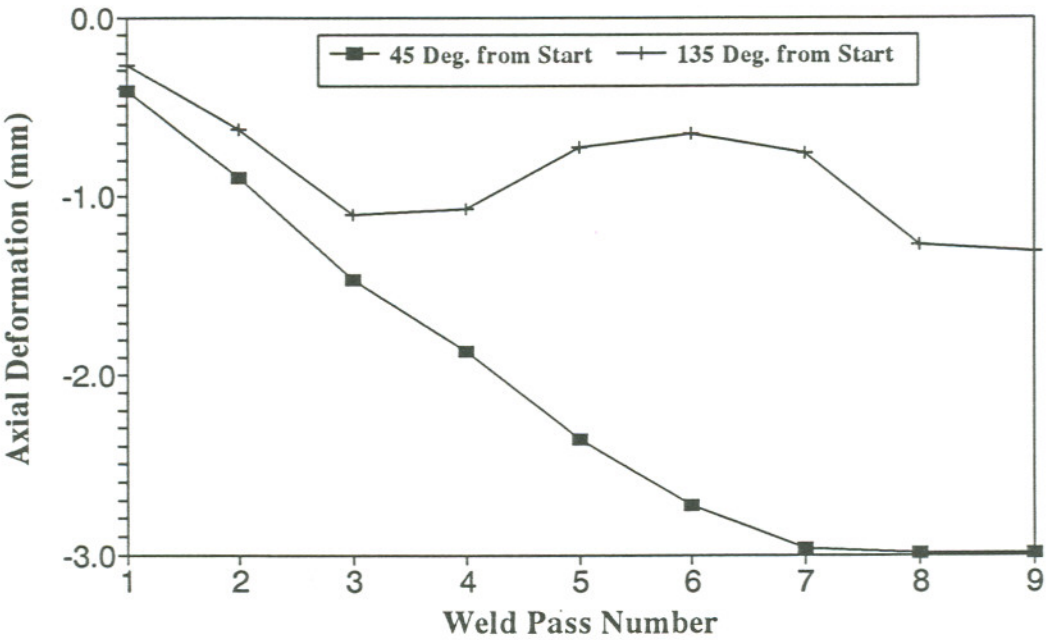

Figure 85. Axial Deformations as a Function of Weld Pass Number

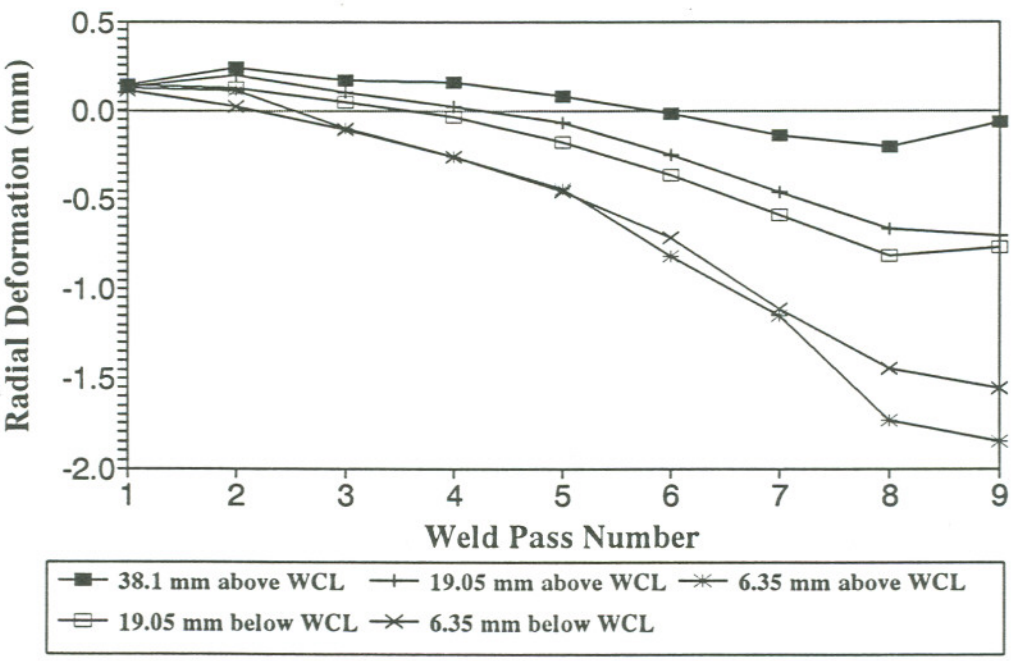

Figure 86. Radial Deformations at 0° from Welding Start as a Function of Weld Pass Number

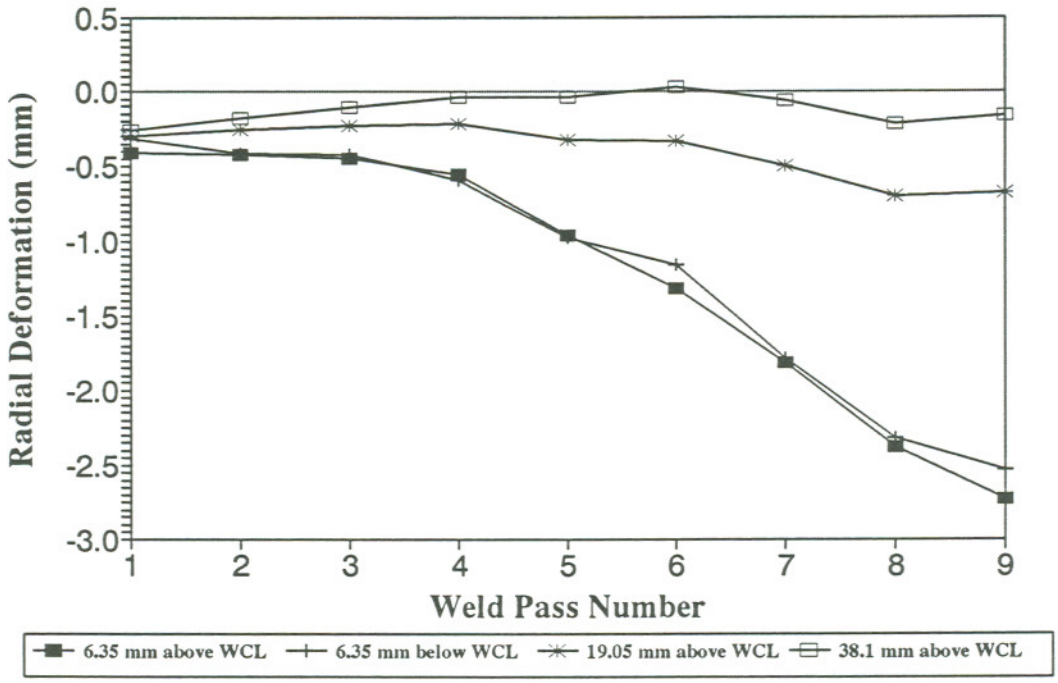

Figure 87. Radial Deformations at 180° from Welding Start as a Function of Weld Pass Number

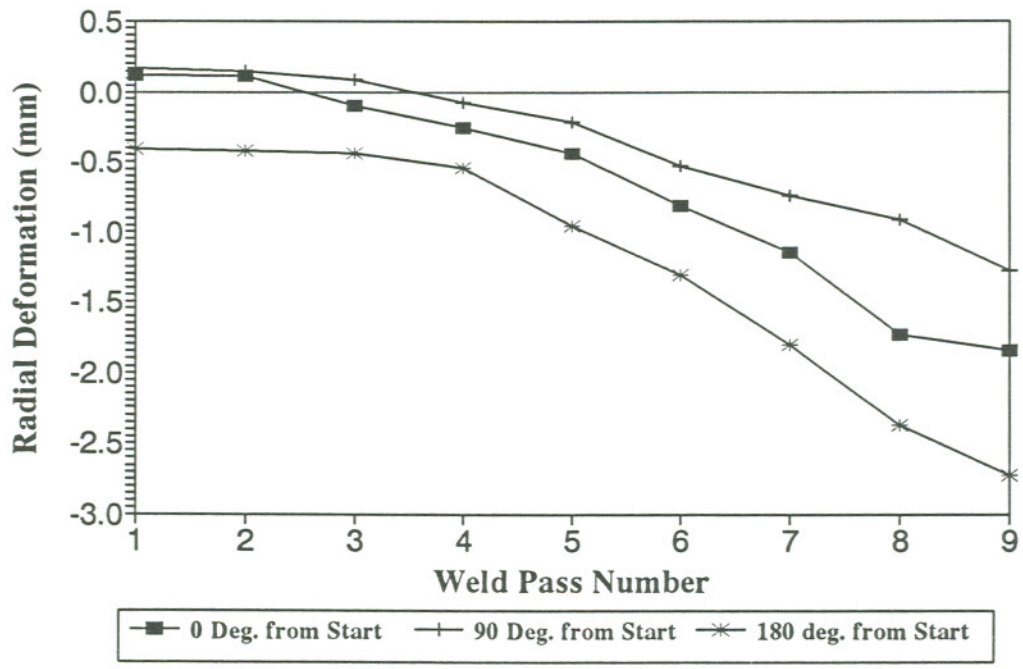

Figure 88. Radial Deformations at 6.35 mm above WCL as a Function of Weld Pass Number

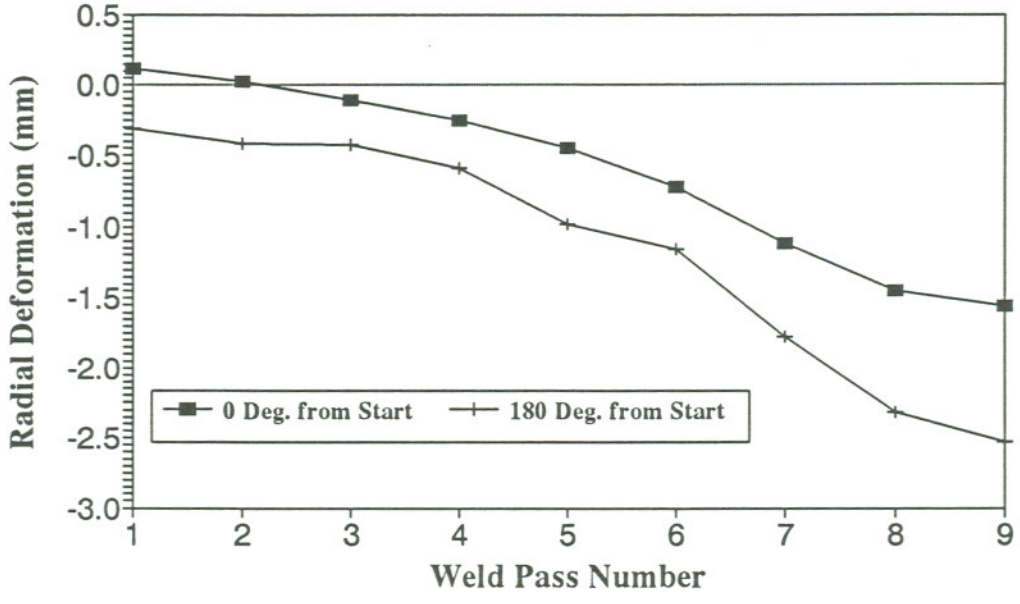

Figure 89. Radial Deformations at 6.35 mm below WCL as a Function of Weld Pass Number

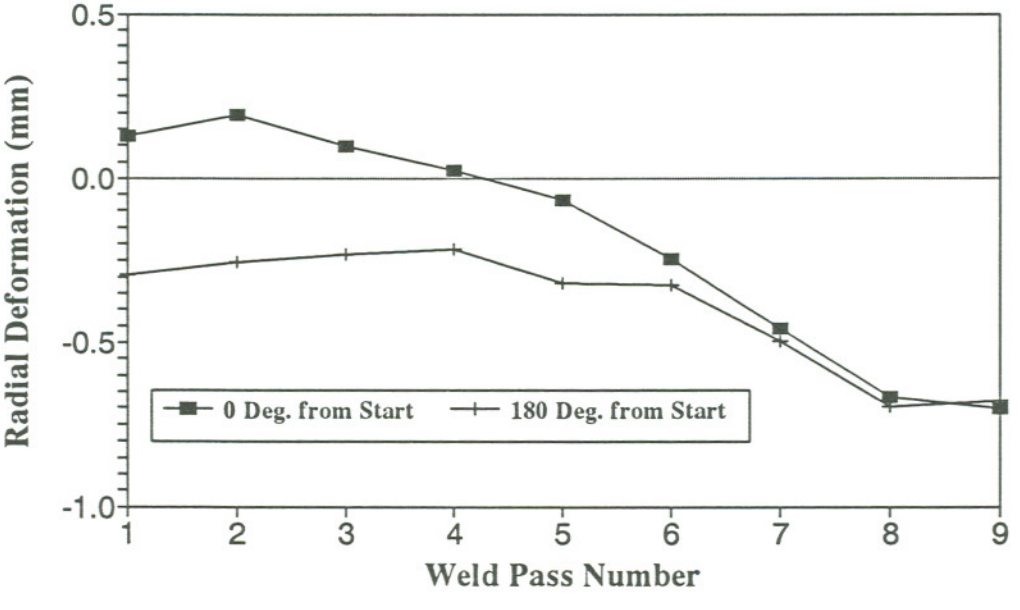

Figure 90. Radial Deformations at 19.05 mm above WCL as a Function of Weld Pass Number

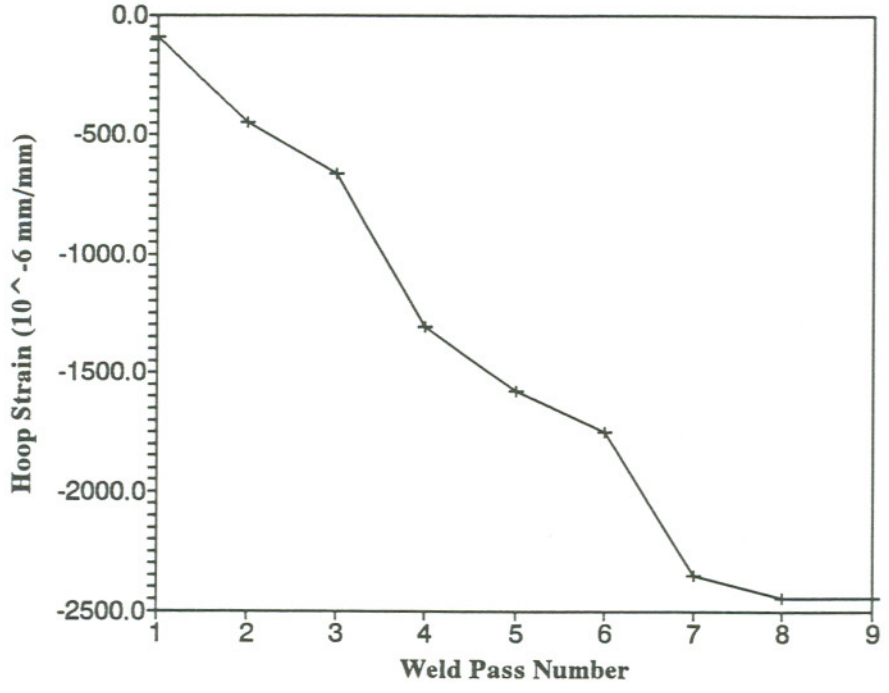

Figure 91. Hoop Strain at 38.1 mm below WCL as a Function of Weld Pass Number

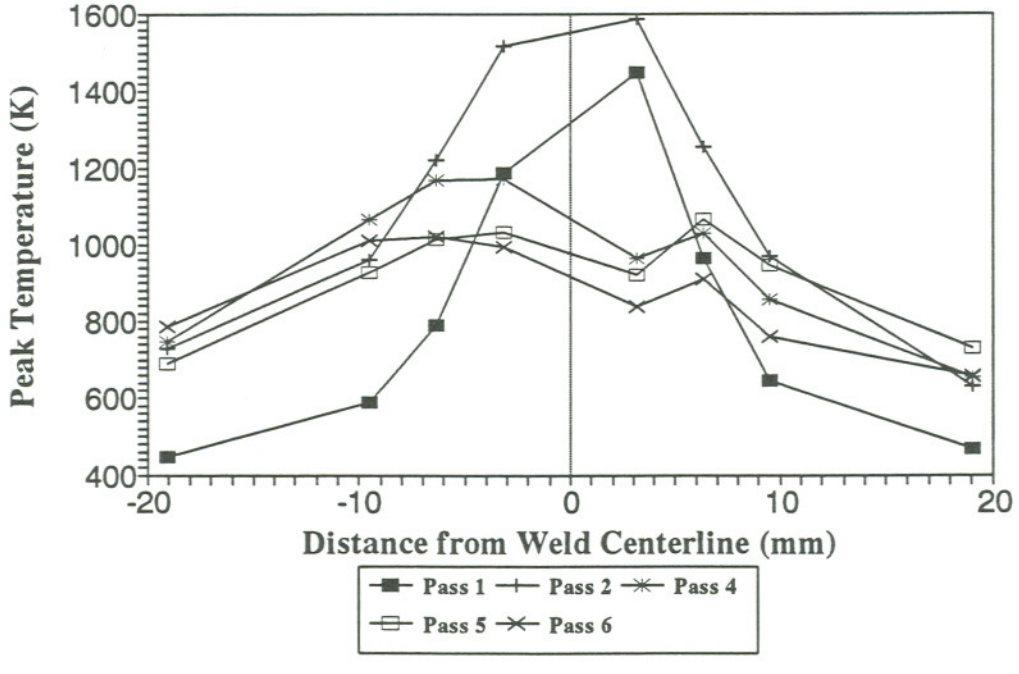

Figure 92. Peak Temperatures at 0° from Welding Start as a Function of Distance from WCL

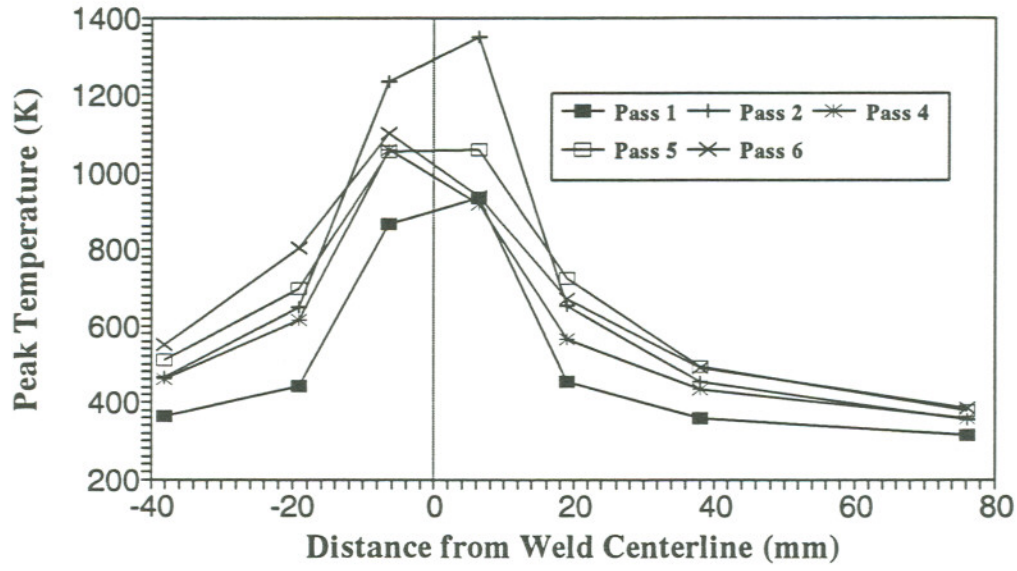

Figure 93. Peak Temperatures at 135° from Welding Start as a Function of Distance from WCL

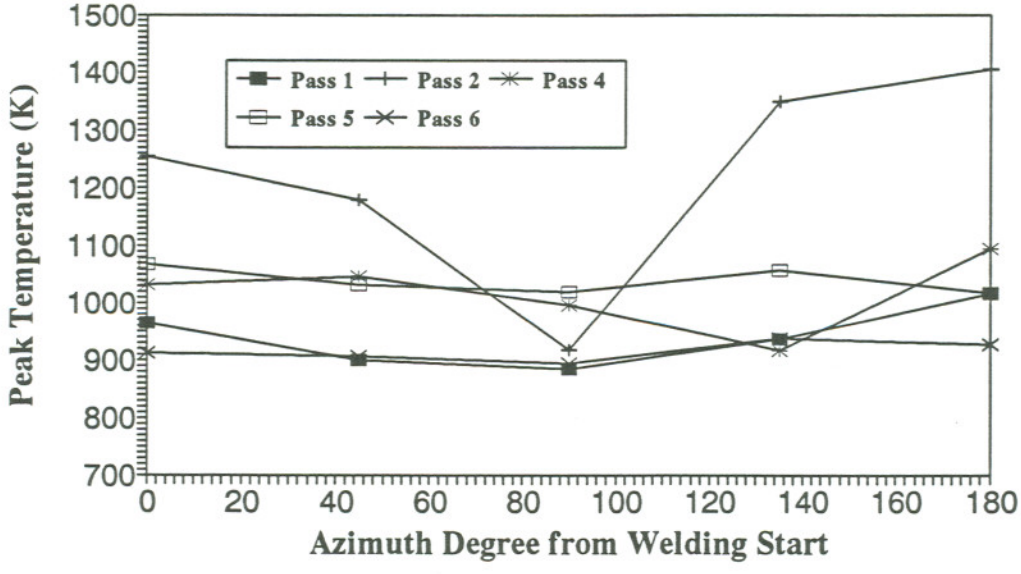

Figure 94. Peak Temperatures at 6.35 mm above WCL as a Function of Azimuthal Position

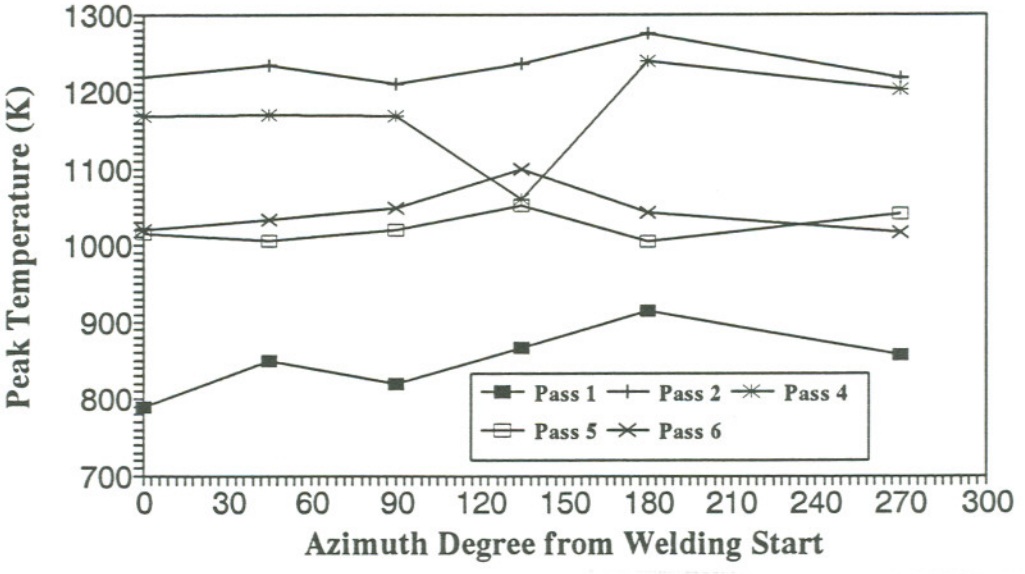

Figure 95. Peak Temperatures at 6.35 mm below WCL as a Function of Azimuthal Position

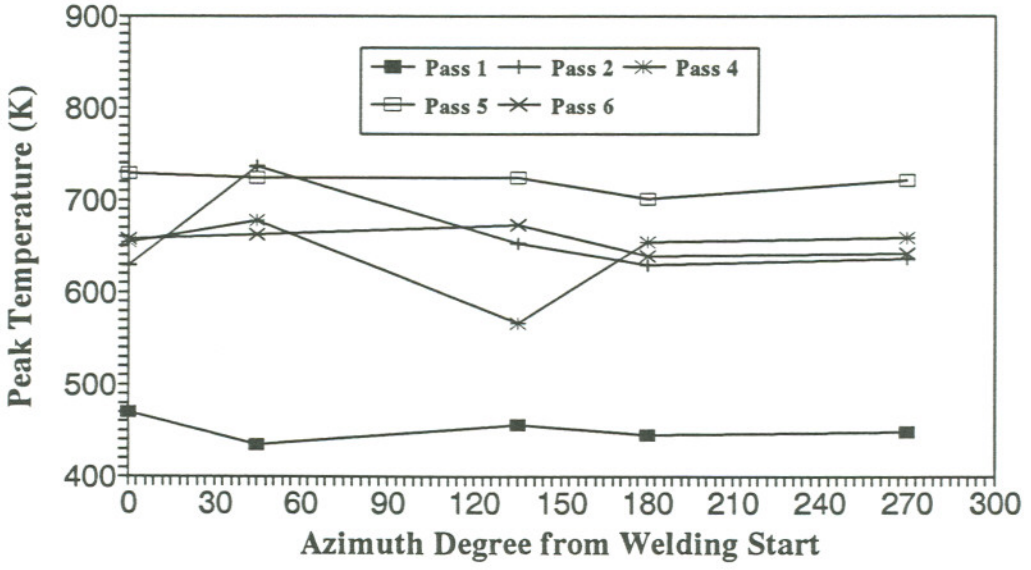

Figure 96. Peak Temperatures at 19.05 mm above WCL as a Function of Azimuthal Position

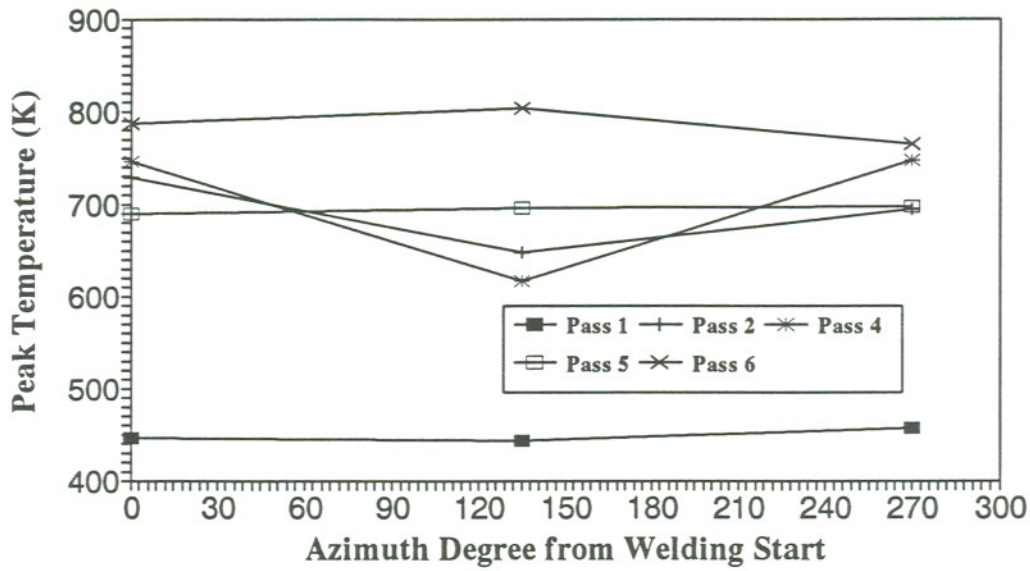

Figure 97. Peak Temperatures at 19.05 mm below WCL as a Function of Azimuthal Position

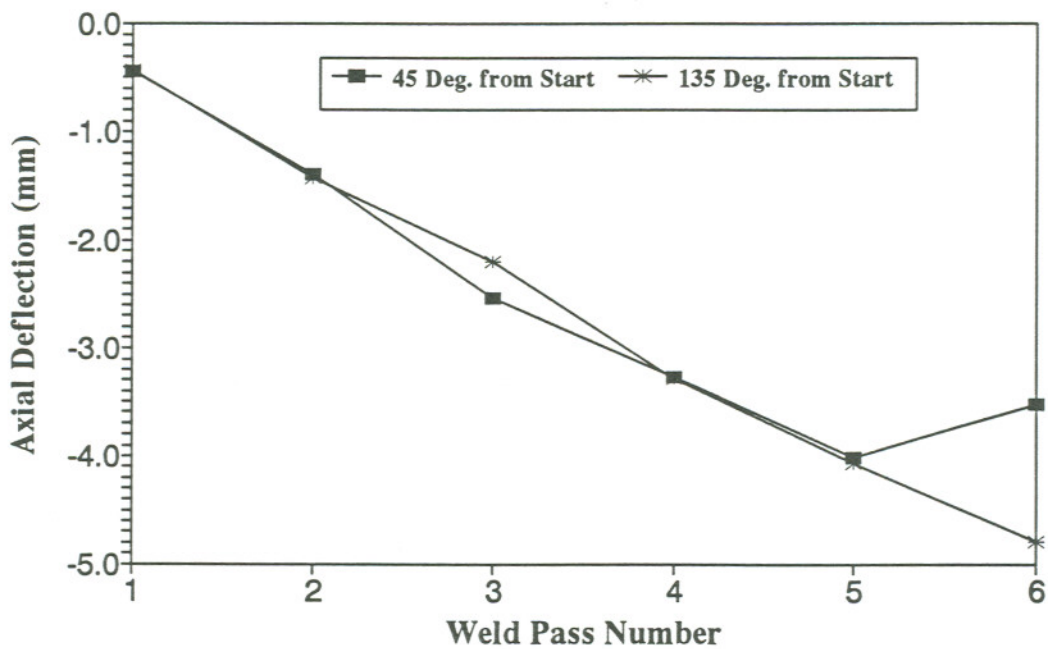

Figure 98. Axial Deformations as a Function of Weld Pass Number

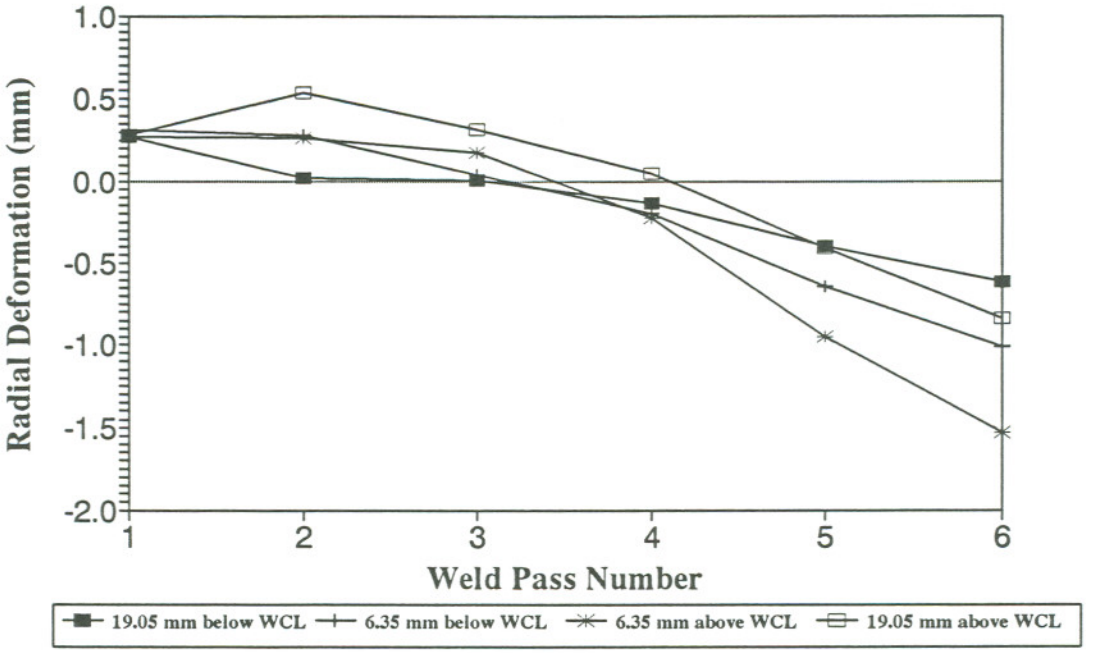

Figure 99. Radial Deformations at 0° from Welding Start as a Function of Weld Pass Number

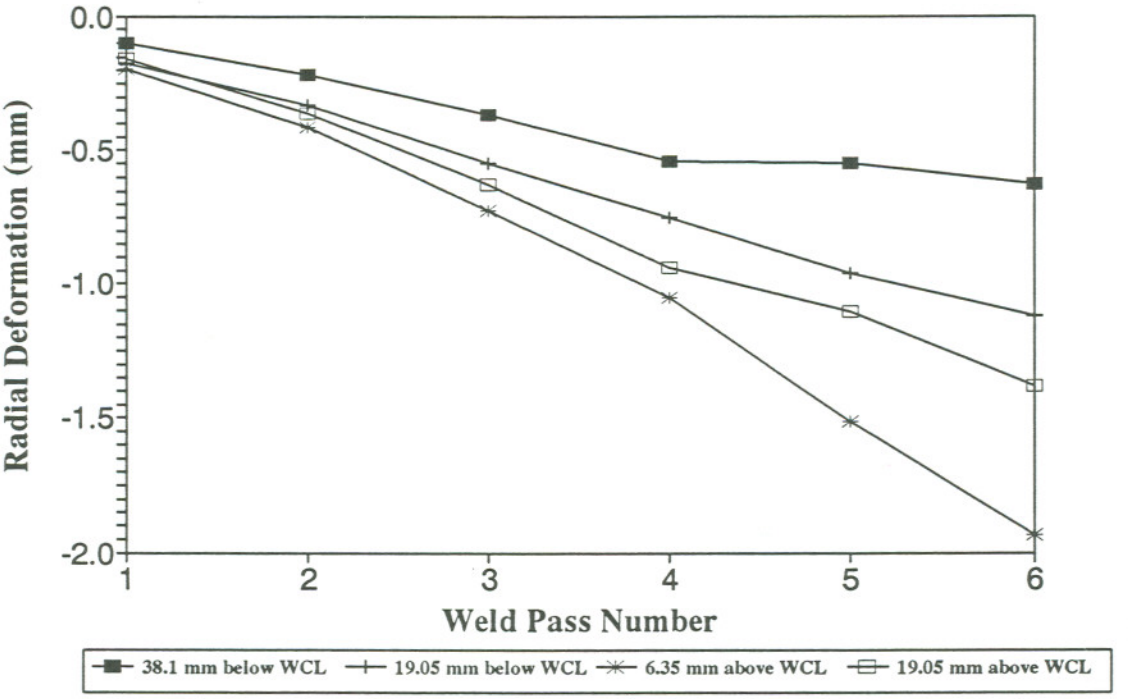

Figure 100. Radial Deformations at 180° from Welding Start as a Function of Weld Pass Number

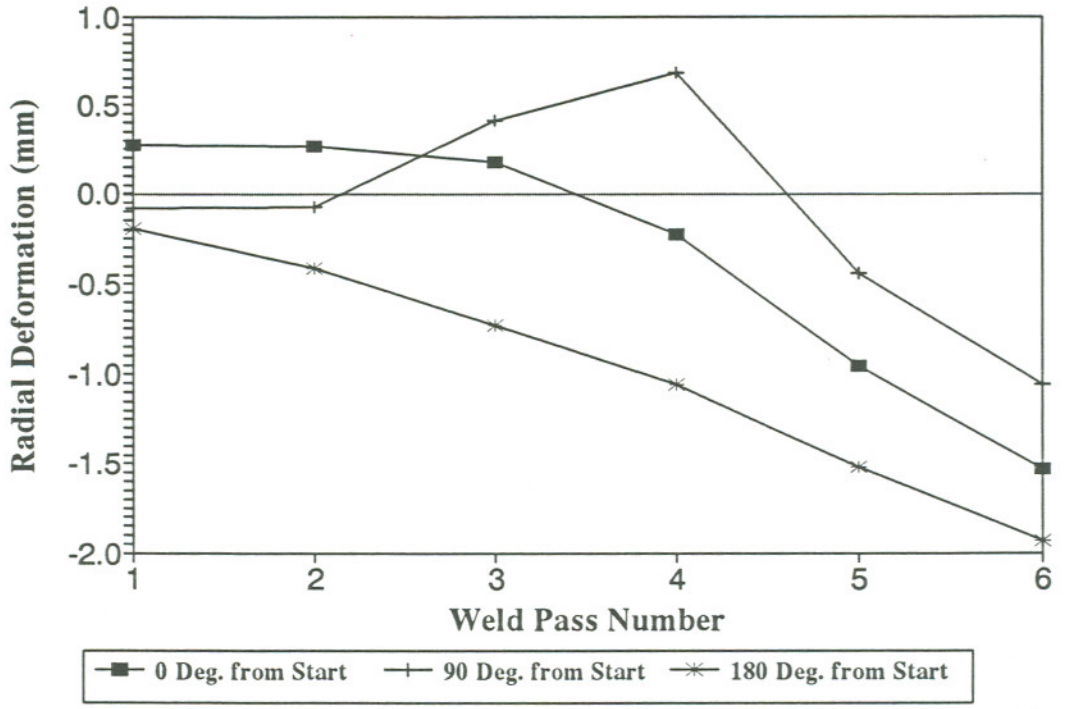

Figure 101. Radial Deformations at 6.35 mm above WCL as a Function of Weld Pass Number

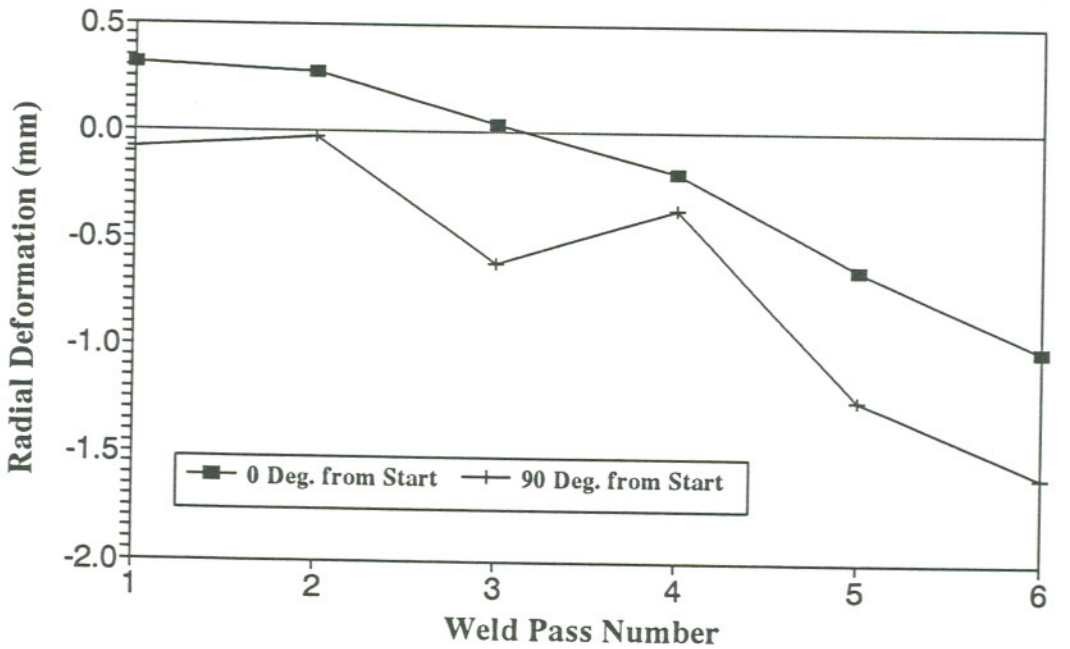

Figure 102. Radial Deformations at 6.35 mm below WCL as a Function of Weld Pass Number

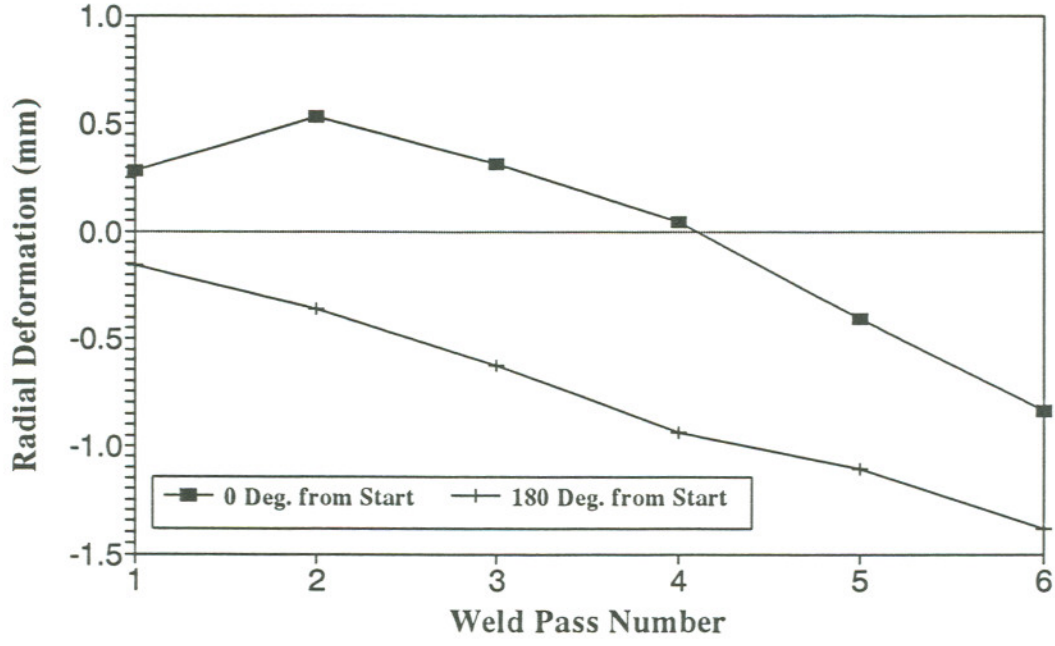

Figure 103. Radial Deformations at 19.05 mm above WCL as a Function of Weld Pass Number

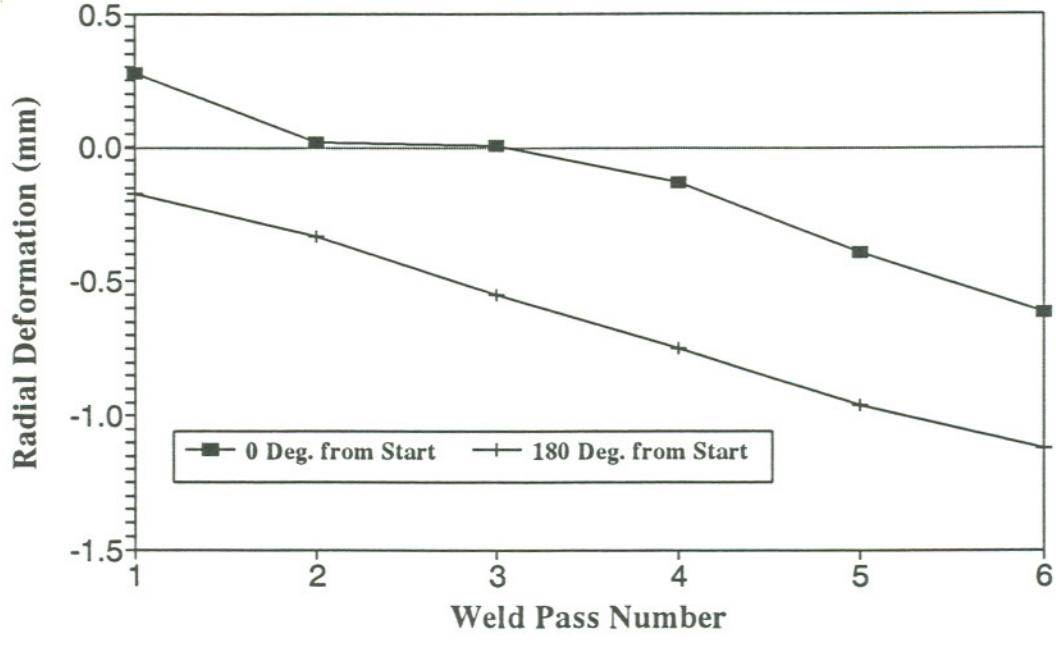

Figure 104. Radial Deformations at 19.05 mm below WCL as a Function of Weld Pass Number

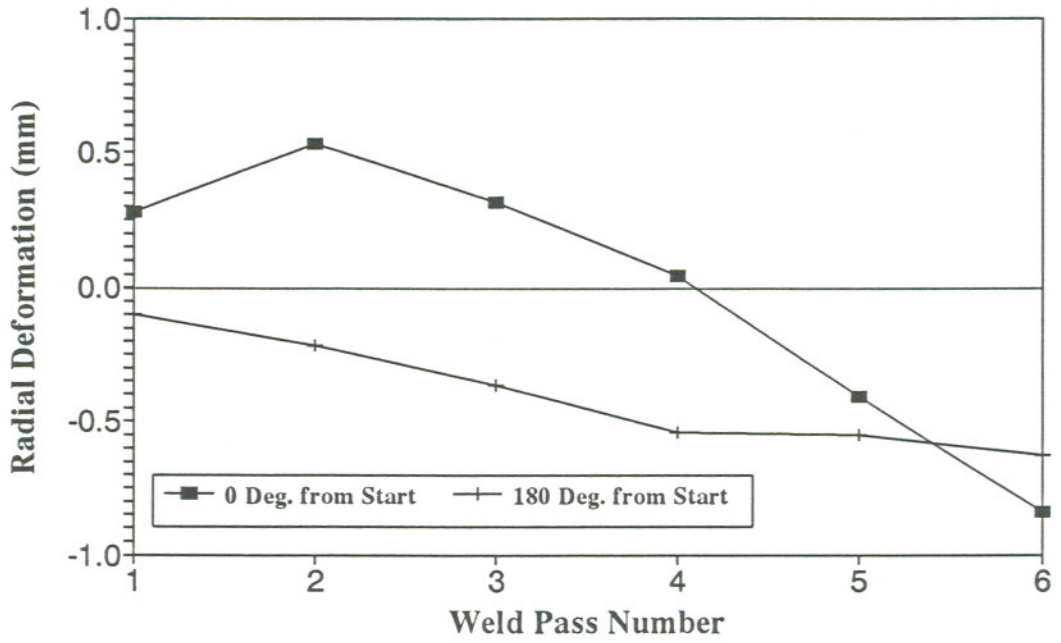

Figure 105. Radial Deformations at 38.1 mm below WCL as a Function of Weld Pass Number

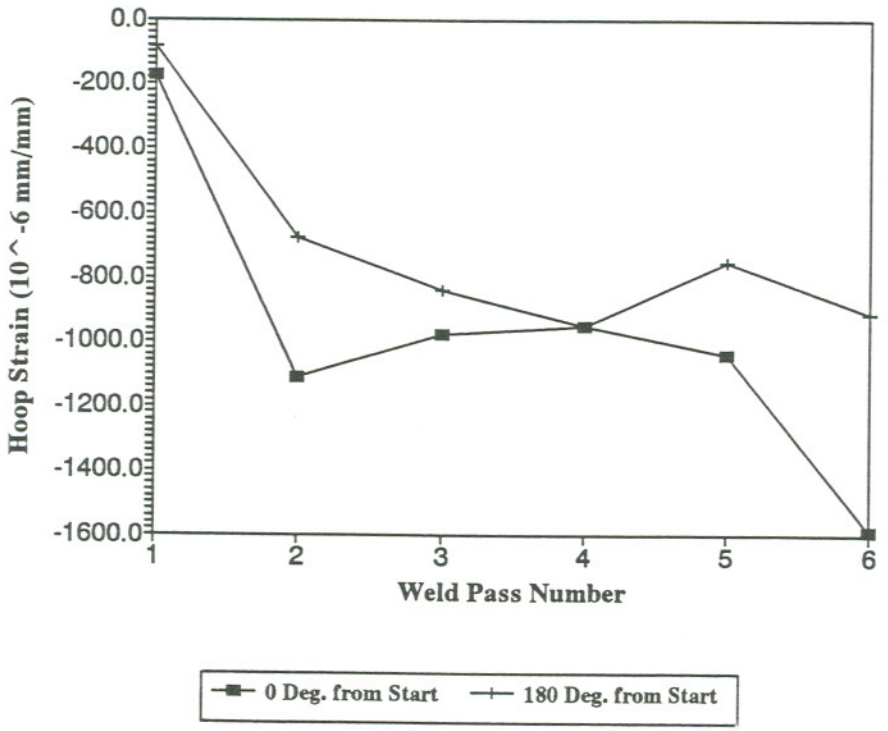

Figure 106. Hoop Strains at 38.1 mm above WCL as a Function of Weld Pass Number

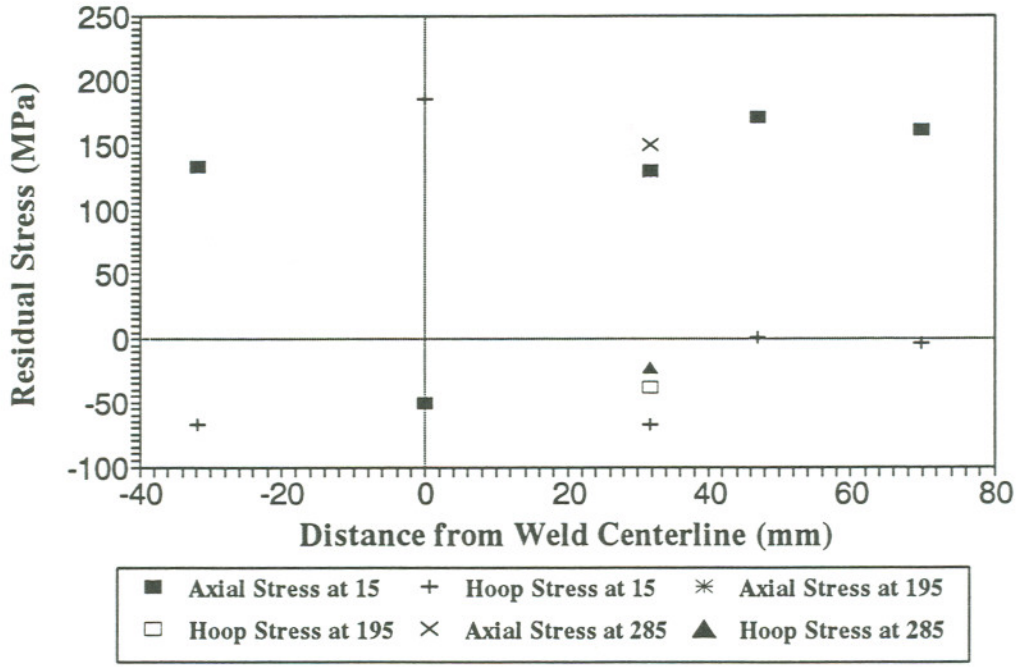

Figure 107. Residual Stresses Measured on OGI Weldment

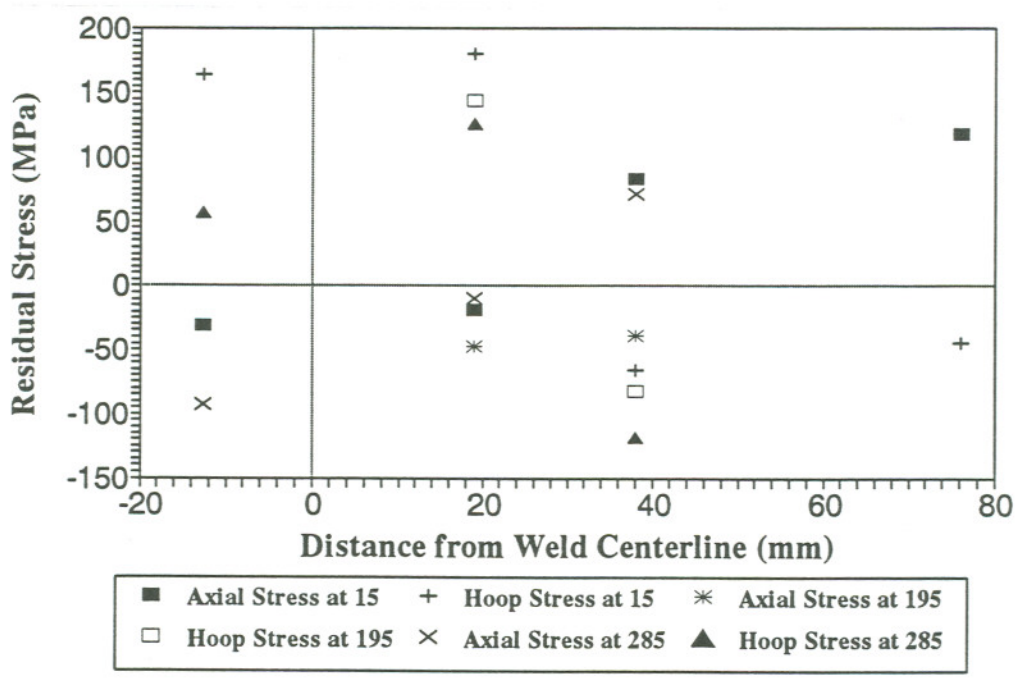

Figure 108. Residual Stresses Measured on Four-Pass Weldment

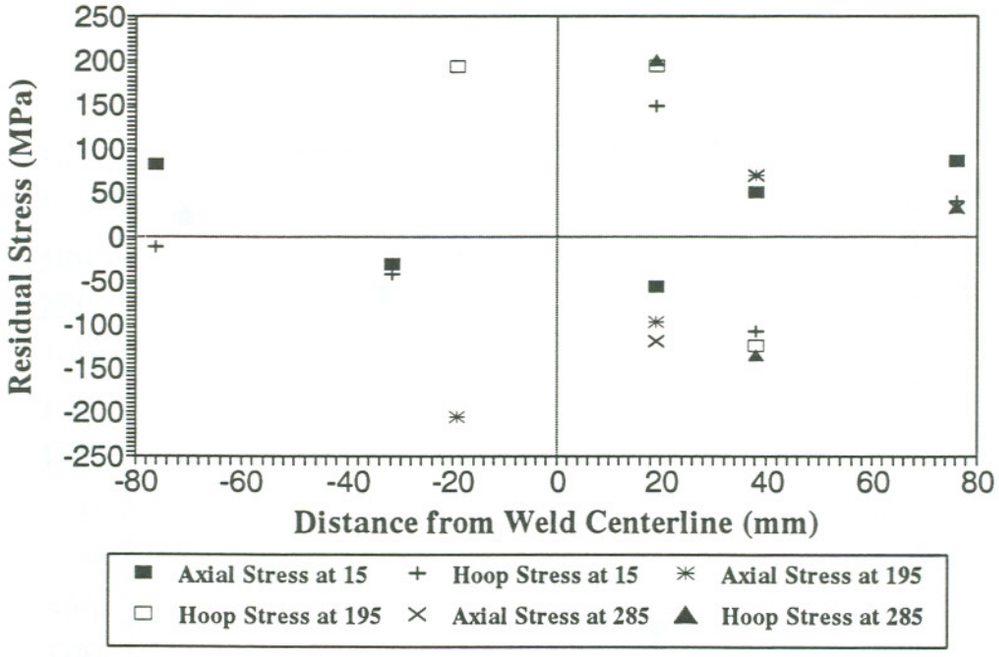

Figure 109. Residual Stresses Measured on Six-Pass Weldment

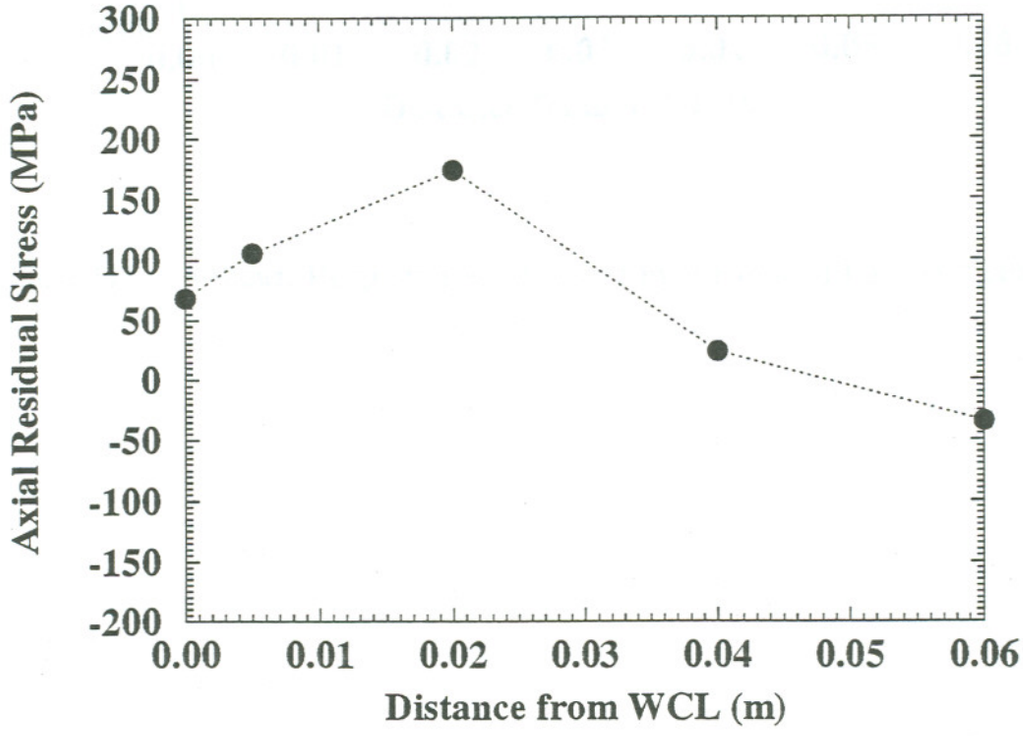

Figure 110. Residual Axial Stresses Measured by Neutron Diffraction Method

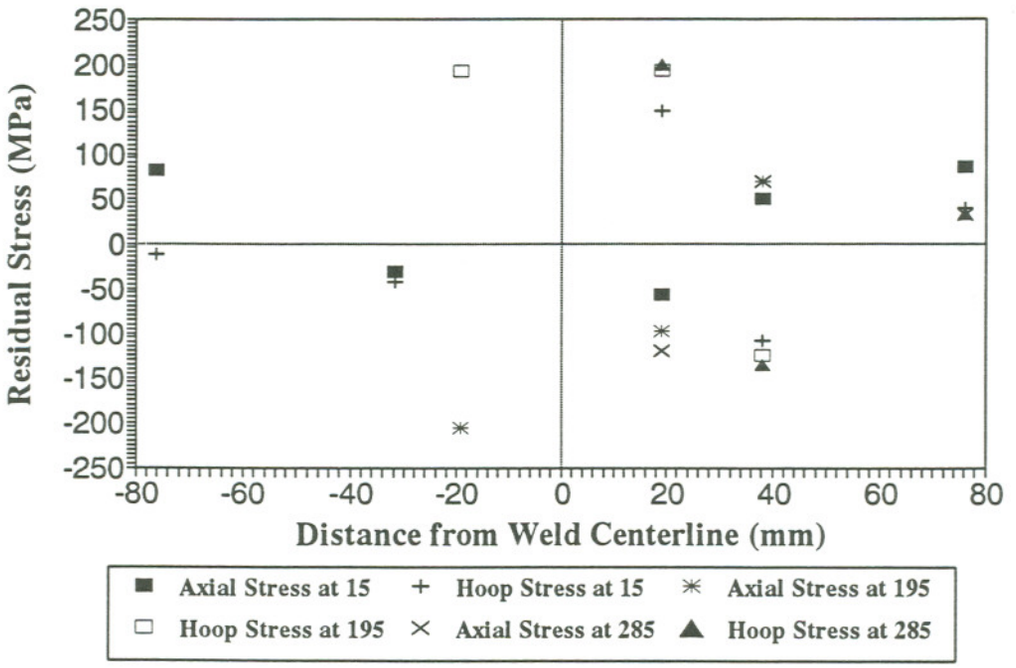

Figure 109. Residual Stresses Measured on Six-Pass Weldment

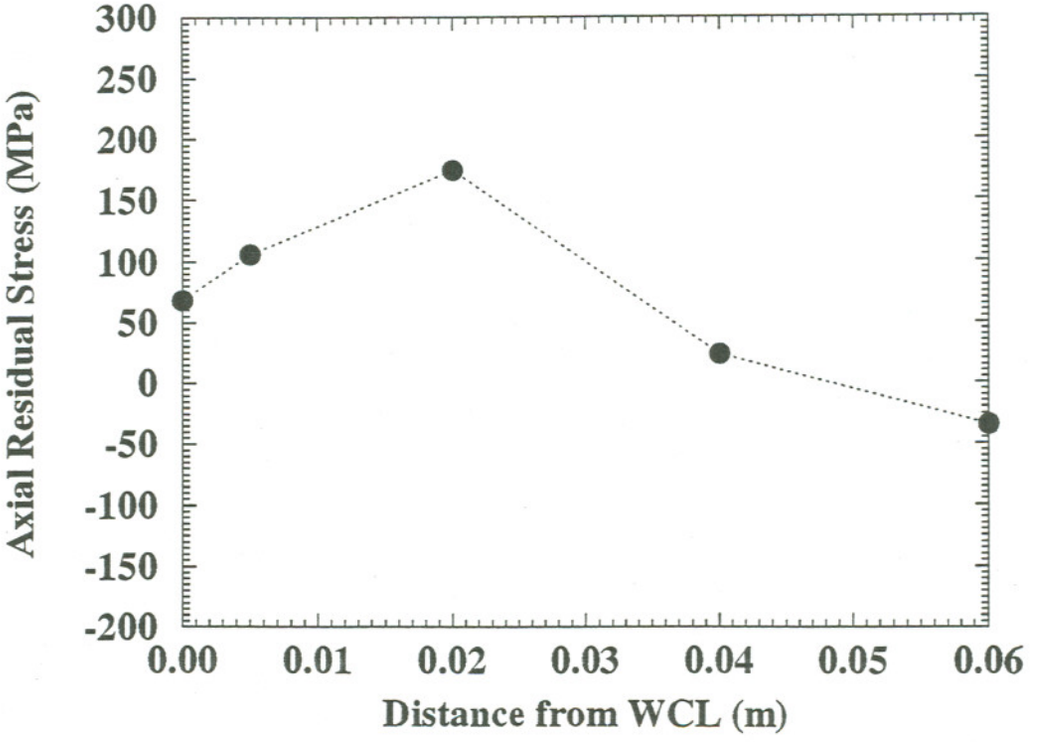

Figure 110. Residual Axial Stresses Measured by Neutron Diffraction Method

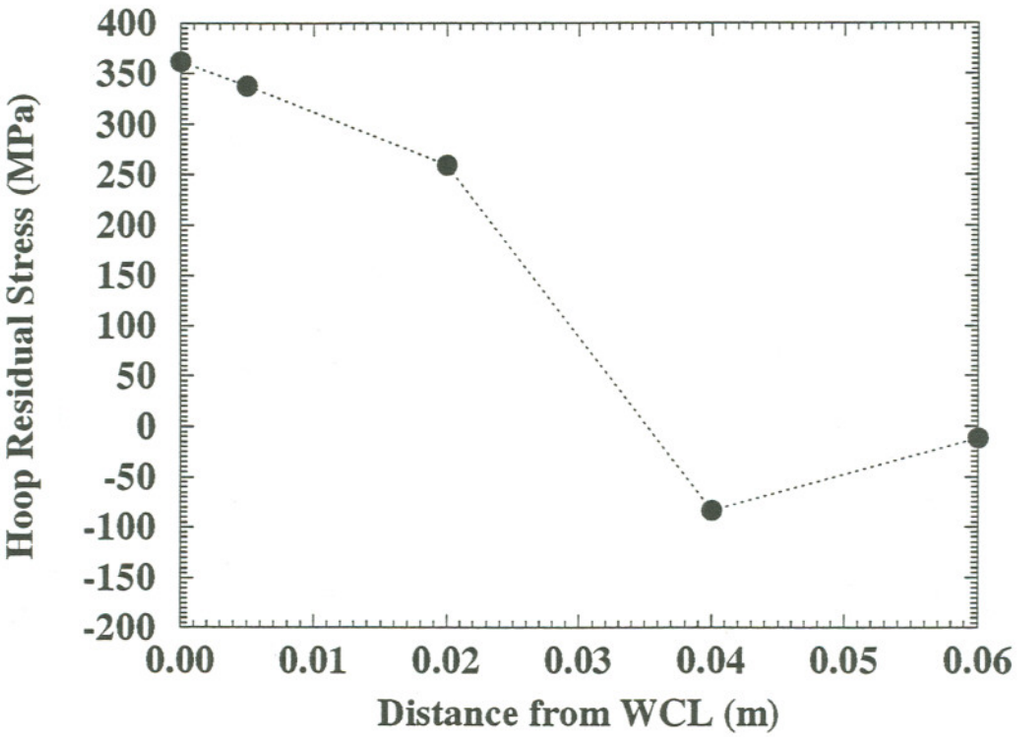

Figure 111. Residual Hoop Stresses Measured by Neutron Diffraction Method

CHAPTER 6
NUMERICAL RESULTS

3D MODELING OF THE NARROW GAP WELDING PROCESS

The narrow gap welding process is analyzed by using 3D finite element modeling technique. The reasons to model the narrow gap welding process instead of the other welding processes are: 1). the narrow gap welding process involved the least welding passes; 2). the narrow gap weldment was welded continuously with one start-stop position; 3). the weld beads in the narrow gap weldment were placed symmetrically in the middle of the groove, it is possible to only model half pipe section instead of the whole pipe. The 3D finite element model of this narrow gap welding process consists of two sequential parts, thermal analysis and stress analysis.

Thermal Analysis

This thermal analysis is a transit heat conduction analysis. The finite element code, finite element mesh generation, material thermal properties, boundary condition of the model, modeling considerations for filler metal addition and moving heat source, thermal loads of the model, and the weld heat flux distribution parameters have been discussed in numerical procedure section of this thesis. They will not be repeated again.

As stated before, use of a heat conduction code to model the complete weld pool physics provides only a crude approximation of the actual heat transfer solution. In addition, the assumed heat flux profiles for the arc are not a true representation of the gas tungsten arc physics. As a result, "tuning" of the heat conduction thermal model is necessary in this study.

This "tuning" of the thermal solution was done by using experimental data to baseline the numerical calculations. It was accomplished by bringing the calculated temperature histories into agreement with the temperature histories measured by the thermocouples at 6.35 mm from WCL during the narrow gap pipe welding process. The "free" parameters in the thermal model, which included the spatial distribution of the heat source, the vaporization efficiency under the arc, and liquid thermal conductivity, were adjusted to fit the numerical results to the experimental data. This"tuning" process takes several iterations to reach the final results which will be presented in the following section.

The calculated peak temperatures at 6.35 mm from WCL and different weld passes as a function of azimuthal position from welding start are illustrated in Figure 112. From this plot, the effect of the welding start-stop on the peak temperatures, or the effect of pass-by-pass weld heat input adjustment, is clearly noted at the area around 0° from the welding start. The peak temperatures are, in general, axisymmetrically distributed around the pipe, the exception is at area closed to 0° from the welding start for the first three welding passes. These observations are in agreement with what was noticed from the experimental data.

Figure 113 shows the typical comparison between the calculated and experimentally measured temperature histories at 6.35 mm from WCL and different azimuthal positions. These temperature histories can be represented by the peak temperatures which are exhibited in Figure 114, 115, 116, and 117 for pass 1, 2, 3, and 4, respectively. As indicated by these figures, the correlation between the experimental and numerical results, in general, is satisfactory. The differences between the experimental and numerical results are mainly due to factors which are hard to control under present conditions. These factors are: 1). the numerical model used the preset parameters in Table 6, however, the weld heat input was not constant during a given pass, this required the dynamic recording of heat input parameters during welding which was not done in the experiment; 2). knowledge of thermocouple placement was not

accurately enough, thus it is impossible to precisely match node locations (where temperatures were calculated) with thermocouple locations (where temperatures were measured) for all thermocouples; 3). in order to save computing time, only half pipe section was modeled, in realty, there exists temperature differences between the comparable positions above and below WCL due to the chimney effect; 4). it took about one month under current computing condition to run a complete thermal analysis, this limits the number of iterations to fine tuning the thermal model. However, the numerical thermal results presented here represent the best efforts which can be achieved under current computing condition.

The sole purpose of adjusting the free parameters in the thermal solution was to provide a means of depositing the GTA weld energy in the pipe in approximately the right place at the right time. Once this was accomplished, the ability of the numerical model to predict the residual stress distribution in the as-welded pipe could be assessed. Calculations of the thermal stresses generated during and after welding were made without further parametric adjustments.

Stress Analysis

This stress analysis is a static nonlinear thermal stress analysis. The finite element mesh is the same mesh generated in thermal analysis. The material mechanical properties, boundary condition of the model, load condition of the model have been reported before and will not be presented here again. In order to save space, only the results from last load step was stored in the computer, thus the results reported here will be the final residual stress results or the room temperature residual stress results. As stated before, the area of most concern in this narrow gap weldment is the area at pipe inner surface and adjacent to the weld. On the surface, the two principal stress components are axial and hoop stress. The calculated residual axial and hoop stresses on the pipe inner surface will be presented in the following section.

The inner surface axial and hoop residual stresses, as a function of distance from WCL, at 0°, 15°, 45°, 90°, 135°, 180°, and 270°, are shown in Figure 118, 119, 120, 121, 122, 123, and 124, respectively. Basically, these figures show same trends. They are: 1). the axial residual stress is always tensile while the hoop residual stress changes from tensile at the position near WCL to compressive at the position far from WCL, the transition from tensile to compressive occurs at about 30 mm from WCL; 2). the tensile axial residual stress is always larger than the tensile hoop residual stress; 3). the maximum tensile axial and hoop residual stress are at place very close to WCL, but not at the WCL. The area with both tensile residual axial and hoop stress is about 30 mm from WCL at each side. This is the area of most concern. In this model, the boundary condition at the end of the pipe was intentionally set as rigid condition due to computational difficulty if it were set as free boundary condition. This explains why there exist certain value of residual axial and hoop stress at the end of the pipe. This boundary condition is certainly not true but it will not substantially change the residual stress profile at area close to WCL.

The residual axial and hoop stress at pipe inner surface and 6.35 mm from WCL as a function of azimuthal position from the welding start is exhibited in Figure 125. Basically, the distribution of the axial and hoop residual stress at pipe inner surface is axisymmetric with the exception at the area around welding start. This is consistent with the distribution of the peak temperatures from thermal analysis model.

Another major concern in this research is the residual stress distribution through pipe wall thickness, especially at inner sub-surface where the distribution of residual stress will influence the crack propagation if cracking does occur at pipe inner surface. In other words, the amount (or the percentage) of pipe wall thickness which is under tensile residual stresses is what concerned here. The pipe thickness residual stress distributions at 0, 1.59, 3.18, 6.35, 19.05, and 38.1 mm from WCL are illustrated in Figure 126, 127, 128, 129, 130, and 131, respectively. The trends noted from these figures are: 1). the residual hoop stress is basically tensile all way through the pipe

thickness for distance up to 19.05 mm from WCL, while the residual hoop stress is all compressive in the pipe thickness at 38.1 mm from WCL; 2). the residual axial stress is tensile for most of the pipe thickness, especially at about 5 mm from inner surface, the compressive stress may distribute in the middle or outer section of the thickness, the axial residual stress is all tensile in the pipe thickness at 38.1 mm from WCL; 3). the axial residual stress is almost always at its maximum on pipe inner surface; 4). the radial residual stress is not very significant through the pipe thickness, except at WCL.

2D MODELING OF THE NARROW GAP WELDING AND CSI PROCESSES

As stated before, the purpose of this numerical study is to model the newly proposed post-weld stress mitigation treatment - Cooling Stress Improvement (CSI). This model requires the knowledge of the post-weld residual stress distribution in pipe weldment prior to application of the CSI treatment. Hence, modeling of the welding process is necessary before starting the numerical study of the CSI process. The CSI process is, in nature, an axisymmetric process. Thus, a 2D axisymmetric finite element model was established in this work to study the thermal and stress development during welding and CSI of 406-mm-diameter, Type 304L stainless steel (SS), schedule 40 (12.7 mm thickness) pipe. The actual experimental pipe weld that was modeled has a narrow gap groove joint configuration and was welded in four continuous/symmetric passes. Due to the symmetric placement of the weld beads, only half pipe section is modeled in this study. This model consists of four sequential parts. They are: 1) thermal analysis for welding process, 2). thermal analysis for CSI process, 3). stress analysis for welding process, and 4). stress analysis for CSI process. The results of this model will be presented in the following sections.

Thermal Analysis for Welding Process

This thermal analysis is a transit heat conduction analysis. The finite element code, finite element mesh generation, material thermal properties, boundary condition of the model, modeling considerations for filler metal addition, thermal loads of the model, and the weld heat flux distribution parameters have been presented before. They will not be discussed again.

As stated before, use of a heat conduction code to model the complete weld pool physics provides only a crude approximation of the actual heat transfer solution. In addition, the assumed heat flux profiles for the arc are not a true representation of the gas tungsten arc physics. As a result, "tuning" of the heat conduction thermal model is necessary in this study.

This "tuning" of the thermal solution was done by using experimental data to baseline the numerical calculations. It was accomplished by bringing the calculated temperature histories into agreement with the temperature histories measured by the thermocouple at 9.525 mm from WCL during the narrow gap pipe welding process. The "free" parameters in the thermal model, which included the spatial distribution of the heat source, the vaporization efficiency under the arc, and liquid thermal conductivity, were adjusted to fit the numerical results to the experimental data. This"tuning" process takes several iterations to reach the final result.

The comparison between calculated and measured temperature history at 9.525 mm from WCL is shown in Figure 132. As indicated by this plot, the correlation is excellent. This means that the GTA weld energy was deposited in the pipe in approximately the right place at the right time. Once this was accomplished, there were no further parametric adjustments during subsequent thermal and stress analyses.

Thermal Analysis for CSI Process

Again, this thermal analysis is a transient heat conduction analysis. Same boundary conditions, mesh, and material thermal properties used in welding analysis are employed here.

Figure 133 shows the cooling cycle of a post-weld CSI treatment at 9.525 mm from WCL and the pipe inner surface. This cooling cycle consists of three steps. The first step involves the rapid or forced cooling from room temperature to liquid nitrogen temperature (77 K). The second step involves holding at 77 K for certain amount of time. The last step is the natural convection step in which the temperature is gradually changed from 77 K to room temperature equilibrium. This cooling cycle was imposed on the inner surface of the pipe weldment for a length of 38 mm from WCL. The temperature distribution along the pipe outer and inner surface during the cooling cycle of a post-weld CSI treatment can be seen in Figure 134. A length of 50 mm from WCL on the pipe outer surface was kept at temperature of 323 K for certain amount of time during CSI process. The temperature difference between the pipe outer surface (323 K) and inner surface (77 K) around the WCL is the key to applying the CSI technique. Maintaining this temperature difference for a finite time (6 minute here) would eventually change the stress state upon reaching room temperature equilibrium.

Stress Analysis for Welding Process

This stress analysis is a static structural analysis. Same mesh generated in thermal analysis is used here. The material mechanical properties, model boundary conditions, and load conditions have been reported before. They will not be repeated here.

The residual axial and hoop stress distribution along the pipe inner surface is shown in Figure 135. Basically, the residual axial and hoop stress on the pipe inner

surface share the same trend in which the stress is rapidly changed from tensile to compressive as the distance from WCL increases. At end of the pipe, both stresses reach very small stead-state values as required by the free boundary condition. The area with tensile axial residual stress is about 8 mm from WCL while the area with tensile hoop stress is about 18 mm. Tensile residual axial and hoop stress peaks exist at position very close to WCL (about 1 mm from WCL for residual axial stress and 3 mm from WCL for residual hoop stress) and the axial peak is larger than the hoop peak.

Figure 136 and 137 shows the residual axial and hoop stress distribution at pipe cross section, respective. The area with gray color in the plots is under compressive stress while the area with no color is under tensile stress. The residual stress distribution at pipe cross section area close to WCL and inner surface is of the greatest concern. It is interesting to note that only a very small portion of inner surface and inner sub-surface, which is essentially around the WCL, is under tensile axial stress. The residual tensile hoop stress is distributed all the way across the pipe thickness for about 18 mm from WCL.

Stress Analysis for CSI Process

Again, this stress analysis is a static structural analysis. The mesh, material mechanical properties, and boundary conditions used in previous analysis are employed here.

The axial residual stresses along the inner surface of a pipe girth weldment after welding and welding plus CSI treatment are illustrated in Figure 138. Figure 139 shows the corresponding hoop residual stresses along the inner surface of a pipe girth weldment after welding and welding plus CSI treatment. It can be seen from Figures 138 and 139 that the tensile residual stresses at the inner surface of pipe girth weldment are reversed into compressive residual stresses after CSI treatment.

The residual axial and hoop stress distribution at pipe wall section after welding

plus CSI treatment are shown in Figure 140 and 141, respectively. The effects of the CSI treatment on altering the residual stress state in the pipe wall thickness are clearly demonstrated by comparing the residual stress distribution in pipe wall thickness after welding (see Figure 136 and 137) with the stress distribution after welding plus CSI treatment. It should also be pointed out that the CSI treatment is more effective on altering the hoop stress than on altering the axial stress.

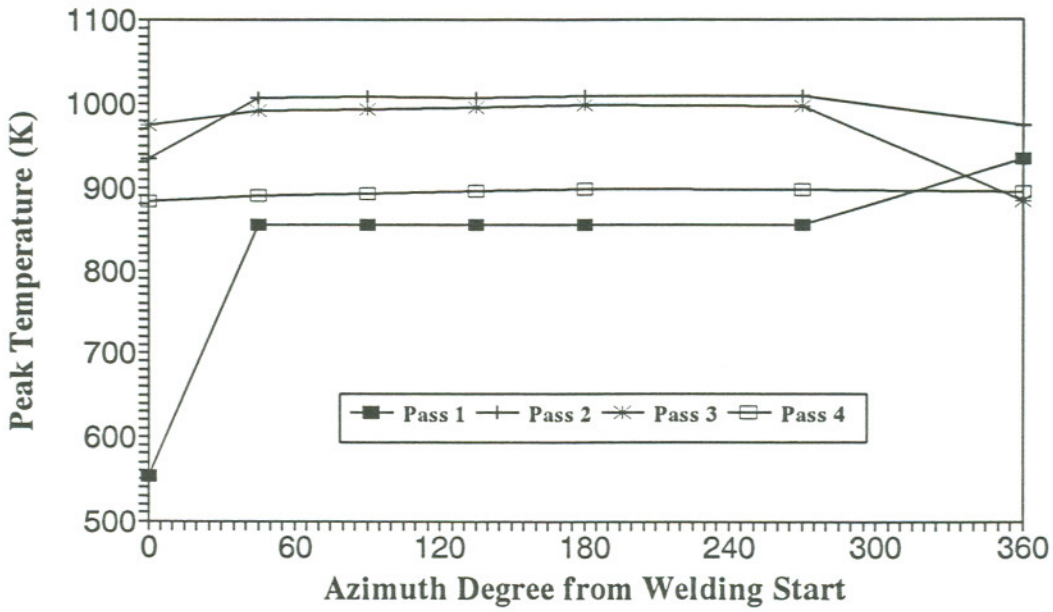

Figure 112. The Calculated Peak Temperatures at 6.35 mm from WCL

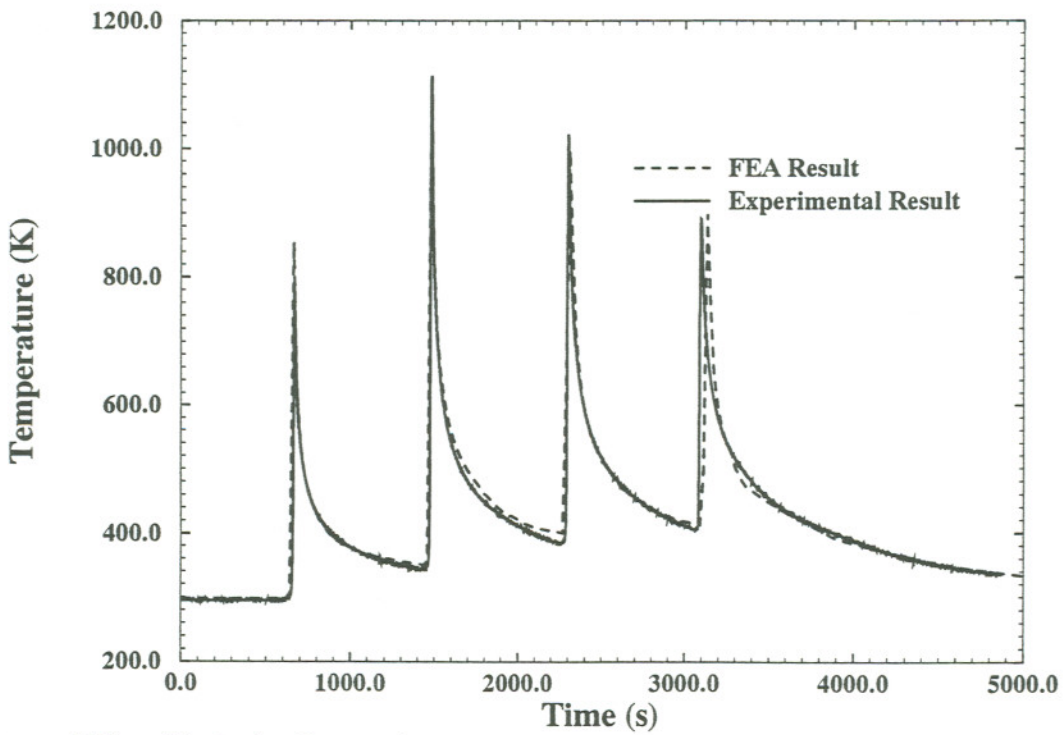

Figure 113. Typical Comparison between Calculated and Measured Thermal Histories at 6.35 mm from WCL

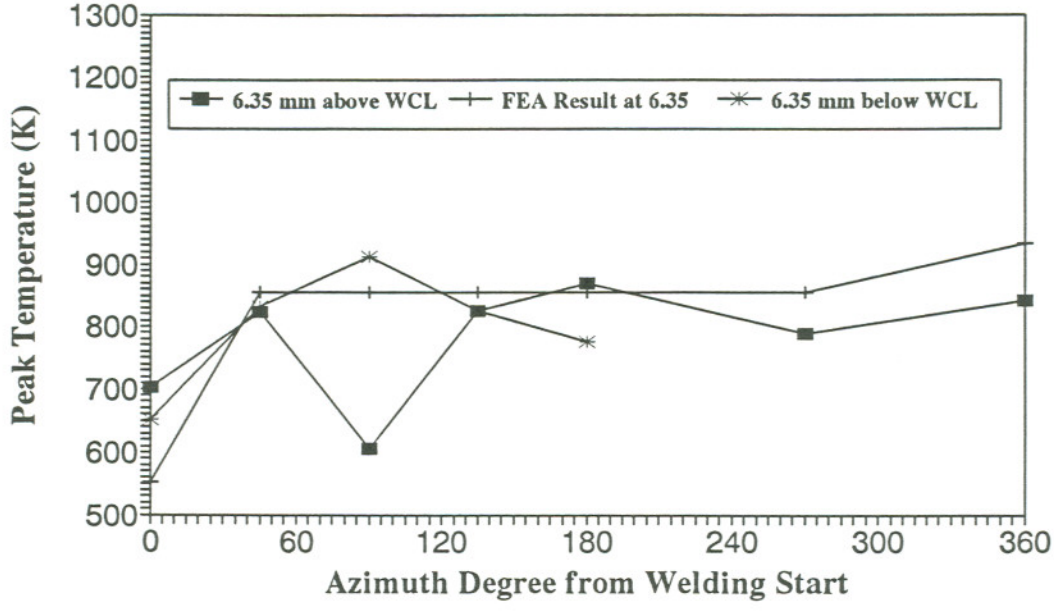

Figure 114. Comparison between Measured and Calculated Peak Temperature at Pass 1

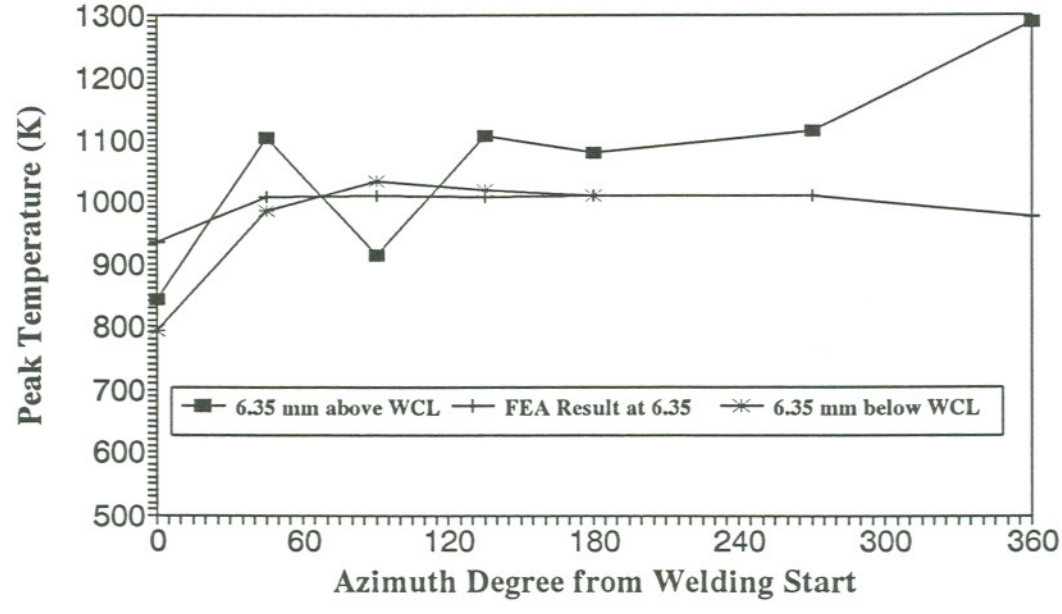

Figure 115. Comparison between Measured and Calculated Peak Temperature at Pass 2

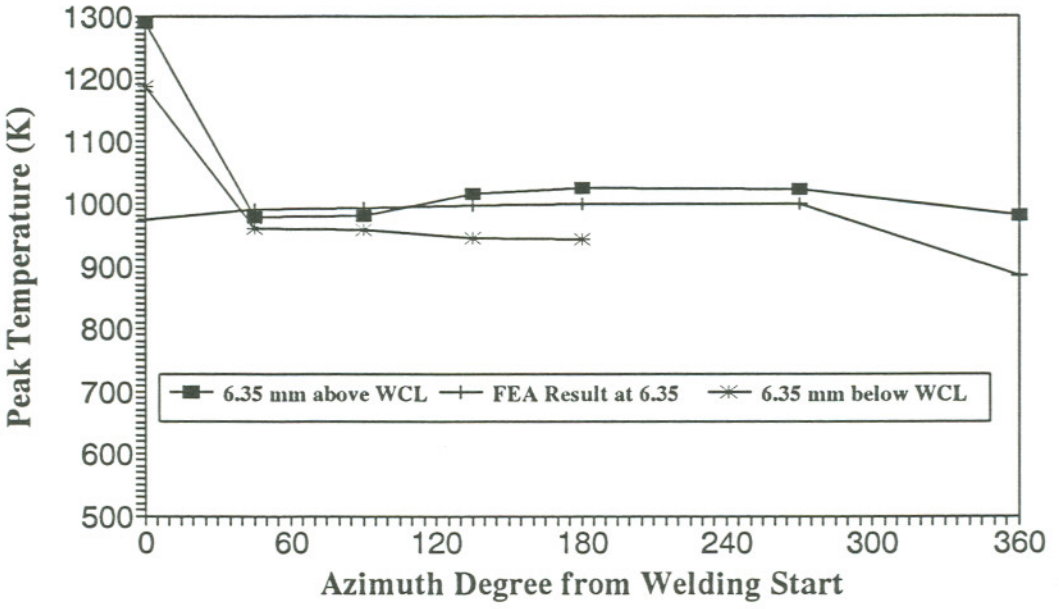

Figure 116. Comparison between Measured and Calculated Peak Temperature at Pass 3

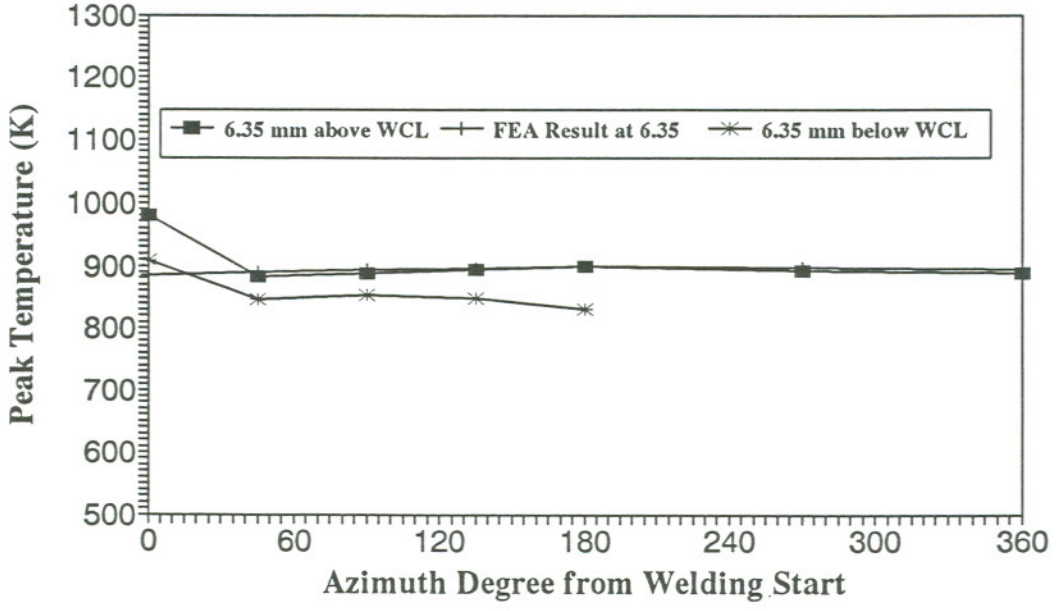

Figure 117. Comparison between Measured and Calculated Peak Temperature at Pass 4

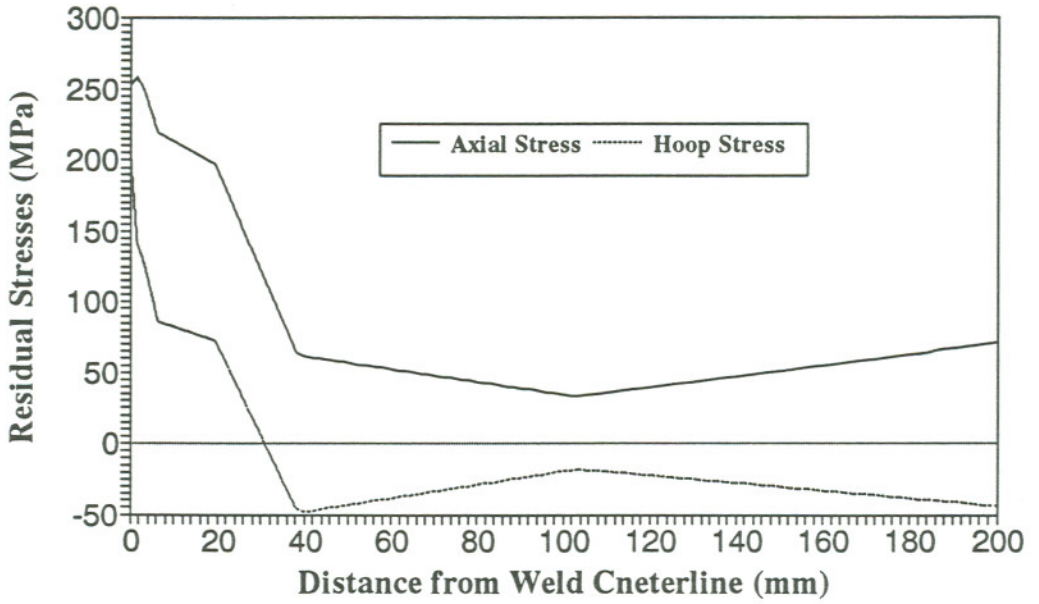

Figure 118. Inner Surface Axial and Hoop Residual Stress Distribution (Calculated) at 0° from Welding Start

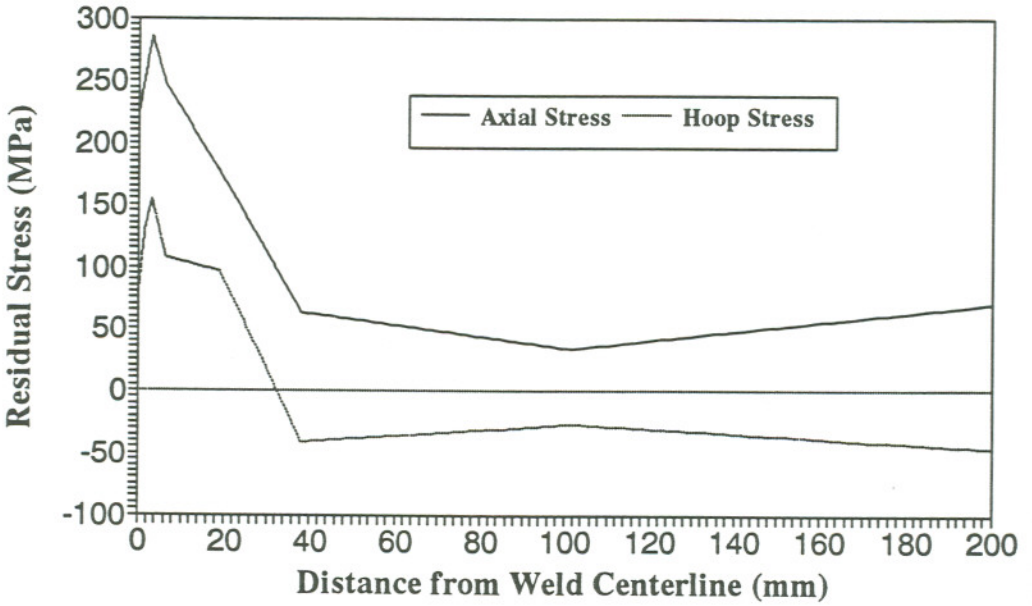

Figure 119. Inner Surface Axial and Hoop Residual Stress Distribution (Calculated) at 15° from Welding Start

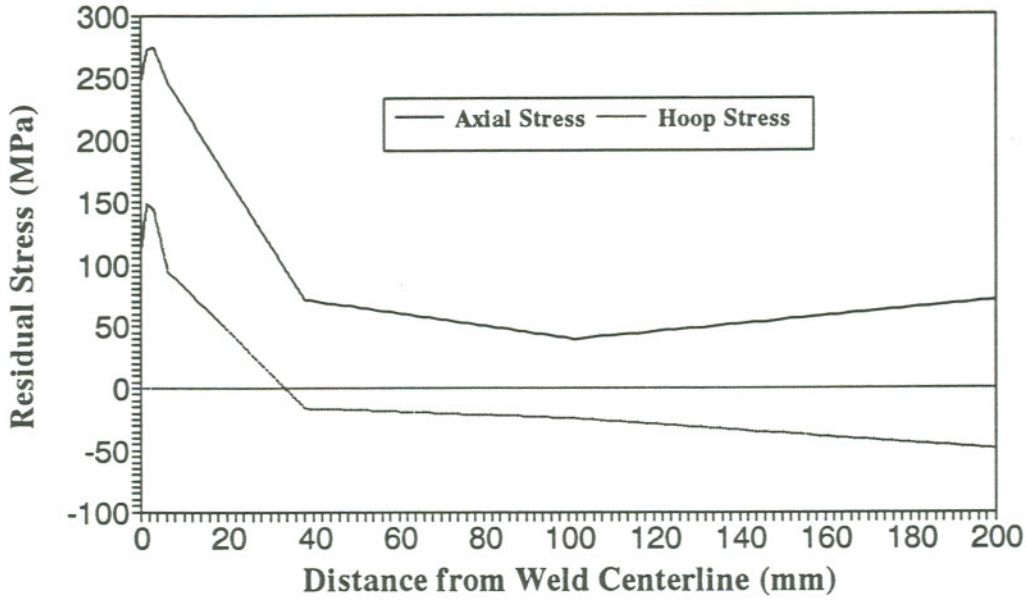

Figure 120. Inner Surface Axial and Hoop Residual Stress Distribution (Calculated) at 45° from Welding Start

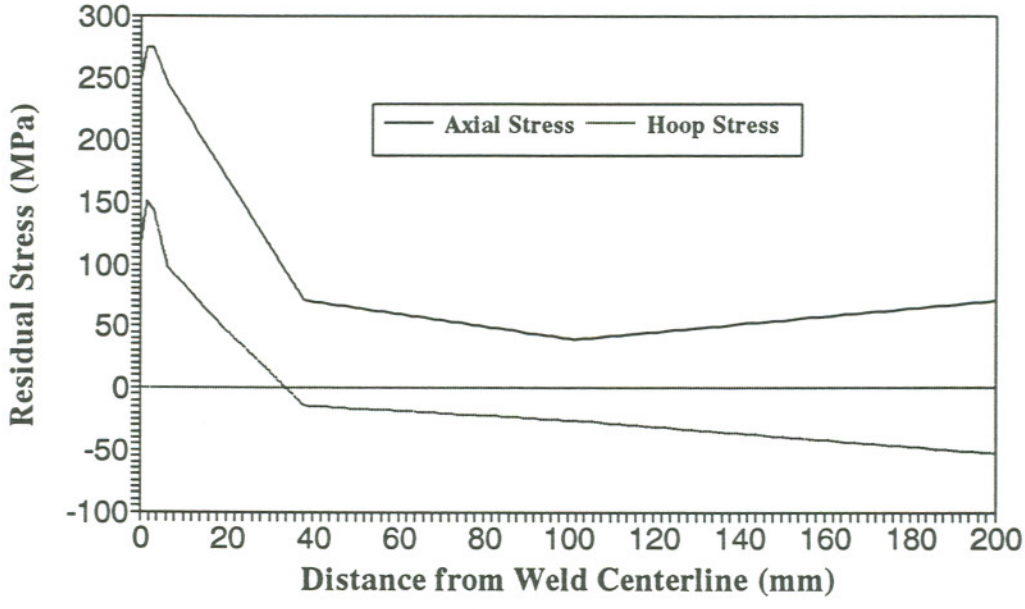

Figure 121. Inner Surface Axial and Hoop Residual Stress Distribution (Calculated) at 90° from Welding Start

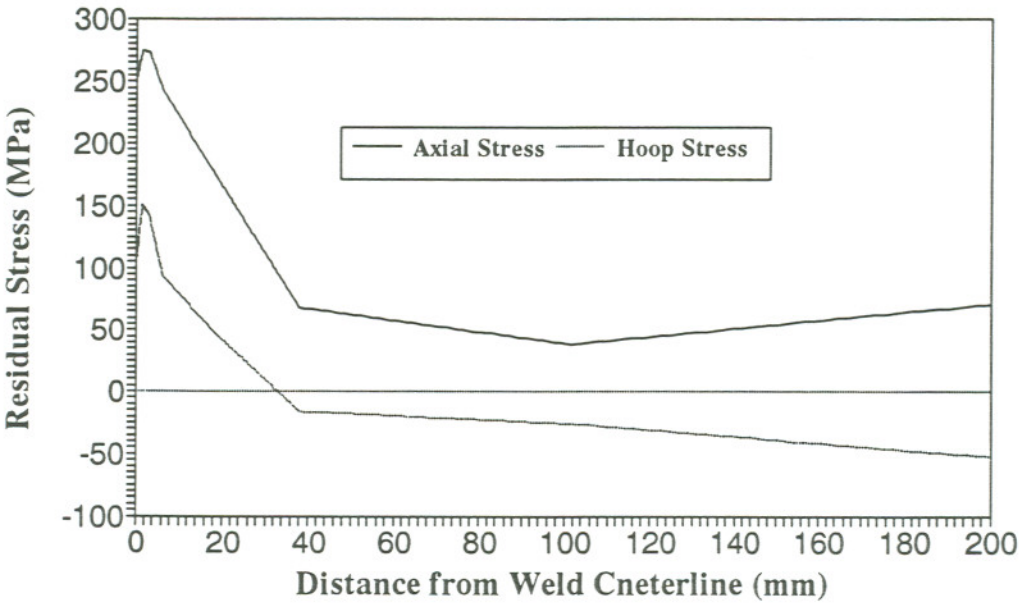

Figure 122. Inner Surface Axial and Hoop Residual Stress Distribution (Calculated) at 135° from Welding Start

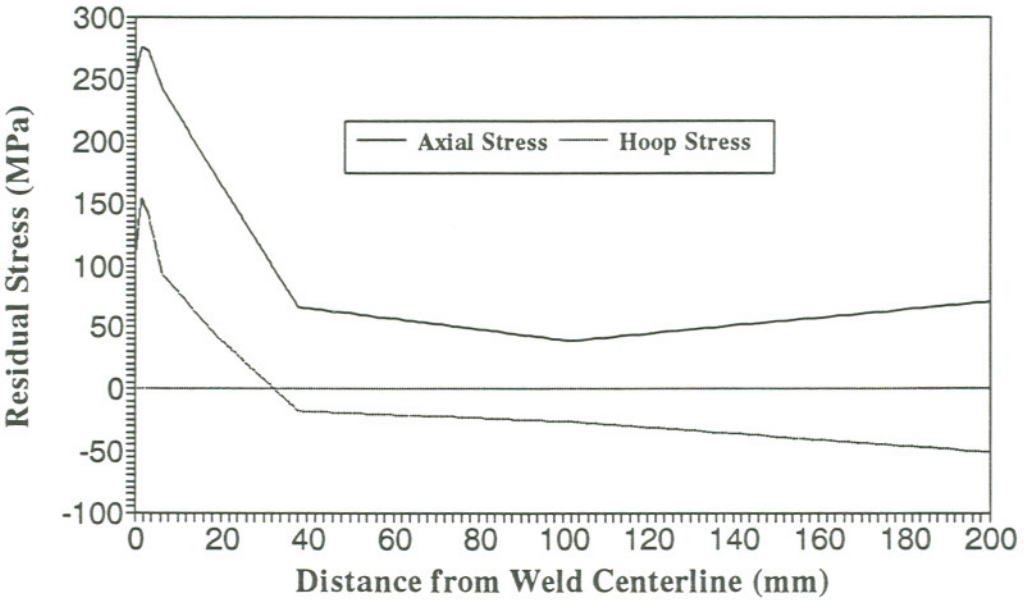

Figure 123. Inner Surface Axial and Hoop Residual Stress Distribution (Calculated) at 180° from Welding Start

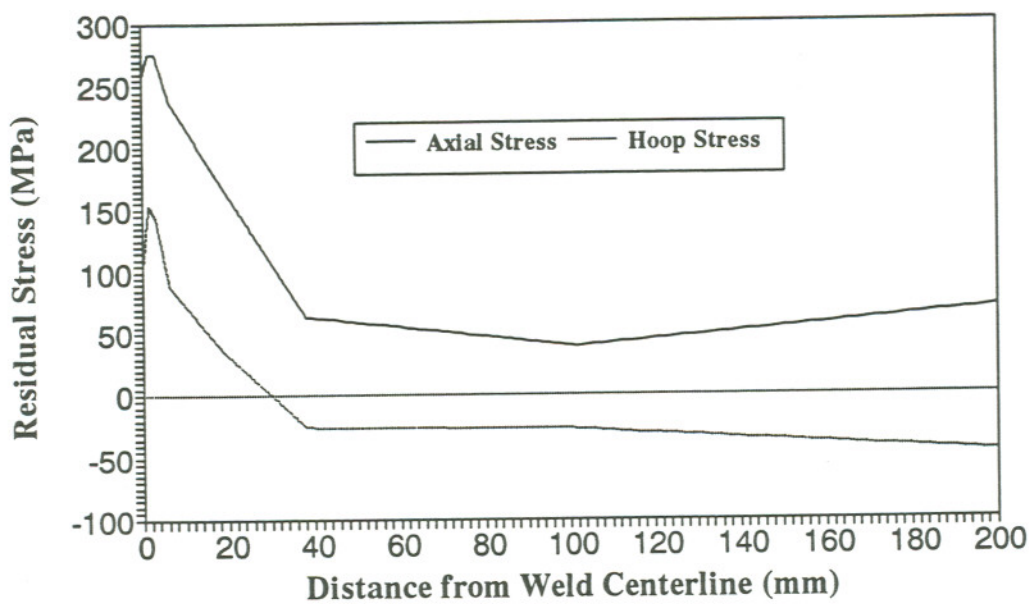

Figure 124. Inner Surface Axial and Hoop Residual Stress Distribution (Calculated) at 270° from Welding Start

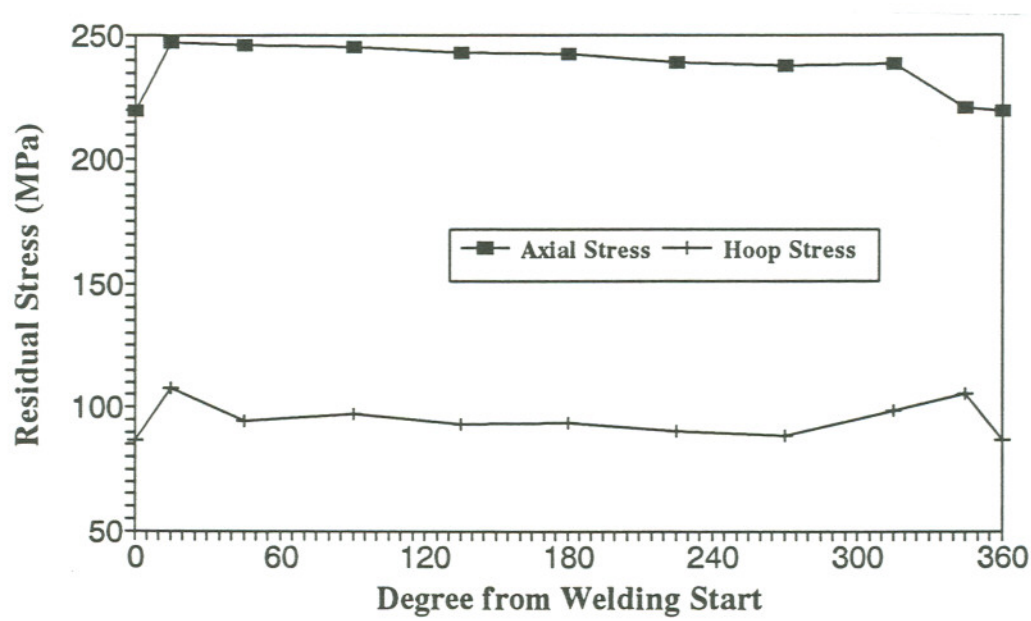

Figure 125. Residual Axial and Hoop Stress at Pipe Inner Surface and 6.35 mm from WCL as a Function of Azimuthal Position

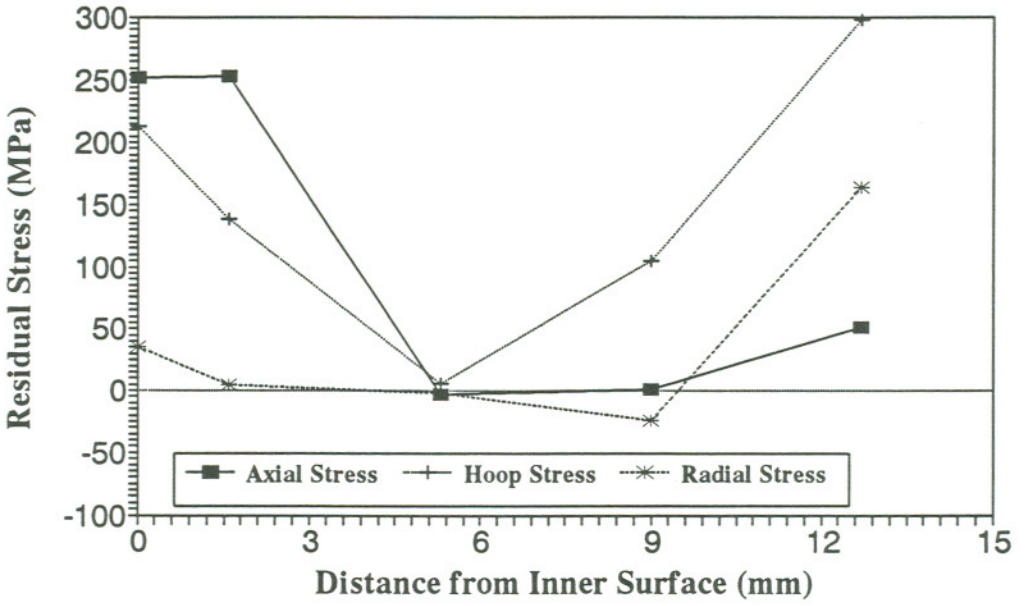

Figure 126. Residual Stress Distribution in Pipe Wall Thickness at 0 mm from WCL

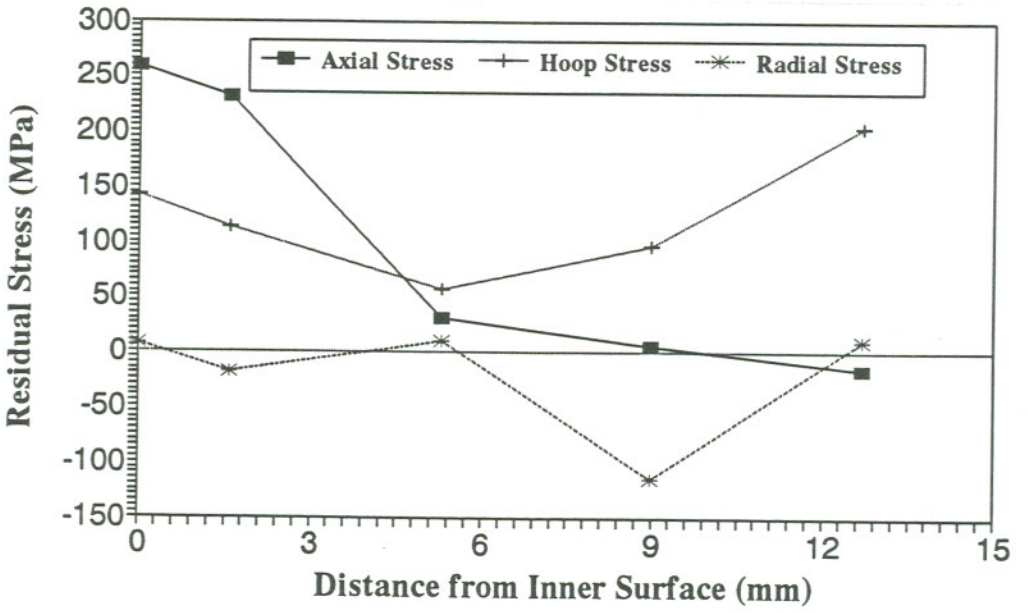

Figure 127. Residual Stress Distribution in Pipe Wall Thickness at 1.59 mm from WCL

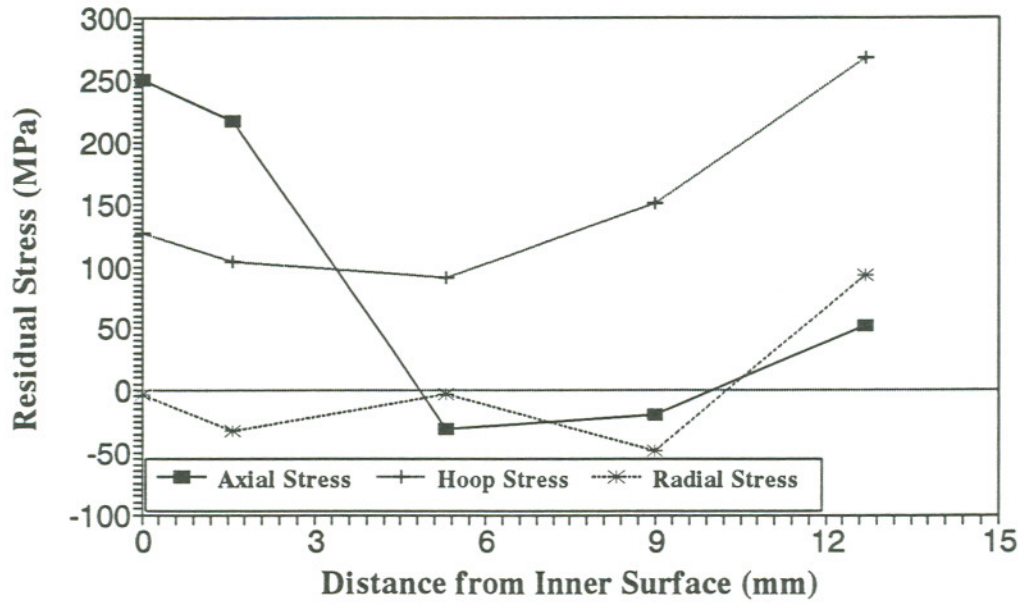

Figure 128. Residual Stress Distribution in Pipe Wall Thickness at 3.18 mm from WCL

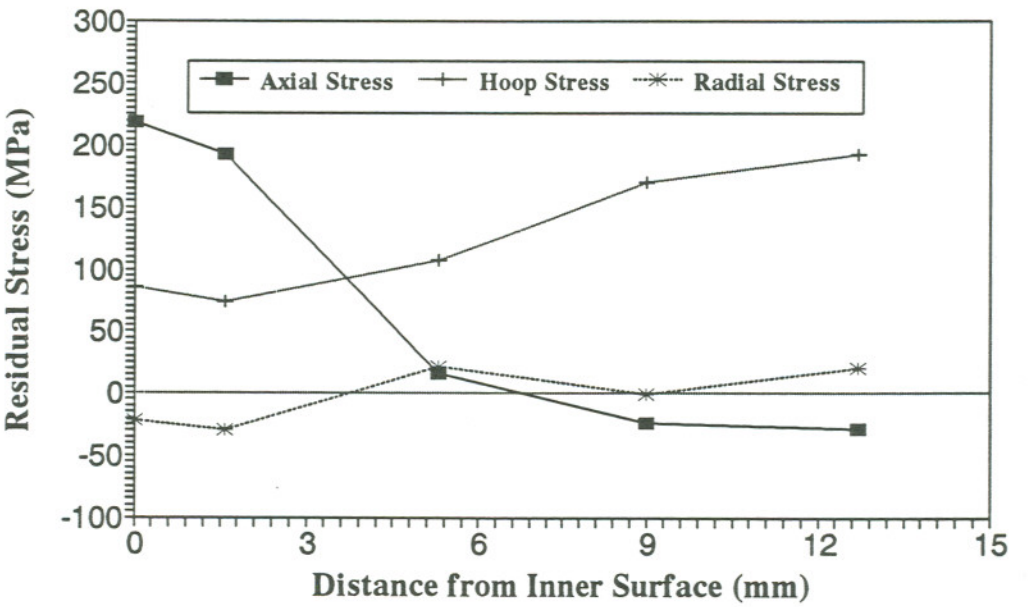

Figure 129. Residual Stress Distribution in Pipe Wall Thickness at 6.35 mm from WCL

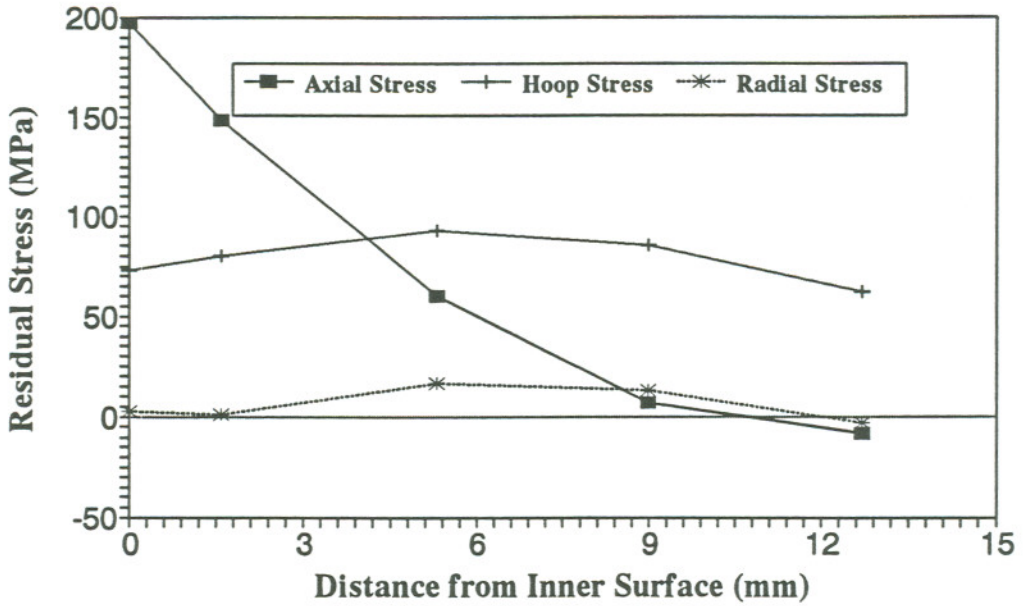

Figure 130. Residual Stress Distribution in Pipe Wall Thickness at 19.05 mm from WCL

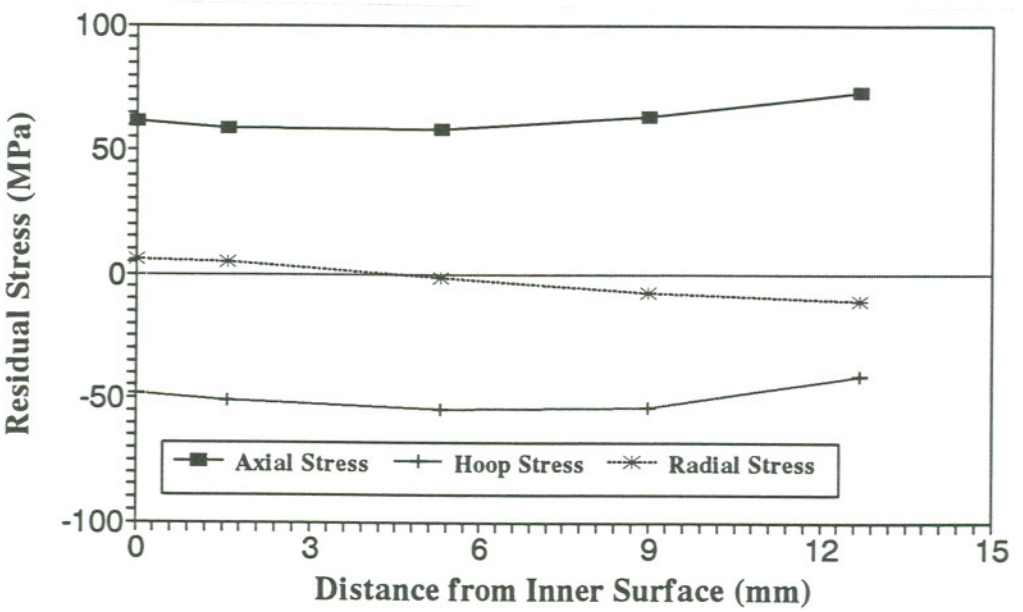

Figure 131. Residual Stress Distribution in Pipe Wall Thickness at 38.1 mm from WCL

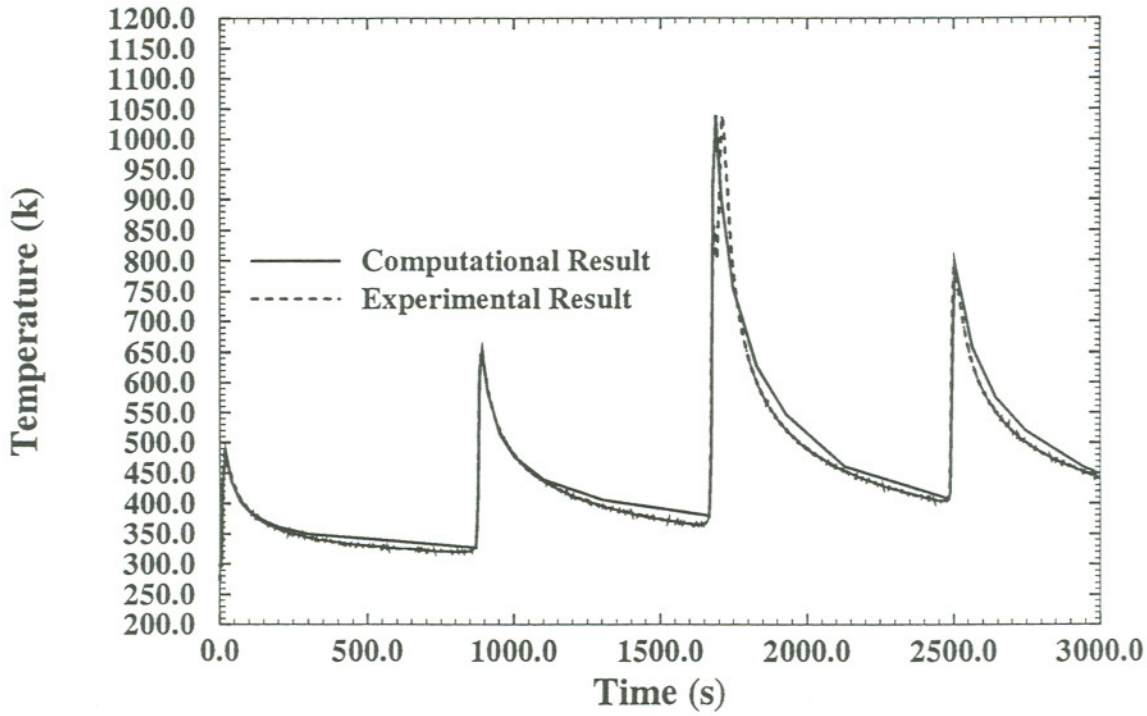

Figure 132. Comparison between Calculated and Measured Temperature History at 9.525 mm from WCL

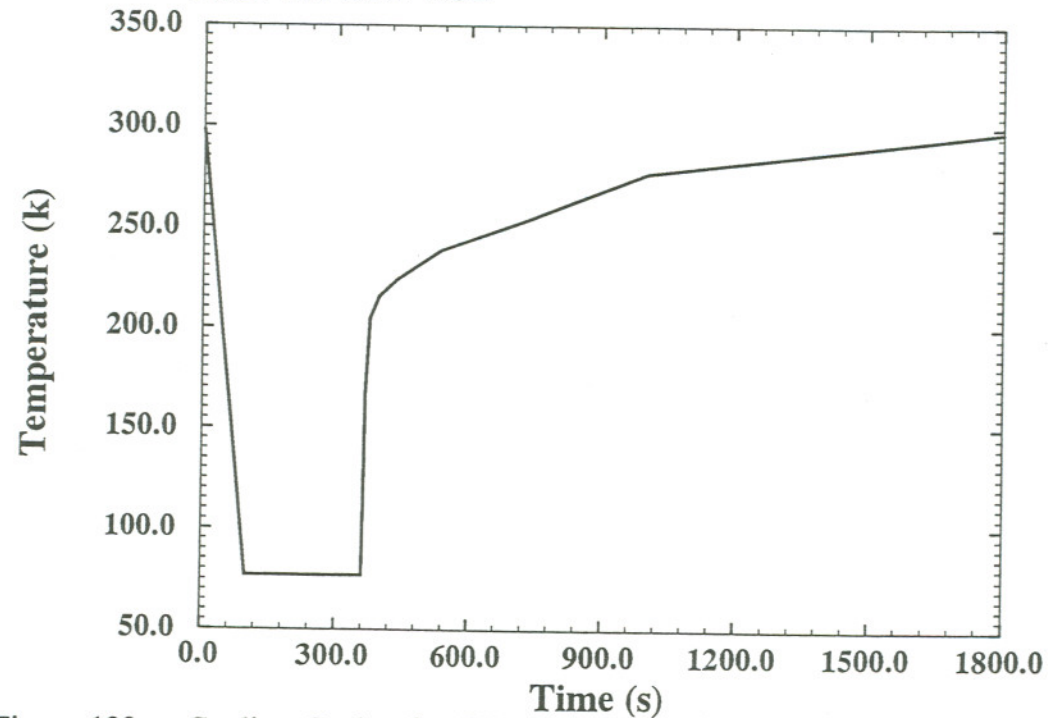

Figure 133. Cooling Cycle of a CSI Treatment at 9.525 mm from WCL and at Pipe Inner Surface

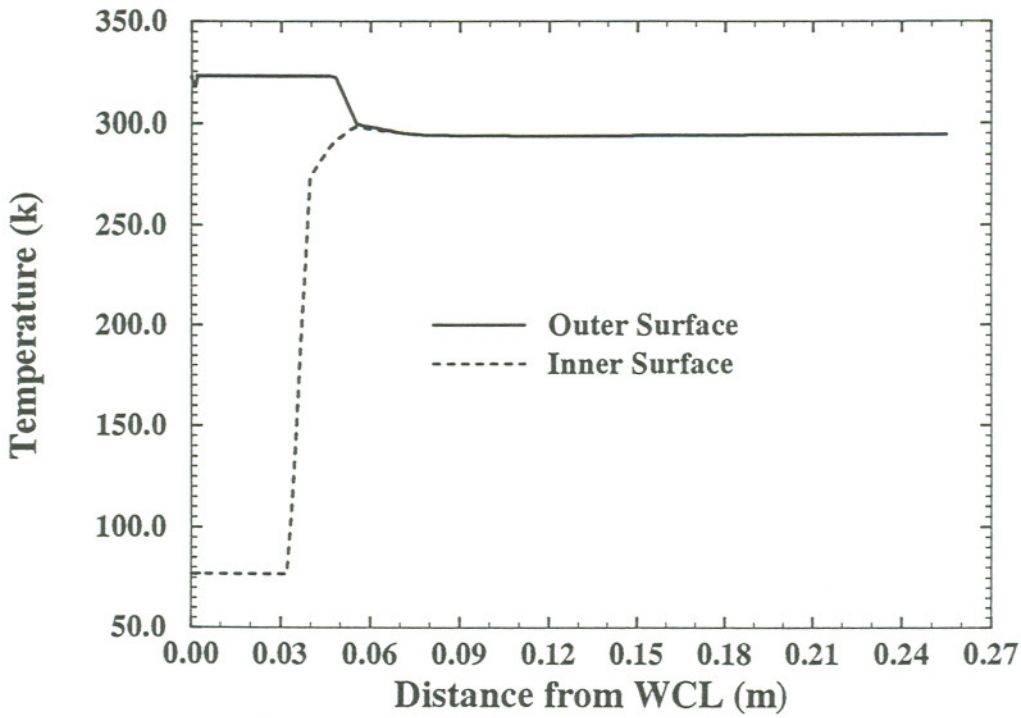

Figure 134. Temperature Distributions at Pipe Inner and Outer Surface during CSI Process

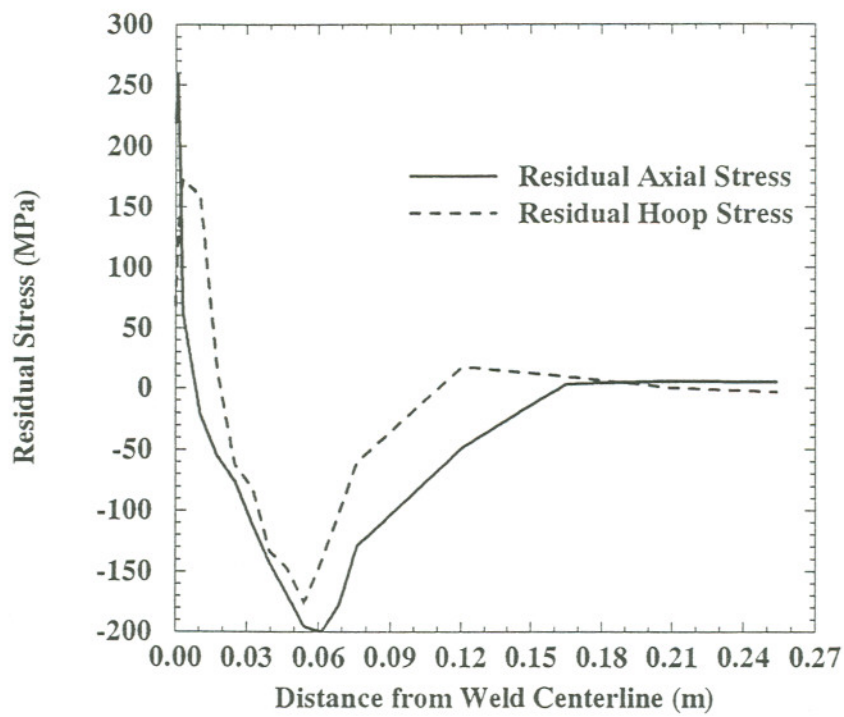

Figure 135. Welding Residual Axial and Hoop Stress Distribution at Pipe Inner Surface

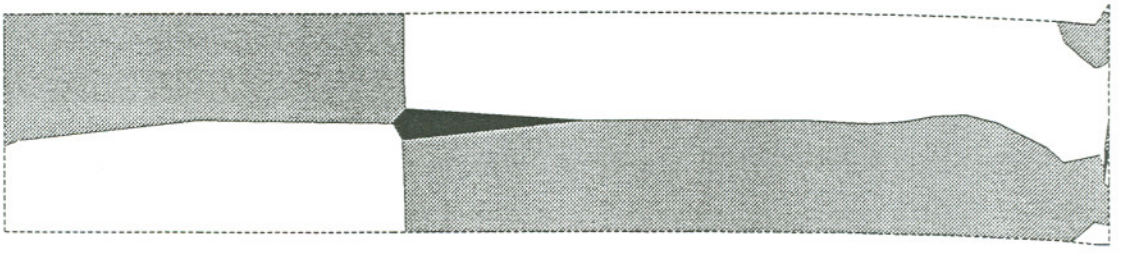

Figure 136. Welding Residual Axial Stress Distribution in Pipe Wall Section

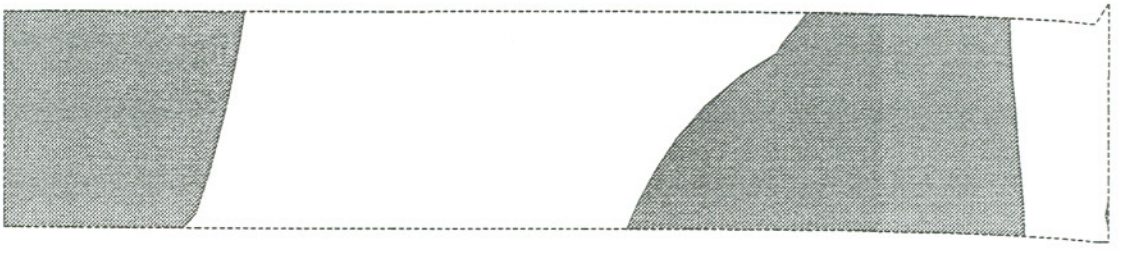

Figure 137. Welding Residual Hoop Stress Distribution in Pipe Wall Section

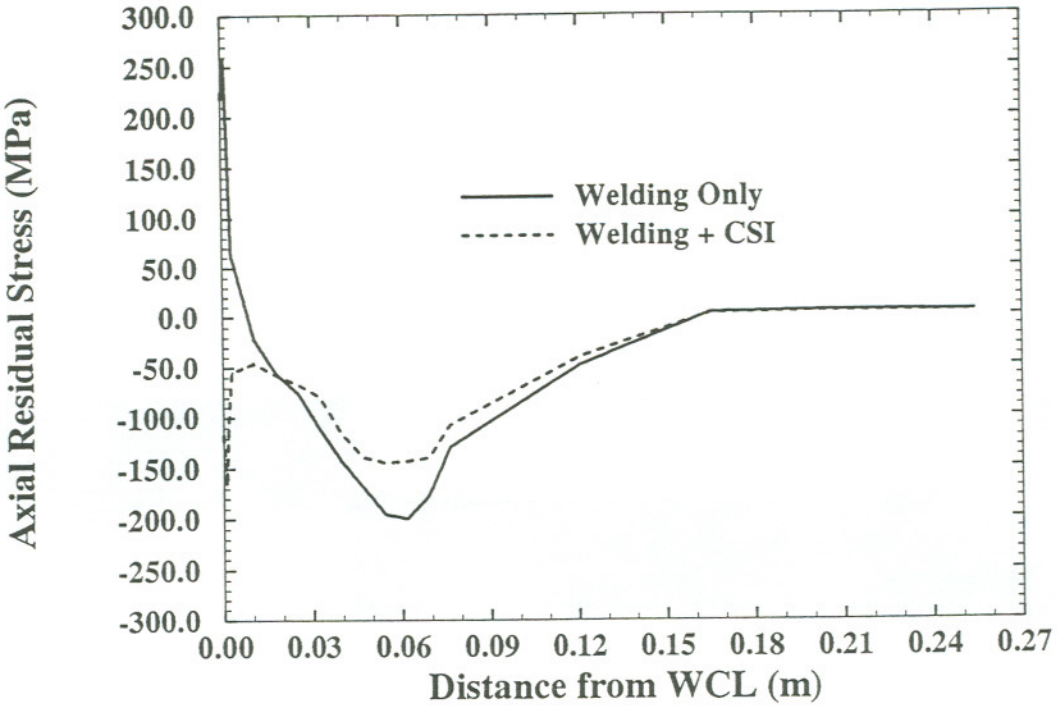

Figure 138. Axial Residual Stress Distributions at Pipe Inner Surface (Welding and Welding Plus CSI)

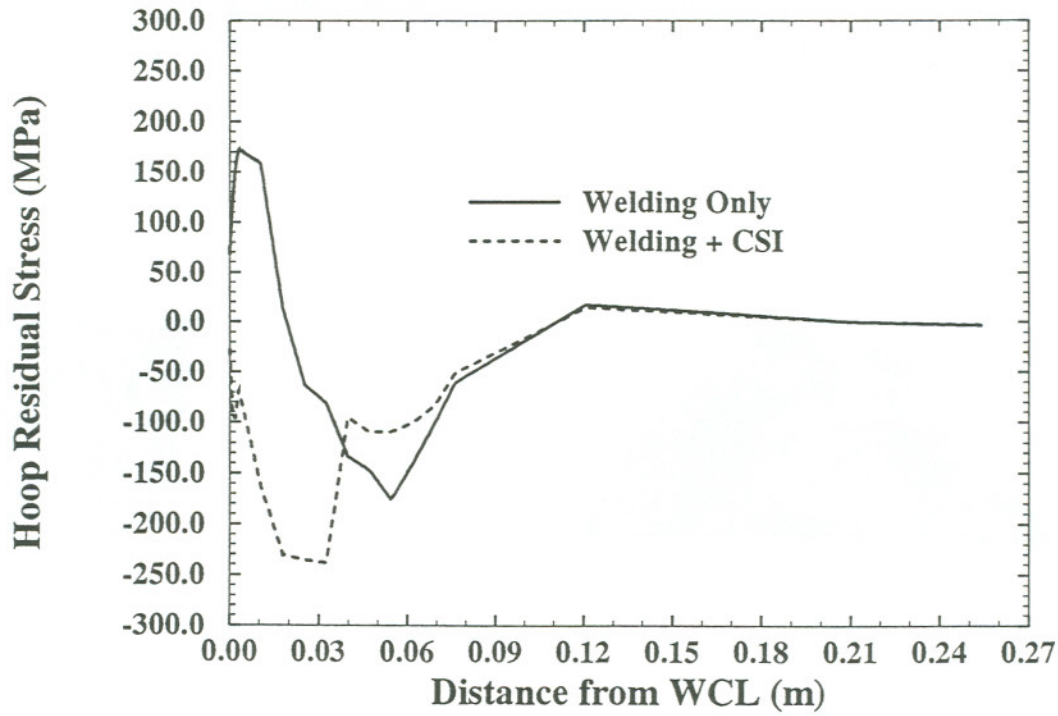

Figure 139. Hoop Residual Stress Distributions at Pipe Inner Surface (Welding and Welding Plus CSI)

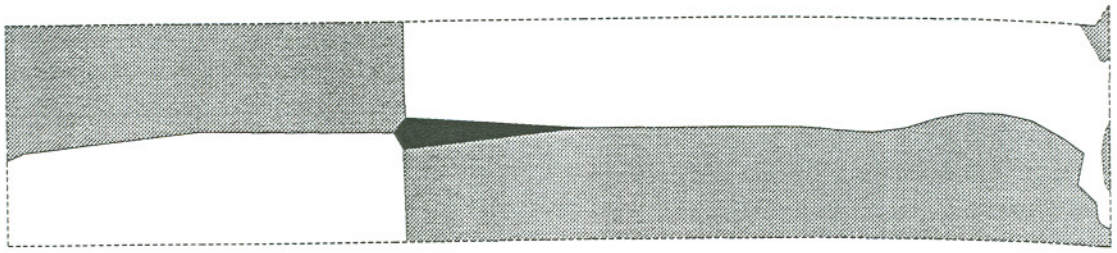

Figure 140. Axial Residual Stress Distribution in Pipe Wall Section after CSI Treatment

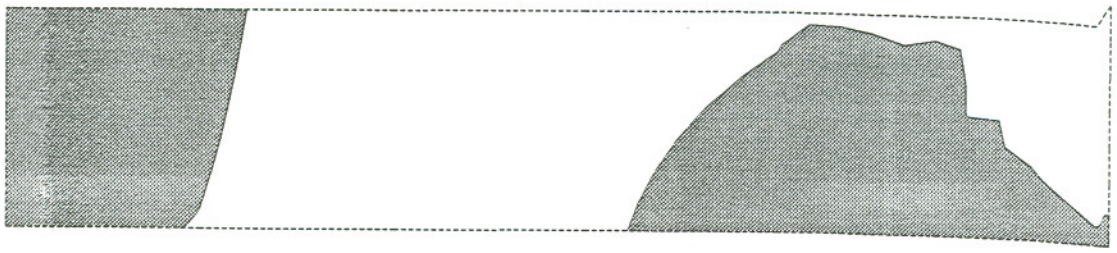

Figure 141. Hoop Residual Stress Distribution in Pipe Wall Section after CSI Treatment

CHAPTER 7
DISCUSSION

THERMOMECHANICAL HISTORY MEASUREMENTS

The experimental results from the thermomechanical history measurements of three pipe welding clearly demonstrate the temperature and deformation differences among the three pipe weldments. These thermal and mechanical differences are primary due to different welding parameters, welding sequences, and weld groove preparations used before and during welding. The final products of the thermomechanical history in the pipe weldments are microstructural change and residual stress formation. The state and distribution of the residual stress on the pipe weldment inner surface are main the concerns in this research. It is expected that there exist residual stress differences at comparable positions on the inner surface among the three pipe weldments, due to the thermomechanical history differences during pipe welding.

As discussed before, the thermal history would influence the deformation history during pipe welding. Hence, the residual stress in the pipe weldment is directly related to the development of deformation during welding. In this study, hoop strain, radial and axial deformation histories were recorded during welding. Out of these strain/deformation histories, radial deformation plays the dominant roles in deciding the residual stress state/distribution on pipe weldment. This was experimentally verified by the research works in MIT (20,119-122) and The Welding Institute (TWI) (123), and can be explained by the elastic thin cylinder theory developed by Timosenko and Woinowski-Krieger (124).

Timoshenko and Woinowaki-Krieger (124) give the inward radial deflection w resulting from axisymmetric shear force Q_o and moment M_o per unit length applied to

a cylinder (see Figure 142) as:

$$w = -\frac{e^{-\beta x}}{2\beta^3 D}\left[\beta M_o(\cos\beta x - \sin\beta x) + Q_o\cos\beta x\right] \qquad (41)$$

and hence

$$\frac{dw}{dx} = \frac{e^{-\beta x}}{2\beta D}\left[2\beta M_o\cos\beta x + Q_o(\cos\beta x + \sin\beta x)\right] \qquad (42)$$

$$\frac{d^2w}{dx^2} = -\frac{e^{-\beta x}}{\beta D}\left[\beta M_o(\cos\beta x + \sin\beta x) + Q_o\sin\beta x\right] \qquad (43)$$

where

$$\beta = \left[\frac{3(1-\mu^2)}{R^2t^2}\right]^{\frac{1}{4}} \qquad (44)$$

and

$$D = \frac{Et^3}{12(1-\mu^2)} \qquad (45)$$

To model the deflection caused by a circumferential butt weld centered at x = 0, the applied forces Q_o and M_o are related to the angular distortion Ω and tendon force F (see Figure 143) which characterize the shrinkage of the weld.

The radial shear force is related to the tendon force F by considering radial equilibrium at x = 0:

$$Q_o = -\frac{F}{2R} \qquad (46)$$

The bending moment M_o is found by setting dw/dx = -Ω/2 at x = 0 in (125). Hence:

$$M_o = -\frac{1}{2\beta}(\beta^2 D\Omega + Q_o) \qquad (47)$$

Substitution for M_o and Q_o in (41)-(43) gives the radial deflection and its derivatives at any distance from the weld. Outside the tension zone, the membrane component of the hoop stress is proportional to the radial deflection:

$$\sigma_{\theta m} = -\frac{Ew}{R} \qquad (48)$$

The axial bending stresses induced by weld radial shrinkage on the inner and outer surface at any section inside or outside the tensile zone are a function of the curvature:

$$\sigma_{xb} = \pm\frac{Et}{2(1-\mu^2)} \cdot \frac{d^2w}{dx^2} \qquad (49)$$

The hoop curvature $1/R \bullet d^2w/d\theta^2$ is zero because of axial symmetry, hence the hoop stresses have a Poisson bending component:

$$\sigma_{\theta b} = \mu\sigma_{xb} \qquad (50)$$

The axial bending stress at the weld centerline can be obtained by combining (41), (44), (45) and (47) and setting $x = 0$. Hence, the bending stress on the inside surface is given by:

$$\sigma_{xo} = \frac{3}{\beta t^2}(\beta^2 D\Omega - \frac{F}{2R}) \qquad (51)$$

Thus, the Poisson bending component in the hoop stress is:

$$\sigma_{bo} = \frac{3\mu}{\beta t^2}(\beta^2 D\Omega - \frac{F}{2R}) \qquad (52)$$

It was found that the tendon force F was in practice largely dependent on

thickness t. Hence, if the pipe radius R and thickness t are given, the axial bending stress and the Poisson bending component in the hoop stress on the pipe inside surface and near WCL are proportional to the angular distortion Ω. This angular distortion Ω is, in general, dependent on the radial deflection w and increases as w increases. Thus, if the pipe geometry is given, the axial bending stress and the Poisson bending component in the hoop stress on pipe inner surface and area close to WCL are roughly proportional to the radial deflection w.

It is known that the residual stresses in the circumferential butt weld are predominantly bending stresses due to the weld shrinkage. This is:

$$\sigma_x \approx \sigma_{xb} \tag{53}$$

and

$$\sigma_\theta \approx \sigma_{\theta m}+\sigma_{\theta b} \tag{54}$$

Hence, it is safe to conclude that the residual stresses on the inner surface of pipe weldment near WCL are roughly proportional to the radial deflection there.

From the above analysis and discussion, based upon the experimental radial deformation data, it is now possible to qualitatively compare the residual stresses on the inner surface of pipe weldment and comparable position among three pipe weldments. Figure 144, 145, and 146 show the comparison of the radial deflections at comparable distances from WCL among three pipe weldments and at 0°, 90°, and 180° from the welding start, respectively. From these three plots, the results from the four-pass narrow groove weldment clearly demonstrate the lowest radial deformations among the three pipe weldments on the pipe inner surface at area close to WCL. As suggested by above analysis, the radial deformations control the final residual stress level in the weldment. Thus, the four-pass narrow gap groove weldment is expected to have the lowest residual stress level of all three weldments at area close to WCL. The radial deformation results for six-pass weldment at area near WCL is lower than that for nine-pass weldment. It

suggests that the six-pass weldment may have lower overall residual stress level than nine-pass weldment at area near WCL.

Axial deflections for the three pipe weldments measured at pipe outer surface and 180° from the welding start as a function of weld pass number are shown in Figure 147. From this plot, it is found that the six-pass weldment has the highest per pass axial deflection while the nine-pass weldment has the largest overall axial deflection among three pipe weldments. This is mainly due to high heat input used in six-pass weldment and more passes employed in nine-pass weldment. The comparison of axial deflections on pipe inner surface and different azimuthal position among three pipe weldments can be seen in Figure 148. The contribution of axial deflection to the residual stresses in pipe weldment is not well documented in the literature. However, it should be point out that the four-pass weldment has the lowest axial deformation among the three pipe weldments.

One general conclusion reached from the thermomechanical history measurement results is that the four-pass narrow gap weldment is expected to have the least degree of residual stress level among the three pipe weldments.

RESIDUAL STRESS MEASUREMENTS

Residual Stress Measurements by Hole-Drilling Method

This research used the abrasive jet hole drilling method to measure the residual stresses on outer surface of the three pipe weldments. This stress measurement should have been performed on the inner surface of pipe weldment as the residual stress state/distribution on the inner surface of pipe weldment is the concern in this research. But the equipment used to drill hole just could not be fitted into the pipe inside diameter. This is one of the major limitations of using the hole drilling method.

A second limitation of this stress measurement technique is that the hole drilling

method can only measure the surface stress value. As discussed before, the distribution of residual stresses in pipe wall, especially in the inner sub-surface area, is as important as the residual stress distribution on inner surface of pipe weldment as it will influence the crack propagation if cracking does occur on the pipe inner surface.

A third limitation of this stress measurement is that it requires fairly large sized strain rosette (about 8-10 mm here). This is fine for the area far from WCL, where the gradient of stress is expected to be small. This is not so applicable at the area near WCL as a large stress gradient is anticipated here. The measured stress would not be representative as it is averaged by the rosette size.

The above mentioned limitations of this stress measurement are expected to be overcame by the ongoing residual stress measurements, which are being conducted at Oak Ridge National Laboratory (ORNL) by using the neutron diffraction stress measurement facility there. The neutron beam can penetrate into the pipe wall and measure the stress distribution through thickness. The neutron diffraction technique can measure stresses for a volume element as small as 2 mm x 2 mm x 2 mm. This is a very useful technique for measuring the stress at area close to WCL.

Although there exists the above mentioned limitations in the hole-drilling residual stress measurements, the results from the measurements are still very valuable to this research as they provide the experimental data base for the validation of the finite element model which will be discussed later. The comparison of residual stress at comparable position between four-pass and six-pass weldments (see Figure 149) further verifies the conclusion that the four-pass weldment has the lowest stress level among three pipe weldments.

Residual Stress Measurements by Neutron Diffraction Method

The strain (ϵ) measured by the neutron diffraction method can be expressed as:

$$\epsilon = \frac{\sin\theta_o}{\sin\theta} - 1 \qquad (55)$$

where θ_o is the diffraction angle of the stress-free planes and θ is the diffraction angle of the stressed planes. This equation clearly shows the importance of determining stress-free d-spacing or diffraction angle. At $2\theta_o = 96.4°$, a 0.01° shift of the stress-free reference sample's peak position would produce an erratic strain value of 7.8×10^{-5}. The d-spacing or diffraction angle is decided by the material lattice structure and parameter which are in turn determined by the material microstructure, chemical composition, and grain structure. This poses a problem for the weldment as the weldment is a complicated composite structure. The chemical composition, microstructure, and grain structure are changed from the base metal to the weld in a weldment. This is much obvious for the 304L stainless steel weldment which gives the columnar and epitaxial grain structure in the weld, as compared with the random grain orientation in the base metal. It also gives the as-solidified 304L weld metal an austenitic (fcc) structure with about 8 volume percent of ferrite (bcc) phase, as compared with the austenitic base metal, which typically has up to 4 volume percent ferrite in the matrix. Thus, even in a stress-free weldment, the diffraction angles for the base metal and the weld are expected to be different, this requires measuring a stress-free reference weldment under identical conditions to the measurement for the pipe weldment. In this experiment, as restricted by the neutron beam time, the stress-free reference diffraction angle was not measured, instead the diffraction angle θ at the position of 160 mm from the WCL was measured as the stress-free reference diffraction angle θ_o and at a value of 48.143°. This is under the assumption that the residual stresses in the pipe weldment would be faded away as the distance from the WCL increases and the stress at 160 mm from the WCL can be neglected, as compared with the stress in the weld zone. This assumption could be hold for the base metal but not for the weld metal. This partly explains why the neutron diffraction measured residual stresses have unexpected values in the weld zone. This problem is expected to be solved in the future neutron diffraction measurements by

measuring the similar stress-free weldment at corresponding positions before starting the neutron diffraction stress measurement on the pipe weldment.

FEA MODELING OF THE NARROW GAP WELDING AND CSI PROCESSES

Effects of Model Selection on the Numerical Results

In this study, two FEA models were established to model the narrow gap welding process. The difference between two models is that one is 3D analysis while the other is 2D axisymmetric model. The 3D model aims at studying the narrow gap welding process in detail by considering the moving heat source and filler metal addition during welding, while the 2D model is part of the numerical analysis to evaluate the effectiveness of CSI on pipe weldment and tries to simulate the narrow gap welding process as simply as possible. In other words, the 3D model is a dynamic model, while 2D model is quasi-steady model. These two different approaches to the modeling of narrow gap welding process results in two different residual stress distributions on the inner surface of pipe weldment (see Figure 150). Basically, the results from both models reach almost same peak tensile axial/hoop stress values but differ from each other in the size of tensile zone and the distribution of the stresses along the axial direction. The tensile zone from 3D model is much larger than that from 2D model, especially in terms of axial residual stress. The stresses calculated from the 2D model change from tensile to compressive state very rapidly as the distance from WCL increases, while the stresses got from 3D model change relatively slow. The 2D model results have large compressive stress values, while the 3D results have small or no compressive stresses. The boundary condition difference between the 2D and 3D models causes the different stress distributions at the end of the pipe, with zero stress for 2D model and certain stress levels for 3D model. This difference should not influence the stress distribution in the weld and HAZ area. It is felt that the results from the 3D model is much closer

to reality than that from 2D model. This can be supported by comparing the modeling results with the neutron diffraction measured residual stress results on the pipe inner surface as shown in Figure 151. From this figure, it can be seen that the residual stresses calculated from the 3D model give more satisfactory bounds to the experimental data than the residual stresses calculated from the 2D model. The reason is simply that the pipe girth welding process is never an axisymmetric process. It is possible that quasi-steady or axisymmetric distribution of temperature may be reached at the area far from the welding start and stop point. But it is impossible to reach the stress quasi-steady distribution at any place in the weldment. Nevertheless, 2D model is still very helpful in terms of roughly estimating stress distribution in the first place as it requires little computing resources and short time to complete, while the 3D model needs tremendous computing power and long turn-around time. Based on the results from the 3D model, the 2D model can also be modified to produce more accurate results at different azimuthal positions. This will cut down computing cost and time a lot but requires 3D model at first place.

Comparison of the Modeling Results with the Experimental Results

The comparison of residual stress distributions on pipe outer surface between experimental measurement and 2D model prediction is shown in Figure 152. The comparison of residual stress distributions on the pipe inner surface is given in Figure 151. Basically, the experimental result has fair agreement with numerical prediction. With this stress agreement and previous reported temperature agreement, the results calculated from the modeling of CSI process should be reasonable. This shows the very promising potential of practical application of CSI process. However, there exist lots of practical problems to be solved and it is still very necessary to experimentally verify this process before applying it to the field.

The comparisons of residual stress distributions on pipe outer surface between

experimental measurements and 3D model predictions is presented in Figure 153. The comparison of residual stress distributions on the pipe inner surface is sown in Figure 151. The numerical results are basically within the range of experimental results. The differences between them are primary due to: 1). the heat inputs used in the model are pre-set constant values for each pass, while the real heat input for each pass welding was dynamically adjusted during welding which required to record the welding parameters in real time during each pass welding, this was not done in this experiment; 2). only the experimental thermocouple data was used to "calculated" the model, besides matching the calculated temperature with thermocouple data, the calculated weld fusion zone profile should match the experimental weld fusion zone profile, which was not done in the model; 3). it is found that at high temperature, the combined isotropic-kinematic strain hardening model is more applicable than kinematic strain hardening model, also at high temperature, strain rate dependent mechanical properties are more appreciate than strain rate independent mechanical properties, these two points are impossible to be implanted into the current model due to limited ANSYS software capabilities; 4). the mechanical properties used in the model are not accurate at high temperature, especially at temperatures close to and beyond the fusion temperature; 5). the mesh under heat source is not fine enough, this is evident in Figure 151, if there were one more node position at 0.06 m from WCL, the calculated stress distribution could be shown much clearer; 6). the chimney effect gives different thermomechanical history at different pipe sections. Some of these points are impossible to be implanted into the present model, while other points can be taken into account in future modeling work. The biggest drawback of this model is that it requires hugh computing time and power. And sometime it is just unrealistic to try to model the welding process with as detail as possible, or desired. After all, this 3D model represents the state-of-art numerical analysis which the finite element analysis technique can presently offer for modeling the full pipe girth welding multipass process.

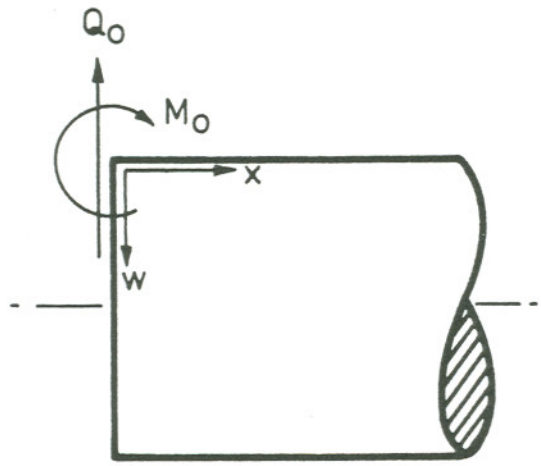

Figure 142. Edge Loads at WCL for a Pipe Girth Weld (123)

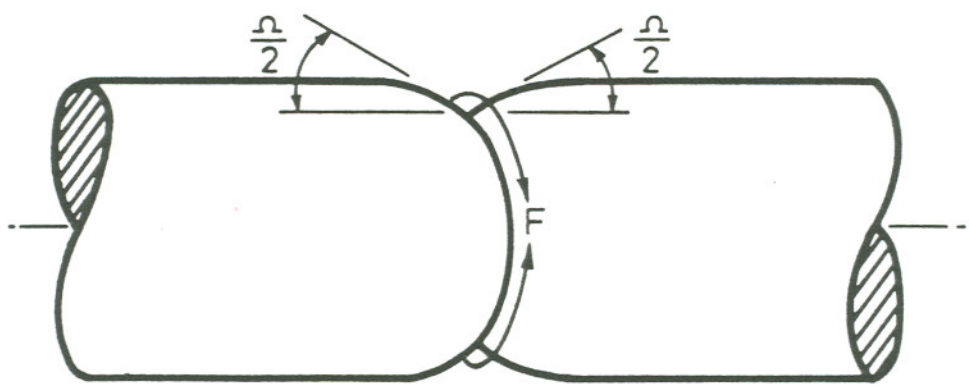

Figure 143. Shrinkage Parameters Ω and F for a Pipe Girth Weld (123)

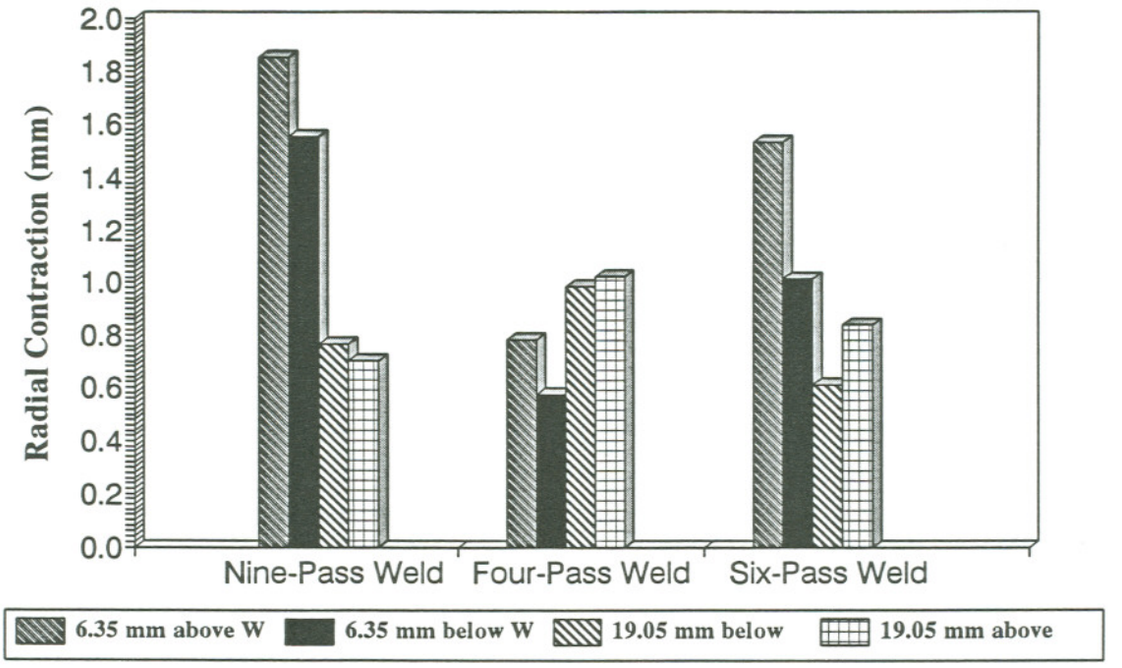

Figure 144. Radial Deflections at 0° for Three Pipe Weldments

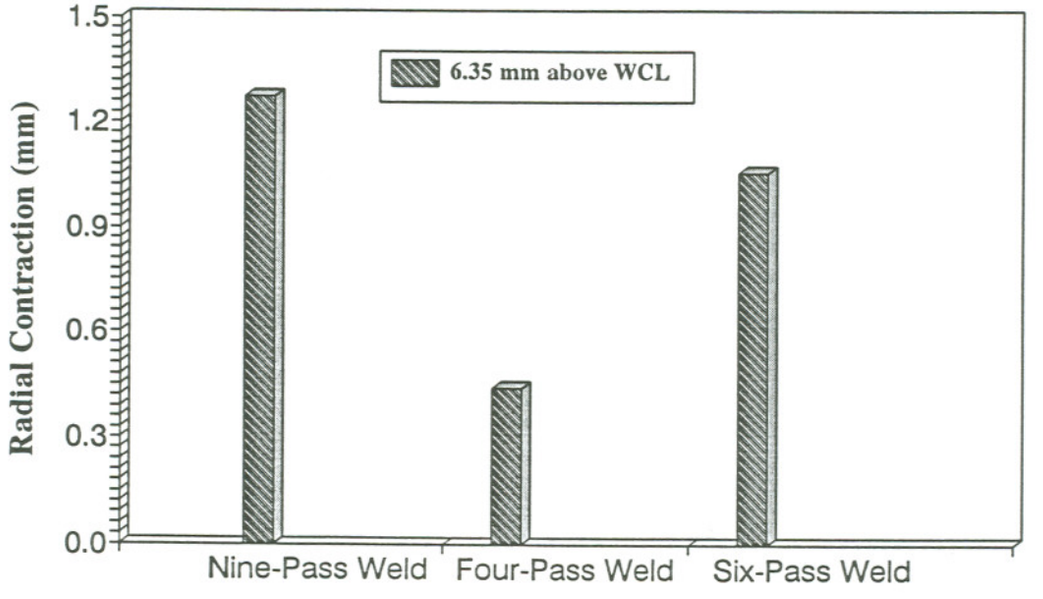

Figure 145. Radial Deflections at 90° for Three Pipe Weldments

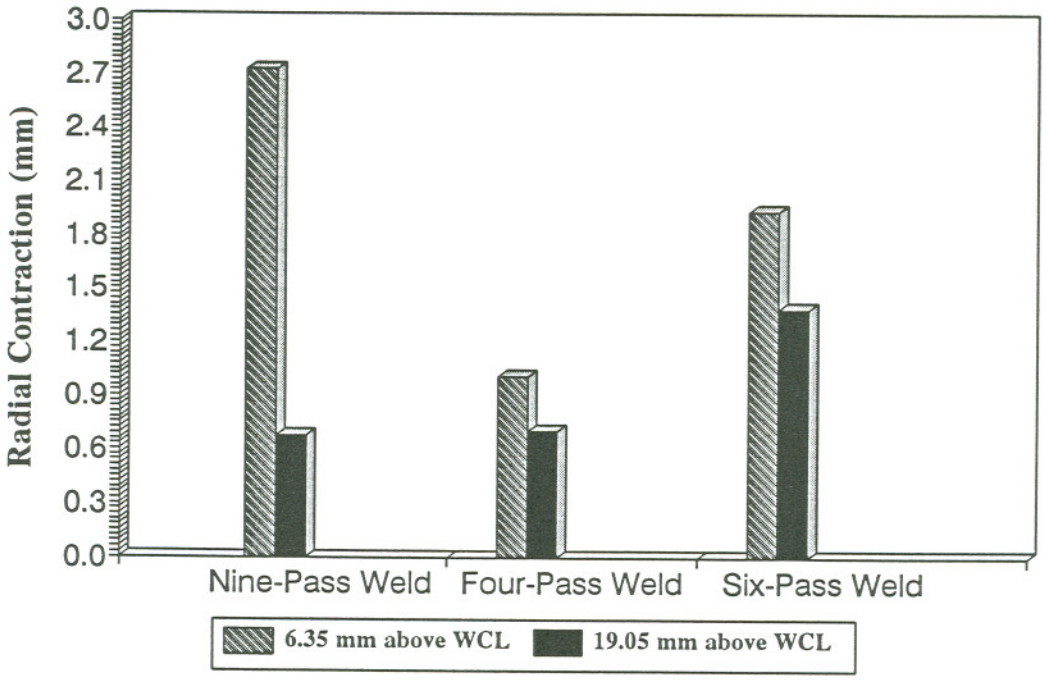

Figure 146. Radial Deflections at 180° for Three Pipe Weldments

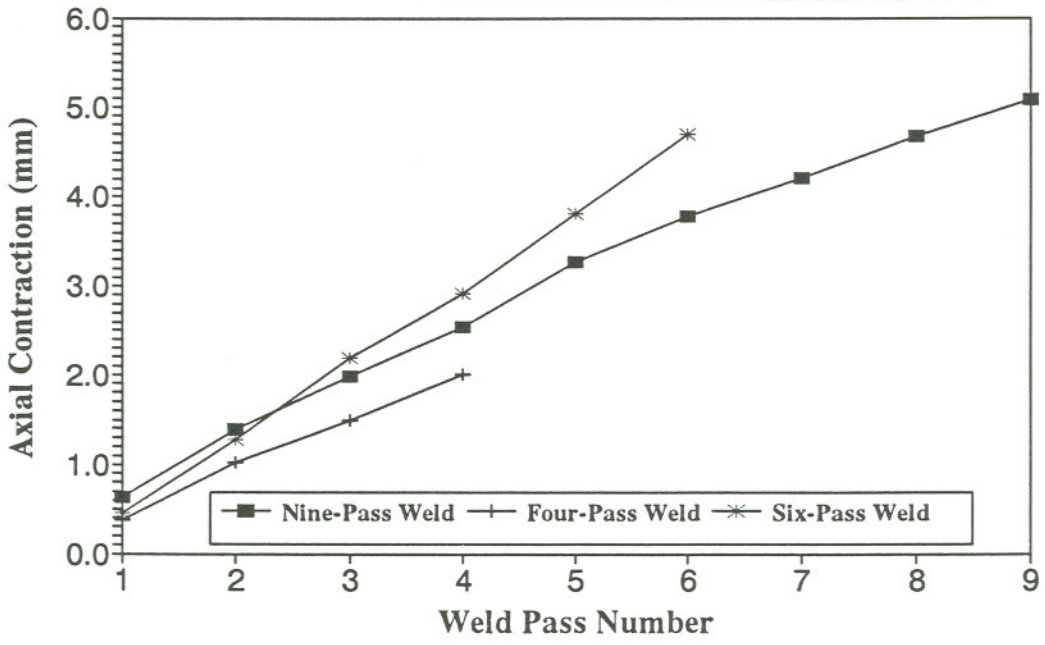

Figure 147. Axial Deflections at 180° and Pipe Outer Surface for Three Weldments

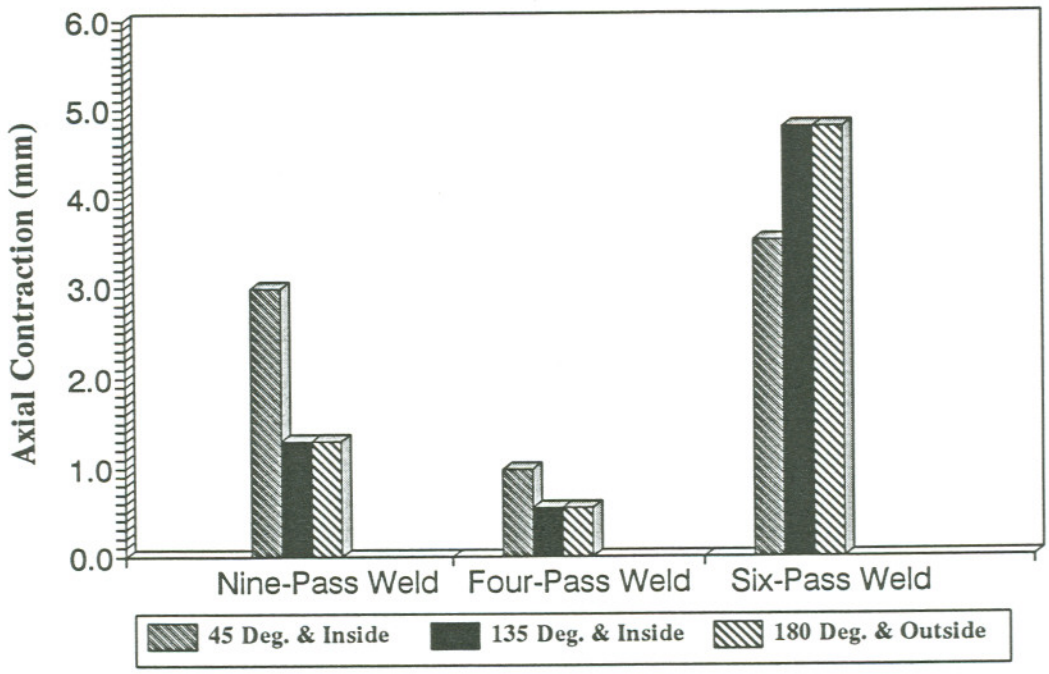

Figure 148. Axial Deflection Comparison on the Pipe Inner Surface among Three Weldments

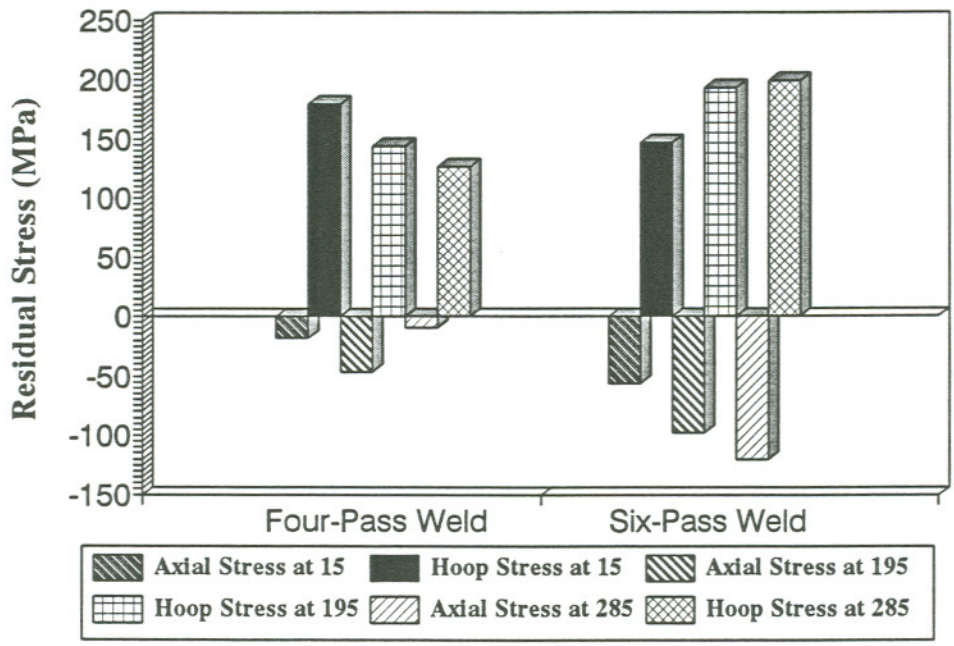

Figure 149. Measured Residual Stress Comparison between Four and Six Pass Weldments

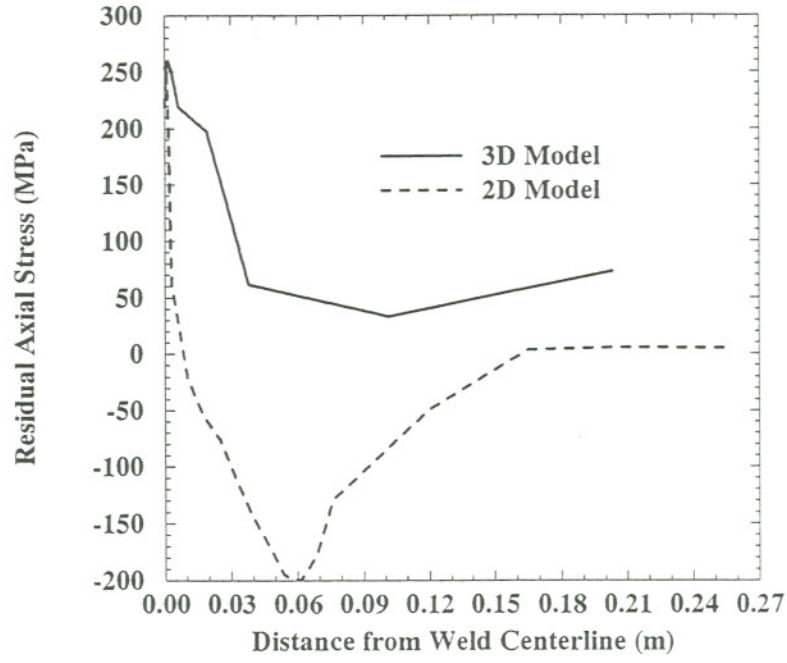

(a)

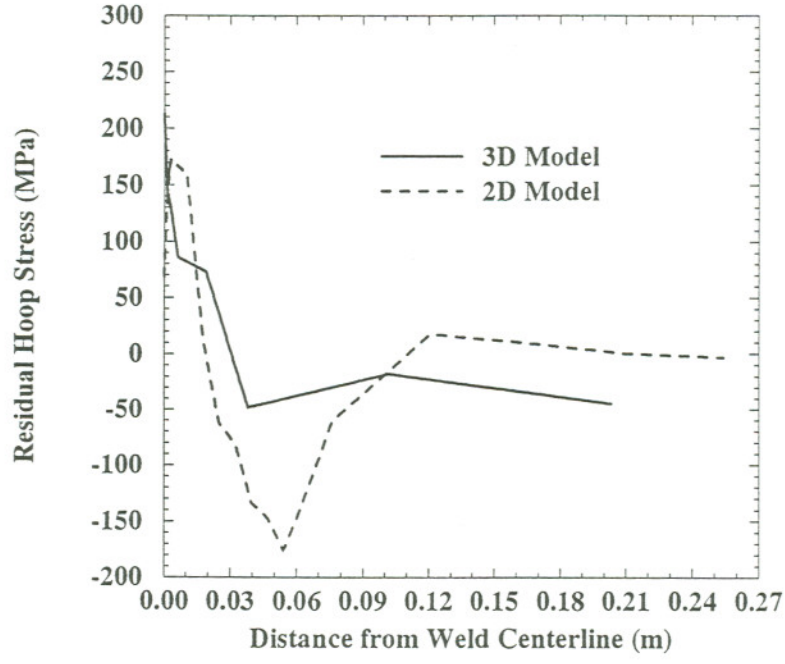

(b)

Figure 150. 3D and 2D Model Stress Results on Pipe Inner Surface (a) Axial Stress and (b) Hoop Stress

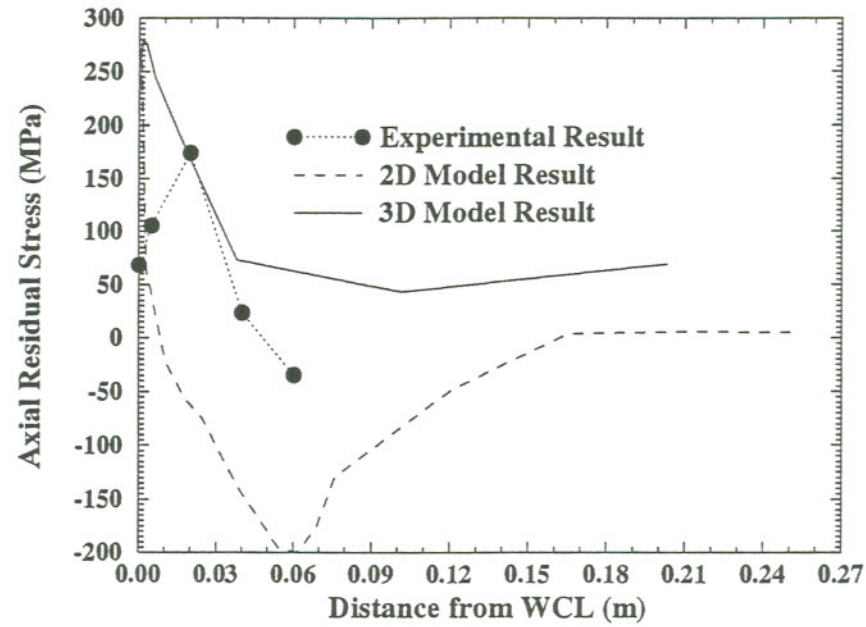

(a)

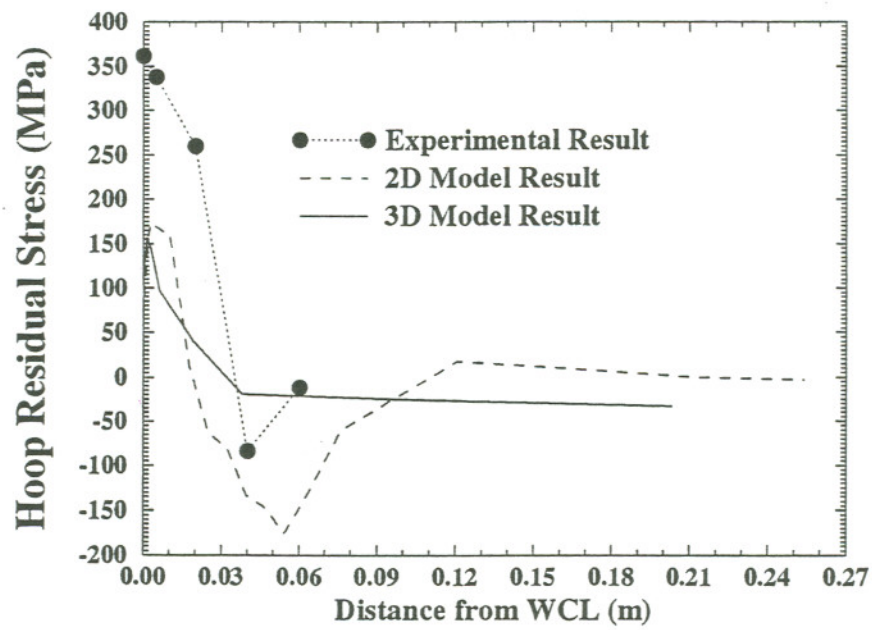

(b)

Figure 151. Comparison of Modeling Residual Stress Results with Experimental Residual Stresses Results on Pipe Inner Surface
(a) Axial Stress and (b) Hoop Stress

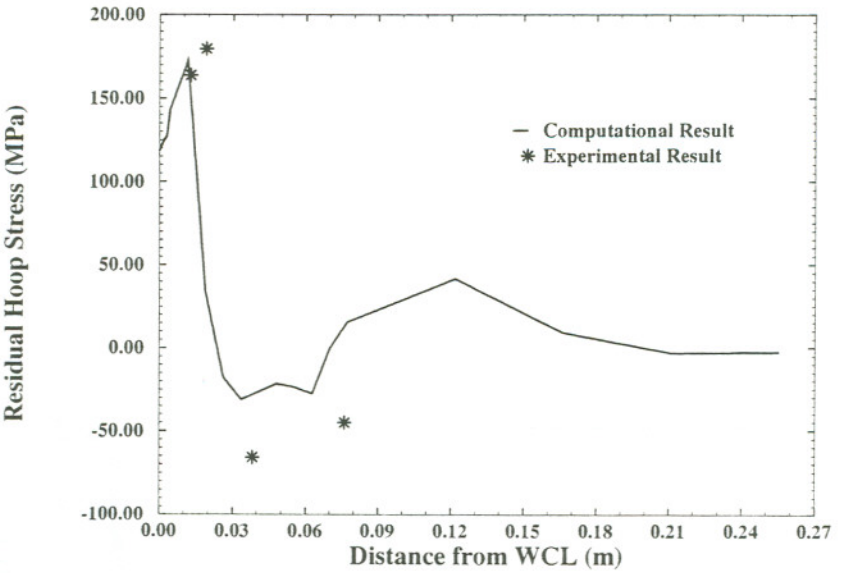

(a)

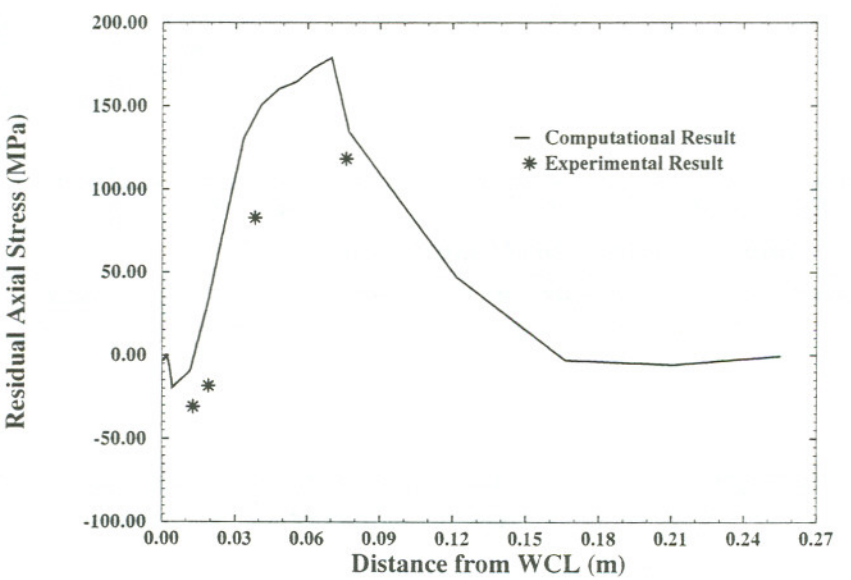

(b)

Figure 152. Calculated and Measured Residual Stresses Comparison on Pipe Outer Surface for 2D Model (a) Axial Stress and (b) Hoop Stress

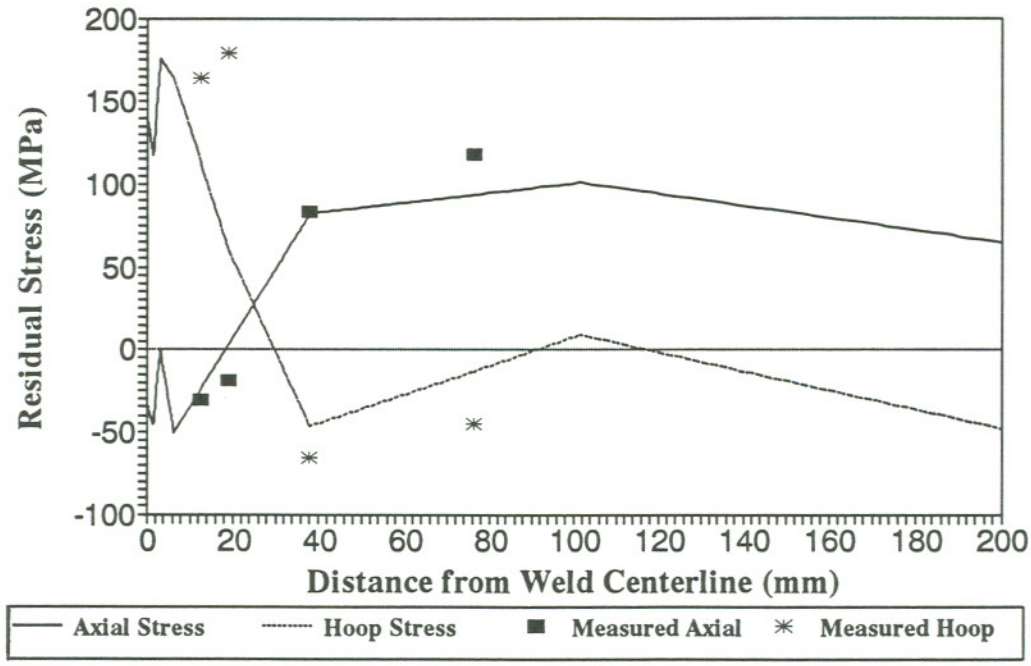

Figure 153. Calculated and Measured Residual Stresses Comparison on Pipe Outer Surface for 3D Model at 15° from Welding Start

CHAPTER 8
SUMMARY

The experimental work of this research started with recording the thermal and deformation/strain history measurements by a computer data acquisition system for three 406-mm-diameter, Type 304L stainless steel (SS), schedule 40 (12.7 mm thickness) pipe girth welds. Two weld groove preparations were standard V grooves while the third was a narrow groove configuration. The welding parameters for the three pipe welds simulated expected field practice as closely as possible. The narrow gap weld was completed in four continuous passes with one start-stop position while the other two welds required six and nine (discontinuous) passes with multiple start-stop positions, due to the use of different weld wire diameters and welding parameters. Thermomechanical history measurements were taken on the inner counterbore surface, encompassing the weld centerline and heat-affected zone (HAZ), as well as 10 cm of inner counterbore surface on either side of the weld centerline; a total of 47 data acquisition instruments were used for each weld. These instruments monitored: 1). weld shrinkages parallel to the pipe axis, 2). surface temperatures, 3). surface strains parallel to weld centerline, and, 4). radial deformations. These instruments were carefully positioned to record as much information as possible. The experimental techniques developed in this research proved to be effective in demonstrating the development of thermomechanical history in pipe girth welding. The results analyzed from the experimental data give the general conclusions: 1). the temperature profile in the pipe weldment with multiple start-stop positions is, in general, axisymmetric; 2). the temperature profile in the pipe weldment with one start-stop position is axisymmetric in the area far from WCL, but is not axisymmetric at area near start-stop position; 3). the strain/deformation histories are controlled by the thermal histories, the final strain/deformation value is largely decided

by the last one or two weld passes; 4). the strain/deformation profile in the weldment is not axisymmetric; this suggests that the residual stress in a pipe weldment is not axisymmetrically distributed; 5). the four-pass narrow gap weldment has the lowest level of radial deformation among the three pipe weldments, this indicates that the narrow gap weldment would have the lowest overall residual stress level among three pipe weldments.

This research also performed residual stress measurements on the outer surface of the OGI, four-pass, and six-pass weldments by using air-abrasive hole-drilling method and on the pipe inner surface of the four-pass narrow gap weldment by using neutron diffraction method. The results show that the residual stresses are not axisymmetrically distributed around the pipe weldment. The results also show that there exists a tensile zone on the pipe inner surface and in the area close to the WCL. The comparison of the residual stress results between the four- and six-pass weldments supports the above conclusion that the four-pass weldment has the least residual stress level among the three pipe weldments.

The numerical work of this research started with a 3D finite element analysis model established to simulate a multipass, narrow gap pipe girth welding process. The pipe simulated was a Type 304L stainless steel pipe with a diameter of 406 mm, a thickness of 12.7 mm, and a narrow groove configuration. This pipe was finished in four continuous welding passes with one start-stop position. Temperatures, deformations and strains were recorded in real time during pipe welding. The thermal results from this model were tuned to match the calculated temperature histories with the comparable experimental thermal cycles. The calculated temperature histories are axisymmetrically distributed around the pipe except at area close to the welding start-stop position. This is in good agreement with what was observed from the experimental data. The calculated stress results show that the tensile residual stress zone on the pipe inner surface is about 30 mm from WCL at each side and the tensile residual stress zone in the pipe wall thickness is about 5 mm from the pipe inner surface for up to 19.05 mm from WCL.

The calculated residual stresses are, in general, axisymmetrically distributed around the pipe except at the area near the welding start-stop position. This is not in agreement with what was noted from the experimental results. The comparison between the calculated stress results with the limited experimental residual stress measurements on the pipe inner and outer surface demonstrates reasonable agreement between them. This 3D model is the first attempt to try to simulate a full multipass girth pipe welding process. There certainly exist a lot of rooms for improvement. And more experimental residual stress measurements on pipe weldment is needed to verify this model. Nevertheless, this 3D model represents the best numerical effort which can be achieved under current computing condition.

An axisymmetric 2D finite element thermal and residual stress analysis of a 406-mm-diameter, schedule 40, Type 304L stainless steel pipe was also conducted for narrow gap girth welding and welding plus a newly proposed post-weld stress mitigating treatment - cooling stress improvement (CSI). Again, the calculated thermal profile was tuned to match with the experimental data. The calculated stress results indicate that the weld induced stresses on the pipe inner surface are tensile in the weld region and remain so for a certain distance from the weld center line. CSI treatment after welding can convert the tensile weld residual stresses to compressive values. Thus, this computational modeling study demonstrates the feasibility of the CSI process and shows great promise for industrial application of this process. However, experimental work is necessary to thoroughly evaluate the effectiveness of CSI. The calculated stress results also show that the CSI is more effective on hoop stress than on axial stress. The comparison between the calculated and measured welding residual stresses shows good agreement between them. The comparison between the numerical and experimental residual stress results suggests that the 3D model is more realistic as the 2D model has a very narrow tensile region on the pipe inner surface.

REFERENCES

1. Danko, J.C. Effects of Residual Stresses on the Stress-Corrosion Cracking of Austenitic Stainless Steel Pipe Weldments. In: *Practical Applications of Residual Stress Technology*, edited by Rudd, C. Materials Park, Ohio: ASM International, 1991, p. 27-37.

2. Danko, J.C., Sasaki, R., Itow, H., Iwasaki, S., Saiga, Y. and Nojima, K. Stress Corrosion Cracking and Mitigation Measures for Welded Stainless Steel Piping in Boiling Water Reactors. In: *Proceedings of International Conference on Stainless Steels*, Chiba, Japan: ISIJ, 1991, p. 161-167.

3. Danko, J.C. Altering Residual Stresses in Welded Austenitic Stainless Steel Piping. In: *Advances in Welding Science and Technology*, edited by David, S.A. Materials Park, Ohio: ASM International, 1986, p. 545-549.

4. Danko, J.C. A Review of Weld Residual Stresses in Austenitic Stainless Steel Pipes. In: *Recent Trends in Welding Science and Technology*, edited by David, S.A. and Vitek, J.M. Materials Park, Ohio: ASM International, 1989, p. 113-118.

5. Strauss, B., Schottky, H. and Hinnuber, J. *Z. Anorg. Allg. Chem.* 188:309, 1930.

6. Bain, E.C., Aborn, R.H. and Rutherford, J.J.B. *Trans.Am.Soc.Steel Treating* 21:481, 1933.

7. Atteridge, D.G. and Bruemmer, S.M. *Evaluation of Welded and Repair-Welded Stainless Steel for LWR Service*, Washington, DC:NUREG/CR-3613, U.S. Nuclear Regulatory Commission, 1986.

8. Bruemmer, S.M. and Atteridge, D.G. Prediction of HAZ Sensitization Development in 300 Series Stainless Steel Pipe Welds. In: *Advances in Welding Science and Technology*, edited by David, S.A. Materials Park, Ohio: ASM International, 1986, p. 801-804.

9. Bruemmer, S.M. *Quantitative Measurement and Modeling of Sensitization Development in Stainless Steels*, Ph.D. Thesis, Oregon Graduate Center, 1988.

10. Cedeño, C.A. *Thermal Cycle Effect on Stainless Steel Sensitization*, M.S. Thesis, Oregon Graduate Institute of Science and Technology, 1990.

11. Advani, A.H. *Deformation Effects on the Development of Grain Boundary Chromium Depletion (Sensitization) in Type 316 Austenitic Stainless Steels*, Ph.D. Thesis, Oregon Graduate Institute of Science and Technology, 1990.

12. Simmons, J.W. *Effects of Prior Deformation Continuous Cooling of Type 316 Austenitic Stainless Steel*, M.S. Thesis, Oregon Graduate Center, 1989.

13. Atteridge, D.G., Li, M., Simmons, J.W., Bruemmer, S.M. and Lundin, C.D. Model Predictions of HAZ Grain Boundary Chromium Depletion Development for Austenitic Stainless Steel. In: *International Trends in Welding Science and Technology*, edited by David, S.A. and Vitek, J.M. Materials Park, Ohio: ASM International , 1993, p. 681-685.

14. Ueda, Y., Nakacho, K. and Shimizu, T. Improvement of Residual Stresses of Circumferential Joint of Pipe by Heat-Sink Welding. *Journal of Pressure Vessel Technology, Transactions of the ASME* 108:14-23, 1986.

15. Shack, W.J., Ellingson, W.A. and Pahis, L.E. *Measurement of Residual Stresses in Type-304 Stainless Steel Piping Butt Weldments*, EPRI NP-1413, 1980.

16. Masubuchi, K. *Analysis of Welded Structures*, New York, NY:Pergamon Press, 1980.

17. Wohlfahrt, H. Residual Stresses due to Welding: their Origin, Calculation and Evaluation. In: *Residual Stresses*, edited by Macherauch, E. and Hauk, V. Alle Rechte vorbehalten., Germany: DGM Informationsgesellschaft mbH, 1986, p. 81-112.

18. *Metals Handbook - Volume 6: Welding, Brazing, and Soldering*, Ed. 10, Materials Park, Ohio:ASM International, 1992.

19. Vaidynathan, S., Todaro, A.F. and Finnie, I. Residual Stresses Due to circumferential Welds. *Journal of Engineering Materials and Technology, Transactions of the ASME* 95:233-237, 1973.

20. DeBiccari, A. *Control of Distortion and Residual Stresses in Girth Welded Pipes*, Ph.D. Thesis, Dept. of Ocean Engineering, M.I.T., 1986.

21. Disney, J.A. *Welding of Nuclear Grade Materials to Minimize Residual Welding Stresses*, EPRI NDE Center, 1985.

22. Atteridge, D.G. and Anderson, W.E. HAZ Thermomechanical History for a Large-Diameter Stainless Steel Pipe Weld. In: *Advances in Welding Science and Technology*, edited by David, S.A. Materials Park, Ohio: ASM International, 1986, p. 825-828.

23. Atteridge, D.G. and Anderson, W.E. Cyclic work hardening induced in the heat-affected zone during multipass welding of a 61 cm diameter type 304 SS pipe. In: *Third International Conference on Welding and Performances of Pipelines*, edited by Hart, P.H.M. Cambridge, UK: The Welding Institute, 1986, p. 31.

24. Jonsson, M. and Josefson, B.L. Experimentally Determined Transient and Residual Stresses in a Butt-Welded Pipe. *Journal of Strain Analysis* 23:25-31, 1988.

25. Josefson, B.L. and Karlsson, C.T. FE-calculated Stresses in a Multi-pass Butt-welded Pipe - A Simplified Approach. *Int. J. Pres. Ves. & Piping* 38:227-243, 1989.

26. Jonsson, M., Josefson, B.L. and Näsström, M. Experimentally Determined Deformations and Stresses in Narrow Gap and Single-U Multi-Pass Butt-Welded Pipes. In: *Proceedings of the 10th International Conference on Offshore Mechanics and Arctic Engineering - Volume III-A, Materials Engineering*, edited by Salama, M.M., Toyoda, M., Liu, S., Dos Santos, J.F. and Kocak, M. New York, NY: The American Society of Mechanical Engineers, 1991, p. 17-24.

27. Hibbitt, H.D. *A Numerical Thermal-Mechanical Model for the Welding and Subsequent Loading of a Fabricated Structure*, Ph.D. Thesis, Brown University, 1972.

28. Carslaw, H.S. and Jeger, J.C. *Conduction of Heat in Solids*, Ed. 2, London, UK:Oxford University Press, 1959.

29. Chapman, A.J. *Fundamentals of Heat Transfer*, New York, NY:MacMillan, Inc., 1987.

30. Ule, R.L., Joshi, Y. and Sedy, E.B. A New Technique for Three-Dimensional Transient Heat Transfer Computations of Autogenous Arc Welding. *Metallurgical Transactions B* 21B:1033-1047, 1990.

31. Bathe, K. *Finite Element Procedures in Engineering Analysis*, Englewood Cliffs, NJ:Prentice-Hall, Inc., 1982.

32. Cook, R.D., Malkus, D.S. and Plesha, M.E. *Concepts and Applications of Finite Element Analysis*, Ed. 3, New York, NY:John Wiley & Sons, Inc., 1989.

33. Szekely, J. The Mathematical Modeling of Arc Welding Operations. In: *Advances in Welding Science and Technology*, edited by David, S.A. Materials Park, Ohio: ASM International, 1986, p. 3-14.

34. Wang, Y.H. and Kou, S. Driving Forces for Convection in Weld Pools. In: *Advances in Welding Science and Technology*, edited by David, S.A. Materials Park, Ohio: ASM International, 1986, p. 65-69.

35. Tekriwal, P. and Mazumder, J. Finite Element Modeling of Arc Welding Processes. In: *Advances in Welding Science and Technology*, edited by David, S.A. Materials Park, Ohio: ASM International, 1986, p. 71-80.

36. Matsunawa, A. Modeling of Heat and Fluid Flow in Arc Welding. In: *International Trends in Welding Science and Technology*, edited by David, S.A. and Vitek, J.M. Materials Park, Ohio: ASM International , 1993, p. 3-16.

37. DebRoy, T. Mass Transfer in Welding. In: *International Trends in Welding Science and Technology*, edited by David, S.A. and Vitek, J.M. Materials Park, Ohio: ASM International, 1993, p. 17-25.

38. David, S.A., DebRoy, T. and Vitek, J.M. Phenomenological Modeling of Fusion Welding Processes. *MRS Bulletin* XIX:29-35, 1994.

39. Rosenthal, D. Mathematical Theory of the Heat Distribution During Welding and Cutting. *Welding Journal* 20:220-234, 1941.

40. Solomon, H.D. and Levy, S. HAZ Temperatures and Cooling Rates as Determined by a Simple Computer Program. In: *Proceedings of the Conference on Trends in Welding Research in the United States*, edited by David, S.A. Materials Park, Ohio: ASM International, 1982, p. 173-205.

41. Goldak, J.A., Chakravarti, A. and Bibby, M.J. A New Finite Element Model for Welding Heat Source. *Trans. AIME* 15B:299-305, 1984.

42. Goldak, J.A., Bibby, M.J., Moore, J.E., House, R. and Patel, B. Computer Modeling of Heat Flow in Welds. *Metallurgical Transactions B* 17B:587-600, 1986.

43. Goldak, J., McMill, M., Oddy, A., House, R., Chi, X. and Bibby, M. Computational Heat Transfer for Weld Mechanics. In: *Advances in Welding Science and Technology*, edited by David, S.A. Materials Park, Ohio: ASM International , 1986, p. 15-20.

44. Mahin, K.W., Shapiro, A.B. and Hallquist, J. Assessment of Boundary Condition Limitations on the Development of a General Computer Model for Fusion Welding. In: *Advances in Welding Science and Technology*, edited by David, S.A. Materials Park, Ohio: ASM International, 1986, p. 215-224.

45. Mahin, K.W., Winters, W., Holden, T.M., Hosbons, R.R. and MacEwen, S.R. Prediction and Measurement of Residual Elastic Strain Distributions in Gas Tungsten Arc Welds. *Welding Journal* 70:245s-260s, 1991.

46. Goldak, J. and Bibby, M. Computational Thermal Analysis of Welds: Current Status and Further Directions. In: *Modeling and Control of Casting and Welding Processes IV*, edited by Giamei, A.F. and Abbaschian, G.J. Warrendale, PA: TMS, 1988, p. 153-166.

47. Argyris, J.H., Szimmat, J. and Willam, K.J. Computational Aspects of Welding Stress Analysis. *Computer Methods in Applied Mechanics and Engineering* 33:635-666, 1982.

48. Goldak, J., Oddy, A., Gu, M., Ma, W., Mashaie, A. and Hughes, E. Coupling Heat Transfer, Microstructure Evolution and Thermal Stress Analysis in Weld Mechanics. In: *Mechanical Effects of Welding (IUTAM Symposium Luleå/Sweden 1991)*, edited by Karlsson, L., Lindgren, L.E. and Jonsson, M. Berlin, Germany: Springer-Verlag, 1992, p. 1-30.

49. Leung, C.K., Pick, R.J. and Mok, D.H.B. *Finite Element Modeling of a Single Pass Weld*, New York, NY:Bulletin 356, Welding Research Council, 1990.

50. Tekriwal, P.K. *Three-Dimensional Transient Thermo-Elasto-Plastic Modeling of Gas Metal Arc Welding Using the Finite Element Method*, PH.D. Thesis, University of Illinois at Urbana-Champaign, 1989.

51. Tekriwal, P. and Mazumder, J. Transient and Residual Thermal Strain-Stress Analysis of GMAW. *Journal of Engineering Materials and Technology, Transactions of the ASME* 113:336-343, 1991.

52. Goldak, J., Bibby, M.J., Downey, D. and Gu, M. Heat and fluid flow in welds. In: *Advanced Joining Technologies*, edited by North, T.H. London, UK: Chapman and Hall, 1990, p. 69-82.

53. Goldak, J. Modeling Thermal Stresses and Distortions in Welds. In: *Recent Trends in Welding Science and Technology*, edited by David, S.A. and Vitek, J.M. Materials Park, Ohio: ASM International, 1989, p. 71-82.

54. Vaidynathan, S., Weiss, H. and Finnie, I. A Further Study of Residual Stresses in Circumferential Welds. *Journal of Engineering Materials and Technology, Transactions of the ASME* 104:223-228, 1982.

55. Rybicki, E.F., Schmueser, D.B., Stonesifer, R.W., Groom, J.J. and Mishler, H.W. A Finite-Element Model for Residual Stresses and Deflections in Girth-Butt Welded Pipes. *Journal of Pressure Vessel Technology, Transactions of the ASME* 100:256-262, 1978.

56. Rybicki, E.F. and Stonesifer, R.B. Computation of Residual Stresses due to Multipass Welds in Piping Systems. *Journal of Pressure Vessel Technology, Transactions of the ASME* 101:149-154, 1979.

57. Rybicki, E.F. and Stonesifer, R.B. An Analysis Procedure for Predicting Weld Repair Residual Stresses in Thick-Walled Vessels. *Journal of Pressure Vessel Technology, Transactions of the ASME* 102:323-331, 1980.

58. Rybicki, Edmund F. CHAPTER 11: COMPUTATIONAL METHODS FOR CALCULATING WELD RESIDUAL STRESSES IN PIPES. In: *WELDING: Theory and Practice (MATERIALS PROCESSING - THEORY AND PRACTICES: VOLUME 8)*, edited by Olson, D.L., Dixon, R. and Liby, A.L. Amsterdam, The Netherlands: NORTH-HOLLAND, 1989, p. 325-336.

59. Rybicki, E.F. and McGuire, P.A. A Computational Model for Improving Weld Residual Stresses in Small Diameter Pipes by Induction Heating. *Journal of Pressure Vessel Technology, Transactions of the ASME* 103:294-299, 1981.

60. Rybicki, E.F., McGuire, P.A., Shadley, J.R., Koch, R.L. and Merah, N. *Computational Residual Stress Analysis for Induction Heating of Welded BWR Pipes*, EPRI NP-2662-LD, 1982.

61. Brust, F.W. and Stonesifer, R.B. *Effect of Weld Parameters on Residual Stresses in BWR Piping Systems*, EPRI NP-1743, 1981.

62. Karlsson, R.I. and Josefson, B.L. Three-Dimensional Finite Element Analysis of Temperature and Stresses in Single-Pass Butt-Welded Pipe. *Journal of Pressure Vessel Technology, Transactions of the ASME* 112:76-84, 1990.

63. Karlsson, C.T. Finite Element Analysis of Temperatures and Stresses in a Single-Pass Butt-Welded Pipe - Influence of Mesh Density and Material Modeling. *Engineering Computations* 6:133-141, 1989.

64. Lindgren, L. and Karlsson, L. Deformations and Stresses in Welding of Shell Structures. *International Journal for Numerical Methods in Engineering* 25:635-655, 1988.

65. Wilkening, W.W. and Snow, J.L. Analysis of Welding-Induced Residual Stresses with the ADINA System. *Computers & Structures* 47:767-786, 1993.

66. Hetényi, M. *Handbook of Experimental Stress Analysis*, New York, NY:John Wiley & Sons, 1950.

67. Dove, R.C. and Adams, P.H. *Experimental Stress Analysis and Motion Measurement*, Columbus, Ohio:Charles E. Merrill Books, Inc., 1964.

68. Hendry, A.W. *Elements of Experimental Stress Analysis*, Oxford, UK:Pergamon Press, 1977.

69. Dally, J.W. and Riley, W.F. *Experimental Stress Analysis*, Ed. 2, New York, NY:McGraw-Hill, Inc., 1978.

70. Sirohi, R.S. and Randha Krishna, H.C. *Mechanical Measurements*, Ed. 2, New Delhi, India:John Wiley & Sons, 1991.

71. Kockelmann, H. Mechanical Methods of Determining Residual Stresses. In: *Residual Stresses: Measurement, Calculation, Evaluation*, edited by Hauk, V., Hougardy, H. and Macherauch, E. Germany: DGM Informationsgesellschaft mbh, 1991, p. 37-52.

72. Keil, S. Methods of Determining Residual Stresses in Metal Parts using Strain Gauges. In: *Residual Stresses: Measurement, Calculation, Evaluation*, edited by Hauk, V., Hougardy, H. and Macherauch, E. Germany: DGM Informationsgesellschaft mbh, 1991, p. 53-58.

73. Perry, C.C. and Lissner, H.R. *The Strain Gage Primer*, Ed. 2, New York, NY:McGraw-Hill Book Company, 1962.

74. Rudd, C.O. *Review and Evaluation of Nondestructive Methods for Residual Stress Measurement*, EPRI NP-1971, 1981.

75. TN-503-3: Measurement of Residual Stresses by the Hole-Drilling Strain Gage Method. In: *Measurements Group Tech Note*, Raleigh, NC 27611: Measurements Group, Inc., 1988.

76. *ASTM E837-92: Standard Test Method for Determining Residual Stresses by the Hole-Drilling Strain-Gage Method*, 1994.

77. Popelar, C.H., Barber, T. and Groom, J.J. A Method for Determining Residual Stresses in Pipes. *Journal of Pressure Vessel Technology, Transactions of the ASME* 104:223-228, 1982.

78. Cheng, W. *Computation of Stress Intensity factors and Measurements of Residual Stresses in Welded Thin-Walled Cylinders*, Ph.D. Thesis, University of California at Berkeley, 1984.

79. Cheng, W. and Finnie, I. A Method for Measurement of Axisymmetric Axial Residual Stresses in Circumferentially Welded Thin-Walled Cylinders. *Journal of Engineering Materials and Technology, Transactions of the ASME* 107:181-185, 1985.

80. Cheng, W. and Finnie, I. Measurement of Residual Hoop Stresses in Cylinders Using the Compliance Method. *Journal of Engineering Materials and Technology, Transactions of the ASME* 108:87-92, 1986.

81. Cheng, W. and Finnie, I. A New Method for Measurement of Residual Axial Stress Applied to a Multi-Pass Butt-Welded Cylinder. *Journal of Engineering Materials and Technology, Transactions of the ASME* 109:337-342, 1987.

82. Cheng, W. and Finnie, I. The Crack Compliance Method for Residual Stress Measurement. *Welding in the World* 28:103-110, 1990.

83. Cheng, W., Finnie, I. and Vardar, O. Measurement of Residual Stresses Near the Surface Using Crack Compliance Method. *Journal of Engineering Materials and Technology, Transactions of the ASME* 113:199-204, 1991.

84. Cheng, W. and Finnie, I. A Comparison of the Strains Due to Edge Cracks and Cuts of Finite Width With Applications to Residual Stress Measurement. *Journal of Engineering Materials and Technology, Transactions of the ASME* 115:220-226, 1993.

85. Cheng, W., Finnie, I., Gremaud, M. and Prime, M.B. Measurement of Near Surface Residual Stresses Using Electric Discharge Wire Machining. *Journal of Engineering Materials and Technology, Transactions of the ASME* 116:1-7, 1994.

86. Ueda, Y. and Fukuda, K. Simplified Measuring Methods of Three Dimensional Welding Residual Stresses. *Transactions of the Japanese Welding Research Institute in Osaka University* 11(2):95-104, 1982.

87. Ueda, Y., Fukuda, K. and Kim, Y.C. New Measuring Method of Axisymmetric Three-Dimensional Residual Stresses Using Inherent Strains as Parameters. *Journal of Engineering Materials and Technology, Transactions of the ASME* 108:328-334, 1986.

88. Ueda, Y., Kim, Y.C. and Yuan, M.G. A Predicting Method of Welding Residual Stress Using Source of Residual Stress (Report 1). *Transactions of the Japanese Welding Research Institute in Osaka University* 18:135-141, 1989.

89. *Non-destructive Measurement and Analysis of Residual Stress in and around Welds - A State of Art Survey*, Bulletin 383, Welding Research Council, 1993.

90. Cohen, J.B. X-Ray Techniques for the Measurement of Residual Stresses in the Real World. In: *Residual Stress for Designers and Metallurgists*, edited by Vande Walle, L.J. Metals Park, Ohio: ASM, 1981, p. 211-221.

91. Noyan, I.C. and Cohen, J.B. *Residual Stress: Measurement by Diffraction and Interpretation (Materials Research and Engineering)*, New York, USA:Springer-Verlag, 1987.

92. Peck, C.A. Practical Aspects of Residual Stress Measurement by X-Ray Diffraction. In: *Residual Stress in Design, Process and Materials Selection*, edited by Young, W.B. Materials Park, Ohio: ASM International, 1987, p. 7-9.

93. Hauk, V. Problems of the X-Ray Stress Analysis (RSA) and Their Solutions. In: *Residual Stresses: Measurement, Calculation, Evaluation*, edited by Hauk, V., Hougardy, H. and Macherauch, E. Germany: DGM Informationsgesellschaft mbh, 1991, p. 3-20.

94. Hosbons, R.R., Ibrahim, E.F., Holden, T.M. and Root, J.H. The Use of Neutron Diffraction to Determine Non-Destructively the Residual Strain and Texture in Welds. In: *Recent Trends in Welding Science and Technology*, edited by David, S.A. and Vitek, J.M. Materials Park, Ohio: ASM International, 1990, p. 103-106.

95. Krawitz, A.D. and Holden, T.M. The Measurement of Residual Stresses Using Neutron Diffraction. *MRS Bulletin* XV:57-64, 1990.

96. Hutchings, M.T. Neutron Diffraction Measurement of Residual Stress Fields: Overview and Points for Discussion. In: *Measurement of Residual and Applied Stress Using Neutron Diffraction*, edited by Hutchings, M.T. and Krawitz, A.D. Dordrecht, The Netherlands: Kluwer Academic Publishers, 1992, p. 3-18.

97. Webster, P.J. Welding Applications of Neutron Strain Scanning. In: *International Trends in Welding Science and Technology*, edited by David, S.A. and Vitek, J.M. Materials Park, Ohio: ASM International, 1993, p. 95-98.

98. Root, J.H., Holden, T.M., Schröder, J., Spooner, S., Hubbard, C.A., Dodson, T.A. and David, S.A. Residual Stresses in a Multipass Ferritic Weldment. In: *International trends in Welding Science and Technology*, edited by David, S.A. and Vitek, J.M. Materials Park, Ohio: ASM International, 1993, p. 99-103.

99. Spooner, S., David, S.A., Root, J.H., Holden, T.M., Bourke, M.A.M. and Goldstone, J.A. Residual Stress and Strain Measurements in an Austenitic Steel Plate Containing a Multipass Weld. In: *International Trends in Welding Science and Technology*, edited by David, S.A. and Vitek, J.M. Materials Park, Ohio: ASM International , 1993, p. 139-143.

100. Root, J.H., Holden, T.M., Schröder, J., Hubbard, C.R., Spooner, S., Dodson, T.A. and David, S.A. Residual stress mapping in multipass ferritic steel weld. *Materials Science and Technology* 9:754-759, 1993.

101. Schneider, E. and Goebbels, K. Nondestructive Evaluation of Residual Stress States Using Ultrasonic Techniques. In: *Residual Stresses*, edited by Macherauch, E. and Hauk, V. Alle Rechte vorbehalten., Germany: DGM Informationsgesellschaft mbh, 1986, p. 247-261.

102. Boiling Water Reactor Owners Group, *Boiling Water Reactor Owners Group Intergranular Stress Corrosion Cracking Research Program: Executive Summary Phase 1 (1979-1983)*, EPRI NP-4273-SR, 1985.

103. Umemoto, T. and Tanaka, S. Residual Stress Improvement by Means of Induction Heating. *IHI Engineering Review* 11(4):1978.

104. Rybicki, E.F. and McGuire, P.A. The Effects of Induction Heating Conditions on Controlling Residual Stresses in Welded Pipes. *Journal of Engineering Materials and Technology, Transactions of the ASME* 104:267-273, 1982.

105. Offer, H.P. *Induction Heating Stress Improvement*, EPRI NP-3375, 1983.

106. Koch, R.L., Rybicki, E.F. and Strattan, R.D. A Computational Temperature Analysis for Induction Heating of Welded Pipes. *Journal of Engineering Materials and Technology, Transactions of the ASME* 107:148-153, 1985.

107. Brust, F.W. and Rybicki, E.F. A Computational Model of Backlay Welding for Controlling Residual Stresses in Welded Pipes. *Journal of Pressure Vessel Technology, Transactions of the ASME* 103:226-232, 1981.

108. Brust, F.W. and Kanninen, M.F. Analysis of Residual Stresses in Girth Welded Type 304 Stainless Steel Pipes. *J. Materials for Energy Systems* 3:56-62, 1981.

109. Abel, J.S., Titrington, J., Jordan, R., Porowski, J.S., O'Donnell, W.J., Badlani, M.L. and Hampton, E.J. Mechanical Methods of Improving Resistance to Stress Corrosion Cracking in BWR Piping Systems. *Int. J. Pres. Ves. & Piping* 34:17-29, 1988.

110. Porowski, J.S., O'Donnell, W.J., Badlani, M.L. and Hampton, E.J. New Mechanical and Thermal Processes for Mitigating Stress-Corrosion and Corrosion-Accelerated Fatigue. *Int. J. Pres. Ves. & Piping* 50:63-79, 1992.

111. Ueda, Y. and Murakawa, H. New Trends of Research on Mechanics in Welding and Fabrication in Japan. *Transactions of the Japanese Welding Research Institute in Osaka University* 22(2):189-200, 1993.

112. Anderson, W.E. *Private Communication*, 1992. (Unpublished)

113. *ANSYS 5.0 Engineering Analysis System*, Swanson Analysis System, Inc., 1992.

114. Lancaster, J.F. *The Physics of Welding*, Ed. 2, Oxford, UK:Pergamon Press, 1986.

115. Leibowitz, L. Properties for LMFBR Safety Analysis. *ANL-CEN-RSD-76-1* 116, 1976.

116. Shapiro, A.B. and Mahin, K.W. Thermomechanical Modeling of Gas Tungsten Arc Welding. *Journal of Eng. Comp. and Applications* 1(4):28-34, 1987.

117. Dushman, S. *Scientific Foundations of Vacuum Technique*, Ed.2, New York, N.Y.:John Wiley and Sons, 1962.

118. Block-Bolten, A. and Eagar, T.W. Metal Vaporization from Weld Pools. *Metallurgical Transactions B* 15B:461-469, 1984.

119. Barnes, P.K. *Reduction of Residual Stresses and Distortion in Girth Welded Pipes*, M.S. Thesis, Dept. of Ocean Engineering, M.I.T., 1987.

120. Masubuchi, K., Luebke, W.H. and Itoh, H. Novel Techniques and Their Applications for Measuring Out-of-Plane Distortion of Welded Structures. *Journal of Ship Production* 4(2):73-80, 1988.

121. Masubuchi, K. In-Process Control and Reduction of Residual Stresses and Distortion in Weldments. In: *Practical Applications of Residual Stress Technology*, edited by Rudd, C. Materials Park, Ohio: ASM International, 1991, p. 95-101.

122. Masubuchi, K. Research Activities Examine Residual Stresses and Distortion in Welded Structures. *Welding Journal* 70(12):41-47, 1991.

123. Leggatt, R.H. Residual stresses at circumferential welds in pipes. *The Welding Institute Research Bulletin* 23:181-188, 1982.

124. Timoshenko, S. and Woinowsky-Krieger, S. *Theory of Plates and Shells*, Ed. 2, McGraw-Hill , 1959.

125. Makhnenko, V.I., Shekera, V.M. and Izebenko, L.A. Special Feasures of the Distribution of Stresses and Strains Caused by Making Circumferential Welds in Cylindrical Shells. *Automatic Welding* 23 (10):43-48, 1970.

APPENDIX A

The following program is the ANSYS input file for 3D heat transfer analysis of narrow gap pipe welding process.

```
/PREP7
ET,1,70
mp,dens,1,8000
mp,hf,1,1.0
mptemp,1,0,100,200,300,400,500
mptemp,7,600,700,800,900,1000,1100
mptemp,13,1200,1300,1400,1500,1600,1673
mptemp,19,1673.1,1723,3100
mpdata,kxx,1,1,8.116,9.734,11.352,12.97,14.588,16.206
mpdata,kxx,1,7,17.824,19.442,21.06,22.678,24.296,25.914
mpdata,kxx,1,13,27.532,29.15,30.768,32.386,34.004,35.185
mpdata,kxx,1,19,35.186,41.358,211.111
!mpdata,kxx,1,19,35.186,41.358,111.111
mpdata,c,1,1,465.4,478.76,492.12,505.48,518.84,532.2
mpdata,c,1,7,545.56,558.92,572.28,585.64,599.0,612.36
mpdata,c,1,13,625.72,639.08,652.44,665.8,679.16,688.913
mpdata,c,1,19,688.914,788.0,788.0
mpdata,enth,1,1,0.0,3.77664e08,7.66016e08,1.16505e09,1.57478e09,1.9952e09
mpdata,enth,1,7,2.4263e09,2.86809e09,3.32057e09,3.78374e09,4.2576e09,4.74214e09
mpdata,enth,1,13,5.23737e09,5.74329e09,6.2599e09,6.7872e09,7.32518e09,7.72466e09
mpdata,enth,1,19,9.84466e09,1.014e10,1.88206e10
csys,1
N,1,7.5*0.0254
NGEN,120,1,1,,,,3.0
NGEN,2,120,1,120,1,0.0625*0.0254
NGEN,4,120,121,240,1,0.4375*0.0254/3.0
NGEN,3,600,1,600,1,,,0.0625*0.0254
NGEN,2,600,1201,1800,1,,,0.125*0.0254
NGEN,2,600,1801,2400,1,,,0.5*0.0254
NGEN,2,600,2401,3000,1,,,0.75*0.0254
NGEN,2,600,3001,3600,1,,,2.50*0.0254
```

```
NGEN,2,600,3601,4200,1,,,4.00*0.0254
E,1,2,602,601,121,122,722,721
EGEN,119,1,1
E,120,1,601,720,240,121,721,840
egen,4,120,1,120,1
egen,7,600,1,480,1
wsort,y
save
fini
/solu
antype,trans,new
timint,off
time,1e-06
nropt,full,,on
tunif,298
nsel,s,loc,z,0
dsym,symm,z
nsel,all
esel,s,elem,,121,480
ekill,all
esel,all
esel,s,elem,,601,960
ekill,all
esel,all
esel,s,live
nsle,s
nsel,inve
d,all,temp,298
nsel,all
esel,all
esel,s,live
esel,r,elem,,2881,3360
sfe,all,4,conv,0,-1
sfe,all,4,conv,2,298
esel,all
esel,s,live
esel,r,elem,,1,120
sfe,all,1,conv,0,-1
sfe,all,1,conv,2,298
esel,all
esel,s,live
esel,r,elem,,481,600
```

```
sfe,all,1,conv,0,-1
sfe,all,1,conv,2,298
esel,all
esel,s,live
esel,r,elem,,961,1080
sfe,all,1,conv,0,-1
sfe,all,1,conv,2,298
esel,all
esel,s,live
esel,r,elem,,1441,1560
sfe,all,1,conv,0,-1
sfe,all,1,conv,2,298
esel,all
esel,s,live
esel,r,elem,,1921,2040
sfe,all,1,conv,0,-1
sfe,all,1,conv,2,298
esel,all
esel,s,live
esel,r,elem,,2401,2520
sfe,all,1,conv,0,-1
sfe,all,1,conv,2,298
esel,all
esel,s,live
esel,r,elem,,2881,3000
sfe,all,1,conv,0,-1
sfe,all,1,conv,2,298
esel,all
esel,s,live
esel,r,elem,,1321,1440
sfe,all,6,conv,0,-1
sfe,all,6,conv,2,298
esel,all
esel,s,live
esel,r,elem,,1801,1920
sfe,all,6,conv,0,-1
sfe,all,6,conv,2,298
esel,all
esel,s,live
esel,r,elem,,2281,2400
sfe,all,6,conv,0,-1
sfe,all,6,conv,2,298
```

```
esel,all
esel,s,live
esel,r,elem,,2761,2880
sfe,all,6,conv,0,-1
sfe,all,6,conv,2,298
esel,all
esel,s,live
esel,r,elem,,3241,3360
sfe,all,6,conv,0,-1
sfe,all,6,conv,2,298
esel,all
esel,s,live
esel,r,elem,,1,120
sfe,all,6,conv,0,-1
sfe,all,6,conv,2,298
esel,all
esel,s,live
esel,r,elem,,481,600
sfe,all,6,conv,0,-1
sfe,all,6,conv,2,298
esel,all
esel,s,live
esel,r,elem,,1081,1440
sfe,all,2,conv,0,-1
sfe,all,2,conv,2,298
esel,all
save
solve
pi=acos(-1)
*DO,I,1,119
L=I/3.0
J=NINT(L)
K=3*J+1
*IF,I,LE,3,THEN
outres,erase
outres,all,last
*ELSEIF,I,EQ,K
outres,erase
outres,all,last
*ELSE
outres,erase
outres,all,none
```

```
*ENDIF
*IF,I,EQ,1,THEN
esel,s,live
esel,r,elem,,I,I+480,480
sfedele,all,6,hflux
bfedele,all,hgen
sfe,all,6,conv,0,-1
sfe,all,6,conv,2,298
esel,all
*ELSE
esel,s,live
esel,r,elem,,I-1,I+479,480
sfedele,all,6,hflux
bfedele,all,hgen
sfe,all,6,conv,0,-1
sfe,all,6,conv,2,298
esel,all
esel,s,live
esel,r,elem,,I,I+480,480
sfedele,all,6,hflux
bfedele,all,hgen
sfe,all,6,conv,0,-1
sfe,all,6,conv,2,298
esel,all
*ENDIF
timint,on
kbc,0
autots,on
nsubst,100
time,(2*i*pi*7.5625*60/3.7/120)
ncnv,0,
esel,s,live
esel,r,elem,,I
sfedele,all,6,conv
sfe,all,6,hflux,,0,29195938.0,12937921.0,0
bfe,all,hgen,5,0,1.87207e10,8.29647e09,0
bfe,all,hgen,1,0,8.29647e09,3.67675e09,0
esel,all
esel,s,live
esel,r,elem,,I+480
sfedele,all,6,conv
sfe,all,6,hflux,,0,0,1287049.8,0
```

```
bfe,all,hgen,5,0,0,8.25270e08,0
bfe,all,hgen,1,0,0,3.6573e08,0
esel,all
esel,s,live
esel,r,elem,,I+1
sfedele,all,6,conv
sfe,all,6,hflux,,12512545.0,0,0,5544823.1
bfe,all,hgen,5,8.02318e09,0,0,3.55563e09
bfe,all,hgen,1,3.55563e09,0,0,1.57575e09
esel,all
esel,s,live
esel,r,elem,,I+481
sfedele,all,6,conv
sfe,all,6,hflux,,0,0,0,321762.46
bfe,all,hgen,5,0,0,0,2.06317e08
bfe,all,hgen,1,0,0,0,9.1433e07
esel,all
save
solve
*ENDDO
outres,erase
outres,all,last
esel,s,live
esel,r,elem,,120,600,480
sfedele,all,6,hflux
bfedele,all,hgen
sfe,all,6,conv,0,-1
sfe,all,6,conv,2,298
esel,all
esel,s,live
esel,r,elem,,119,599,480
sfedele,all,6,hflux
bfedele,all,hgen
sfe,all,6,conv,0,-1
sfe,all,6,conv,2,298
esel,all
esel,s,live
esel,r,elem,,1,481,480
sfedele,all,6,conv
esel,all
esel,s,live
esel,r,elem,,120
```

```
sfedele,all,6,conv
sfe,all,6,hflux,,0,29195938.0,12937921.0,0
bfe,all,hgen,5,0,1.87207e10,8.29647e09,0
bfe,all,hgen,1,0,8.29647e09,3.67675e09,0
esel,all
esel,s,live
esel,r,elem,,600
sfedele,all,6,conv
sfe,all,6,hflux,,0,0,1287049.8,0
bfe,all,hgen,5,0,0,8.25270e08,0
bfe,all,hgen,1,0,0,3.6573e08,0
esel,all
esel,s,live
esel,r,elem,,1081
sfedele,all,2,conv
esel,all
nsel,s,node,,241,242
ddele,all,temp
nsel,all
nsel,s,node,,841,842
ddele,all,temp
nsel,all
esel,s,elem,,121
ealive,all
sfe,all,5,conv,0,-1
sfe,all,5,conv,2,298
sfe,all,3,conv,0,-1
sfe,all,3,conv,2,298
sfe,all,6,hflux,,12512545.0,0,0,5544823.1
bfe,all,hgen,5,8.02318e09,0,0,3.55563e09
bfe,all,hgen,1,3.55563e09,0,0,1.57575e09
esel,all
esel,s,elem,,601
ealive,all
sfe,all,5,conv,0,-1
sfe,all,5,conv,2,298
sfe,all,3,conv,0,-1
sfe,all,3,conv,2,298
sfe,all,6,hflux,,0,0,0,321762.46
bfe,all,hgen,5,0,0,0,2.06317e08
bfe,all,hgen,1,0,0,0,9.1433e07
esel,all
```

```
nsubst,100
time,(2*pi*7.5625*60/3.7)
save
solve
fini
/exit
resu
/solu
antype,,restart
*DO,I,1,119
L=I/3.0
J=NINT(L)
K=3*J+1
*IF,I,LE,3,THEN
outres,erase
outres,all,last
*ELSEIF,I,EQ,K
outres,erase
outres,all,last
*ELSE
outres,erase
outres,all,none
*ENDIF
*IF,I,EQ,1,THEN
esel,s,elem,,I+1,I+481,480
sfedele,all,6,conv
esel,all
esel,s,elem,,120,600,480
sfedele,all,6,hflux
bfedele,all,hgen
sfe,all,6,conv,0,-1
sfe,all,6,conv,2,298
esel,all
esel,s,elem,,121,601,480
sfedele,all,6,hflux
sfedele,all,3,conv
bfedele,all,hgen
sfe,all,6,conv,0,-1
sfe,all,6,conv,2,298
esel,all
*ELSE
esel,s,elem,,I+1,I+481,480
```

```
sfedele,all,6,conv
esel,all
esel,s,elem,,I+119,I+599,480
sfedele,all,6,hflux
bfedele,all,hgen
sfe,all,6,conv,0,-1
sfe,all,6,conv,2,298
esel,all
esel,s,elem,,I+120,I+600,480
sfedele,all,6,hflux
sfedele,all,3,conv
bfedele,all,hgen
sfe,all,6,conv,0,-1
sfe,all,6,conv,2,298
esel,all
*ENDIF
esel,s,elem,,I+120
sfedele,all,6,conv
sfe,all,6,hflux,,0,39706475.0,17595572.0,0
bfe,all,hgen,5,0,2.54602e10,1.12832e10,0
bfe,all,hgen,1,0,3.03134e08,1.34339e08,0
esel,all
esel,s,elem,,I+600
sfedele,all,6,conv
sfe,all,6,hflux,,0,0,1750387.8,0
bfe,all,hgen,5,0,0,1.12237e09,0
bfe,all,hgen,1,0,0,13363073.0,0
esel,all
esel,s,elem,,I+1081
sfedele,all,2,conv
esel,all
*IF,I,LT,119,THEN
nsel,s,node,,I+242,I+842,600
ddele,all,temp
nsel,all
esel,s,elem,,I+121
ealive,all
sfe,all,3,conv,0,-1
sfe,all,3,conv,2,298
sfe,all,6,hflux,,17017061.0,0,0,7540959.5
bfe,all,hgen,5,1.09115e10,0,0,4.83566e09
bfe,all,hgen,1,1.29914e08,0,0,5.75740e07
```

```
esel,all
esel,s,elem,,I+601
ealive,all
sfe,all,3,conv,0,-1
sfe,all,3,conv,2,298
sfe,all,6,hflux,,0,0,0,437596.94
bfe,all,hgen,5,0,0,0,2.80592e08
bfe,all,hgen,1,0,0,0,3340768.3
esel,all
*ELSE
esel,s,elem,,121,601,480
sfedele,all,5,conv
esel,all
esel,s,elem,,I+121
ealive,all
sfe,all,6,hflux,,17017061.0,0,0,7540959.5
bfe,all,hgen,5,1.09115e10,0,0,4.83566e09
bfe,all,hgen,1,1.29914e08,0,0,5.75740e07
esel,all
esel,s,elem,,I+601
ealive,all
sfe,all,6,hflux,,0,0,0,437596.94
bfe,all,hgen,5,0,0,0,2.80592e08
bfe,all,hgen,1,0,0,0,3340768.3
esel,all
*ENDIF
time,(2*i*pi*(7.5625+(8.0-7.5625)/3.0)/8.0)+770.53928
save
solve
*ENDDO
outres,erase
outres,all,last
esel,s,elem,,240,720,480
sfedele,all,6,hflux
bfedele,all,hgen
sfe,all,6,conv,0,-1
sfe,all,6,conv,2,298
esel,all
esel,s,elem,,239,719,480
sfedele,all,6,hflux
bfedele,all,hgen
sfe,all,6,conv,0,-1
```

```
sfe,all,6,conv,2,298
esel,all
esel,s,elem,,121,601,480
sfedele,all,6,conv
esel,all
esel,s,elem,,240
sfedele,all,6,conv
sfe,all,6,hflux,,0,39706475.0,17595572.0,0
bfe,all,hgen,5,0,2.54602e10,1.12832e10,0
bfe,all,hgen,1,0,3.03134e08,1.34339e08,0
esel,all
esel,s,elem,,720
sfedele,all,6,conv
sfe,all,6,hflux,,0,0,1750387.8,0
bfe,all,hgen,5,0,0,1.12237e09,0
bfe,all,hgen,1,0,0,13363073.0,0
esel,all
esel,s,elem,,1201
sfedele,all,2,conv
esel,all
nsel,s,node,,361,362
ddele,all,temp
nsel,all
nsel,s,node,,961,962
ddele,all,temp
nsel,all
esel,s,elem,,241
ealive,all
sfe,all,5,conv,0,-1
sfe,all,5,conv,2,298
sfe,all,3,conv,0,-1
sfe,all,3,conv,2,298
sfe,all,6,hflux,,17017061.0,0,0,7540959.5
bfe,all,hgen,5,1.09115e10,0,0,4.83566e09
bfe,all,hgen,1,1.29914e08,0,0,5.75740e07
esel,all
esel,s,elem,,721
ealive,all
sfe,all,5,conv,0,-1
sfe,all,5,conv,2,298
sfe,all,3,conv,0,-1
sfe,all,3,conv,2,298
```

```
sfe,all,6,hflux,,0,0,0,437596.94
bfe,all,hgen,5,0,0,0,2.80592e08
bfe,all,hgen,1,0,0,0,3340768.3
esel,all
nsubst,100
time,(2*120*pi*(7.5625+(8.0-7.5625)/3.0)/8.0)+770.53928
save
solve
fini
/exit
resu
/solu
antype,,restart
*DO,I,1,119
L=I/3.0
J=NINT(L)
K=3*J+1
*IF,I,LE,3,THEN
outres,erase
outres,all,last
*ELSEIF,I,EQ,K
outres,erase
outres,all,last
*ELSE
outres,erase
outres,all,none
*ENDIF
*IF,I,EQ,1,THEN
esel,s,elem,,I+121,I+601,480
sfedele,all,6,conv
esel,all
esel,s,elem,,240,720,480
sfedele,all,6,hflux
bfedele,all,hgen
sfe,all,6,conv,0,-1
sfe,all,6,conv,2,298
esel,all
esel,s,elem,,241,721,480
sfedele,all,6,hflux
sfedele,all,3,conv
bfedele,all,hgen
sfe,all,6,conv,0,-1
```

```
sfe,all,6,conv,2,298
esel,all
*ELSE
esel,s,elem,,I+121,I+601,480
sfedele,all,6,conv
esel,all
esel,s,elem,,I+239,I+719,480
sfedele,all,6,hflux
bfedele,all,hgen
sfe,all,6,conv,0,-1
sfe,all,6,conv,2,298
esel,all
esel,s,elem,,I+240,I+720,480
sfedele,all,6,hflux
sfedele,all,3,conv
bfedele,all,hgen
sfe,all,6,conv,0,-1
sfe,all,6,conv,2,298
esel,all
*ENDIF
esel,s,elem,,I+240
sfedele,all,6,conv
sfe,all,6,hflux,,0,54090340.0,23969654.0,0
bfe,all,hgen,5,0,3.46833e10,1.53706e10,0
bfe,all,hgen,1,0,4.12945e08,1.83004e08,0
esel,all
esel,s,elem,,I+720
sfedele,all,6,conv
sfe,all,6,hflux,,0,0,2384474.3,0
bfe,all,hgen,5,0,0,1.52895e09,0
bfe,all,hgen,1,0,0,18203912.0,0
esel,all
esel,s,elem,,I+1201
sfedele,all,2,conv
esel,all
*IF,I,LT,119,THEN
nsel,s,node,,I+362,I+962,600
ddele,all,temp
nsel,all
esel,s,elem,,I+241
ealive,all
sfe,all,3,conv,0,-1
```

```
sfe,all,3,conv,2,298
sfe,all,6,hflux,,23181574.0,0,0,10272709.0
bfe,all,hgen,5,1.48643e10,0,0,6.58740e09
bfe,all,hgen,1,1.76977e08,0,0,7.84305e07
esel,all
esel,s,elem,,I+721
ealive,all
sfe,all,3,conv,0,-1
sfe,all,3,conv,2,298
sfe,all,6,hflux,,0,0,0,596118.58
bfe,all,hgen,5,0,0,0,3.82237e08
bfe,all,hgen,1,0,0,0,4550978.0
esel,all
*ELSE
esel,s,elem,,241,721,480
sfedele,all,5,conv
esel,all
esel,s,elem,,I+241
ealive,all
sfe,all,6,hflux,,23181574.0,0,0,10272709.0
bfe,all,hgen,5,1.48643e10,0,0,6.58740e09
bfe,all,hgen,1,1.76977e08,0,0,7.84305e07
esel,all
esel,s,elem,,I+721
ealive,all
sfe,all,6,hflux,,0,0,0,596118.58
bfe,all,hgen,5,0,0,0,3.82237e08
bfe,all,hgen,1,0,0,0,4550978.0
esel,all
*ENDIF
time,(2*i*pi*(7.5625+(8.0-7.5625)*2.0/3.0)/8.0)+1497.0326
save
solve
*ENDDO
outres,erase
outres,all,last
esel,s,elem,,360,840,480
sfedele,all,6,hflux
bfedele,all,hgen
sfe,all,6,conv,0,-1
sfe,all,6,conv,2,298
esel,all
```

```
esel,s,elem,,359,839,480
sfedele,all,6,hflux
bfedele,all,hgen
sfe,all,6,conv,0,-1
sfe,all,6,conv,2,298
esel,all
esel,s,elem,,241,721,480
sfedele,all,6,conv
esel,all
esel,s,elem,,360
sfedele,all,6,conv
sfe,all,6,hflux,,0,54090340.0,23969654.0,0
bfe,all,hgen,5,0,3.46833e10,1.53706e10,0
bfe,all,hgen,1,0,4.12945e08,1.83004e08,0
esel,all
esel,s,elem,,840
sfedele,all,6,conv
sfe,all,6,hflux,,0,0,2384474.3,0
bfe,all,hgen,5,0,0,1.52895e09,0
bfe,all,hgen,1,0,0,18203912.0,0
esel,all
esel,s,elem,,1321
sfedele,all,2,conv
esel,all
nsel,s,node,,481,482
ddele,all,temp
nsel,all
nsel,s,node,,1081,1082
ddele,all,temp
nsel,all
esel,s,elem,,361
ealive,all
sfe,all,5,conv,0,-1
sfe,all,5,conv,2,298
sfe,all,3,conv,0,-1
sfe,all,3,conv,2,298
sfe,all,6,hflux,,23181574.0,0,0,10272709.0
bfe,all,hgen,5,1.48643e10,0,0,6.58740e09
bfe,all,hgen,1,1.76977e08,0,0,7.84305e07
esel,all
esel,s,elem,,841
ealive,all
```

```
sfe,all,5,conv,0,-1
sfe,all,5,conv,2,298
sfe,all,3,conv,0,-1
sfe,all,3,conv,2,298
sfe,all,6,hflux,,0,0,0,596118.58
bfe,all,hgen,5,0,0,0,3.82237e08
bfe,all,hgen,1,0,0,0,4550978.0
esel,all
nsubst,100
time,(2*120*pi*(7.5625+(8.0-7.5625)*2.0/3.0)/8.0)+1497.0326
save
solve
fini
/exit
resu
/solu
antype,,restart
*DO,I,1,119
L=I/3.0
J=NINT(L)
K=3*J+1
*IF,I,LE,3,THEN
outres,erase
outres,all,last
*ELSEIF,I,EQ,K
outres,erase
outres,all,last
*ELSE
outres,erase
outres,all,none
*ENDIF
*IF,I,EQ,1,THEN
esel,s,elem,,I+241,I+721,480
sfedele,all,6,conv
esel,all
esel,s,elem,,360,840,480
sfedele,all,6,hflux
bfedele,all,hgen
sfe,all,6,conv,0,-1
sfe,all,6,conv,2,298
esel,all
esel,s,elem,,361,841,480
```

```
sfedele,all,6,hflux
sfedele,all,3,conv
bfedele,all,hgen
sfe,all,6,conv,0,-1
sfe,all,6,conv,2,298
esel,all
*ELSE
esel,s,elem,,I+241,I+721,480
sfedele,all,6,conv
esel,all
esel,s,elem,,I+359,I+839,480
sfedele,all,6,hflux
bfedele,all,hgen
sfe,all,6,conv,0,-1
sfe,all,6,conv,2,298
esel,all
esel,s,elem,,I+360,I+840,480
sfedele,all,6,hflux
sfedele,all,3,conv
bfedele,all,hgen
sfe,all,6,conv,0,-1
sfe,all,6,conv,2,298
esel,all
*ENDIF
esel,s,elem,,I+360
sfedele,all,6,conv
sfe,all,6,hflux,,0,41093282.0,18177779.0,0
bfe,all,hgen,5,0,2.63494e10,1.16565e10,0
bfe,all,hgen,1,0,3.13721e08,1.38784e08,0
esel,all
esel,s,elem,,I+840
sfedele,all,6,conv
sfe,all,6,hflux,,0,0,1808305.0,0
bfe,all,hgen,5,0,0,1.15956e09,0
bfe,all,hgen,1,0,0,13805234.0,0
esel,all
esel,s,elem,,I+1321
sfedele,all,2,conv
esel,all
*IF,I,LT,119,THEN
nsel,s,node,,I+482,I+1082,600
ddele,all,temp
```

```
nsel,all
esel,s,elem,,I+361
ealive,all
sfe,all,3,conv,0,-1
sfe,all,3,conv,2,298
sfe,all,6,hflux,,17611407.0,0,0,7790476.5
bfe,all,hgen,5,1.12926e10,0,0,2.99740e09
bfe,all,hgen,1,1.34452e08,0,0,5.94790e07
esel,all
esel,s,elem,,I+841
ealive,all
sfe,all,3,conv,0,-1
sfe,all,3,conv,2,298
sfe,all,6,hflux,,0,0,0,452076.20
bfe,all,hgen,5,0,0,0,2.89876e08
bfe,all,hgen,1,0,0,0,3451308.4
esel,all
*ELSE
esel,s,elem,,361,841,480
sfedele,all,5,conv
esel,all
esel,s,elem,,I+361
ealive,all
sfe,all,6,hflux,,17611407.0,0,0,7790476.5
bfe,all,hgen,5,1.12926e10,0,0,2.99740e09
bfe,all,hgen,1,1.34452e08,0,0,5.94790e07
esel,all
esel,s,elem,,I+841
ealive,all
sfe,all,6,hflux,,0,0,0,452076.20
bfe,all,hgen,5,0,0,0,2.89876e08
bfe,all,hgen,1,0,0,0,3451308.4
esel,all
*ENDIF
time,(2*i*pi*(7.5625+(8.0-7.5625))/8.0)+2237.2704
save
solve
*ENDDO
outres,erase
outres,all,last
esel,s,elem,,480,960,480
sfedele,all,6,hflux
```

```
bfedele,all,hgen
sfe,all,6,conv,0,-1
sfe,all,6,conv,2,298
esel,all
esel,s,elem,,479,959,480
sfedele,all,6,hflux
bfedele,all,hgen
sfe,all,6,conv,0,-1
sfe,all,6,conv,2,298
esel,all
esel,s,elem,,361,841,480
sfedele,all,6,conv
esel,all
esel,s,elem,,480
sfedele,all,6,conv
sfe,all,6,hflux,,0,41093282.0,18177779.0,0
bfe,all,hgen,5,0,2.63494e10,1.16565e10,0
bfe,all,hgen,1,0,3.13721e08,1.38784e08,0
esel,all
esel,s,elem,,960
sfedele,all,6,conv
sfe,all,6,hflux,,0,0,1808305.0,0
bfe,all,hgen,5,0,0,1.15956e09,0
bfe,all,hgen,1,0,0,13805234.0,0
esel,all
esel,s,elem,,361
sfedele,all,6,conv
sfe,all,6,hflux,,17611407.0,0,0,7790476.5
bfe,all,hgen,5,1.12926e10,0,0,2.99740e09
bfe,all,hgen,1,1.34452e08,0,0,5.94790e07
esel,all
esel,s,elem,,841
sfedele,all,6,conv
sfe,all,6,hflux,,0,0,0,452076.20
bfe,all,hgen,5,0,0,0,2.89876e08
bfe,all,hgen,1,0,0,0,3451308.4
esel,all
nsubst,100
time,(2*120*pi*(7.5625+(8.0-7.5625))/8.0)+2237.2704
save
solve
esel,s,elem,,480,960,480
```

```
sfedele,all,6,hflux
bfedele,all,hgen
sfe,all,6,conv,0,-1
sfe,all,6,conv,2,298
esel,all
esel,s,elem,,361,841,480
sfedele,all,6,hflux
bfedele,all,hgen
sfe,all,6,conv,0,-1
sfe,all,6,conv,2,298
esel,all
time,2996.2586
nsubst,100
save
solve
time,3001.2586
nsubst,100
save
solve
time,3006.2586
nsubst,100
save
solve
time,3011.2586
nsubst,100
save
solve
time,3021.2586
nsubst,100
save
solve
time,3031.2586
nsubst,100
save
solve
time,3041.2586
nsubst,100
save
solve
time,3071.2586
nsubst,100
save
```

```
solve
time,3101.2586
nsubst,100
save
solve
time,3161.2586
nsubst,100
save
solve
time,3221.2586
nsubst,100
save
solve
time,3521.2586
nsubst,100
save
solve
time,4121.2586
nsubst,100
save
solve
time,4921.2586
nsubst,100
save
solve
time,6000.0
nsubst,100
save
solve
fini
/exit
```

APPENDIX B

The following program is the ANSYS input file for 3D stress analysis of narrow gap pipe welding process.

```
/PREP7
resume,temp,db,,0
esel,all
nsel,all
ETCHG
mp,alpx,1,16.12e-06,2.85e-09
mp,reft,1,298
mp,nuxy,1,0.2620625,5.97632e-5
mpdata,ex,1,1,202.0e9,200.00e9,199.0e9,197.00e9,191.00e9,184.00e9
mpdata,ex,1,7,177.00e9,169.00e9,159.e9,146.00e9,133.00e9,120.00e9
mpdata,ex,1,13,110.00e9,85.00e9,60.000e9
tref,298
TB,BKIN,1,6
tbtemp,297
tbdata,1,233.10e6,521.670e06
tbtemp,422.00
tbdata,1,179.30e6,420.500e6
tbtemp,589.00
tbdata,1,144.80e6,2000.0e6
tbtemp,755.00
tbdata,1,130.30e6,1300.0e6
tbtemp,922.00
tbdata,1,104.8e6,800.00e6
tbtemp,1089.0
tbdata,1,68.0e6,200.00e6
save
finish
/solu
antype,0,new
time,1e-06
nlgeom,on
```

```
nropt,auto,,on
tunif,298
nsel,s,loc,z,0
dsym,symm,z
nsel,all
nsel,s,node,,4201,4800
d,all,all,0
nsel,all
kbc,0
autots,on
nsubst,10000
neqit,25
save
solve
nsel,s,node,,241,600
d,all,all,0
nsel,all
nsel,s,node,,841,1200
d,all,all,0
nsel,all
ldread,temp,2,,,,temp,rth
save
solve
ldread,temp,3,,,,temp,rth
save
solve
ldread,temp,4,,,,temp,rth
save
solve
ldread,temp,5,,,,temp,rth
save
solve
ldread,temp,17,,,,temp,rth
save
solve
ldread,temp,32,,,,temp,rth
save
solve
ldread,temp,62,,,,temp,rth
save
solve
ldread,temp,92,,,,temp,rth
```

```
save
solve
ldread,temp,119,,,,temp,rth
save
solve
nsel,s,node,,241,242
ddele,all,all
nsel,all
nsel,s,node,,841,842
ddele,all,all
nsel,all
ldread,temp,121,,,,temp,rth
save
solve
*DO,I,1,4
nsel,s,node,,242+I,842+I,600
ddele,all,all
nsel,all
ldread,temp,121+I,,,,temp,rth
save
solve
*ENDDO
nsel,s,node,,247,258
ddele,all,all
nsel,all
nsel,s,node,,847,858
ddele,all,all
nsel,all
ldread,temp,137,,,,temp,rth
save
solve
nsel,s,node,,259,273
ddele,all,all
nsel,all
nsel,s,node,,859,873
ddele,all,all
nsel,all
ldread,temp,152,,,,temp,rth
save
solve
nsel,s,node,,274,303
ddele,all,all
```

```
nsel,all
nsel,s,node,,874,903
ddele,all,all
nsel,all
ldread,temp,182,,,,temp,rth
save
solve
nsel,s,node,,304,333
ddele,all,all
nsel,all
nsel,s,node,,904,933
ddele,all,all
nsel,all
ldread,temp,212,,,,temp,rth
save
solve
nsel,s,node,,334,360
ddele,all,all
nsel,all
nsel,s,node,,934,960
ddele,all,all
nsel,all
ldread,temp,239,,,,temp,rth
save
solve
nsel,s,node,,361,362
ddele,all,all
nsel,all
nsel,s,node,,961,962
ddele,all,all
nsel,all
ldread,temp,241,,,,temp,rth
save
solve
*DO,I,1,4
nsel,s,node,,I+362,I+962,600
ddele,all,all
nsel,all
ldread,temp,I+241,,,,temp,rth
save
solve
*ENDDO
```

```
nsel,s,node,,367,378
ddele,all,all
nsel,all
nsel,s,node,,967,978
ddele,all,all
nsel,all
ldread,temp,257,,,,temp,rth
save
solve
nsel,s,node,,379,393
ddele,all,all
nsel,all
nsel,s,node,,979,993
ddele,all,all
nsel,all
ldread,temp,272,,,,temp,rth
save
solve
nsel,s,node,,394,423
ddele,all,all
nsel,all
nsel,s,node,,994,1023
ddele,all,all
nsel,all
ldread,temp,302,,,,temp,rth
save
solve
nsel,s,node,,424,453
ddele,all,all
nsel,all
nsel,s,node,,1024,1053
ddele,all,all
nsel,all
ldread,temp,332,,,,temp,rth
save
solve
nsel,s,node,,454,480
ddele,all,all
nsel,all
nsel,s,node,,1054,1080
ddele,all,all
nsel,all
```

```
ldread,temp,359,,,,temp,rth
save
solve
nsel,s,node,,481,482
ddele,all,all
nsel,all
nsel,s,node,,1081,1082
ddele,all,all
nsel,all
ldread,temp,361,,,,temp,rth
save
solve
*DO,I,1,4
nsel,s,node,,I+482,I+1082,600
ddele,all,all
nsel,all
ldread,temp,I+361,,,,temp,rth
save
solve
*ENDDO
nsel,s,node,,487,498
ddele,all,all
nsel,all
nsel,s,node,,1087,1098
ddele,all,all
nsel,all
ldread,temp,377,,,,temp,rth
save
solve
nsel,s,node,,499,513
ddele,all,all
nsel,all
nsel,s,node,,1099,1113
ddele,all,all
nsel,all
ldread,temp,392,,,,temp,rth
save
solve
nsel,s,node,,514,543
ddele,all,all
nsel,all
nsel,s,node,,1114,1143
```

```
ddele,all,all
nsel,all
ldread,temp,422,,,,temp,rth
save
solve
nsel,s,node,,544,573
ddele,all,all
nsel,all
nsel,s,node,,1144,1173
ddele,all,all
nsel,all
ldread,temp,452,,,,temp,rth
save
solve
nsel,s,node,,574,600
ddele,all,all
nsel,all
nsel,s,node,,1174,1200
ddele,all,all
nsel,all
ldread,temp,479,,,,temp,rth
save
solve
ldread,temp,481,,,,temp,rth
save
solve
*DO,I,1,4
ldread,temp,481+I,,,,temp,rth
save
solve
*ENDDO
*DO,I,1,5,2
ldread,temp,486+I,,,,temp,rth
save
solve
*ENDDO
ldread,temp,496,,,,temp,rth
save
solve
fini
/exit
```

APPENDIX C

The following program is the ANSYS input file for 2D heat transfer analysis of narrow gap pipe welding and CSI processes.

```
/PREP7
ET,1,55,,,1
mp,dens,1,8000
mp,hf,1,1.0
mptemp,1,0,100,200,300,400,500
mptemp,7,600,700,800,900,1000,1100
mptemp,13,1200,1300,1400,1500,1600,1673
mptemp,19,1673.1,1723,3100
mpdata,kxx,1,1,8.116,9.734,11.352,12.97,14.588,16.206
mpdata,kxx,1,7,17.824,19.442,21.06,22.678,24.296,25.914
mpdata,kxx,1,13,27.532,29.15,30.768,32.386,34.004,35.185
mpdata,kxx,1,19,35.186,41.358,211.111
mpdata,c,1,1,465.4,478.76,492.12,505.48,518.84,532.2
mpdata,c,1,7,545.56,558.92,572.28,585.64,599.0,612.36
mpdata,c,1,13,625.72,639.08,652.44,665.8,679.16,688.913
mpdata,c,1,19,688.914,788.0,788.0
mpdata,enth,1,1,0.0,3.77664e08,7.66016e08,1.16505e09,1.57478e09,1.9952e09
mpdata,enth,1,7,2.4263e09,2.86809e09,3.32057e09,3.78374e09,4.2576e09,4.74214e09
mpdata,enth,1,13,5.23737e09,5.74329e09,6.2599e09,6.7872e09,7.32518e09,7.72466e09
mpdata,enth,1,19,9.84466e09,1.014e10,1.88206e10
K,1,7.5*0.0254
K,2,7.5*0.0254,0.12*0.0254
K,3,7.5*0.0254,3*0.0254
K,4,7.5625*0.0254,3*0.0254
K,5,8*0.0254,3*0.0254
K,6,8*0.0254,0.125*0.0254
K,7,8.05*0.0254
K,8,7.5625*0.0254
K,9,7.5625*0.0254,0.12*0.0254
K,10,7.5*0.0254,10*0.0254
K,11,7.5625*0.0254,10*0.0254
```

```
K,12,8.0*0.0254,10*0.0254
L,1,2
L,2,3
L,3,4
L,4,5
L,5,6
L,6,7
L,7,8
L,8,9
L,9,2
L,8,1
L,9,6
L,9,4
L,3,10
L,10,11
L,11,12
L,12,5
L,4,11
LESIZE,1,,,3
LESIZE,2,,,10
LESIZE,3,,,1
LESIZE,4,,,6
LESIZE,5,,,10
LESIZE,6,,,3
LESIZE,7,,,6
LESIZE,8,,,3
LESIZE,9,,,1
LESIZE,10,,,1
LESIZE,11,,,6
LESIZE,12,,,10
LESIZE,13,,,4
LESIZE,14,,,1
LESIZE,15,,,6
LESIZE,16,,,4
LESIZE,17,,,4
AL,1,9,8,10
AL,2,3,12,9
AL,4,5,11,12
AL,6,7,8,11
AL,3,13,14,17
AL,4,17,15,16
amesh,all
```

```
wsort,y
save
fini
/solu
antype,trans,new
timint,off
time,1e-06
nropt,full,,on
tunif,298
nsel,s,loc,y,0
dsym,symm,y
nsel,all
esel,s,elem,,74,91
ekill,all
esel,all
esel,s,live
nsle,s
nsel,inve
d,all,temp,298
nsel,all
esel,all
esel,s,live
nsel,r,loc,x,8.0*0.0254
sf,all,conv,-1,298
nsel,all
esel,all
esel,s,live
nsel,r,loc,x,7.5*0.0254
sf,all,conv,-1,298
nsel,all
esel,all
esel,s,live
nsel,r,loc,y,10.0*0.0254
sf,all,conv,-1,298
nsel,all
esel,all
esel,s,live
nsel,r,loc,x,7.5625*0.0254
nsel,r,loc,y,,0.12*0.0254
sf,all,conv,-1,298
nsel,all
esel,all
```

```
esel,s,live
nsel,r,loc,x,7.5625*0.0254,8.0*0.0254
nsel,r,loc,y,0.12*0.0254,0.125*0.0254
sf,all,conv,-1,298
nsel,all
esel,all
save
solve
pi=acos(-1)
timint,on
kbc,0
autots,on
ncnv,0
nsubsb,10000
time,(2*pi*7.5625/7.4)
esel,s,live
esel,r,elem,,1
sfedele,all,2,conv
sfe,all,2,hflux,,18712337,13407975
bfe,all,hgen,1,5.3173959e09,1.199855e10,8.597336e09,3.8100806e09
esel,all
esel,s,live
esel,r,elem,,2
sfedele,all,2,conv
sfe,all,2,hflux,,0,4932518.5
bfe,all,hgen,1,0,0,3.1627833e09,1.4016503e09
esel,all
esel,s,live
esel,r,elem,,3
sfedele,all,2,conv
sfe,all,2,hflux,,0,931632.42
bfe,all,hgen,1,0.0,0.0,5.973725e08,2.6473755e08
esel,all
save
solve
esel,s,live
esel,r,elem,,1,3
sfedele,all,2,hflux
bfedele,all,hgen
sfe,all,2,conv,0,-1
esel,all
time,10
```

```
save
solve
time,20
save
solve
time,40
save
solve
time,70
save
solve
time,100
save
solve
time,150
save
solve
time,200
save
solve
time,300
save
solve
time,(2*pi*7.5625*60/3.7)
save
solve
esel,s,elem,,1,3
sfedele,all,2,conv
esel,all
esel,s,elem,,23,33,10
sfedele,all,2,conv
esel,all
nsel,s,node,,109,112
ddele,all,temp
nsel,all
nsel,s,node,,101,102
ddele,all,temp
nsel,all
esel,s,elem,,79
ealive,all
bfe,all,hgen,1,0.0,13181341.0,0.0,0.0
esel,all
```

```
esel,s,elem,,85
ealive,all
bfe,all,hgen,1,0.0,6.978848e07,0.0,0.0
esel,all
esel,s,elem,,91
ealive,all
bfe,all,hgen,1,0.0,1.8970475e08,2.6475431e08,0.0
esel,all
esel,s,elem,,90
ealive,all
sfe,all,4,hflux,,34679351,24848841
bfe,all,hgen,1,1.5933342e10,5.2631979e09,7.345384e09,2.2237e10
esel,all
esel,s,elem,,84
ealive,all
sfe,all,4,hflux,,0.0,9141378.2
bfe,all,hgen,1,5.8615488e09,1.9362223e09,0.0,0.0
esel,all
esel,s,elem,,78
ealive,all
sfe,all,4,hflux,,0.0,1726583.2
bfe,all,hgen,1,7.807103e08,3.6570516e08,0.0,0.0
esel,all
time,(2*pi*(7.5625+(8.0-7.5625)/3.0)/8.0)+770.53928
save
solve
esel,s,elem,,78,90,6
sfedele,all,4,hflux
bfedele,all,hgen
sfe,all,4,conv,0,-1
esel,all
esel,s,elem,,79,91,6
bfedele,all,hgen
esel,all
time,781.59339
save
solve
time,791.59339
save
solve
time,811.59339
save
```

```
solve
time,851.59339
save
solve
time,901.59339
save
solve
time,1001.59339
save
solve
time,1201.59339
save
solve
time,1497.0326
save
solve
esel,s,elem,,78,90,6
sfedele,all,4,conv
esel,all
esel,s,elem,,43,53,10
sfedele,all,2,conv
esel,all
nsel,s,node,,105,108
ddele,all,temp
nsel,all
nsel,s,node,,99,100
ddele,all,temp
nsel,all
esel,s,elem,,77
ealive,all
bfe,all,hgen,1,0.0,31202201.0,0.0,0.0
esel,all
esel,s,elem,,83
ealive,all
bfe,all,hgen,1,0.0,1.6519973e08,0.0,0.0
esel,all
esel,s,elem,,89
ealive,all
bfe,all,hgen,1,0.0,4.4905946e08,6.2671296e08,0.0
esel,all
esel,s,elem,,88
ealive,all
```

```
sfe,all,4,hflux,,82091201,58820916
bfe,all,hgen,1,3.7716e10,1.2459e10,1.738e10,5.2626e10
esel,all
esel,s,elem,,82
ealive,all
sfe,all,4,hflux,,0.0,21639006
bfe,all,hgen,1,1.3875161e10,4.5833273e09,0.0,0.0
esel,all
esel,s,elem,,76
ealive,all
sfe,all,4,hflux,,0.0,4087080.2
bfe,all,hgen,1,1.84805794e09,8.6567869e08,0.0,0.0
esel,all
time,(2*pi*(7.5625+(8.0-7.5625)*2.0/3.0)/8.0)+1497.0326
save
solve
esel,s,elem,,76,88,6
sfedele,all,4,hflux
bfedele,all,hgen
sfe,all,4,conv,0,-1
esel,all
esel,s,elem,,77,89,6
bfedele,all,hgen
esel,all
time,1508.2012
save
solve
time,1518.2012
save
solve
time,1538.2012
save
solve
time,1578.2032
save
solve
time,1658.2032
save
solve
time,1758.2032
save
solve
```

```
time,1958.2032
save
solve
time,2237.2704
save
solve
esel,s,elem,,76,88,6
sfedele,all,4,conv
esel,all
esel,s,elem,,63,73,10
sfedele,all,2,conv
esel,all
nsel,s,node,,103,104
ddele,all,temp
nsel,all
nsel,s,node,,95,98
ddele,all,temp
nsel,all
esel,s,elem,,75
ealive,all
bfe,all,hgen,1,0.0,11595252.0,0.0,0.0
esel,all
esel,s,elem,,81
ealive,all
bfe,all,hgen,1,0.0,6.139094e07,0.0,0.0
esel,all
esel,s,elem,,87
ealive,all
bfe,all,hgen,1,0.0,1.6687789e08,2.3289685e08,0.0
esel,all
esel,s,elem,,86
ealive,all
sfe,all,4,hflux,,30506442,21858821
bfe,all,hgen,1,1.402e10,4.6299e09,6.46e09,1.96e10
esel,all
esel,s,elem,,80
ealive,all
sfe,all,4,hflux,,0.0,8041411.1
bfe,all,hgen,1,5.1562383e09,1.7032399e09,0.0,0.0
esel,all
esel,s,elem,,74
ealive,all
```

```
sfe,all,4,hflux,,0.0,1518826.3
bfe,all,hgen,1,6.867687e08,3.2170045e08,0.0,0.0
esel,all
time,(2*pi+2237.2704)
save
solve
esel,s,elem,,74,86,6
sfedele,all,4,hflux
bfedele,all,hgen
sfe,all,4,conv,0,-1
esel,all
esel,s,elem,,75,87,6
bfedele,all,hgen
esel,all
time,2248.5536
save
solve
time,2258.5536
save
solve
time,2278.5536
save
solve
time,2318.5536
save
solve
time,2398.5536
save
solve
time,2518.5536
save
solve
time,2718.5536
save
solve
time,2991.2526
save
solve
time,6000.0000
save
solve
time,9000.0000
```

```
nsel,all
d,all,temp,298
save
solve
ddele,all,temp
tunif,298
nsel,s,loc,x,7.5*0.0254
nsel,r,loc,y,,1.5*0.0254
d,all,temp,77
sfdele,all,conv
sf,all,conv,-1,77
nsel,all
nsel,s,loc,x,8.0*0.0254
nsel,r,loc,y,,2.0*0.0254
d,all,temp,323
sf,all,conv,-1,323
nsel,all
time,9100.0000
save
solve
time,9200.0000
save
solve
time,9300.0000
save
solve
time,9320.0000
save
solve
time,9360.0000
save
solve
nsel,s,loc,x,7.5*0.0254
nsel,r,loc,y,,1.5*0.0254
ddele,all,temp
sfdele,all,conv
sf,all,conv,-1,298
nsel,all
nsel,s,loc,x,8.0*0.0254
nsel,r,loc,y,,2.0*0.0254
ddele,all,temp
sfdele,all,conv
```

```
sf,all,conv,-1,298
nsel,all
time,9365.0000
save
solve
time,9375.0000
save
solve
time,9395.0000
save
solve
time,9435.0000
save
solve
time,9535.0000
save
solve
time,9735.0000
save
solve
time,11000.0
save
solve
time,20000.0
nsel,all
d,all,temp,298
tunif,298
save
solve
fini
/exit
```

APPENDIX D

The following program is the ANSYS input file for 2D stress analysis of narrow gap pipe welding and CSI processes.

```
/PREP7
resume,temp1,db,,0
esel,all
nsel,all
ETCHG
et,1,42,,,1
mp,alpx,1,16.12e-06,2.85e-09
mp,reft,1,298
mp,nuxy,1,0.2620625,5.97632e-5
mpdata,ex,1,1,202.0e9,200.00e9,199.0e9,197.00e9,191.00e9,184.00e9
mpdata,ex,1,7,177.00e9,169.00e9,159.e9,146.00e9,133.00e9,120.00e9
mpdata,ex,1,13,110.00e9,85.00e9,60.000e9
tref,298
TB,BKIN,1,6
tbtemp,77
tbdata,1,246.8e06,5000.07e06
tbtemp,366.0
tbdata,1,197.9e6,4000.0e06
tbtemp,589.00
tbdata,1,144.80e6,2000.0e6
tbtemp,755.00
tbdata,1,130.30e6,1300.0e6
tbtemp,922.00
tbdata,1,104.8e6,800.00e6
tbtemp,1089.0
tbdata,1,68.0e6,200.00e6
save
finish
/solu
antype,0,new
nlgeom,on
```

```
nropt,auto,,on
nsel,s,loc,y,0
dsym,symm,y
nsel,all
kbc,0
autots,on
nsubst,100
neqit,25
save
solve
nsel,s,node,,95,112
d,all,all,0
nsel,all
ldread,temp,4,,,,temp1,rth
save
solve
ldread,temp,5,,,,temp1,rth
save
solve
ldread,temp,6,,,,temp1,rth
save
solve
ldread,temp,11,,,,temp1,rth
save
solve
nsel,s,node,,109,112
ddele,all,all
nsel,all
nsel,s,node,,101,102
ddele,all,all
nsel,all
ldread,temp,14,,,,temp1,rth
save
solve
ldread,temp,15,,,,temp1,rth
save
solve
ldread,temp,17,,,,temp1,rth
save
solve
ldread,temp,20,,,,temp1,rth
save
```

```
solve
nsel,s,node,,99,100
ddele,all,all
nsel,all
nsel,s,node,,105,108
ddele,all,all
nsel,all
ldread,temp,23,,,,temp1,rth
save
solve
ldread,temp,24,,,,temp1,rth
save
solve
ldread,temp,25,,,,temp1,rth
save
solve
ldread,temp,27,,,,temp1,rth
save
solve
ldread,temp,29,,,,temp1,rth
save
solve
nsel,s,node,,95,98
ddele,all,all
nsel,all
nsel,s,node,,103,104
ddele,all,all
nsel,all
kbc,0
autots,on
nsubst,100000
ncnv,0
ldread,temp,33,,,,temp1,rth
save
solve
ldread,temp,34,,,,temp1,rth
save
solve
ldread,temp,35,,,,temp1,rth
save
solve
ldread,temp,36,,,,temp1,rth
```

```
save
solve
ldread,temp,37,,,,temp1,rth
save
solve
ldread,temp,38,,,,temp1,rth
save
solve
ldread,temp,39,,,,temp1,rth
save
solve
ldread,temp,40,,,,temp1,rth
save
solve
kbc,0
ldread,temp,41,,,,temp1,rth
save
solve
ldread,temp,42,,,,temp1,rth
save
solve
ldread,temp,43,,,,temp1,rth
save
solve
ldread,temp,44,,,,temp1,rth
save
solve
ldread,temp,45,,,,temp1,rth
save
solve
ldread,temp,46,,,,temp1,rth
save
solve
ldread,temp,47,,,,temp1,rth
save
solve
ldread,temp,48,,,,temp1,rth
save
solve
ldread,temp,49,,,,temp1,rth
save
solve
```

```
ldread,temp,50,,,,temp1,rth
save
solve
ldread,temp,51,,,,temp1,rth
save
solve
ldread,temp,52,,,,temp1,rth
save
solve
ldread,temp,53,,,,temp1,rth
save
solve
fini
/exit
```

VITA

The author was born in Shanghai, China on December 7, 1962. He attended Shanghai Jiao Tong University in Shanghai, China, where he received his Bachelor and Master of Engineering degrees in Materials Science and Engineering in 1984 and 1987, respectively.

After graduation the author worked as an Instructor in Department of Materials Science and Engineering of Shanghai University of Engineering Science from 1987 to 1989. He came to Oregon Graduate Institute to pursue his Ph.D. in September, 1989.